PHOTO-INDUCED ELECTRON AND ENERGY TRANSFER IN DONOR-ACCEPTOR SYSTEMS FEATURING A SPIN-COUPLED METAL DIMER

By

Daniela Mariana Arias-Rotondo

A DISSERTATION

Submitted to
Michigan State University
in partial fulfillment of the requirements
for the degree of

Chemistry – Doctor of Philosophy

2018

ABSTRACT

PHOTO-INDUCED ELECTRON AND ENERGY TRANSFER IN DONOR-ACCEPTOR SYSTEMS FEATURING A SPIN-COUPLED METAL DIMER

By

Daniela Mariana Arias-Rotondo

Molecular species containing two or more paramagnetic centers in close proximity may exhibit properties that are distinct from those of the individual centers. In these spin-coupled systems, the spin exchange interaction creates an array of new spin states within both the ground- and excited-state manifolds, thereby impacting magnetic as well as optical properties of the system. Research in our group focuses on the influence that changes in electronic structure due to spin exchange have on reactivity, specifically with regard to photo-induced electron and energy transfer processes.

Previous work in our group has suggested a connection between the strength of spin exchange and the rate constant for bimolecular electron transfer. To circumvent the problems inherent to bimolecular systems (diffusion-limited kinetics, poorly defined donor-acceptor distance and/or relative orientation) we have designed donor-acceptor (D-A) assemblies using a μ-oxo μ-carboxylatodiiron(III) core acceptor covalently linked to a Ru(II) polypyridyl donor, where the strength of spin coupling within the diiron(III) core can be modified by protonating the oxo bridging group. Thus, Heisenberg spin exchange may be used to alter the spin states available to the acceptor without changing its composition and/or structural properties.

In this dissertation, the synthesis and characterization of several D-A systems are discussed; steady-state and time-resolved absorption and emission spectroscopies were

used to explore the effect of spin exchange in electron and energy transfer processes taking place within these assemblies. Our results show that electron transfer into excited spin states may be invoked to explain some of the reactivity trends observed.

The major drawback of the synthetic design used to prepare the D-A systems studied in this work is their lability, which in some cases led to rapid decomposition of the assemblies in solution. Synthetic efforts to build more robust D-A complexes are also described.

Copyright by
DANIELA MARIANA ARIAS-ROTONDO
2018

Para mis viejos, por hacerme firmes las raíces y fuertes las alas.

ACKNOWLEDGMENTS

[the story of grad school] "…is one of idealism, struggle, despair, passion, success, failure and enormously long lunch breaks." –Douglas Adams, *Life, the Universe and Everything*.

To my advisor, Jim McCusker, thank you for all of your encouragement and support through the years, for all the opportunities you gave me, and for entertaining my ideas even when you didn't completely agree with them.

I have my undergrad advisor, Luis Baraldo, to thank for inviting me to work in his lab, and introducing me to ruthenium chemistry (okay, I'm not so sure about that one). Thank you for believing in me, opening many, many doors for me and being a steadfast supporter all these years. And of course, a big shout out to "el T4" (Meli, Cadra, G, Rolo, Bruno), a group of awesome people and great scientists.

To Gary Blanchard, thank you for letting me use the TCSPC many times, for the scientific advice, and for laughing at my jokes. Thank you for always taking the time to help me when I needed it. The chemistry grad students are lucky to have Uncle Gary looking after them.

The McCusker group as a whole has been a massive source of support throughout my graduate career. To each and every one of you, thank you for all the scientific discussions, the proofreading and editing, for putting up with my crankiness, my short fuse, and my language barrier. Thank you for all the lunches, the shenanigans, the amazing quotes, and for making even the worst days bearable. But, also, thank you: **Alli** (for the scientific/grad school related advice, for encouraging me and listening to all of

my ramblings), **Dong** (for all the synthetic advise and the many jokes), **Kate** (for teaching me ruthenium chemistry *via* your lab notebooks, replying all my "please help" emails, and for all the good times at conferences), **Annie** (you have been a mentor, a friend, a fantastic co-worker, a partner-in-craft… I still miss working with you), **Lindsey** (for the synthetic advise, and for being a gentle and surprisingly calm presence in the lab), **Lisa** (for training me on most of the instruments I've been in charge of), **Drew** (I didn't imagine this when we met, but you are by far the labmate I've missed the most; you were always willing to help or just hang out for a while and make me laugh. I'm glad I managed to earn your trust as time went by), **Larry** (you'll always be Hulk to me. Thank you for not smashing anything in my vicinity), **Eileen** (thank you for sharing my Harry Potter/Firefly/Castle enthusiasm), **Tyler** (thank you for taking a chance working with me. It's been amazing to see you grow as a person and a scientist. I'm sure you'll get your sarcastic self far, young grasshopper), **Jennie** (thank you for being the Brain to my Heart and my scientific sister; I'm still not sure how you put up with me for so long), **Monica** (thank you for literally giving me a shoulder to cry on; not only I have awesome memories with you, I also have an absurd amount of your selfies on my phone), **Selene** (thank you for helping me make the group more exotic; also, you're welcome for all those macaroons – please don't hurt me), **Jon** (three words: Shakira for columns; and thank you for brushing my hair when I was stressed), **Bryan** (I'll be calling you to get my horoscope; thank you for the game nights and the impromptu game sessions), **Sara** (thank you for the many conversations we've had, the ridiculous and the serious ones too; I'm going to miss you a lot), **Chris** (thank you for the many geek conversations, for celebrating May

the 4th with me, and for blushing so damn easily), **Matt** (I think we make a pretty good team; thank you for picking up my slack when I got too busy. You're a karaoke legend), **Karl** (I'm glad we have a similar sense of humor; thank you for making me laugh) and **Hayden** (I'm counting on you to help carry the board game torch in the group).

A big thank you to Richard Staples, for solving my crystal structures, even if I didn't always fill in the proper forms, and for being such a pleasant person to talk to. Thank you for all your scientific and non-scientific advice and for being the inorganic students' unofficial therapist. You were probably the only person who thought I smile all the time, but I'm sure I've proven you wrong by now.

To "Keith's friends" (whom now I'm lucky to call my own): Sean, Sheldon, Dustin, Becky, Jess and Dan. Thank you for making me feel one of the group from the beginning, for all the politically incorrect jokes, the numerous hours in the reptile room, the many game nights (special shout out to you, Dustin), the geek times and the ridiculously heated arguments on Facebook. Becky, thank you for being awesome; being able to tell you about whatever is frustrating me at a given time has been a major relief. Your non-judgmental support is invaluable, and I'm very happy to be stuck with you.

To my Argentinean friends, GRACIAS. You guys have been there through thick and thin, even long-distance. Thank you for all the memories we've made, and the ones ahead of us too. Ale, thank you for your very long-lasting friendship and the international adventures; by now I see you as a sister, to be honest. Quique, as much as we both hate saying it, I love you and I miss you. Deal with it. Iani, the distance hasn't changed our friendship, and I'm always looking forward to the next hug and the next beer. Dofi,

you're one of the smartest, most ridiculous people I've ever had the pleasure of meeting. Thank you for the long conversations and making me laugh until I cry. Germán, thank you for being a wonderful mix of labmate and friend, and for sharing in the ridiculousness.

The whole Koonter-Moyses family also deserves a big shout out. You have been kind and welcoming since the day I've met you. I can hardly express how thankful I am to have a family away from home. Troy and Anita, your love and support are part of the reason I now call Michigan home. Klinton, Kristin, Kevin, Tanya – we should go have ice cream to celebrate.

Next, I want to thank my parents, because none of this would have been possible without them. Mom, I'll never forget how heart-broken you were when I told you I'd major in chemistry ("…all those acting and painting lessons...!"). Thank you for not letting that get in the way of having my back and encouraging me. I can safely say that no one has been as supportive of me doing things they didn't quite agree with as you have. Dad, you have been one of the most enthusiastic supporters of my scientific endeavors from day one. And you have taught me that distance doesn't really matter when people love each other; I don't think I would have considered moving out of the country if it hadn't been for your example.

Last, but certainly not least, there's Keith. Thank you for making me so incredibly happy, for making sure I have more than ice cream for dinner (although I still can't understand why you don't think ice cream is its own food group) for the big and small

things you've done to help me through grad school, and for all those times you refused to let me give up. It looks like I'll become Dr. Girlfriend after all.

I'm sure there are people that I haven't mentioned here but I'm still grateful for. Thank you all for helping me get here and for cheering me on along the way. This journey would have been quite different without you.

TABLE OF CONTENTS

LIST OF TABLES xiv

LIST OF FIGURES xvii

KEY TO SYMBOLS AND ABBREVIATIONS xxxiii

Chapter 1. The Effects of Spin and Spin Density on Chemical Systems 1
1.1. Introduction: Unpaired Electrons and Spin 1
1.2. Spin Matters: From Simple Redox Reactions to Magnetic Field Effects 3
1.3. Spin Conservation and its Effects on Reactivity 7
1.4. When Spin Centers are not Isolated: Heisenberg Spin Exchange 10
1.4.1. The Anomalous Paramagnetism of Copper Acetate 10
1.4.2. Mathematical Formalism 11
1.5. Spin-Coupled Systems: Optical Properties 15
1.6. Thermodynamic Effects of Spin Coupling: Effect on Redox Potentials 17
1.7. What is Known About the Reactivity of Spin-Coupled Systems? 20
1.8. Diiron(III)-Oxo/Hydroxo Complexes 25
1.9. Bi- and Intramolecular Donor-Acceptor Systems Including a Diiron(III) Core 28
1.10. Contents of This Dissertation 34
REFERENCES 37

Chapter 2. The Photophysics of $[Ru(bpy)_3]^{2+}$ in the Context of this Dissertation 43
2.1. Introduction: Why Ru(II) Polypyridyls? 43
2.2. Optical and Electrochemical Properties 47
2.2.1. Optical Properties 47
2.2.2. Electrochemical Properties 50
2.3. Excited State Kinetics 53
2.3.1. Steady-State Emission 54
2.3.2. Time-Resolved Emission 57
2.4. Excited-State Reactivity of $[Ru(bpy)_3]^{2+}$ 59
2.4.1. Energy Transfer: Förster and Dexter Mechanisms 60
2.4.2. Electron Transfer 65
2.4.2.1. Redox Reactions in the Excited State: Redox Potentials 66
2.5. Stern-Volmer Quenching Studies 68
2.6. Identifying the Nature of the Excited State Reaction 76
2.7. Concluding Remarks 82
REFERENCES 84

Chapter 3. Synthesis and Characterization of a New Donor-Acceptor Pair in the Quest for a tren-Capped Intramolecular Assembly 89
3.1. Introduction 89
3.2. Experimental Section 91
3.2.1. Syntheses 91
3.2.2. Physical Characterization 99
3.2.3. Bimolecular Quenching Studies 103
3.3. Results and Discussion 103
3.3.1. Syntheses 103
3.3.2. Physical Characterization of the Donor and Acceptor 112
3.3.2.1. Crystal Structures 112
3.3.2.2. Ground State Absorption Spectroscopy 115
3.3.2.3. Electrochemistry 118
3.3.2.4. Steady-State and Time-Resolved Emission of $[Ru(tmb)_2(bpyac)](PF_6)_2$ 120
3.3.2.5. Magnetic Properties of $[(tren)_2Fe_2O(\mu\text{-}bpyac)](NO_3)(BPh_4)_2$ 123
3.3.3. Bimolecular Quenching Studies 125
3.4. Concluding Remarks 128
APPENDIX 130
REFERENCES 153

Chapter 4. "First Generation" of Donor-Acceptor Assemblies: Synthesis, Characterization and Challenges 158
4.1. Introduction 158
4.2. Experimental Section 159
4.2.1. Syntheses 160
4.2.2. Physical Characterization 163
4.2.3. Bimolecular Quenching Studies 165
4.2.4. Geometry Optimizations 166
4.3. Results and Discussion 166
4.3.1. Syntheses 166
4.3.2. The Instability of $[RuL_2(bpyac)]^{2+}$ Towards Decarboxylation 176
4.3.3. Photophysics of $[(Tp)_2Fe_2O(\mu\text{-}O_2CCH_3)(\mu\text{-}bpyac)Ru(bpy)_2](PF_6)_2$ 181
4.3.4. Photophysics of $[(Tp)_2Fe_2O(\mu\text{-}O_2CCH_3)(\mu\text{-}bpyac)Ru(tmb)_2](PF_6)_2$ 185
4.3.5. In-Situ Bridge Exchange? 189
4.4. Concluding Comments 191
APPENDIX 193
REFERENCES 203

Chapter 5. In Situ Bridge Exchange: Bimolecular vs. Intramolecular Quenching Mechanisms 207
5.1. Introduction 207
5.2. Experimental Section 208
5.2.1. Syntheses 209
5.2.2. Physical Characterization 212
5.2.3. Geometry Optimizations 214
5.2.4. Bimolecular Quenching Studies 215
5.3. Results and Discussion 215
5.3.1. Syntheses 215
5.3.2. Crystal Structures 219
5.3.3. Bimolecular Quenching Studies 221
5.3.4. Intramolecular Processes 235
5.3.5. Quenching Mechanisms: Bimolecular vs Intramolecular 238
5.3.6. Spin Conservation and Quenching Pathways 243
5.4. Concluding Remarks 247
APPENDIX 249
REFERENCES 266

Chapter 6. Progress Towards the Synthesis of an Intramolecular Assembly Using a Scorpionate Bifunctional Ligand 270
6.1. Introduction 270
6.2. Experimental Section 272
6.2.1. Syntheses 273
6.3. Results and Discussion 284
6.3.1. Attempts Employing a Sonogashira Coupling 284
6.3.2. Building a Scorpionate Ligand from a Bipyridine 289
6.3.3. Use of Boronic Acids to Prepare Scorpionates 292
6.4. Concluding Remarks 294
APPENDIX 296
REFERENCES 314

LIST OF TABLES

Table 3.1. Crystallographic data for **(1)**, **(2)** and $[Ru(tmb)_3](PF_6)_2$ 113

Table 3.2. Selected bond lengths and angles for **(1)**, $[Ru(tmb)_3](PF_6)_2$, and $[Ru(bpy)_3](PF_6)_2$ (from ref. 43) 114

Table 3.3. Selected bond lengths and angles for **(2)** and $[(tren)_2Fe_2O(O_2CCH_2\text{-}C_{10}H_7)]^{3+}$ (from ref. 7) 115

Table 3.4. Redox potentials for **(1)** and $[Ru(tmb)_3](PF_6)_2$ in acetonitrile. All values are referenced to the ferrocene/ferrocenium couple 119

Table 3.5. Photophysical properties of **(1)** and $[Ru(tmb)_3](PF_6)_2$. All measurements were done at room temperature, in deoxygenated acetonitrile solution 121

Table 3.6. ΔG_0^{ET}, spectral overlap integral, Förster radius, and quenching rate constant for each donor, with **(2)** as the acceptor 127

Table 3.7. Crystal data and structure refinement for 4-methyl-2,2'-bipyridine 133

Table 3.8. Bond lengths for 4-methyl-2,2'-bipyridine 133

Table 3.9. Bond angles for 4-methyl-2,2'-bipyridine 134

Table 3.10. Bond lengths for the X-ray structure of compound **(1)** 139

Table 3.11. Bond angles for the X-ray crystal structure of **(1)** 140

Table 3.12. Bond lengths for the X-ray crystal structure of $[Ru(tmb)_3](PF_6)_2$ 142

Table 3.13. Bond angles for the X-ray crystal structure of $[Ru(tmb)_3](PF_6)_2$ 143

Table 3.14. Bond lengths for the X-ray structure of compound **(2)** 145

Table 3.15. Bond lengths for the X-ray structure of compound **(2)** 146

Table 3.16. Crystallographic data for $[Fe(tmb)_3](PF_6)_2$ 148

Table 3.17. Bond lengths for the crystal structure of $[Fe(tmb)_3](PF_6)_2$ 148

Table 3.18. Bond angles for the crystal structure of $[Fe(tmb)_3](PF_6)_2$ 149

Table 4.1. Time-resolved and steady-state emission results for samples used in the study of **(4)** 182

Table 4.2. Time-resolved and steady-state emission results for samples used in the study of **(5)** 186

Table 4.3. Crystallographic data for $[Ru(tmb)_2(mmb)](PF_6)_2$ 198

Table 4.4. Bond lengths for the crystal structure of $[Ru(tmb)_2(mmb)](PF_6)_2$ 199

Table 4.5. Bond angles for the crystal structure of $[Ru(tmb)_2(mmb)](PF_6)_2$ 200

Table 5.1. Crystallographic data for Rumcb, RumcbEt, and $[(Tp)_2Fe_2(OH)(O_2CCH_3)_2](OTf)$ 219

Table 5.2. Driving forces for electron transfer for the D-A pairs studied in this chapter 222

Table 5.3. Values of k_q for Rumcb and RumcbEt obtained from Stern-Volmer quenching studies 224

Table 5.4. Driving forces for electron transfer for the D-A pairs using Ru^Fmcb as the donor. The D-A distances were determined using geometry optimizations for the assemblies. See text for details 237

Table 5.5. Measured lifetimes for Ru^FmcbEt with and without quenchers, and calculated lifetimes for RumcbEt in the presence of quenchers. See text for details 239

Table 5.6. All possible values of S_T for the reactants and products of eq 5.1 (electron transfer) 244

Table 5.7. All possible values of S_T for the reactants and products of eq 5.2 (energy transfer) 246

Table 5.8. Bond lengths for the X-ray structure of Rumcb 253

Table 5.9. Bond angles for the X-ray crystal structure of Rumcb 253

Table 5.10. Bond lengths for the X-ray crystal structure of RumcbEt 255

Table 5.11. Bond angles for the X-ray crystal structure of RumcbEt 256

Table 5.12. Bond lengths for the X-ray crystal structure of $[(Tp)_2Fe_2(OH)(O_2CCH_3)_2](OTf)$ 258

Table 5.13. Bond angles for the X-ray crystal structure of $[(Tp)_2Fe_2(OH)(O_2CCH_3)_2](OTf)$ 258

Table 5.14. Electrochemical and photophysical data for the Ru(II) donors used in this chapter 263

Table 6.1. Crystallographic data for $[Ru(bpy)_2(bpy\text{-}Ph\text{-}TMS)](PF_6)_2$ and $[Ru(bpy)_2(bpy\text{-}Ph\text{-}Br)](PF_6)_2$ 292

Table 6.2. Bond lengths for the X-ray structure of $[Ru(bpy)_2(bpy\text{-}Ph\text{-}Br)](PF_6)_2$ 306

Table 6.3. Bond angles for the X-ray structure of $[Ru(bpy)_2(bpy\text{-}Ph\text{-}Br)](PF_6)_2$ 306

Table 6.4. Bond lengths for the X-ray structure of $[Ru(bpy)_2(bpy\text{-}Ph\text{-}TMS)](PF_6)_2$ 310

Table 6.5. Bond angles for the X-ray structure of $[Ru(bpy)_2(bpy\text{-}Ph\text{-}TMS)](PF_6)_2$ ... 311

LIST OF FIGURES

Figure 1.1. *d*-orbital diagrams for the reduction of a low-spin [$Co^{III}L_6$] species to a high-spin [$Co^{II}L_6$] one. 4

Figure 1.2. Photolysis of dibenzyl ketone, showing MIE-induced isotope sorting pathways. 5

Figure 1.3. Electron-transfer pathways for a D-C-A system. *CS* = charge separation; *ISC* = intersystem crossing; *CRT* = charge recombination (triplet state); *CRS* = charge recombination (singlet state); *GSR* = ground state recovery. Adapted from ref. 27. 6

Figure 1.4. Molecular structure of the D–A assemblies used to study the conservation of spin during energy transfer. From ref. 31. Reprinted with permission from AAAS. 8

Figure 1.5. Reaction schemes for Re_3Cr (A) and Re_3Co (B) showing the spin states of reactants and products. From ref. 31. Reprinted with permission from AAAS 9

Figure 1.6. Spin ladders for a system consisting of two S = ½ centers. The antiferromagnetic interaction is shown on the left; the ferromagnetic, on the right. 14

Figure 1.7. Spectra at 10 K of $MnCl_2$ doped with Ti^{2+} (upper trace) and $MgCl_2$ doped with Ti^{2+} (lower trace). In the $MnCl_2$ spectrum all bands below 17,500 cm^{-1} are due to Ti^{2+}. Reprinted from ref. 34, with permission from Elsevier. 16

Figure 1.8. π absorption spectrum of the $^6A_1 \rightarrow {}^4A_1$ region of $CsMg_{0.95}Mn_{0.05}Cl_3$ at various temperatures. The highest energy band corresponds to a single-ion transition. Inset: observed band areas (dots) and Boltzmann populations (full lines) calculated using the coupling constant for this system. Reprinted from ref. 39. Copyright 1984 American Chemical Society. 17

Figure 1.9. Schematic representation of the active sites of [2Fe-2S] ferredoxins (left) and rubredoxins (right). 19

Figure 1.10. Normalized electron transfer rate constant versus the spin-coupling constant (*J*). The arrows indicate the range of *J* values for which the ground state is ½ or $^9/_2$ respectively. The dotted line corresponds to the minimum activation barrier for the pathway starting from S = ½, whereas the solid

line is the minimum barrier from S = $^9/_2$. Reprinted with permission from ref. 29. Copyright 1997 American Chemical Society 23

Figure 1.11. Reversible binding of dioxygen to deoxyHr to form oxyHr. Reprinted with permission from ref. 9. Copyright 1999 American Chemical Society. See text for details 25

Figure 1.12. Left: Tp-capped diferric oxo/hydroxo-bridged cores. Right: Spin ladder for a system with two antiferromagnetically coupled $S = {}^5/_2$ spin centers 27

Figure 1.13. Plot of the logarithm of the quenching constant (corrected for diffusion, k'_q) versus the driving force for photoinduced electron transfer from a Ru(II) donor to a diiron(III) acceptor. The red circles correspond to oxo-bridged iron(III) dimers; the blue circles represent hydroxo-bridged acceptors. Adapted from ref. 67. See text for details..... 31

Figure 1.14. Two ways to covalently attach the donor and the {Fe_2O} acceptor explored in this dissertation..... 32

Figure 1.15. Drawing of $[Fe_2O(O_2CCH_2C_{10}H_7)_2(TACN\text{-}Me_3)_2]^{2+}$, shown as 50% thermal ellipsoids. The distance between the ring containing C15 on one naphthalene group and the C5 atom on the other is only 4 Å, short enough to favor excimer formation. Reprinted with permission from ref. 71. Copyright 2002 American Chemical Society 33

Figure 2.1. Tris(2,2'-bipyridine) ruthenium(II), $[Ru(bpy)_3]^{2+}$ 44

Figure 2.2. Simplified kinetic scheme for a general quenching process..... 45

Figure 2.3. Electronic absorption spectrum of $[Ru(bpy)_3](PF_6)_2$ in acetonitrile solution at room temperature. The inset shows an expanded view of the metal-to-ligand charge transfer band. See text for details 48

Figure 2.4. A qualitative representation of a metal-to-ligand charge-transfer state in $[Ru(bpy)_3]^{2+}$. The spatial separation of charge within the molecule following light absorption is the underlying reason for the redox activity of the excited state 49

Figure 2.5. Simplified molecular orbital diagram for an octahedral compound with π-acceptor ligands. The three main types of electronic transitions typically observed in metal polypyridyl complexes are indicated by the arrows ... 50

Figure 2.6. Cyclic voltammogram of $[Ru(bpy)_3](PF_6)_2$ in CH_3CN, using 0.1 M tetrabutylammonium hexafluorophosphate ($TBAPF_6$) as supporting

electrolyte. Potentials are referenced to the ferrocene/ferrocenium couple 51

Figure 2.7. Simplified potential energy surface diagram for $[Ru(bpy)_3]^{2+}$ 54

Figure 2.8. Electronic absorption spectrum (black trace) and steady state emission spectrum (red trace) of $[Ru(bpy)_3](PF_6)_2$ in acetonitrile solution at room temperature 55

Figure 2.9. Time-resolved emission data (grey line) for $[Ru(bpy)_3]^{2+}$ in acetonitrile solution at room temperature. The sample was excited at 475 nm and emission was detected at 620 nm (as shown in the inset). The red trace shows the fit to a single exponential decay with τ = 930 ns 58

Figure 2.10. Electron and energy transfer mechanisms 60

Figure 2.11. Simplified diagram showing the coupling of the donor (D) and acceptor (A) transition dipoles. Transitions represented in the same color are coupled together 62

Figure 2.12. Schematic emission spectrum of the donor and absorption spectrum of the acceptor. The shaded region is the spectral overlap reflecting the resonance condition needed for Förster energy transfer to occur 62

Figure 2.13. Thermodynamic cycle relating the excited and ground state redox potentials of $[Ru(bpy)_3]^{2+}$ 67

Figure 2.14. Simulated Stern-Volmer plots based on time-resolved (blue) and steady-state (red) emission experiments. The lines correspond to the fits according to equations 2.30, 2.32 or 2.33. For these simulations, K_D = 6000 M^{-1}, K_S = 1000 M^{-1} 75

Figure 2.15. Kinetic traces for $[Ru(bpy)_3]^{2+}$ following MLCT excitation at 475 nm in acetonitrile solution. Left: λ_{probe} = 450 nm. The negative signal (i.e., "bleach") is due to the presence of Ru^{III} (loss of Ru^{II}) in the excited state relative to the ground state. Right: λ_{probe} = 370 nm. This positive feature arises due to the presence of the reduced ligand in the MLCT excited state 77

Figure 2.16. Left: schematic absorption spectra of the ground and excited states. Right: schematic representation of a transient absorption plot. The positive feature is shown in red, the bleach is in blue 79

Figure 2.17. Simulated TA traces for $[Ru(bpy)_3]^{2+}$ following MLCT excitation with no quencher (a, b), in the presence of an energy transfer acceptor (c, d); in the presence of an electron donor (e, f); and in the presence of an electron acceptor (g, h) 81

Figure 3.1. Two possible bifunctional bridging ligands for the tren-capped intramolecular assembly 104

Figure 3.2. Synthetic route used to prepare 2,2'-bipyridine-4-acetic acid (bpyac). The yields for each individual step are shown below the corresponding molecule 105

Figure 3.3. General strategy to make heteroleptic Ru(II) compounds in two steps. "X" may also be a solvent molecule 107

Figure 3.4. Synthesis of compound **(1)**, $[Ru(tmb)_2(bpyac)](PF_6)_2$ 108

Figure 3.5. Synthesis of compound **(2)**, $[(tren)_2Fe_2O(\mu\text{-}bpyac)](NO_3)(BPh_4)_2$ 109

Figure 3.6. Representative examples of the many routes explored to synthesize a tren-capped D-A assembly 110

Figure 3.7. ORTEP drawing of $[Fe(tmb)_3]^{2+}$ obtained from a single-crystal X-ray structure determination. When possible, atoms are represented as 50% probability thermal ellipsoids. Only one possible molecule in the disorder is shown. Hydrogen atoms and anions are omitted for clarity. The full lists of bond lengths and angles are compiled in the appendix to this chapter 112

Figure 3.8. ORTEP drawings of $[Ru(tmb)_2(bpyac)]^{2+}$ **(1)** (left) and $[(tren)_2Fe_2O(\mu\text{-}bpyac)]^{3+}$ **(2)** (right) obtained from single-crystal X-ray structure determinations. Atoms are represented as 50% probability thermal ellipsoids. Hydrogen atoms and anions are omitted for clarity. The full lists of bond lengths and angles are compiled in the appendix to this chapter 114

Figure 3.9. Electronic absorption spectrum of **(1)** in acetonitrile solution at room temperature. The inset shows the MLCT band. See text for details 116

Figure 3.10. Electronic absorption spectrum of **(2)** (black trace) and $[(tren)_2Fe_2O(\mu\text{-}O_2CCH_3)_2](ClO_4)_3$ (red trace) in acetonitrile solution, and bpyac in aqueous solution (blue trace; its absorbance was normalized at 280 nm). All spectra were taken at room temperature. The inset shows the lower energy features. See text for details 118

Figure 3.11. Cyclic voltammogram of **(1)** in acetonitrile with 0.1 M $TBAPF_6$ as supporting electrolyte. The insets show the DPV traces 119

Figure 3.12. Cyclic voltammogram of **(2)** in acetonitrile with 0.1 M $TBAPF_6$ as supporting electrolyte. The inset shows the DPV trace 120

Figure 3.13. Steady-state emission spectra of **(1)** (black trace) and $[Ru(tmb)_3](PF_6)_2$ (red trace) in deoxygenated acetonitrile solution at room temperature 121

Figure 3.14. Time resolved emission traces for **(1)** (black trace) and $[Ru(tmb)_3](PF_6)_2$ (red trace) in deoxygenated acetonitrile solution at room temperature 123

Figure 3.15. Effective magnetic moment as a function of temperature for **(2)** obtained with an applied magnetic field of 2.50 T. The black circles are the experimental data points, and the red trace is a fit to eq 3.2 with $J = -124\ cm^{-1}$ 124

Figure 3.16. Quenching data for **(1)** (black circles) and $[Ru(tmb)_3](PF_6)_2$ (red circles) with varying concentrations of **(2)**. The lines correspond to fits to the Stern–Volmer equation 125

Figure 3.17. Overlay of the normalized emission spectra for **(1)** (black trace) and $[Ru(tmb)_3](PF_6)_2$ (red trace), and the electronic absorption spectrum of **(2)** (green trace). All spectra taken in acetonitrile 126

Figure 3.18. ^1H NMR of (2-pyridacyl)pyridinium iodide in DMSO-d_6 131

Figure 3.19. ESI-MS of (2-pyridacyl)pyridinium iodide. Top: calculated isotope pattern for $[M–I]^+$ ($C_{12}H_{11}N_2O$). Bottom: experimental result 131

Figure 3.20. ^1H NMR of 4-methyl-2,2'-bipyridine in $CDCl_3$ 132

Figure 3.21. ESI-MS of 4-methyl-2,2′-bipyridine. Top: calculated isotope pattern for $[M+H]^+$ ($C_{11}H_{11}N_2$). Bottom: experimental result 132

Figure 3.22. ORTEP drawing of 4-methyl-2,2'-bipyridine obtained from single-crystal X-ray structure determination. Atoms are represented as 50% probability thermal ellipsoids. Hydrogen atoms are omitted for clarity 133

Figure 3.23. ^1H NMR of 2,2′-bipyridine-4-acetic acid in DMSO-d_6 134

Figure 3.24. ESI-MS of 2,2′-bipyridine-4-acetic acid. Top: calculated isotope pattern for $[M+H]^+$ ($C_{12}H_{11}N_2O_2$). Bottom: experimental result 135

Figure 3.25. ^{1}H NMR of 4,4',5,5'-tetramethyl-2,2'-bipyridine in $CDCl_3$ 135

Figure 3.26. ^{1}H NMR spectrum of $Ru(tmb)_2Cl_2$ in DMSO-d_6 136

Figure 3.27. ^{1}H NMR spectrum of $Ru(bpy)_2Cl_2$ in DMSO-d_6 136

Figure 3.28. ^{1}H NMR spectrum of **(1)** in CD_3CN 137

Figure 3.29. ESI-MS of **(1)** 137

Figure 3.30. ESI-MS of **(1)**. Top left: calculated isotope pattern for $[M–2PF_6]^{2+}$ ($C_{40}H_{42}N_6O_2Ru$). Bottom left: experimental result. Top right: calculated isotope pattern for $[M–PF_6]^+$ ($C_{40}H_{42}N_6O_2RuPF_6$). Bottom right: experimental result 138

Figure 3.31. ORTEP drawing of $[Ru(tmb)_2(bpyac)]^{2+}$ obtained from single-crystal X-ray structure determination, showing all the atom labels. Atoms are represented as 50% probability thermal ellipsoids. Hydrogen atoms and anions are omitted for clarity 138

Figure 3.32. ^{1}H NMR of $[Ru(tmb)_3](PF_6)_2$ in CD_3CN 141

Figure 3.33. ESI-MS of $[Ru(tmb)_3](PF_6)_2$. Top left: calculated isotope pattern for $[M–2PF_6]^{2+}$ ($C_{42}H_{48}N_6Ru$). Bottom left: experimental result. Top right: calculated isotope pattern for $[M–PF_6]^+$ ($C_{42}H_{48}N_6RuPF_6$). Bottom right: experimental result 141

Figure 3.34. ORTEP drawing of $[Ru(tmb)_3]^{2+}$ obtained from single-crystal X-ray structure determination, showing the atom labels; half of the atoms are symmetry equivalent and their labels are not included. Atoms are represented as 50% probability thermal ellipsoids. Hydrogen atoms and anions are omitted for clarity 142

Figure 3.35. ESI-MS of **(2)**. Top: calculated isotope pattern for $[M–BPh_4]^+$ ($C_{48}H_{65}N_{11}BO_6Fe_2$). Bottom: experimental result 144

Figure 3.36. ORTEP drawing of $[(tren)_2Fe_2O(\mu\text{-bpyac})]^{3+}$ obtained from single-crystal X-ray structure determination. Atoms are represented as 50% probability thermal ellipsoids. Hydrogen atoms and anions are omitted for clarity 144

Figure 3.37. ORTEP drawing of $[Fe(tmb)_3]^{2+}$ obtained from a single-crystal X-ray structure determination. When possible, atoms are represented as 50%

probability thermal ellipsoids. Only one possible molecule in the disorder is shown. Hydrogen atoms and anions are omitted for clarity.....147

Figure 3.38. Electronic absorption spectrum of $[Ru(tmb)_3](PF_6)_2$ in acetonitrile solution at room temperature.....150

Figure 3.39. Cyclic Voltammogram for $[Ru(tmb)_3](PF_6)_2$ in acetonitrile with 0.1 M $TBAPF_6$ as supporting electrolyte. The insets show the DPV traces 151

Figure 3.40. Effective magnetic moment (black circles) as a function of temperature for $[(tren)_2Fe_2O(\mu\text{-bpyac})](NO_3)(BPh_4)_2$ measured at 1.00 T. The red trace is a fit to eq 3.2 with $J = -128$ cm^{-1}.....151

Figure 3.41. Time-resolved emission traces for $[Ru(tmb)_2(bpyac)]^{2+}$ in the presence of increasing concentrations of $[(tren)_2Fe_2O(\mu\text{-bpyac})](NO_3)(BPh_4)_2$. The data points up to 0.055 μs were omitted when fitting the data to an exponential decay 152

Figure 3.42. Time-resolved emission traces for $[Ru(tmb)_3](PF_6)_2$ in the presence of increasing concentrations of $[(tren)_2Fe_2O(\mu\text{-bpyac})](NO_3)(BPh_4)_2$. The data points before 0.045 μs were omitted when fitting the data to an exponential decay 152

Figure 4.1. Bridge-exchange reaction to prepare $(Tp)_2Fe_2O(\mu\text{–bpyac})_2$.....167

Figure 4.2. Synthesis of compound **(3)**, $[Ru(bpy)_2(bpyac)](PF_6)_2$.....168

Figure 4.3. Bridge exchange reaction to synthesize $[(Tp)_2Fe_2O(\mu\text{-}O_2CCH_3)(\mu\text{-bpyac})Ru(bpy)_2](PF_6)_2$ **(4)** 168

Figure 4.4. ESI-MS of **(4)**. Top left: predicted isotope pattern for $[M–PF_6]^+$ for a formate-bridged assembly ($C_{51}H_{46}N_{18}O_5B_2Fe_2RuPF_6$). Top right: predicted pattern for $[M–PF_6]^+$ ($C_{52}H_{48}N_{18}O_5B_2Fe_2RuPF_6$). Bottom: Experimental results ...169

Figure 4.5. Geometry optimization of a possible intramolecular assembly incorporating two Ru(II) donors. See text for details.....170

Figure 4.6. Top: Simulated electronic absorption spectrum of **(4)** (black trace), generated by adding the spectra of **(3)** (red trace) and $(Tp)_2Fe_2O(O_2CCH_3)_2$ (blue trace). Bottom: Representative electronic absorption spectra for SEC fractions in the synthesis of **(4)**. The dashed black trace is the simulated spectrum of the assembly; the red trace corresponds to early column fractions; the green traces, to intermediate ones. Later fractions are shown in purple 172

Figure 4.7. Ball-and-stick renderings of $[Ru(bpy)_2(bpyac)]^{2+}$ (left), $[Ru(bpy)_2(mmb)]^{2+}$ (center; these two are based on the crystal structure of **(1)**) and $(Tp)_2Fe_2O(\mu\text{-}O_2CCH_3)_2$ (right, from its crystal structure). Shown in green are the longest atom-to-atom distances in each molecule (in Å) 174

Figure 4.8. Synthesis of bpyester 175

Figure 4.9. Synthesis of compound **(6),** $[Ru(tmb)_2(bpyester)](PF_6)_2$ 176

Figure 4.10. ESI-MS of "**(3)**". Top: predicted isotope pattern for $[M\text{-}CO_2\text{–}2PF_6]^{2+}$ ($[Ru(bpy)_2(mmb)]^{2+}$). Middle: isotope pattern for $[M\text{-}CO_2\text{–}PF_6]^{+}$ ($[Ru(bpy)_2(mmb)](PF_6)^{+}$). Bottom: spectrum obtained 178

Figure 4.11. ORTEP drawing of $[Ru(tmb)_2(mmb)]^{2+}$ obtained from single-crystal X-ray structure determinations. Atoms are represented as 50% probability thermal ellipsoids. Anions are omitted for clarity. All bond lengths and angles are compiled in the appendix to this chapter 179

Figure 4.12. HPLC-MS results for **(1)**. Bottom: full elution profile for the sample; the arrows indicate the relevant peaks. Center: elution profile for $[Ru(tmb)_2(mmb)]^{2+}$, extracted from the full profile. Top: elution profile for $[Ru(tmb)_2(bpyac)]^{2+}$, extracted from the full profile. The peak at ~0.8 min corresponds to a portion of the sample that did not interact with the HPLC column material and was eluted with the solvent front. The identity of other peaks is unclear. 180

Figure 4.13. Steady-state emission spectra for **(3)** (black trace), **(4)** (red trace) and a 100:1 mixture of $(Tp)_2Fe_2O(\mu\text{-}O_2CCH_3)_2$ and **(3)** (green trace). Left: the emission intensity at each point was divided by the absorbance of that sample at the excitation wavelength. Right: all traces normalized to their emission maximum 183

Figure 4.14. Steady-state emission spectra for **(1)** (black trace), **(5)** (red trace) and a 1:1 mixture of $(Tp)_2Fe_2O(\mu\text{-}O_2CCH_3)_2$ and **(1)** (green trace). Left: the emission intensity at each point was divided by the absorbance of that sample at the excitation wavelength. Right: all traces normalized to their emission maximum 186

Figure 4.15. Overlay of the steady-state emission spectra for **(4)** (purple trace) and **(5)** (red trace), and the absorption spectrum for $(Tp)_2Fe_2O(\mu\text{-}O_2CCH_3)_2$ (black trace) 187

Figure 4.16. Steady-state emission spectra for **(1)** (black trace), **(5)** (red trace) and the same sample of **(5)** 24 hours after being prepared, kept under argon (blue trace)..... 188

Figure 4.17. Quenching data for **(1)** (red) and **(6)** (blue) in the presence of increasing concentrations of $[(Tp)_2Fe_2(OH)(\mu\text{-}O_2CCH_3)_2]^+$. The open circles correspond to time-resolved emission results, and the full circles, to steady-state emission. Left: all datasets shown. Right: the steady-state data for **(1)** are omitted..... 189

Figure 4.18. ESI-MS of $(Tp)_2Fe_2O(bpyac)_2$. Top: predicted isotope pattern for $[M+H]^+$ ($C_{42}H_{39}N_{16}O_5B_2Fe_2$). Bottom: experimental result..... 194

Figure 4.19. ^1H NMR of (presumed) **(3)** in CD_3CN..... 194

Figure 4.20. ESI-MS of **(3)**. Top: predicted isotope pattern for $[M–2PF_6]^{2+}$ ($C_{32}H_{26}N_6O_2Ru$). Bottom: experimental result..... 195

Figure 4.21. ESI-MS of **(4)**. Top: predicted isotope pattern for $[M–2PF_6]^{2+}$ ($C_{52}H_{48}N_{18}O_5B_2Fe_2Ru$). Bottom: experimental result..... 195

Figure 4.22. ESI-MS of **(5)**. Top: predicted isotope for $[M–2PF_6]^{2+}$ of the formate-bridged assembly ($C_{59}H_{62}N_{18}O_5B_2Fe_2Ru$). Middle: predicted isotope pattern for $[M–2PF_6]^{2+}$ ($C_{60}H_{64}N_{18}O_5B_2Fe_2Ru$). Bottom: experimental results..... 196

Figure 4.23. ESI-MS of **(5)**. Top: predicted isotope for $[M–PF_6]^{2+}$ ($C_{60}H_{64}N_{18}O_5B_2Fe_2RuPF_6$). Bottom: experimental result..... 196

Figure 4.24. ^1H NMR of bpyester in $CDCl_3$..... 197

Figure 4.25. ESI-MS of bpyester. Left: predicted isotope pattern for $C_{13}H_{13}N_2O_2$. Right: experimental result..... 197

Figure 4.26. ^1H NMR of **(6)** in CD_3CN. The peaks at $\delta < 3$ ppm correspond to solvents used when working up the reaction..... 198

Figure 4.27. ORTEP drawing of $[Ru(tmb)_2(mmb)]^{2+}$ obtained from single-crystal X-ray structure determinations, showing the labelling system. Atoms are represented as 50% probability thermal ellipsoids. Anions are omitted for clarity..... 199

Figure 4.28. Time-resolved emission traces for **(3)** (black), **(4)** (red) and a 100:1 mixture of $(Tp)_2Fe_2O(\mu\text{-}O_2CCH_3)_2$ and **(3)** (green). All samples prepared in deoxygenated acetonitrile, all spectra collected at room temperature..... 202

Figure 4.29. Time-resolved emission traces for **(1)** (black), **(5)** (red), and a 1:1 mixture of $(Tp)_2Fe_2O(\mu\text{-}O_2CCH_3)_2$ and **(1)** (green). All samples prepared in deoxygenated acetonitrile, spectra collected at room temperature 202

Figure 5.1. Donors used in this chapter, both in their acid and ester forms 217

Figure 5.2. Diiron(III) cores used as acceptors in this chapter 217

Figure 5.3. ORTEP drawings of $[Ru(bpy)_2(mcb)]^{2+}$ (left) and $[Ru(bpy)_2(mcbEt)]^{2+}$ (right) obtained from single-crystal X-ray structure determinations. Hydrogens, counterions, and solvent molecules are omitted for clarity. Atoms are represented as 50% probability ellipsoids. The lists of bond lengths and angles are compiled in the appendix to this chapter 220

Figure 5.4. ORTEP drawing of $[(Tp)_2Fe_2(OH)(O_2CCH_3)_2]^+$ obtained from single-crystal X-ray structure determination. Atoms are represented as 50% probability ellipsoids. Hydrogen positions were calculated geometrically, except for the H on O1, which was found by difference Fourier methods and refined isotropically. The triflate ion and crystallization solvent are omitted for clarity. The full list of bond lengths and angles is included in the appendix to this chapter 221

Figure 5.5. Stern-Volmer data for RumcbEt in the presence of $[(Tp)_2Fe_2(OH)(O_2CCH_2Cl)_2](ClO_4)$ (blue) and with $(Tp)_2Fe_2O(O_2CCHCl_2)_2$ (green). Full circles: SSEm data, open circles: TREm data 223

Figure 5.6. Left: Stern-Volmer plots for $[(Tp)_2Fe_2(OH)(O_2CCH_2Cl)_2](ClO_4)$ quenching RumcbEt (blue) and Rumcb (red). Right: data for $(Tp)_2Fe_2O(O_2CCHCl_2)_2$ quenching RumcbEt (green) and Rumcb (purple). Full circles: SSEm data, open circles: TREm data 224

Figure 5.7. Left: Time-resolved emission results for Rumcb with variable concentrations of $[(Tp)_2Fe_2(OH)(O_2CCH_2Cl)_2](ClO_4)$ (red circles) and $(Tp)_2Fe_2O(O_2CCHCl_2)_2$ (purple cirlces). The solid lines are fits to the Stern-Volmer equation. Right: Overlay of the steady-state emission spectrum of RumcbEt (black trace) and the electronic absorption spectra of $(Tp)_2Fe_2O(O_2CCHCl_2)_2$ (purple trace) and $[(Tp)_2Fe_2(OH)(O_2CCH_2Cl)_2](ClO_4)$ (red trace) 225

Figure 5.8. Time-resolved emission data for Rumcb in the presence of $(Tp)_2Fe_2O(O_2CCHCl_2)_2$ (purple), $[(Tp)_2Fe_2(OH)(O_2CCH_2Cl)_2]^+$ (green, open squares), and $[(Tp)_2Fe_2(OH)(O_2CCH_3)_2]^+$ (green, full squares). See text for details 226

Figure 5.9. Normalized steady-state emission spectra for Rumcb without quencher (black trace). Left: in the presence of $(Tp)_2Fe_2O(O_2CCHCl_2)_2$ 51 μM (blue trace). Right: in the presence of $[(Tp)_2Fe_2(OH)(O_2CCH_3)_2](OTf)$ 41 μM (red trace)..... 227

Figure 5.10. Steady-state emission data for Rumcb in the presence of 20 μM $(Tp)_2Fe_2O(O_2CCHCl_2)_2$ (purple trace), and 21 μM $[(Tp)_2Fe_2(OH)(O_2CCH_3)_2](OTf)$ (red trace) 228

Figure 5.11. TCSPC data for Rumcb with 0.17 mM $[(Tp)_2Fe_2(OH)(O_2CCH_3)_2](OTf)$ (left) and 0.23 mM $(Tp)_2Fe_2O(O_2CCHCl_2)_2$ (right)..... 229

Figure 5.12. Left: Steady-state emission spectrum of Ru^FmcbEt alone (black trace) and in the presence of $(Tp)_2Fe_2O(O_2CCHCl_2)_2$ (green trace). Right: Ru^Fmcb without quencher (black trace) and combined with $(Tp)_2Fe_2O(O_2CCHCl_2)_2$ (purple trace). The concentration of the quencher is the same in both cases 230

Figure 5.13. Normalized steady-state emission spectra for Ru^Fmcb without quencher (black trace). Left: in the presence of: $(Tp)_2Fe_2O(O_2CCHCl_2)_2$ 51 μM (green trace) and 0.20 mM (blue trace). Right: in the presence of: $[(Tp)_2Fe_2(OH)(O_2CCH_3)_2](OTf)$ 41 μM (orange trace) and 0.17 mM (red trace)..... 231

Figure 5.14. Time-resolved emission traces for Ru^FmcbEt without quenchers (black, dashed), and in the presence of $[(Tp)_2Fe_2(OH)(O_2CCH_3)_2]^+$ (blue) and $(Tp)_2Fe_2O(O_2CCHCl_2)_2$ (green). The quencher concentrations are comparable in both cases. See text for details..... 232

Figure 5.15. TREm data for Ru^Fmcb in the presence of increasing concentrations of $(Tp)_2Fe_2O(O_2CCHCl_2)_2$ (purple) and $[(Tp)_2Fe_2(OH)(O_2CCH_3)_2]^+$ (red, right). The full black line corresponds to Ru^Fmcb in the absence of quenchers, and the black dashed trace is for Ru^FmcbEt..... 233

Figure 5.16. TREm traces for Ru^Fmcb (purple) and Ru^FmcbEt (green), both in the presence of 0.24 mM $(Tp)_2Fe_2O(O_2CCHCl_2)_2$. The inset shows the trace at shorter times (purple trace), along with the IRF of the instrument (dashed black line)..... 235

Figure 5.17. Time-resolved emission traces for Ru^Fmcb in the presence of the different acceptors. Left: $(Tp)_2Fe_2O(O_2CCHCl_2)_2$ (blue), $(Tp)_2Fe_2O(O_2CCF_3)_2$ (green). Right: $[(Tp)_2Fe_2(OH)(O_2CCH_3)_2](OTf)$. The red lines are fits to a monoexponential decay..... 237

Figure 5.18. Overlay of the steady-state emission spectra of RumcbEt (purple trace) and Ru^{F}mcbEt (red trace) and the electronic absorption spectrum of $(Tp)_2Fe_2O(O_2CCHCl_2)_2$ (black trace) 239

Figure 5.19. Transient absorption data (λ_{pump}: 475 nm, λ_{probe}: 450 nm). Top left: RumcbEt. Bottom left: RumcbEt + $[(Tp)_2Fe_2(OH)(O_2CCH_3)_2](OTf)$. Top right: Ru^{F}mcbEt. Bottom right: Ru^{F}mcbEt + $[(Tp)_2Fe_2(OH)(O_2CCH_3)_2](OTf)$ 240

Figure 5.20. Overlay of the steady-state emission spectrum of Ru^{F}mcbEt (red trace) and the electronic absorption spectra of $(Tp)_2Fe_2O(O_2CCF_3)_2$ (blue trace) and $(Tp)_2Fe_2O(O_2CCHCl_2)_2$ (green trace). All spectra were collected in acetonitrile 241

Figure 5.21. Simulated plot of k_{ET} vs. the D-A distance for the Ru^{F}mcb systems. Dexter transfer is shown in blue, and Förster in red 242

Figure 5.22. Left: Spin ladder for a mixed-valence iron dimer. Right: Spin ladder for an excited diferric core 244

Figure 5.23. ^{1}H NMR of 4,4'-dimethyl-2,2'-bipyridine in $CDCl_3$ 250

Figure 5.24. ^{1}H NMR of 4'-methyl-2,2'-bipyridine-4-carboxaldehyde in $CDCl_3$ 250

Figure 5.25. ^{1}H NMR of 4'-methyl-2,2'-bipyridine-4-carboxylic acid in DMSO-d_6 251

Figure 5.26. ^{1}H NMR of Rumcb in CD_3CN 251

Figure 5.27. ESI-MS of Rumcb. Top left: predicted isotope pattern for $[M–2PF_6]^{2+}$ ($C_{32}H_{26}N_6O_2Ru$). Top right: predicted isotope pattern for $[M–PF_6]^{+}$ ($C_{32}H_{26}N_6O_2RuPF_6$).Bottom: experimental results 252

Figure 5.28. ORTEP drawing of $[Ru(bpy)_2(mcb)]^{2+}$ obtained from single-crystal X-ray structure determination, showing all atomic labels. Atoms are represented as 50% probability thermal ellipsoids. Hydrogen atoms and anions are omitted for clarity 252

Figure 5.29. ORTEP drawing of $[Ru(bpy)_2(mcbEt)]^{2+}$ obtained from single-crystal X-ray structure determination, showing all atomic labels. Atoms are represented as 50% probability thermal ellipsoids. Hydrogen atoms and anions are omitted for clarity 255

Figure 5.30. ORTEP drawing of $[Tp_2Fe_2(OH)(O_2CCH_3)_2]^{+}$ obtained from single-crystal X-ray structure determination, showing the atom labels. Atoms are

represented as 50% probability thermal ellipsoids. Hydrogen atoms and anions are omitted for clarity 257

Figure 5.31. ESI-MS of Ru^{F}mcb. Top left: predicted isotope pattern for $[M–2PF_6]^{2+}$ ($C_{36}H_{22}N_6O_2F_{12}Ru$). Top right: predicted isotope pattern for $[M–PF_6]^{+}$ ($C_{36}H_{22}N_6O_2F_{12}RuPF_6$).Bottom: experimental results..... 260

Figure 5.32. ^{1}H NMR of Ru^{F}mcb in CD_3CN 260

Figure 5.33. Time-resolved emission traces for Rumcb in the presence of varying concentrations of $(Tp)_2Fe_2O(O_2CCHCl_2)_2$ 261

Figure 5.34. Time-resolved emission traces for Rumcb in the presence of varying concentrations of $[(Tp)_2Fe_2(OH)(O_2CCH_2Cl)_2](ClO_4)$ 261

Figure 5.35. Left: Stern-Volmer plots for $[(Tp)_2Fe_2(OH)(O_2CCH_2Cl)_2](ClO_4)$/Rumcb (red), $[(Tp)_2Fe_2(OH)(O_2CCH_2Cl)_2](ClO_4)$/RumcbEt (blue). Right: Stern-Volmer plots for $(Tp)_2Fe_2O(O_2CCHCl_2)_2$/Rumcb (purple) and $(Tp)_2Fe_2O(O_2CCHCl_2)_2$/RumcbEt (green) 262

Figure 5.36. Steady-state emission spectra for Rumcb (black trace) and RumcbEt (red trace) in deoxygenated acetonitrile solution at room temperature 262

Figure 5.37. Left: Steady-state emission spectrum of Ru^{F}mcbEt alone (black trace) and in the presence of $[(Tp)_2Fe_2(OH)(O_2CCH_3)_2](OTf)$ (blue trace). Right: Ru^{F}mcb without quencher (black trace) and combined with $[(Tp)_2Fe_2(OH)(O_2CCH_3)_2](OTf)$ (red trace). The concentration of the quencher is the same in both cases 263

Figure 5.38. Steady-state emission spectra for Ru^{F}mcb (black trace) and Ru^{F}mcbEt (red trace) in deoxygenated acetonitrile solution at room temperature 263

Figure 5.39. Time-resolved emission trace for Ru^{F}mcb in the absence of a quencher, showing no short-lived processes in the timescale relevant to the D-A assemblies 264

Figure 5.40. Time-resolved emission traces for Ru^{F}mcb in the presence of $(Tp)_2Fe_2O(O_2CCF_3)_2$ 0.16 mM (orange trace), 0.18 mM (purple trace) and 0.20 mM (blue trace) 264

Figure 5.41. Ball-and-stick renderings of the Ru^{F}mcb-containing D-A assemblies, as obtained from geometry optimizations. From left to right: $(Tp)_2Fe_2O(O_2CCHCl_2)_2$, $(Tp)_2Fe_2O(O_2CCF_3)_2$ and $[(Tp)_2Fe_2(OH)(O_2CCH_3)_2]^{+}$ 265

Figure 5.42 Transient absorption data (λ_{pump}: 475 nm). Top left: RumcbEt (λ_{probe}: 370 nm). Bottom left: RumcbEt + $[(Tp)_2Fe_2(OH)(O_2CCH_3)_2](OTf)$ (λ_{probe}: 560 nm). Top right: Ru^FmcbEt (λ_{probe}: 370 nm). Bottom right: Ru^FmcbEt + $[(Tp)_2Fe_2(OH)(O_2CCH_3)_2](OTf)$ (λ_{probe}: 610 nm) 265

Figure 6.1. Possible bifunctional ligand designs incorporating a trispyrazolyl borate unit and a 2,2'-bipyridine. Their syntheses are discussed in this chapter 271

Figure 6.2. Previously attempted route to make *ext*-Tp via a Stille coupling 271

Figure 6.3. Use of a Sonogashira coupling to modify scorpionate ligands post-coordination. Adapted from Ref. 7 285

Figure 6.4. Synthetic route to prepare X-Ph-TpK. 289

Figure 6.5. ORTEP drawing of $[Ru(bpy)_2(bpy\text{-}Ph\text{-}Br)]^{2+}$ (left) and $[Ru(bpy)_2(bpy\text{-}Ph\text{-}TMS)]^{2+}$ (right) obtained from single-crystal X-ray structure determinations. Atoms are represented as 50% probability thermal ellipsoids. Hydrogen atoms and anions are omitted for clarity. The complete lists of bond lengths and angles are compiled in the appendix to this chapter 291

Figure 6.6. ^1H NMR of 2,2'-bipyridine-N-oxide in $CDCl_3$ 297

Figure 6.7. ^1H NMR of 4-nitro-2,2'-bipyridine-N-oxide in $CDCl_3$ 297

Figure 6.8. ^1H NMR of 4-bromo-2,2'-bipyridine-N-oxide in $CDCl_3$. The small peaks correspond to 4-bromo-2,2'-bipyridine, which is obtained as a side product 298

Figure 6.9. ^1H NMR of 4-bromo-2,2'-bipyridine in $CDCl_3$ 298

Figure 6.10. ^1H NMR of 4-((trimethylsilyl)ethynyl)-2,2'-bipyridine in $CDCl_3$ 299

Figure 6.11. ^1H NMR of 4-ethynyl-2,2'-bipyridine in $CDCl_3$ 299

Figure 6.12. ^1H NMR of p-(trimethylsilyl)iodobenzene in $CDCl_3$. The small peaks at 7.42 ppm and 7.53 ppm correspond to p-diiodobenzene and p-bis(trimethylsilyl)benzene, respectively 300

Figure 6.13. ^1H NMR of (4-iodophenyl)dibromoborane in $CDCl_3$ 300

Figure 6.14. ^{1}H NMR of potassium (4-iodophenyl)tris(1-pyrazolyl)borate in CD_3OD 301

Figure 6.15. HRMS (ESI-TOF) of (4-iodophenyl)tris(1-pyrazolyl)borate. Top: predicted pattern for $[M–K]^-$ ($C_{15}H_{13}N_6BI$). Bottom: experimental result 301

Figure 6.16. HRMS (ESI-TOF) of potassium (4-([2,2'-bipyridin]-4-ylethynyl)phenyl)tris(1-pyrazolyl)borate. Top: predicted isotope pattern for $[M–K]^-$ ($C_{27}H_{20}N_8B$). Bottom: experimental result 302

Figure 6.17. ESI-MS of $[Ru(bpy)_2(ebpy\text{-}Tp)](PF_6)$. Top: predicted isotope pattern for $[M–PF_6]^+$ ($C_{47}H_{36}N_{12}BRu$). Bottom: experimental result 302

Figure 6.18. ^{1}H NMR of 2-[4-(4-bromophenyl)-2-ethoxy-3,4-dihydro-2H-pyran-6-yl]pyridine in $CDCl_3$ 303

Figure 6.19. ^{1}H NMR of 4-(4-bromophenyl)-2,2'-bipyridine in $CDCl_3$. The peaks at 3.5 ppm (d, J = 5.2 Hz, 3H) and 0.9 ppm (q, J = 5.2 Hz, 1H) correspond to MeOH, used to recrystallize the compound 303

Figure 6.20. ESI-MS of 4-(4-bromophenyl)-2,2'-bipyridine. Top: predicted isotope pattern for $[M+H]^+$ ($C_{16}H_{12}N_2Br$). Bottom: experimental result 304

Figure 6.21. ^{1}H NMR of $[Ru(bpy)_2(bpy\text{-}Ph\text{-}Br)](PF_6)_2$ in CD_3CN 304

Figure 6.22. ESI-MS of $[Ru(bpy)_2(bpy\text{-}Ph\text{-}Br)](PF_6)_2$. Top left: predicted isotope pattern for $[M–2PF_6]^{2+}$ ($C_{36}H_{27}N_6BrRu$). Bottom left: experimental result. Top right: predicted isotope pattern for $[M–PF_6]^+$ ($C_{36}H_{27}N_6BrRuPF_6$). Bottom right: experimental result 305

Figure 6.23 ORTEP drawing of $[Ru(bpy)_2(bpy\text{-}Ph\text{-}Br)]^{2+}$ showing the labelling system. Atoms are represented as 50% probability thermal ellipsoids. Anions and solvent molecules omitted 305

Figure 6.24. ^{1}H NMR of 4-(4-(trimethylsilyl)phenyl)-2,2'-bipyridine in $CDCl_3$ 308

Figure 6.25. ESI-MS of 4-(4-(trimethylsilyl)phenyl)-2,2'-bipyridine. Top: predicted isotope pattern for $[M+H]^+$ ($C_{19}H_{21}N_2Si$). Bottom: experimental result 308

Figure 6.26. ^{1}H NMR of $[Ru(bpy)_2(bpy\text{-}Ph\text{-}TMS)](PF_6)_2$ in CD_3CN 309

Figure 6.27. ESI-MS of $[Ru(bpy)_2(bpy\text{-}Ph\text{-}TMS)](PF_6)_2$. Top left: predicted isotope pattern for $[M–2PF_6]^{2+}$ ($C_{39}H_{36}N_6RuSi$). Bottom left: experimental result.

Top right: predicted isotope pattern for $[M–PF_6]^+$ ($C_{39}H_{36}N_6RuSiPF_6$). Bottom right: experimental result.....309

Figure 6.28. ORTEP drawing of $[Ru(bpy)_2(bpy\text{-}Ph\text{-}TMS)]^{2+}$ showing the labelling system. Atoms are represented as 50% probability thermal ellipsoids. Anions and solvent molecules omitted.....310

Figure 6.29. ESI-MS of sodium phenyltris(1-pyrazolyl)borate. Top left: predicted isotope pattern for $[M–Na]^-$ ($C_{15}H_{14}N_6B$). Bottom left: experimental result. Top right: predicted isotope pattern for $[2M+Na]^-$ ($C_{30}H_{28}N_{12}B_2Na$). Bottom right: experimental result.....313

Figure 6.30. ESI-MS of sodium 4-[tris(1-pyrazolyl)borate]-2,2'-bipyridine. Top: predicted isotope pattern for $[M–Na]^+$ ($C_{19}H_{16}N_8B$). Bottom: experimental result.....313

KEY TO SYMBOLS AND ABBREVIATIONS

HDVV: Heisenberg-Dirac-Van Vleck

SQUID: Superconducting Quantum Interference Device

D–A: Donor-Acceptor

E_0: Zero-Point Energy Gap

CV: Cyclic Voltammetry

DPV: Differential-Pulse Voltammetry

MLCT: Metal-to-Ligand Charge Transfer

k_r: Rate Constant for Radiative Decay

k_{nr}: Rate Constant for Non-Radiative Decay

Φ: Radiative Quantum Yield

k_0: Observed Rate Constant (donor only)

τ: Lifetime

k_{obs}: Observed Rate Constant (with quencher)

FRET: Förster Energy Transfer

k_q: Quenching Rate Constant

K_D: Dynamic Quenching Constant

K_S: Static Quenching Constant

TA: Transient Absorption Spectroscopy

SSEm: Steady-State Emission

TREm: Time-Resolved Emission

TCSPC: Time-Correlated Single Photon Counting

GS: Ground State

ES: Excited State

DFT: Density Functional Theory

bpy: 2,2'-bipyridine

dmb: 4,4'-dimethyl-2,2'-bipyridine

tmb: 4,4',5,5'-tetramethyl-2,2'-bipyridine

mmb: 4-methyl-2,2'-bipyridine

bpyac: 2,2'-bipyridine-4-acetic acid

mcb: 4'-methyl-2,2'-bipyridine-4-carboxylic acid

mcbEt: 4'-methyl-4-ethylcarboxy-2,2'-bipyridine

KTp: Potassium hydrotris(1-pyrazolyl)borate

tren: Tris(2-aminoethyl)amine

$TBAPF_6$: Tetrabutylammonium hexafluorophosphate

NMP: N-methyl-2-pyrrolidone

DMSO: Dimethyl Sulfoxide

MeOH: Methanol

EtOH: Ethanol

ESI-MS: Electrospray Ionization Mass Spectrometry

SEC: Size-Exclusion Chromatography

IRF: Instrument Response Function

Chapter 1. The Effects of Spin and Spin Density on Chemical Systems

"The phenomenon of interaction between metal centers occupies a crossing point of two scientific areas which, without that, would ignore themselves, namely the physics of the magnetic materials and the role of the polymetallic sites in the biological processes." –Olivier Kahn[1]

1.1. Introduction: Unpaired Electrons and Spin

Electronic angular momentum (spin) is a fundamental property of nature; its existence was postulated in 1925 by Uhlenbeck and Goudsmit, who suggested that electrons behave as minuscule gyroscopes.[2] This addendum to the Schrödinger equation allowed them to explain, among other observations, why there are two closely spaced lines in the atomic spectrum of sodium (at 589.59 nm and 588.99 nm) instead of a single one at 590 nm, as predicted. It was Dirac, in the 1930s, who developed an extension to quantum mechanics where the concept of electronic spin arose naturally instead of being imposed on a previous theory, as before.

The notion that electrons carry spin is one of the basics of quantum mechanics. In the same way, one of the starting points of any discussion about magnetism is that species containing unpaired electrons have a non-zero magnetic moment.[3,4]

Scientists have studied spin and magnetism in a wide variety of chemical systems for decades;[4] areas of intense research include single-molecule magnets,[5–7] bioinorganic chemistry,[8–10] materials science,[11] and more recently, quantum computing[12–15] and spintronics.[16–18] The spin of a system is also key to interpret their optical properties: one

of the best-known examples are the different timescales of fluorescence (a spin–allowed process, where the spins of the initial and final states are the same) and phosphorescence (a spin–forbidden process).[19,20]

In the words of A. Buchachenko, "contributing almost nothing in chemical energy, being negligibly small and traditionally ignored, magnetic interactions produce spin conversion and switch over the reaction from spin forbidden to spin-allowed channels (or vice versa). Ultimately, they implement a spin control of the reactions, they modify chemical reactivity of the reagents, and they write a new, magnetic scenario of chemical reactions."[21] Remarkably, despite how intensely studied some aspects of magnetism are, the possibility of affecting chemical reactions by manipulating the spin of the reagents has been, as this author said, ignored for a number of years. Most of the efforts along these lines have focused on the effect of magnetic fields on reactions; this line of research will be briefly reviewed in section 1.2.

Our group is interested in the effects that spin and spin polarization have on the reactivity of a system, in the absence of a magnetic field. This is an area much less explored, probably in part because of how complex it can be. This chapter will examine examples of the work done on the effects of spin on reactivity, initially focusing on systems with only one paramagnetic center, then moving on to exchange-coupled systems and the effects that spin has on their optical, magnetic, and redox properties. This will not be an extensive review, as only select examples to put this research in context will be presented. Lastly, the donor–acceptor systems that are the focus of this dissertation will be introduced, along with previous work done in the area.

1.2. Spin Matters: From Simple Redox Reactions to Magnetic Field Effects

When talking about spin, an important (albeit subtle) distinction must be made: in broad terms, "spin" may refer to the total number of unpaired electrons in a molecule. However, a more specific definition of spin is concerned with the special orientation of the spin vector, even when the number of unpaired electrons does not change (this is particularly important when discussing spin-coupled systems, starting on section 1.4). Both the magnitude and orientation of the spin of a system will be examined in this chapter, and in many cases these two will be tied together. It is, however, important to be aware of this discrepancy.

As will become clear from the discussion and examples to follow, the spin state of a system influences many of its properties and its reactivity, both in terms of kinetics and thermodynamics. The first example we will discuss is the effect of the spin of a transition-metal compound on the kinetics of electron transfer.

Electron transfer (i.e., redox) reactions are ubiquitous in both chemistry and biology.[22] It is not uncommon for an electron transfer to be coupled to a change in the spin state of the system; for example, a semiquinone can be reduced to a catechol, thus going from a paramagnetic to a diamagnetic species.[23] Another very well-known example are coordination compounds, particularly those of first-row transition metals, where coordination compounds exist either in low-spin or high-spin forms.[24] Let us consider the reduction from hexacoordinated Co(III) to Co(II), where Co(III) is low-spin (LS) and Co(II) is high-spin (HS) (this is the case for $[Co(NH_3)_6]^{2+/3+}$, among others),[25] as shown in Figure 1.1.

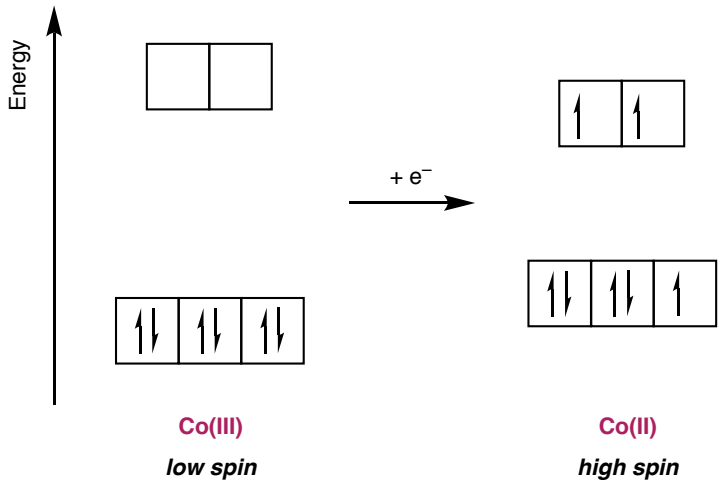


Figure 1.1. *d*-orbital diagrams for the reduction of a low-spin $[Co^{III}L_6]$ species to a high-spin $[Co^{II}L_6]$ one.

As a result of this reduction, two electrons are placed in the *d*-orbitals of the e_g set, which are antibonding with respect to the M–L bond. This change in the occupation of the *d*-orbitals of the compound has two consequences: (a) the change in the spin of the molecule and (b) a lengthening of the M–L bonds in the compound, which greatly affects the reorganization energy for this reaction. Because of this large reorganization barrier, this redox reaction is slower than one where the spin state of the system does not change, such as the reduction of $[Ru(NH_3)_6]^{3+}$. However, this is not always the case: if the spin crossover is faster than the thermal electron transfer for a given reaction, then the reorganization energy does not limit the overall reaction rate.[24] This kind of redox reaction is probably one of the simplest examples of how the spin of a system[i] can impact its reactivity, even in the absence of a magnetic field.

[i]Here, spin is understood as the total number of unpaired electrons in the molecule, regardless of the orientation of the spin vector.

An area of intense research within physical-organic chemistry, known as "spin chemistry",[21,26] studies the influence of magnetic fields on chemical reactions. This has been developed mostly in relation to photochemical organic reactions, which often involve radical species. One of the many phenomena studied in this area are magnetic isotope effects (MIEs). These highlight the effect that nuclear spin can have on reaction rates; they also "sort" isotopes, directing them towards different reaction products. For example, the photolysis of dibenzyl ketone shows MIE-induced isotope sorting, as shown in Figure 1.2.[21] Upon photoexcitation, the molecule fragments, forming a triplet radical pair; triplet-singlet (T-S) conversion then leads to recombination of the pair to produce dibenzyl ketone again. This T-S conversion is faster when one radical of the pair contains a magnetic nucleus (^{13}C) than when only non-magnetic ^{12}C is present. As a result, pairs with a ^{13}C atom recombine and regenerate the ketone, while the slower T-S conversion of the non-magnetic pairs leads to their dissociation and formation of the products (CO and 1,2-diphenylethane).[21]

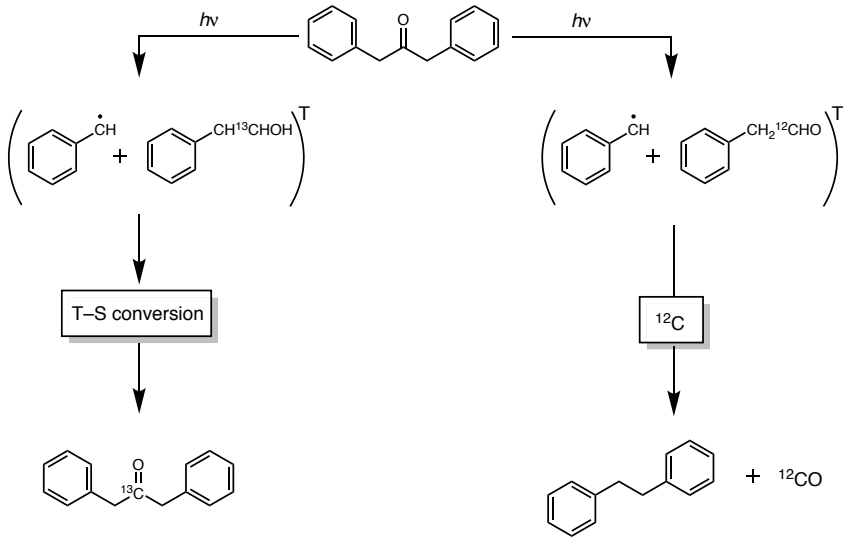


Figure 1.2. Photolysis of dibenzyl ketone, showing MIE-induced isotope sorting pathways.[21]

The effect of spin on charge transport in molecular wires has potential applications in fields such as photonics and spintronics. Along these lines, Wasielewski and coworkers have studied donor-chromophore-acceptor (D-C-A) systems, looking at the formation of a charge-separated state (D^+-C-A^-) upon excitation of the chromophore and how the fate of said state is affected by the spin of the triad. For example, attaching the TEMPO (2,2,6,6-tetramethylpiperidinoxyl) radical to the acceptor in these triads accelerates the intersystem crossing (ISC) from the singlet to the triplet radical-ion pair as a result of the strong local magnetic field that TEMPO induces on the system.[27] The fate of the charge separated state varies depending on its spin; these processes are schematized in Figure 1.3. The available pathways and their relative energies remain mostly unchanged, but their relative rate constants vary when TEMPO is present. This phenomenon is known as "spin catalysis"[28] or "enhanced ISC".[21] Another example of spin catalysis, prevalent in spectroscopy and photophysics, is the heavy atom effect.[28]

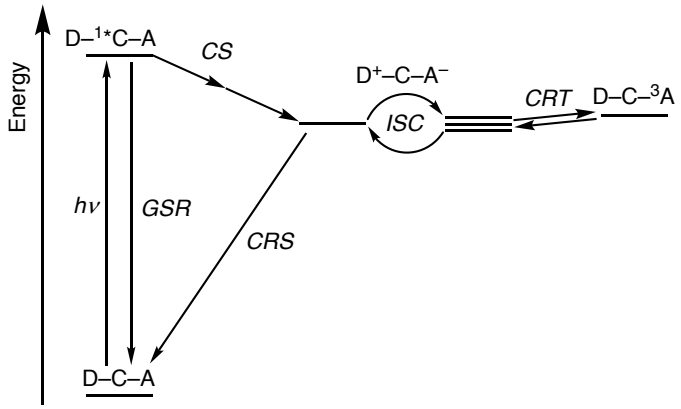


Figure 1.3. Electron-transfer pathways for a D-C-A system. *CS* = charge separation; *ISC* = intersystem crossing; *CRT* = charge recombination (triplet state); *CRS* = charge recombination (singlet state); *GSR* = ground state recovery. Adapted from ref. 27.

As was mentioned before, spin chemistry is concerned with the effect(s) of a magnetic field in chemical processes; such a magnetic field may be applied externally or

generated by a radical species (the "spin catalyst"), such as TEMPO. When explaining those effects, the details may not be simple, but there is one main theme: the presence of a magnetic field removes the degeneracy of the $\pm m_s$ levels of a spin state, which will be populated according to the Boltzmann distribution (depending on their energy, the temperature of the system, and their relaxation lifetimes). This is known as the Zeeman effect,[3] which is by definition associated to the presence of a magnetic field. However, even at zero-field the spin state of a system has an impact on its physical and photophysical properties. The remainder of this chapter will focus on zero-field phenomena.

1.3. Spin Conservation and its Effects on Reactivity

Spin, and more specifically, spin conservation, is a key concept when analyzing optical spectra.[19,20] The idea that spin must be conserved in chemical reactions is not a new concept, [9,21,26,29,30] but it is rarely used to predict or explain why some processes are (un)favorable. Previously, our group developed a formalism to incorporate the conservation of spin to the criteria for the feasibility of a reaction.[31] To this end, an intramolecular donor-acceptor system was specifically designed so that only Förster energy transfer[ii] could take place. The structure of the D–A assembly is shown in Figure 1.4: the Re(I) moiety acts as the donor, and the $M^{III}(acac)_3$ core as the acceptor. Three assemblies were prepared, with $M^{III} = Cr^{3+}$, Co^{3+} and Ga^{3+} (referred to as Re_3Cr, Re_3Co and Re_3Ga). Cobalt and chromium were used as potential acceptors, whereas gallium was

[ii]This energy transfer mechanism will be discussed in detail in Chapter 2.

chosen as a way to study the photophysical properties of the Re(I) donor in the assembly, but in the absence of an acceptor (Ga^{3+} has a d^{10} valence electronic configuration; it is thus redox inert and does not possess any electronic excited states in the visible region of the spectrum).

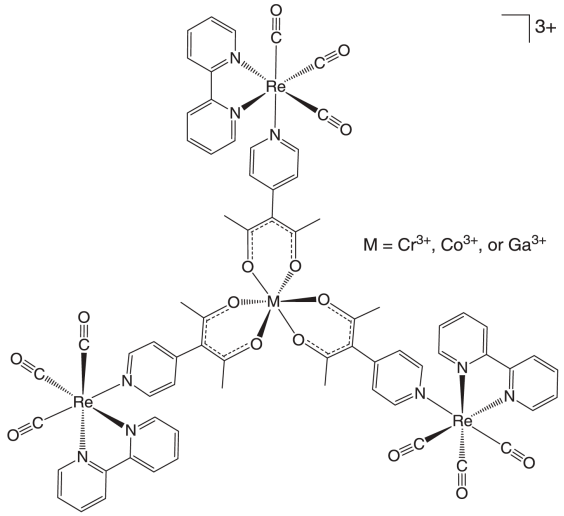


Figure 1.4. Molecular structure of the D–A assemblies used to study the conservation of spin during energy transfer. From ref. 31. Reprinted with permission from AAAS.

As expected, the emission from the Re(I) luminophore is quenched by the {$Cr(acac)_3$} acceptor in Re_3Cr. However, this is not the case for Re_3Co: the steady-state and time-resolved emission of this assembly and that of Re_3Ga are indistinguishable, indicating that no energy transfer takes place between the Re(I) and Co(III) moieties. Since the systems were designed to make Förster energy transfer favorable, the explanation to this difference in reactivity must lie elsewhere. Indeed, when the spin of the reactants and products is taken into account, the observed reactivity is easily explained. In general, for a photo-induced energy transfer as the one in (1.1), the total spin of the reactants (D* and A in this case) and the total spin of the products (D and A*) can be written as shown in equations 1.2 and 1.3.

$$D^* + A \xrightarrow{EnT} D + A^* \quad \textbf{(1.1)}$$

$$|S_T^R| = |S_{D^*} + S_A|, |S_{D^*} + S_A - 1|, \ldots, |S_{D^*} - S_A| \quad \textbf{(1.2)}$$

$$|S_T^P| = |S_D + S_{A^*}|, |S_D + S_{A^*} - 1|, \ldots, |S_D - S_{A^*}| \quad \textbf{(1.3)}$$

A reaction is considered spin-allowed if $|S_T^R|$ and $|S_T^P|$ have at least one value in common; Figure 1.5 shows the different spin values for the Re_3Cr and Re_3Co systems, which explain the absence of quenching in the latter. This report was the first example of spin conservation being explicitly invoked to explain differences in reactivity.

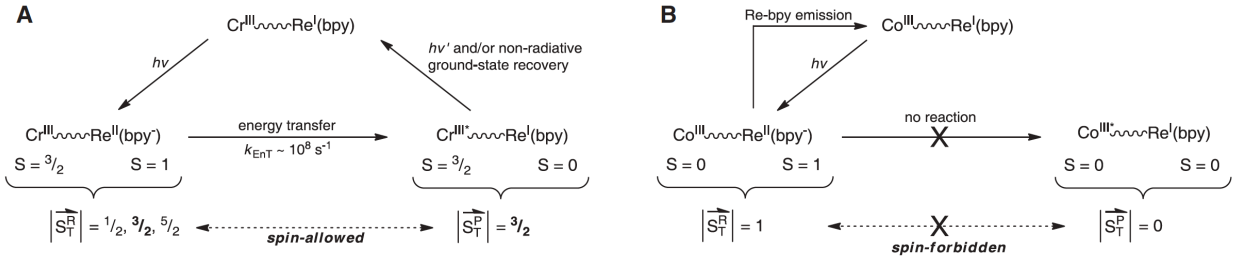


Figure 1.5. Reaction schemes for Re_3Cr (A) and Re_3Co (B) showing the spin states of reactants and products. From ref. 31. Reprinted with permission from AAAS.

So far, we have discussed how the spin state of a system can affect its properties, and, more importantly, its reactivity. In this last example, changing the spin state of the system drastically altered its reactivity towards photo-induced energy transfer. A caveat of these systems is that changing their spin state meant significantly changing their composition; ideally, we would want to alter the spin of a molecule with minimal or no changes to its structure and composition, to then study the effect of that spin change on its properties. As will be discussed below, Heisenberg spin exchange is a means to achieve this goal. In the following sections, Heisenberg spin exchange will be described,

and examples of its effects of physical and photophysical properties of chemical systems will be reviewed.

1.4. When Spin Centers are not Isolated: Heisenberg Spin Exchange

Up to this point, our discussion has focused on molecules with only one paramagnetic center, within "magnetically dilute" systems (i.e., the spin centers are so far apart from each other that they behaved as if they were isolated). However, it is not hard to imagine that when two (or more) spin centers are close to each other they may interact. Indeed, such interaction occurs, and it may lead to changes in the structure and properties of the system. This section focuses on the physical and mathematical description of such interaction.

Let us consider two or more paramagnetic centers infinitely apart from each other. The properties of a system thus defined are a linear combination of the individual properties of each center. Now, if those paramagnetic centers are allowed to come closer together, the electronic communication between them will affect the properties of the system so that they will no longer be just a linear combination of the individual ones. Such electronic communication is known as Heisenberg spin exchange; its description and, more importantly, its consequences are the focus of the rest of this chapter.

1.4.1. The Anomalous Paramagnetism of Copper Acetate

In 1951, Guha published a study on the magnetic properties of several transition-metal salts at low temperature. In this article, he divided the Cu(II) salts in three groups

based on their magnetic properties and noted that the magnetic susceptibility of copper acetate monohydrate[iii] decreased very quickly as the temperature was lowered, falling well below the spin-only value. The explanation for those three types of behavior, he said, must be attributed to their different crystalline fields. However, there was not enough structural information about copper acetate monohydrate to draw any further conclusions.[32]

A year later, Bleaney and Bowers[33] reported their own results on copper acetate monohydrate, which were in good agreement with Guha's "most surprising" data. These authors showed that at 90 K the paramagnetic resonance spectrum of copper acetate was like those of nickel salts where the Ni(II) ion had a spin of 1. To explain these observations, they proposed that pairs of Cu(II) ions were interacting to form a triplet state (parallel spins) and a singlet state (antiparallel spins). Furthermore, the singlet state had to be lower in energy, accounting for the drop of the susceptibility at very low temperatures. At the time, there were no reliable x-ray data for this compound; later experiments showed that the model proposed by Bleaney and Bowers agreed with the crystal structure of copper acetate.[4]

1.4.2. Mathematical Formalism

The pairwise interaction described by Bleaney and Bowers is known as Heisenberg spin exchange or electronic exchange coupling. This is an electrostatic interaction that arises from Pauli's exclusion principle, but may be described as the coupling between the

[iii]At the time (before X-ray structure data were available), this is the name the compound was given. It is now known as diaquatetra–μ–acetate dicopper (II). See ref. 4 for more information.

spin operators of both centers.[4,34] As such, the Hamiltonian shown in (1.4), known as Heisenberg-Dirac-Van Vleck (HDVV) Hamiltonian, can be used for a system with two spin centers. In this equation, S_1 and S_2 are the individual spins, and J is the coupling constant, which measures the strength of the electronic communication between the spin centers. It is important to highlight that this Hamiltonian can be generalized to systems with more than two spin centers,[4] although that will not be discussed in this chapter, as all the compounds studied in this dissertation have only two coupled spin centers.

$$\widehat{H} = -2J\widehat{S_1}\widehat{S_2} \qquad \textbf{(1.4)}$$

The HDVV Hamiltonian has two limitations worth noting at this point: (a) it only works for spin-only ions: this equation is no longer valid if there is orbital moment, because this leads to spin-orbit coupling, in which case S is no longer a good quantum number;[34] and (b) it is not valid in the case of magnetic class III mixed-valence dimers.[35,36] This dissertation focuses almost exclusively on diiron(III), and to a much lesser extent, dicopper(II) compounds. In both these cases spin-orbit coupling is not an issue (in general, orbital angular momentum is quenched when symmetry is lower than octahedral; in particular, it is quenched for Fe(III) even as a free ion)[37] and therefore the HDVV Hamiltonian shown above can be used. Mixed-valence compounds will not be discussed beyond this chapter.

Notice that eq 1.4 does not include any information about the mechanism of this coupling, and therefore lacks predictive character; thus the HDVV Hamiltonian is considered phenomenological.[4] J is related to electrostatic interactions, not only between the two spin centers, but between the electrons of the system as a whole. The problem is

that writing the genuine electrostatic Hamiltonian results in a much more complex equation that has no analytical solution.[1]

The solutions for (1.4) can be calculated taking $S_T = S_1 + S_2$ (known as the Kambé approximation)[38] and are shown in (1.5).

$$E(S_T) = -J[S_T(S_T + 1) - S_1(S_1 + 1) - S_2(S_2 + 1)] \qquad \textbf{(1.5)}$$

The simplest case of an exchange-coupled system consists of two centers with S = ½, like the Cu(II) dimers that Bleaney and Bowers studied. These two spins can either be parallel to each other, giving a total spin of 1 (a triplet state), or they can be antiparallel, for a total spin of 0 (a singlet state). If the singlet state is lower in energy than the triplet, then the system is said to be antiferromagnetically coupled, as shown on the left side of Figure 1.6. Conversely, if the triplet state is lower in energy, the system is ferromagnetically coupled (see right side of Figure 1.6). With the Hamiltonian written as in (1.4), a positive value of J corresponds to a ferromagnetic interaction, whereas an antiferromagnetic interaction has a negative value of J. Later in this chapter, we will examine the spin exchange in diiron(III) compounds, which have two $S = {}^5/_2$ centers. The ideas outlined here will still apply, albeit with a larger number of spin states resulting from the coupling.

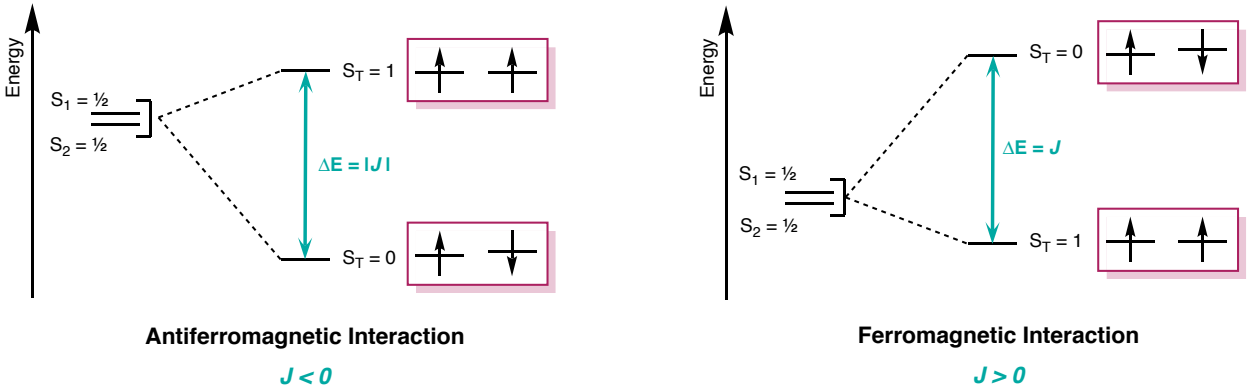


Figure 1.6. Spin ladders for a system consisting of two S = ½ centers. The antiferromagnetic interaction is shown on the left; the ferromagnetic, on the right.

For any exchange-coupled system, the population of the spin states is determined by the Boltzmann distribution.[34] This, in turn, is affected by the value of *J* and the temperature. In other words, the specific population of the spin states for a given compound depends solely on temperature. Thus, it is possible to change the spin of the system without altering its composition. It is also important to notice that, unlike the phenomena studied in the context of "spin chemistry", spin coupling is a zero-field effect. That is, different spin states have different energies even in the absence of a magnetic field.

The exchange-coupled systems discussed in this chapter and the rest of this dissertation are such that the interionic spin coupling interactions are much smaller than ligand-field effects and electron–electron repulsion. As such, Heisenberg spin exchange may be considered as a perturbation on the system,[34] and the electronic structure described mainly in terms of basic coordination chemistry concepts.

1.5. Spin-Coupled Systems: Optical Properties

As was mentioned before, spin coupled systems present unique properties, which stem from the alterations that exchange coupling causes in their electronic structure. It is worth reiterating that, because of spin coupling, the properties of these systems are not additive with respect to their components. For example, the systems shown in Figure 1.6 will have very different magnetic behaviors; at low temperatures, the system on the left will be diamagnetic while the one on the right will have a permanent magnetic dipole. One would expect that, as a result of their altered electronic structure, the unique properties of spin coupled systems go beyond their magnetism. That is indeed the case; much research has focused on the magnetic and optical properties of these systems, and, to a lesser extent, on their redox properties and reactivity.

The spectra in Figure 1.7 correspond to $MnCl_2$ (upper trace) and $MgCl_2$ (lower trace), both doped with Ti^{2+}. In the case of Ti^{2+}–doped $MnCl_2$, there is an exchange interaction between the Ti^{2+} and Mn^{2+} ions. The transitions marked $^3T_{2g}$ and $^3T_{1g}$ are spin-allowed d-d bands, and thus are not appreciably affected by spin-coupling. However, the sharp feature below 10,000 cm^{-1} corresponds to a spin-forbidden d-d transition, and its intensity is enhanced by more than two orders of magnitude as a consequence of exchange coupling.[34] The mechanism by which the intensity of spin-forbidden bands is enhanced in these systems is known as "Tanabe mechanism" and will not be reviewed here; however, McCarthy and Güdel discuss them in great detail.[34]

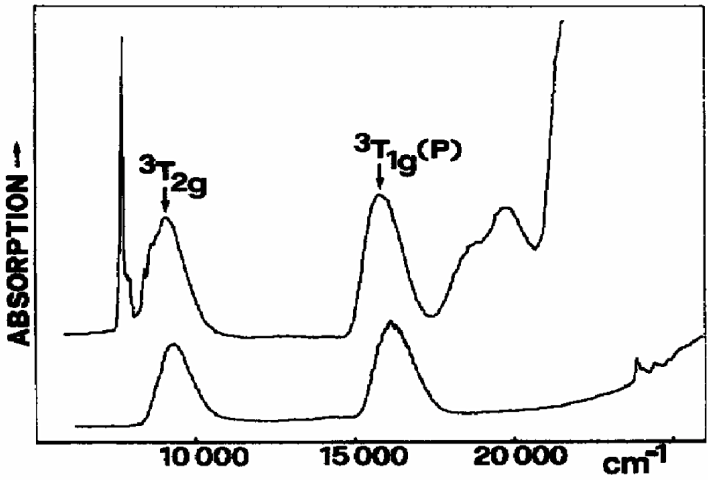


Figure 1.7. Spectra at 10 K of $MnCl_2$ doped with Ti^{2+} (upper trace) and $MgCl_2$ doped with Ti^{2+} (lower trace). In the $MnCl_2$ spectrum all bands below 17,500 cm^{-1} are due to Ti^{2+}. Reprinted from ref. 34, with permission from Elsevier.

Another effect of Heisenberg spin exchange on spin-forbidden d-d bands can be observed in Figure 1.8; the absorption spectra in this figure correspond to $CsMg_{0.95}Mn_{0.05}Cl_3$, where pairs of Mn^{2+} ions are spin-coupled (the authors proposed the presence of $[Mn_2Cl_9]^{5-}$ units).[39] The bands labeled A, B and C are considered "hot bands" because they only appear at higher temperatures (none of this are seen if the spectrum is taken at very low temperature). The inset in Figure 1.8 shows the calculated Boltzmann population of each spin state in this system, overlaid with the area observed for each band, both as a function of temperature. It can be seen that the intensity of these bands decreases with temperature, which is coincident with those spin states being depopulated (i.e., not thermally accessible at that temperature). In other words, these bands arise from spin states other than the ground state for the pairs of Mn^{2+} ions; as these states are populated, the bands become more intense. At any given temperature, band A is more intense than B or C; this is because the bands originate in progressively higher-energy spin states, which means that the spin state that gives rise to band A always has a larger

population than those for bands B and C. Additionally, in this work, the authors observe a more pronounced temperature dependence in the spectrum of the bromide analog ($CsMg_{1-x}Mn_xBr_3$), which they attribute to the Mn^{2+} pairs being less strongly coupled than in the chloride compound.[39]

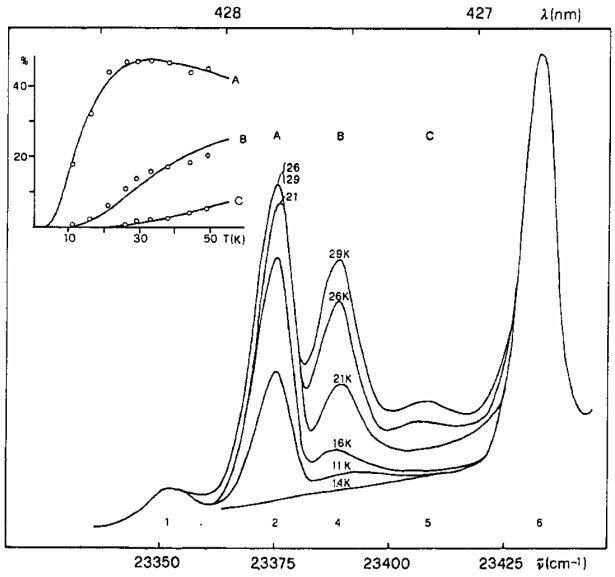


Figure 1.8. π absorption spectrum of the $^6A_1 \rightarrow {}^4A_1$ region of $CsMg_{0.95}Mn_{0.05}Cl_3$ at various temperatures. The highest energy band corresponds to a single-ion transition. Inset: observed band areas (dots) and Boltzmann populations (full lines) calculated using the coupling constant for this system. Reprinted from ref. 39. Copyright 1984 American Chemical Society.

1.6. Thermodynamic Effects of Spin Coupling: Effect on Redox Potentials

Metalloproteins have been the subject of intensive research for decades, from a biological and also physicochemical perspective.[8,9,40–45] In the case of proteins with only one metal ion in their active site, research has focused on the relationship between electronic structure, optical/electrochemical properties and biological function.[46] For proteins containing clusters with two or more metal ions in their active sites, the emphasis

has been on the spectroscopic and magnetic characterization, but the effect of spin exchange on the properties of these proteins and the way it affects their function has received considerably less attention. Many groups have researched the interplay between redox processes, mixed-valences and electron exchange;[36,47–49] with most of these studies being theoretical, and using metalloproteins or model systems, as will become apparent in the rest of this section and the next.

In the early 1980s, Bertrand and Gayda examined the Fe^{III}/Fe^{II} reduction potentials of a series of [2Fe-2S] ferredoxins and rubredoxins,[50] iron-sulfur proteins that are involved in electron transfer processes in a large number of biological systems. The active center of ferredoxins consists of two $Fe^{III}S_4$ tetrahedra that share two vertices, as shown on the left side of Figure 1.9, while rubredoxins only have one $Fe^{III}S_4$ tetrahedron (see Figure 1.9, right). Based on previously reported data (Mössbauer, UV-visible, and infrared spectra), the reducible Fe(III) ions in both kinds of proteins are very similar (in their 3+ as well as the 2+ forms), which validates their comparison. The redox potential of the Fe(III) center in ferredoxins is lowered by 100 mV or more with respect to that of rubredoxins. The stabilization of the oxidized state is likely to be caused by Heisenberg spin exchange between the two Fe(III) ions; the authors suggested that these exchange coupling interactions were closely linked to (and very likely responsible for) the difference in reduction potentials. The authors provided data to support that geometry and/or composition of the coordination environment are not responsible for these changes in redox potentials; for example, substitution of S for Se in the [2Fe-2S] clusters affects the absorption spectrum of the system but the redox potential remains

unchanged.[51] This was the first report where Heisenberg spin exchange having an effect on the redox properties of a system was proposed.

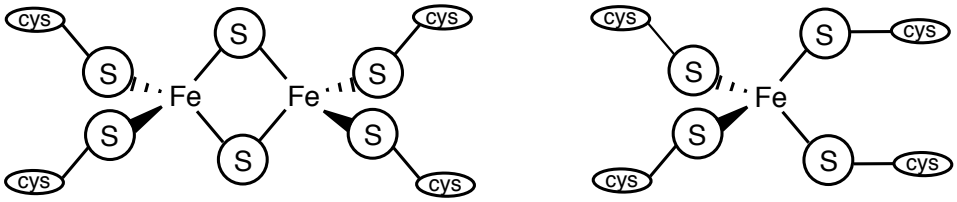


Figure 1.9. Schematic representation of the active sites of [2Fe-2S] ferredoxins (left) and rubredoxins (right).[50]

This work sparked the curiosity of others; Mouesca et al.[52] did not limit their study to [2Fe-2S] ferredoxins, but also worked with Fe-S clusters with one and four Fe atoms. They used density functional calculations to quantify the effect of not only electron exchange but also solvation and electron delocalization on redox potentials. Overall, their results for 1Fe and 2Fe clusters agree with those reported by Bertrand and Gayda.[50]

Seeing that the changes in the electronic structure brought about by Heisenberg spin exchange lead to unique optical and redox properties, one may wonder if the reactivity of a system will be affected by spin coupling, and more specifically, how can Heisenberg spin exchange be used as a small perturbation to alter the spin state of a molecule and its reactivity as a consequence. That is the main question that this dissertation tries to answer, with emphasis on photo-induced electron and energy transfer.

1.7. What is Known About the Reactivity of Spin-Coupled Systems?

Much of the initial interest on spin-coupled systems stemmed from the study of metalloproteins which have two or more metallic ions in their active sites,[40] and significant effort has been devoted to understanding the relationship between the structure of the active sites and the function of the corresponding proteins. To simplify these studies, numerous model compounds have been prepared and characterized. It is not surprising, then, that a considerable amount of the work that will be reviewed here focuses on biologically relevant molecules (either proteins or their models). It is also worth noting that a large volume of this work has been theoretical.

Another class of compounds that have been studied in relation with spin exchange are mixed-valence complexes.[35] The interplay between spin exchange and intramolecular electron transfer in these systems has been the object of much interest: in a theoretical paper, Girerd[36] explored the effect of spin exchange in mixed-valence dimers. In these compounds, the extra electron can "hop" between two metal centers, leading to double exchange, which stabilizes high-spin states.[36,53] In antiferromagnetically coupled compounds, the rate of electron transfer slows down, which may explain why most dimers with antiferromagnetic coupling belong to class II (according to the classification by Robin and Day).[35] Within this model, the activation energy for electron transfer between the ions is spin-dependent.

Blondin and Girerd[47] expanded on these ideas, looking at dinuclear compounds as well as tri- and tetranuclear ones. When both intramolecular electron transfer and electron exchange are present, the spin Hamiltonian in (1.4) must be modified to account

for the electron hopping (or double exchange) effects. For a dinuclear compound, the solutions to that Hamiltonian are shown in (1.6).

$$E_{\pm}(S_T) = -\frac{1}{2}J_0 S_T(S_T + 1) \pm B\left(S_T + \frac{1}{2}\right) \qquad \textbf{(1.6)}$$

In this equation, J_0 is analogous to J in (1.4), whereas B is an interaction energy related to double exchange; Mouesca et al. defined it as the resonance delocalization parameter for the extra electron.[52] If the spin coupling is antiferromagnetic in nature ($J_0 < 0$), there is a competition between the stabilization of the low-spin states (because of the antiferromagnetic coupling) and the effect of double exchange (stabilization of high-spin states). If the spin coupling dominates, the system is antiferromagnetically coupled and localization (or "valence trapping") occurs. Conversely, if double exchange prevails, the system becomes ferromagnetically coupled and delocalization is more favorable. On the other hand, if the nature of the spin coupling is ferromagnetic ($J_0 > 0$), this does not compete with double exchange, as both have the same effect.

In a very thorough theoretical paper, Bominaar et al.[29] studied the effect of spin exchange and double exchange on the kinetics of electron transfer. Their system consisted of a $[Fe_2S_2]^+$ donor and a diamagnetic mononuclear acceptor. If the acceptor is kept unchanged throughout the experiments, the rate constant for electron transfer depends solely on the properties of the donor. In this way, they systematically varied the strength of the spin coupling within the donor and calculated the rate constant for electron transfer in different sets of conditions. The authors noted that since electron transfer is "essentially electrostatic in nature", it is subject to spin conservation. Thus, combining this selection rule with the available spin states for the donor as a function of J, they calculated the

energetics of each possible pathway for electron transfer, originating from the ground state as well as from the excited states. When the driving force for the ground-state generated pathway is large, the excited-state pathways become important and may dominate the electron transfer process. This is possible as long as *J* is small enough to allow for thermal population of the excited states at room temperature.[iv] Figure 1.10 shows a plot of the rate constant for electron transfer as a function of *J*. Since in this case the only variable changing is the magnitude of exchange coupling in the donor, this is direct (albeit theoretical) evidence that Heisenberg spin exchange can affect the reactivity of a system. Furthermore, this suggests that a spin-coupled system could act as a "switch" for electron transfer. In other words, it should be possible to drastically affect the reactivity of a spin-coupled system by changing its coupling constant. In the case of the diiron(III) systems which are the focus of this dissertation, the coupling constant can be reduced by an order of magnitude by protonation of one of the bridging ligands.[54] This concept could find an application in the design of molecular switches; we will revisit this idea later in this dissertation.

[iv]Strictly speaking, this is true at any given temperature, but all the calculations in this paper were done at 300 K because they were focused on systems that operate under physiological conditions.

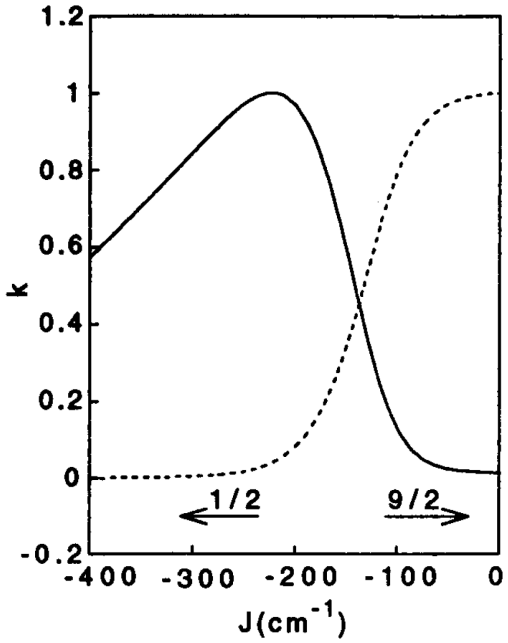


Figure 1.10. Normalized electron transfer rate constant versus the spin-coupling constant (J). The arrows indicate the range of J values for which the ground state is ½ or $^9/_2$ respectively. The dotted line corresponds to the minimum activation barrier for the pathway starting from S = ½, whereas the solid line is the minimum barrier from S = $^9/_2$. Reprinted with permission from ref. 29. Copyright 1997 American Chemical Society.

Later, these authors revisited the semi-classical model used in their 1997 paper.[30] In this new work, they expanded their model using a quantum mechanical approach. The details of their study are beyond the scope of this review, but it is important to note that their more accurate results agreed qualitatively with those from the semi-classical model. They also noted that the rate constant for electron transfer from a spin-coupled cluster cannot be calculated based on the electronic couplings of each separate metal center (in the donor) with the acceptor. Furthermore, they predicted these effects would be exacerbated for clusters with more than two paramagnetic centers (such as those present

in [3Fe-3S] and [4Fe-4S] ferredoxins), due to the higher density of spin states associated with a larger number of metal ions.

Hemerythrin (Hr) is one of the most thoroughly studied spin-coupled metalloproteins;[41] this is one of the three main proteins that can reversibly bind oxygen (the other two being hemoglobin and hemocyanin), and, unlike the other two, it has two iron ions in its active site, which are bridged by an oxo group and two carboxylates.[41] In a series of two papers, Brunold and Solomon[8,9] used DFT calculations (validated by comparison to experimental data) to study the mechanism of oxygenation of hemerythrin; the reaction (shown in Figure 1.11) involves two electron transfers from the Fe(II) centers to O_2. In the first of these two papers, they determined that the exchange coupling between the two Fe(II) centers in deoxyHr (the deoxygenated form) is weaker than in oxyHr (the oxygenated form) because the bridge in the former is a hydroxo group, versus an oxo group in the latter. The coupling is antiferromagnetic in both cases, with $J_{\text{deoxyHr}} \approx -14$ cm^{-1} and $J_{\text{oxyHr}} \approx -77$ cm^{-1}. The binding of O_2 by deoxyHr then leads to the formation of the more strongly coupled oxyHr; the authors proposed that this stronger coupling stabilizes the singlet ground state of the diiron(III) core and thus contributes to increase the driving force for the oxygenation process.

It is worth noting that these authors mention that all the spin states in deoxyHr are populated at room temperature and can take part in the reaction with O_2.[9] This suggests a link between the availability of reaction pathways with different spins and the spontaneity of the reaction, but no further discussion was provided.

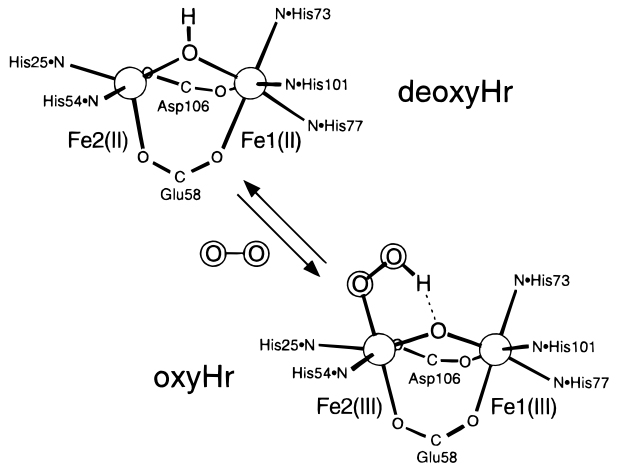


Figure 1.11. Reversible binding of dioxygen to deoxyHr to form oxyHr. Reprinted with permission from ref. 9. Copyright 1999 American Chemical Society. See text for details.

Not all of the work in this area has been theoretical. There has been a handful of reports investigating electron and energy transfer involving spin-coupled polymetallic clusters;[55–58] however, in many of these the relationship between Heisenberg spin exchange and the reactivity observed in the systems was not explored.

In summary, despite the large amount of theoretical studies on the effect of spin coupling on electron transfer involving metalloproteins and/or model systems, and the studies involving polymetallic clusters as donors or acceptors in electron/energy transfer, the impact of the spin of a system on its reactivity has remained largely uncharted.

1.8. Diiron(III)-Oxo/Hydroxo Complexes

Many proteins with two or more metal centers in their active sites are known; the desire to understand the relationship between their structure and properties has led to the study and characterization of a variety of metal clusters as model compounds, mainly

in the context of biochemistry and bioinorganic chemistry.[29,30,40,47,50] In particular, diiron(III)-oxo complexes are among the most studied by inorganic and bioinorganic chemists, with reports dating back to the 1930s.[59–62] Of the many examples available, the main motif discussed in this dissertation uses Tp (hydrotris(1-pyrazolyl)borate) as the capping ligand. The properties of diiron(III)-oxo complexes present little variation, regardless of the capping ligands used;[60] however, the following paragraphs will review these properties using almost exclusively Tp-capped dimers as examples.

As was mentioned before, hemerythrin is one of the three proteins that can reversibly bind oxygen. As such, it has been intensely studied, both by chemists and biologists.[41] One of the goals of these studies was to synthesize a compound that would replicate the active center of Hr, both in structure and properties. In 1983, Armstrong and Lippard reported the synthesis and characterization of such a model compound, $(Tp)_2Fe_2(\mu\text{-}O)(\mu\text{-}O_2CCH_3)_2$ (Figure 1.12).[63] This compound contains two Fe^{3+} ions which are antiferromagnetically coupled: its spin ladder is shown in Figure 1.12. In the following years, their work included the synthesis of other iron(III) dimers, with other carboxylate bridges[10,64] and also the reversible protonation of the oxo bridge, which causes the coupling constant, *J*, to decrease from –121 cm^{-1} in $(Tp)_2Fe_2(\mu\text{-}O)(\mu\text{-}O_2CCH_3)_2$ to –17 cm^{-1} for $[(Tp)_2Fe_2(\mu\text{-}OH)(\mu\text{-}O_2CCH_3)_2](ClO_4)$.[54]

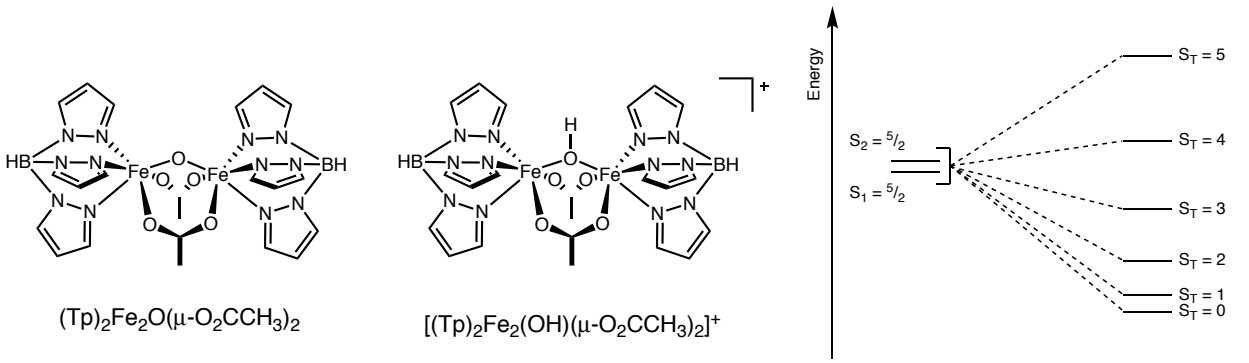


Figure 1.12. Left: Tp-capped diferric oxo/hydroxo-bridged cores. Right: Spin ladder for a system with two antiferromagnetically coupled $S = \mathbf{5/2}$ spin centers.

To understand this drastic change in the strength of spin coupling upon protonation, our group has used DFT calculations to study the orbital mechanisms of superexchange[v] in these complexes.[65] Three compounds were modeled: $(Tp)_2Fe_2(\mu\text{-}O)(\mu\text{-}O_2CCH_3)_2$, $[(Tp)_2Fe_2(\mu\text{-}OH)(\mu\text{-}O_2CCH_3)_2]^+$, and $[(Tp)_2Fe_2(\mu\text{-}O^*)(\mu\text{-}O_2CCH_3)_2]^+$, which has the same geometry as the OH-bridged dimer, but it was not protonated. This last compound allowed to distinguish the effects of the geometry of the core from those of protonation.

For the oxo-bridged dimer, six main superexchange pathways were found, five of which were mediated by the oxo group, and one (the weakest) by the acetates. In this compound, the Fe-O(oxo) bonds are shorter than the Fe-O(acetate) ones, whereas for the OH-bridged dimer all those lengths are within error of each other. As a result of the longer Fe-O^H bond distance, the hydroxo-mediated pathways are weaker than their oxo-counterparts, but the acetate-based one is not significantly affected. Additionally, one of

[v]This refers to spin coupling mediated by a diamagnetic bridge, as opposed to direct exchange. Only superexchange is operative in the dimers studied in this dissertation. See ref. 4 for further details.

the oxo/hydroxo pathways becomes much less efficient upon protonation, But, even in the absence of the proton, many of the oxo-mediated pathways are weakened because of the geometric changes. The extra proton removes electronic density from the oxygen bridge: as a result, one of the magnetic orbitals involved in the exchange becomes localized almost exclusively on the metals, and the contribution from the OH bridge decreases.

Their relative ease of synthesis, coupled with the possibility to reversibly protonate their oxo bridge makes these dimers extremely interesting platforms to study the effect of spin and Heisenberg spin exchange on reactivity. Previous work in our group along these lines will be reviewed in the next section, and the work presented in this dissertation will also be outlined.

1.9. Bi- and Intramolecular Donor-Acceptor Systems Including a Diiron(III) Core

In the past, our group[66] showed that both $(Tp)_2Fe_2(\mu\text{-}O)(\mu\text{-}O_2CH_3)_2$ and $[(Tp)_2Fe_2(\mu\text{-}OH)(\mu\text{-}O_2CH_3)_2]^+$ can engage in electron transfer with $[Ru(dmb)_3]^{2+}$ (dmb is 4,4'-dimethyl-2,2'-bipyridine), according to (1.7).

$$[Ru(dmb)_3]^{2+*} + (Fe^{III}Fe^{III}) \xrightarrow{k_{et}} [Ru(dmb)_3]^{3+} + (Fe^{II}Fe^{III}) \quad \textbf{(1.7)}$$

Remarkably, the quenching of the Ru(II)-based emission is much faster in the case of the μ-hydroxo dimer.[66] Based on the absorption spectra of both diiron(III) cores and the emission spectrum of $[Ru(dmb)_3]^{2+}$, the μ-oxo compound can also act as an acceptor for Förster energy transfer, whereas the μ-hydroxo dimer cannot.[66,67] The main

differences between the two acceptors are: (a) the strength of their spin coupling (*vide supra*) and (b) a positive shift of ca. 55 mV for the reduction of $[(Tp)_2Fe_2OH(\mu\text{-}O_2CH_3)_2]^+$ compared to $(Tp)_2Fe_2O(\mu\text{-}O_2CH_3)_2$. Even though the latter increases the driving force for electron transfer to the μ-hydroxo acceptor, such difference in ΔG_0 is not enough to account for the difference in quenching rates observed.[66] However, these data were not enough to unequivocally establish a link between the spin coupling in these diiron(III) systems and their reactivity.

Following up on this work, Weldon et al.[67] sought to decouple the variations in ΔG_0 from those in the strength of spin exchange. To this end, they prepared several diiron(III) compounds of the form $(Tp)_2Fe_2O(\mu\text{-}O_2CR)_2$ or $[(Tp)_2Fe_2(OH)(\mu\text{-}O_2CR)_2]^+$; independently of the identity of the carboxylate bridge, the oxo-bridged diiron(III) complexes are antiferromagnetically coupled with $J = -119 \pm 4$ cm^{-1}, whereas for their hydroxo-bridged counterparts $J = -18 \pm 2$ cm^{-1}.[67] This result is not surprising considering that the main superexchange pathways involve the oxo/hydroxo bridge while the carboxylates play only a minor role.[65] The carboxylate bridges, however, do have an effect on the reduction potential of the diiron(III) core. Combining this series of acceptors with three $[Ru(bpy')_3]^{2+}$ donors (where bpy' = bpy, dmb or tmb),[vi] it is possible to span a *ca.* 900 meV range electron transfer driving force. What is more important, this strategy allowed for D–A pairs with the same ΔG_0 and different J values.

[vi] bpy = 2,2'-bipyridine; dmb = 4,4'-dimethyl-2,2'-bipyridine; tmb = 4,4',5,5'-tetramethyl-2,2'-bipyridine.

The main results of this work are plotted in Figure 1.13. Two key observations can be made from these data: in the first place, the quenching by oxo-bridged dimers is slower than that by the hydroxo-bridged dimers, even when the driving force for electron transfer is the same. Secondly, the quenching rate for the hydroxo-bridged compounds is practically insensitive to changes in the driving force. The average value of k'_q in this case is 4.52×10^9 s^{-1}, which is consistent with diffusion-limited kinetics.[68] This limitation made it impossible to properly quantify the quenching rates for the hydroxo-bridged compounds, which in turn meant that no further conclusions could be drawn. This was, however, a strong indication that spin exchange plays a role on reactivity. Furthermore, these results agreed with what Bominaar et al. had predicted:[29,30] at a given temperature, for the hydroxo-bridged dimers, more spin states are populated than in the oxo-bridged compounds. Therefore, the former have more accessible reaction pathways, which could account for the differences in reactivity of both sets of acceptors.

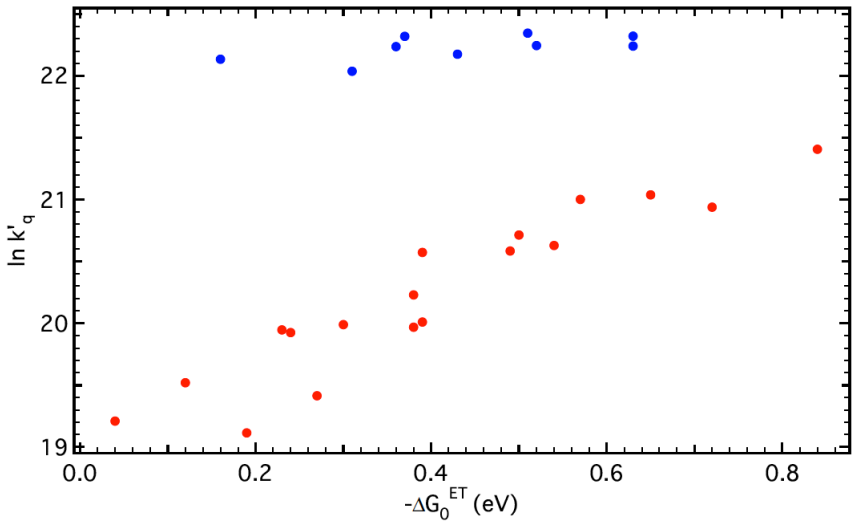


Figure 1.13. Plot of the logarithm of the quenching constant (corrected for diffusion, k'_q) versus the driving force for photoinduced electron transfer from a Ru(II) donor to a diiron(III) acceptor. The red circles correspond to oxo-bridged iron(III) dimers; the blue circles represent hydroxo-bridged acceptors. Adapted from ref. 67. See text for details.

This work successfully explored how to independently control driving force and spin exchange, providing very useful insight into these matters. Unfortunately, the bimolecular approach employed by Weldon et al. has two main caveats: (a) the quenching kinetics for the μ-hydroxo cores are diffusion-limited; (b) the electronic coupling between donor and acceptor (H_{ab} in Marcus theory[22,69]) as well as the distance and relative orientations between them are not unequivocally defined (and therefore cannot be controlled). As was mentioned before, these prevented the authors from drawing firmer conclusions about the effect of Heisenberg spin exchange on reactivity. One way to get around these pitfalls is to covalently attach the donor and the acceptor; Figure 1.14 shows two strategies to achieve this. The first motif, shown on the left, is synthetically more accessible, and has been employed on a variety of D–A systems before, by our group and others.[70–74] However, because it uses the carboxylate bridges to append the donor, this

strategy does not allow for changes in the redox potential of the diiron(III) core. Motif 2 (right side of Figure 1.14) recovers that tunability, and is therefore more desirable, despite its synthesis being more challenging.[75,76]

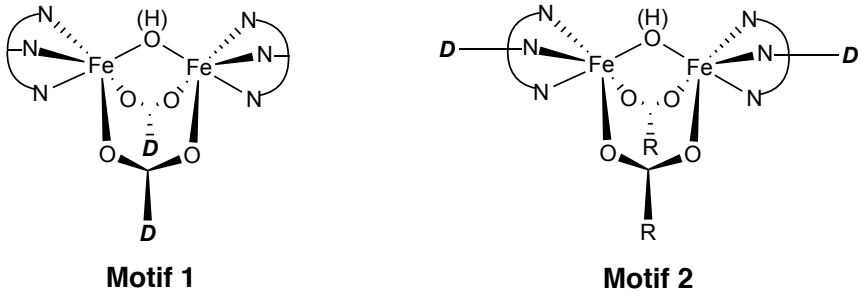


Figure 1.14. Two ways to covalently attach the donor and the {Fe_2O} acceptor explored in this dissertation.

One of the simplest systems that could be prepared using the first motif employed naphthalene as the donor. Initial work on our group focused on an assembly containing two naphthalene groups appended *via* carboxylate groups, $[Fe_2O(O_2CCH_2C_{10}H_7)_2(TACN\text{-}Me_3)_2](PF_6)_2$ (where TACN-Me_3 is 1,4,7-trimethyl-1,4,7-triazacyclononane), shown in Figure 1.15.[71] As expected, the diiron(III) core in this system is antiferromagnetically coupled, and its coupling constant is the same as for other compounds of this class (J = –105 cm^{-1}).[10,67,71] However, the emission kinetics of this compound were more complex than initially expected, due to the formation of an excimer upon photoexcitation, as a consequence of the two naphthalene groups being very close to each other. This same phenomenon was observed by Nakai et al. in a diruthenium(III) system with two naphthyl moieties.[77]

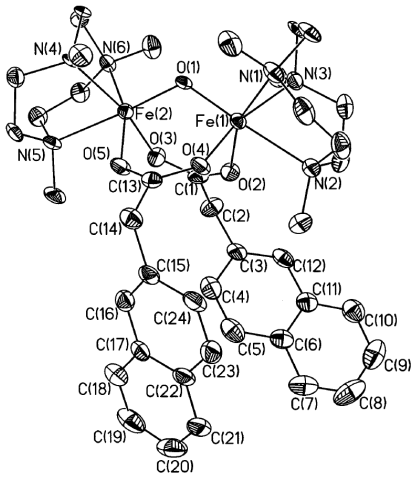


Figure 1.15. Drawing of $[Fe_2O(O_2CCH_2C_{10}H_7)_2(TACN\text{-}Me_3)_2]^{2+}$, shown as 50% thermal ellipsoids. The distance between the ring containing C15 on one naphthalene group and the C5 atom on the other is only 4 Å, short enough to favor excimer formation. Reprinted with permission from ref. 71. Copyright 2002 American Chemical Society.

This result, albeit interesting on its own, complicated the analysis of the photophysics of the assembly and prevented the study of any quenching involving the diiron(III) core. To prevent the formation of such excimer, new diiron(III) compounds were prepared, using tris(2-aminoethyl)amine (tren) and tris(2-pyridyl)amine (TPA) as capping ligands; these tetradentate ligands leave only two coordination positions available to attach one carboxylate group (and therefore, one naphthalene donor). Additionally, using Tp as the capping ligand it was possible to make $Fe_2O((O_2CCH_2)_2C_{10}H_7)(Tp)_2$ and $Fe_2O(O_2CCH_2C_{10}H_7)_2(Tp)_2$; the less rigid geometry of the diiron(III)-oxo core in the latter did not lead to the formation of an excimer; thus, all the compounds reported in this work allowed for the study of the energy transfer between the naphthalene donor and the diiron(III) acceptors.[73] In all these systems, the emission of the naphthalene donor was quenched in the presence of the $\{Fe_2O\}$ acceptor. Despite both electron and energy transfer being in principle possible, no evidence of electron transfer was observed. The

most striking feature of these assemblies was the quenching of both the S_1 and T_1 excited states of naphthalene. The authors postulated that one of the reasons for this dual reactivity is the distinctive electronic structure of the acceptor due Heisenberg spin exchange; the large number of spin states available for the acceptor gives rise to several reaction pathways that conserve spin for both the S_1 and T_1 states of the donor.

An important disadvantage of these systems was the large overlap between the emission of the naphthalene donor and the absorption of the diiron(III)-oxo cores, which prevented an accurate determination of the emission quantum yields of the assemblies. Additionally, the overlap of absorptive features due to the naphthyl groups and the diiron(III)-oxo cores made transient absorption measurements particularly challenging.[73]

In light of these results, it is necessary to use a donor that has absorptive and emissive features that are well separated from the absorption spectrum of the acceptor. Additionally, we desire to study electron transfer in D-A assemblies of this kind (as a complement to other lines of research in our group that study exclusively Dexter[74] or Förster[31,78] energy transfer). Given their well-known photophysics and synthetic accessibility,[79] as well as the work done by Weldon et al.,[67] Ru(II) polypyridyl compounds are a sound choice. The work presented in this dissertation focuses on the synthesis and characterization of such assemblies, utilizing both motifs shown in Figure 1.14.

1.10. Contents of This Dissertation

The work complied herein revolves around the synthesis of covalently linked D-A systems, and the study of their photophysics as well as those of their individual

components. The Ru(II)-based donors in these assemblies have given us a clear spectroscopic handle to study the different processes taking place. To better understand the analysis of the results in subsequent chapters, Chapter 2 introduces the photophysics of Ru(II) polypyridyls (using $[Ru(bpy)_3]^{2+}$ as their best-known representative) in the context of this research. The discussion is focused on the processes and experiments that are relevant to this dissertation, and the concepts defined in this chapter will be applied many times in the course of this dissertation.

In Chapter 3, the first donor and acceptor synthesized in the quest for covalently linked D-A assemblies are presented; their syntheses are described, as well as the unsuccessful attempts to prepare the corresponding D-A system. Bimolecular quenching studies using this D-A pair were carried out, and they are used to illustrate some points that will be relevant in later discussions.

Using the same donor introduced in Chapter 3, new D-A assemblies were pursued, which are extensively discussed in Chapter 4. Unfortunately, these assemblies were very unstable in solution; however, valuable lessons were learned, and new directions were suggested by the results examined in this chapter.

The possibility of forming D-A assemblies *in situ* instead of synthesizing them in a prior step was explored in Chapter 5. This strategy allowed us to measure the lifetime of these assemblies, varying the donor and the acceptor. The contributions from Dexter and Förster energy transfer, as well as electron transfer, were assessed, leading to a more in-depth understanding of the quenching mechanisms in these systems.

Despite the convenience of the approach used in Chapter 5, our goal is to prepare and isolate D-A assemblies, to study their photophysics without the interference of bimolecular processes. Chapter 6 details the synthetic routes pursued towards assemblies based on motif 2 (Figure 1.14); while not all the proposed strategies have worked, some of them have shown promise and we are currently investigating them.

REFERENCES

REFERENCES

(1) Kahn, O. In *Magneto-Structural Correlations in Exchange Coupled Systems*; Willet, R. D., Gatteschi, D., Kahn, O., Eds.; D. Reidel Publishing Company, 1985; pp 37–56.

(2) McQuarrie, D. A.; Simon, J. D. *Physical Chemistry: a Molecular Approach*, 1st ed.; University Science Books, 1997.

(3) Carlin, R. L. *Magnetochemistry*, 1st ed.; Springer-Verlag: Berlin, 1986.

(4) Kahn, O. *Molecular Magnetism*; VCH Publishers: New York, 1993.

(5) Gatteschi, D.; Sessoli, R. *Angew. Chem. Int. Ed.* **2003**, *42*, 268–297.

(6) Demir, S.; Jeon, I.-R.; Long, J. R.; Harris, T. D. *Coord. Chem. Rev.* **2015**, *289–290*, 149–176.

(7) Ferrando-Soria, J.; Vallejo, J.; Castellano, M.; Martínez-Lillo, J.; Pardo, E.; Cano, J.; Castro, I.; Lloret, F.; Ruiz-García, R.; Julve, M. *Coord. Chem. Rev.* **2017**, *339*, 17–103.

(8) Brunold, T. C.; Solomon, E. I. *J. Am. Chem. Soc.* **1999**, *121*, 8288–8295.

(9) Brunold, T. C.; Solomon, E. I. *J. Am. Chem. Soc.* **1999**, *121*, 8277–8287.

(10) Armstrong, W. H.; Spool, A.; Papaefthymiou, G. C.; Frankel, R. B.; Lippard, S. J. *J. Am. Chem. Soc.* **1984**, *106*, 3653–3667.

(11) Hayami, S.; Holmes, S. M.; Halcrow, M. A. *J. Mater. Chem. C* **2015**, *3*, 7775–7778.

(12) Schulman, L. J. *Nature* **2005**, *438*, 431–432.

(13) Mooij, H. *Science* **2005**, *307*, 1210–1211.

(14) Mehring, M. *Phys. Stat. Sol.* **2007**, *244*, 3868–3873.

(15) Denschlag, J. H. *Nature* **2007**, *448*, 422–423.

(16) Chambers, S. A.; Yoo, Y. K. *MRS Bull.* **2003**, *28*, 706–710.

(17) Rocha, A. R.; García-Suárez, V. M.; Bailey, S. W.; Lambert, C. J.; Ferrer, J.; Sanvito, S. *Nat. Mater.* **2005**, *4*, 335–339.

(18) Bogani, L.; Wernsdorfer, W. *Nat. Mater.* **2008**, *7*, 179–186.

(19) Drago, R. S. *Physical Methods for Chemists*; Saunders College Pub: Philadelphia, 1992.

(20) Lakowicz, J. R. *Principles of Fluorescence Spectroscopy*, 3rd ed.; Springer US: Boston, 2006.

(21) Buchachenko, A. L. *Pure Appl. Chem.* **2000**, *72*, 2243–2258.

(22) Barbara, P. F.; Meyer, T. J.; Ratner, M. A. *J. Phys. Chem.* **1996**, *100*, 13148–13168.

(23) Guo, D.; McCusker, J. K. *Inorg. Chem.* **2007**, *46*, 3257–3274.

(24) Turner, J. W.; Schultz, F. A. *Coord. Chem. Rev.* **2001**, *219–221*, 81–97.

(25) Cotton, F. A.; Wilkinson, G. *Advanced Inorganic Chemistry*, 1st ed.; John Wiley & Sons, Inc.: New York, NY, 1962.

(26) Hayashi, H. *J. Chinese Chem. Soc.* **2002**, *49*, 137–160.

(27) Mi, Q.; Chernick, E. T.; McCamant, D. W.; Weiss, E. A.; Ratner, M. A.; Wasielewski, M. R. *J. Phys. Chem. A* **2006**, *110*, 7323–7333.

(28) Buchachenko, A. L.; Berdinsky, V. L. *Chem. Rev.* **2002**, *102*, 603–612.

(29) Bominaar, E. L.; Achim, C.; Borshch, S. A.; Girerd, J.-J.; Münck, E. *Inorg. Chem.* **1997**, *36*, 3689–3701.

(30) Bominaar, E. L.; Achim, C.; Borshch, S. A. *J. Chem. Phys.* **1999**, *110*, 11411–11422.

(31) Guo, D.; Knight, T. E.; McCusker, J. K. *Science* **2011**, *334*, 1684–1687.

(32) Guha, B. C. *Proc. R. Soc. A Math. Phys. Eng. Sci.* **1951**, *206*, 353–373.

(33) Bleaney, B.; Bowers, K. D. *Proc. R. Soc. A Math. Phys. Eng. Sci.* **1952**, *214*, 451–465.

(34) McCarthy, P. J.; Güdel, H. U. *Coord. Chem. Rev.* **1988**, *88*, 69–131.

(35) Robin, M. B.; Day, P. *Adv. Inorg. Chem. Radiochem.* **1968**, *10*, 247–422.

(36) Girerd, J.-J. *J. Chem. Phys.* **1983**, *79*, 1766–1775.

(37) Mabbs, F. E.; Machin, D. J. *Magnetism and Transition Metal Complexes*, 2nd ed.; Dover Publications: Mineola, N.Y., 2008.

(38) Kambe, K. *J. Phys. Soc. Japan* **1950**, *5*, 48–51.

(39) McCarthy, P. J.; Güdel, H. U. *Inorg. Chem.* **1984**, *23*, 880–887.

(40) *Metal Clusters in Proteins*; Que, L., Ed.; ACS Symposium Series; American Chemical Society: Washington, DC, 1988; Vol. 372.

(41) Stenkamp, R. E. *Chem. Rev.* **1994**, *94*, 715–726.

(42) Kitajima, N.; Moro-oka, Y. *Chem. Rev.* **1994**, *94*, 737–757.

(43) Lamotte, B.; Mouesca, J.-M. *C. R. Acad. Sci. Paris Ser. IIB - Mech.* **1997**, *324*, 117–132.

(44) Solomon, E. I.; Randall, D. W.; Glaser, T. *Coord. Chem. Rev.* **2000**, *200–202*, 595–632.

(45) Wang, V. C. C.; Maji, S.; Chen, P. P. Y.; Lee, H. K.; Yu, S. S. F.; Chan, S. I. *Chem. Rev.* **2017**, *117*, 8574–8621.

(46) Holm, R. H.; Kennepohl, P.; Solomon, E. I. *Chem. Rev.* **1996**, *96*, 2239–2314.

(47) Blondin, G.; Girerd, J.-J. *Chem. Rev.* **1990**, *90*, 1359–1376.

(48) Borshch, S. A.; Bominaar, E. L.; Blondin, G.; Girerd, J.-J. *J. Am. Chem. Soc.* **1993**, *115*, 5155–5168.

(49) Bominaar, E. L.; Hu, Z.; Muenck, E.; Girerd, J.-J.; Borshch, S. A. *J. Am. Chem. Soc.* **1995**, *117*, 6976–6989.

(50) Bertrand, P.; Gayda, J. P. *BBA - Bioenerg.* **1982**, *680*, 331–335.

(51) Bertrand, P.; Gayda, J.-P. *Biochim. Biophys. Acta - Protein Struct.* **1980**, *625*, 337–342.

(52) Mouesca, J.-M.; Chen, J. L.; Noodleman, L.; Bashford, D.; Case, D. A. *J. Am. Chem. Soc.* **1994**, *116*, 11898–11914.

(53) Anderson, P. W.; Hasegawa, H. *Phys. Rev.* **1955**, *100*, 675–681.

(54) Armstrong, W. H.; Lippard, S. J. *J. Am. Chem. Soc.* **1984**, *106*, 4632–4633.

(55) Monzyk, M. M.; Holwerda, R. A. *Inorg. Chem.* **1992**, *31*, 1969–1971.

(56) Wall, Jr., M. H.; Akimoto, S.; Yamazaki, T.; Ohta, N.; Yamazaki, I.; Sakuma, T.; Kido, H. *Bull. Chem. Soc. Jpn.* **1999**, *72*, 1475–1481.

(57) Hammarström, L.; Sun, L.; Åkermark, B.; Styring, S. *Spectrochim. Acta Part A Mol. Biomol. Spectrosc.* **2001**, *57*, 2145–2160.

(58) Obata, M.; Tanihara, N.; Nakai, M.; Harada, M.; Akimoto, S.; Yamazaki, I.; Ichimura, A.; Kinoshita, I.; Mikuriya, M.; Hoshino, M.; Yano, S. *Dalt. Trans.* **2004**, 3283–3287.

(59) Murray, K. S. *Coord. Chem. Rev.* **1974**, *12*, 1–35.

(60) Kurtz, D. M. *Chem. Rev.* **1990**, *90*, 585–606.

(61) Pfeiffer, P.; Breith, E.; Lübbe, E.; Tsumaki, T. *Justus Liebigs Ann. Chem.* **1933**, *503*, 84–130.

(62) Gaines, A.; Hammett, L. P.; Walden, G. H. *J. Am. Chem. Soc.* **1936**, *58*, 1668–1674.

(63) Armstrong, W. H.; Lippard, S. J. *J. Am. Chem. Soc.* **1983**, *105*, 4837–4838.

(64) Armstrong, W. H.; Lippard, S. J. *J. Am. Chem. Soc.* **1985**, *107*, 3730–3731.

(65) Rodriguez, J. H.; McCusker, J. K. *J. Chem. Phys.* **2002**, *116*, 6253–6270.

(66) Kirby, J. P.; Weldon, B. T.; McCusker, J. K. *Inorg. Chem.* **1998**, *37*, 3658–3659.

(67) Weldon, B. T.; Wheeler, D. E.; Kirby, J. P.; McCusker, J. K. *Inorg. Chem.* **2001**, *40*, 6802–6812.

(68) Rehm, D.; Weller, A. *Isr. J. Chem.* **1970**, *8*, 259–271.

(69) Marcus, R. A. *Angew. Chem. Int. Ed.* **1993**, *32*, 1111–1121.

(70) Neves, A.; Herrmann, W.; Wieghardt, K. *J. Am. Chem. Soc.* **1984**, *106*, 5532–5537.

(71) Picraux, L. B.; Weldon, B. T.; McCusker, J. K. *Inorg. Chem.* **2002**, *42*, 273–282.

(72) Tanihara, N.; Obata, M.; Harada, M.; Mikata, Y.; Hamazawa, A.; Kinoshita, I.; Isobe, K.; Ichimura, A.; Hoshino, M.; Mikuriya, M.; Yano, S. *Inorg. Chem. Commun.* **2003**, *6*, 447–450.

(73) Picraux, L. B.; Smeigh, A. L.; Guo, D.; McCusker, J. K. *Inorg. Chem.* **2005**, *44*, 7846–7859.

(74) Soler, M.; McCusker, J. K. *J. Am. Chem. Soc.* **2008**, *130*, 4708–4724.

(75) Weldon, B. T. Correlations Between Heisenberg Spin Exchange and Photo-Induced Electron/Energy Transfer in Polynuclear Transition Metal Complexes, University of California, Berkeley, 2001.

(76) Picraux, L. B. Studies of Intramolecular Electron and Energy Transfer in Donor-Acceptor Assemblies Incorporating a Heisenberg Spin Coupled Metal Center, University of California, Berkeley, 2003.

(77) Nakai, M.; Funabiki, T.; Ohtsuki, C.; Harada, M.; Ichimura, A.; Tanaka, R.; Kinoshita, I.; Mikuriya, M.; Benten, H.; Ohkita, H.; Ito, S.; Obata, M.; Yano, S. *Inorg. Chem.* **2006**, *45*, 3048–3056.

(78) Knight, T. E.; Guo, D.; Claude, J. P.; McCusker, J. K. *Inorg. Chem.* **2008**, *47*, 7249–7261.

(79) Juris, A.; Balzani, V.; Barigelletti, F.; Campagna, S.; Belser, P.; von Zelewsky, A. *Coord. Chem. Rev.* **1988**, *84*, 85–277.

Chapter 2. The Photophysics of $[Ru(bpy)_3]^{2+}$ in the Context of this Dissertation

"It's not enough to be talented. It's not enough to work hard and to study into the night. You must also become intimately aware of the methods you use to reach your decisions."

–Garry Kasparov

2.1. Introduction: Why Ru(II) Polypyridyls?

As it was described in Chapter 1, the broader goal of this dissertation is to study the effect of spin polarization on reactivity using Heisenberg spin exchange as a tool to affect such polarization. More specifically, the reactivity of interest concerns electron and energy transfer processes. Building upon previous work in our group,[1–3] the D-A systems studied herein have a diiron(III) oxo/hydroxo core as the spin-coupled acceptor, and Ru(II) polypyridyls are used as donors.[1,4–6] Both the donor and the acceptor have been chosen because they are stable, synthetically accessible and their properties may be tweaked with small synthetic changes.[1,7–10] Furthermore, both kinds of compounds have been thoroughly studied, and their behavior documented;[8,11] we have used this wealth of information to guide the choices made in terms of donors and acceptors.

One of the main tools used to study energy and electron transfer in these D-A systems is time-resolved spectroscopy. This is possible because Ru(II) polypyridyls have well-defined spectroscopic signatures and well-characterized photophysics.[8,12–14] The best-known Ru(II) polypyridyl is $[Ru(bpy)_3]^{2+}$ (where bpy is 2,2'-bipyridine, see Figure

2.1);[8,15,16] as such, it will be used as an example to describe the photophysics of these compounds as a class, laying out the basic concepts that will be used in further chapters.

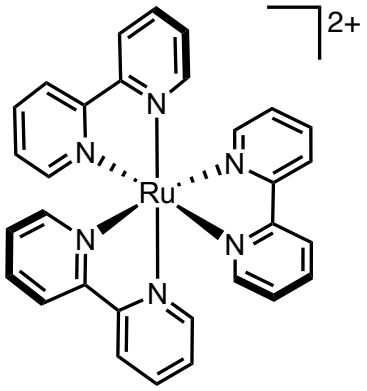


Figure 2.1. Tris(2,2'-bipyridine) ruthenium(II), $[Ru(bpy)_3]^{2+}$.

In principle, any donor could have been chosen, as long as the reaction being studied (be it electron and/or energy transfer) is thermodynamically favorable. However, to study the kinetics of these processes in the systems of interest, it is necessary to have at least one of the components of the D-A system be amenable to time-resolved spectroscopy. Ru(II) polypyridyls meet both conditions: with their emissive long-lived ^{3}MLCT excited states,[8] these compounds are useful emissive "tags" that can be adapted to a variety of systems.[17,18] And, using the appropriate ligands, their properties (redox potentials, excited-state energy, electronic absorption spectrum, etc.) may be adjusted to ensure that the desired reactions are viable.

This dissertation focuses on two types of reactions, electron and energy transfer; these may be studied as bi- or intramolecular processes. In the case of bimolecular reactions, the relevant steps can be represented as shown in Figure 2.2;[8,19] for D-A systems that are covalently attached, these steps are intramolecular, but they can still be

rationalized using the concepts described below. The first step is the absorption of a visible light photon by the donor in its ground state (**D**) and its consequent promotion to an electronic excited state (**D***); k_0 represents the rate of excited-state relaxation (in this case ground-state recovery). This process can be radiative (i.e., emission) and/or non-radiative and will be discussed in detail in section 2.3. For the excited donor to react with an acceptor molecule (**A**), both species must diffuse towards each other, forming a "precursor complex". Then, these two species react; after the reaction, the products (**D'** and **A''**) diffuse away from each other. If the two reactants cannot escape the solvent cage fast enough, an unwanted back reaction may take place. This is typically more of a concern with electron (as opposed to energy) transfer processes. In the case of covalently linked D-A systems, the second and fourth steps are no longer relevant.

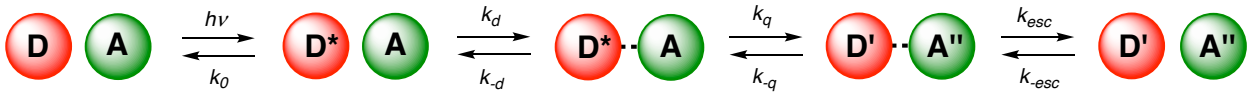


Figure 2.2. Simplified kinetic scheme for a general quenching process.

This relatively simple scheme allows us to outline the main points that need to be considered when choosing and/or designing a donor:

1. Photo-induced reactions make use of the enhanced reactivity of the donor in its excited state. For this reason, it must possess a good absorption cross-section, preferably over a broad range of wavelengths where the acceptor does not absorb.

2. The yield of formation of the reactive excited state should be as high as possible. This will be influenced both by the intrinsic quantum yield of its formation (that is, the

efficiency with which the reactive excited state is formed upon photon absorption) as well as the absorption cross-section as measured by the compound's concentration and molar absorptivity.

3. The excited state must persist long enough to undergo the desired reaction with the acceptor. In the context of Figure 2.2, this means that the excited state of the donor must have a sufficiently long lifetime to enable it to diffuse to the acceptor before relaxing back to the ground state. Diffusion occurs on the nanosecond time scale in most solvents;[20] the bimolecular nature of the reaction places a practical upper limit of approximately $10^9\ s^{-1}$ for k_0 of the excited donor. The use of covalently linked D-A systems removes this requirement;[21,22] however, lifetimes on the order of tens of nanoseconds to a few microseconds can be monitored using simpler instrumentation than processes that happen in the femtosecond to picosecond timescale.

4. The photophysics of the donor must be reversible (i.e., no photodegradation in the absence of quencher). In the case of an electron transfer, reversible electrochemical behavior is preferred, and the excited-state redox potential of the donor must provide for an exergonic reaction.

Given the various criteria just enumerated, polypyridyl complexes of Ru(II) appear to be a sound choice for the donor. These compounds strongly absorb visible light, and while there is overlap between their electronic absorption spectra and those of the diferric oxo/hydroxo cores of interest, the latter have much smaller molar absorptivities (at least an order of magnitude).[1,8] The excited states of Ru(II)-based chromophores are

formed with ~100% efficiency[14] and their lifetimes range from tens of nanoseconds to a few microseconds,[8] which is long enough for them to engage in bimolecular reactions. As a class, these compounds are generally stable with respect to decomposition (both photochemical and thermal) and typically exhibit reversible redox behavior. They are also emissive, which provides a useful handle for quenching studies.

This discussion will be built around the ground- and excited-state properties of $[Ru(bpy)_3]^{2+}$. After detailing the physical and photophysical properties of this compound, we will then focus on the kinetics of electron and energy transfer and provide an overview of the various experimental protocols that allow for discriminating among various mechanistic possibilities. In so doing, the goal is to lay out the basic concepts that will be used to interpret the experimental results in the following chapters of this dissertation.

2.2. Optical and Electrochemical Properties

2.2.1. Optical Properties

The electronic absorption spectrum of $[Ru(bpy)_3](PF_6)_2$ in acetonitrile solution is shown in Figure 2.3. The intense absorption at 285 nm corresponds to a ligand-centered (also called intra-ligand, IL) transition ($\pi_L \rightarrow \pi_L^*$), which has been assigned by comparing it with the absorption spectrum of the protonated ligand.[16] The band in the visible region (λ_{max} = 452 nm) corresponds to a metal-to-ligand charge-transfer (MLCT) transition. As the name implies, this type of excited state can be viewed as the promotion of an electron

from a predominantly metal-based orbital to one that is primarily ligand in character. This transition can therefore be thought of as a simultaneous photo-induced oxidation of the metal center and reduction of the ligand that yields a chemical species that can approximately described as $[Ru^{III}(bpy^{\cdot -})(bpy)_2]^{2+*}$ (Figure 2.4).[23] Because of this spatial redistribution of electron density, this transition is responsible for the enhanced redox activity of the excited state relative to what is observed in the ground state. Charge-transfer transitions are typically very intense:[24] for $[Ru(bpy)_3]^{2+}$ in acetonitrile solution at room temperature, the maximum of the MLCT absorption feature corresponds to molar absorptivity of ~15,000 $M^{-1}\,cm^{-1}$.

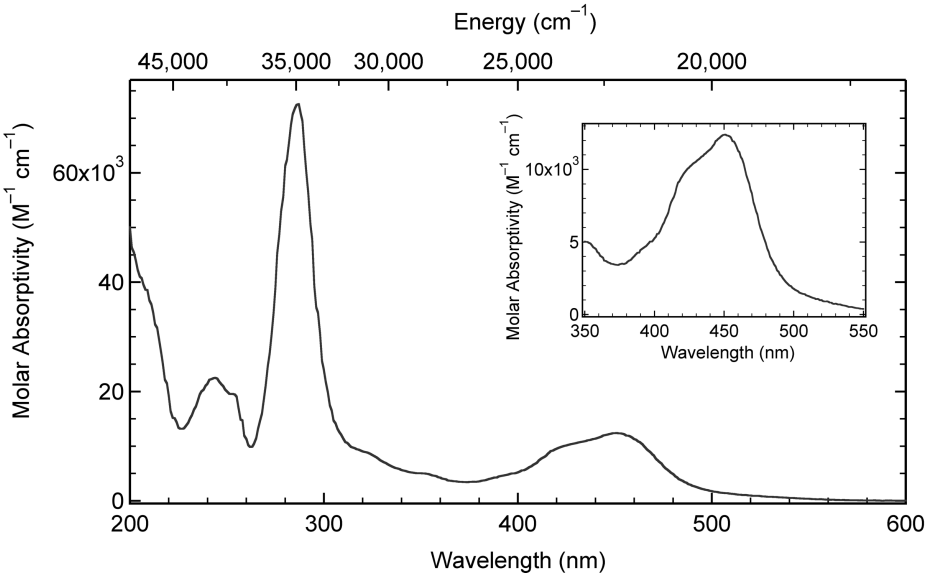


Figure 2.3. Electronic absorption spectrum of $[Ru(bpy)_3](PF_6)_2$ in acetonitrile solution at room temperature. The inset shows an expanded view of the metal-to-ligand charge transfer band. See text for details.

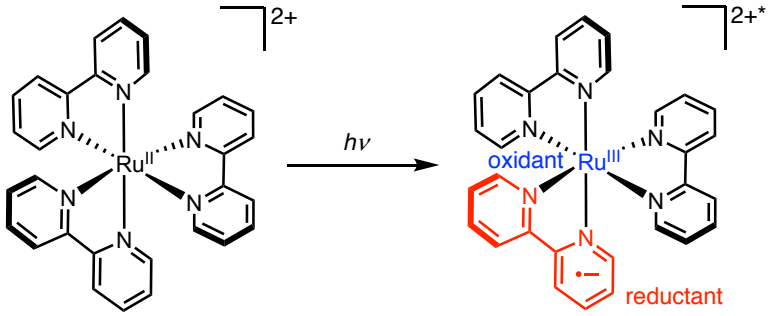


Figure 2.4. A qualitative representation of a metal-to-ligand charge-transfer state in $[Ru(bpy)_3]^{2+}$. The spatial separation of charge within the molecule following light absorption is the underlying reason for the redox activity of the excited state.

Two additional features can be seen in the absorption spectrum of $[Ru(bpy)_3]^{2+}$, one at ~330 nm and the other at 350 nm. Their origin(s) have been the subject of considerable debate over the years, but they are most likely due to ligand-field (so-called "d-d", noted LF) transitions within the d-orbital manifold of the metal. The symmetry-forbidden nature of d-d bands typically limits their absorptivities to the range of 10 - 100 M^{-1} cm^{-1},[24] but the proximity of both the ligand-centered transitions in the ultraviolet and the MLCT envelope in the visible modulates their intensities in the present case. These metal-centered transitions redistribute electronic density into orbitals that are antibonding with respect to the metal-ligand bonds and therefore typically promote photodissociation.[8] A molecular orbital-based description of these various transitions is shown in Figure 2.5.

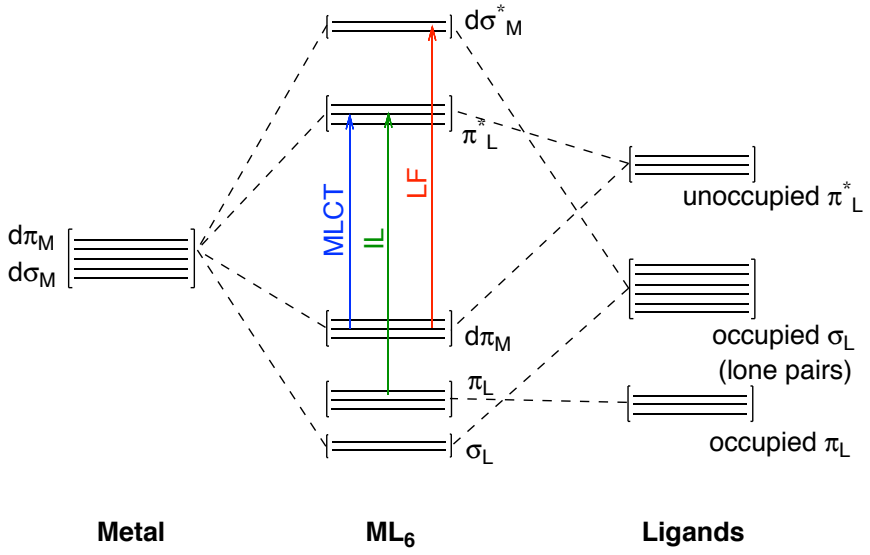


Figure 2.5. Simplified molecular orbital diagram for an octahedral compound with π-acceptor ligands. The three main types of electronic transitions typically observed in metal polypyridyl complexes are indicated by the arrows.

2.2.2. Electrochemical Properties

Of the two kinds of reactivity we are interested in, photo-induced electron transfer is directly related to the redox potentials of the donor and acceptor. Cyclic voltammetry is the most common technique to measure the ground-state redox potentials of a compound.[25–27] The cyclic voltammogram of $[Ru(bpy)_3](PF_6)_2$ in acetonitrile solution is shown in Figure 2.6. The oxidation of the metal center (eq 2.1) occurs at ~0.9 V (referenced to the ferrocene/ferrocenium couple).

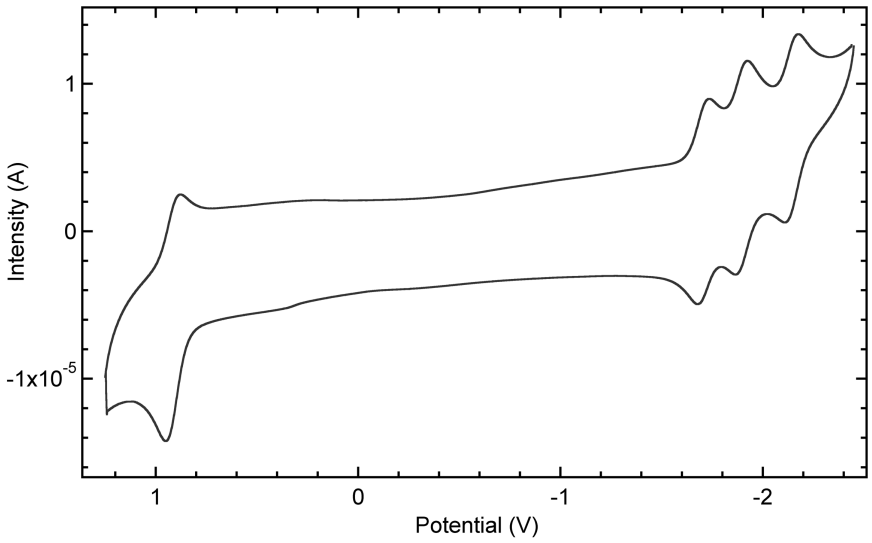


Figure 2.6. Cyclic voltammogram of $[Ru(bpy)_3](PF_6)_2$ in CH_3CN, using 0.1 M tetrabutylammonium hexafluorophosphate ($TBAPF_6$) as supporting electrolyte. Potentials are referenced to the ferrocene/ferrocenium couple.

$$[Ru(bpy)_3]^{2+} \longrightarrow [Ru(bpy)_3]^{3+} + e^- \quad \textbf{(2.1)}$$

Three reductions are also observed, all of which correspond to one-electron reductions of each of the three ligands in succession (equations 2.2–2.4).

$$[Ru(bpy)_3]^{2+} + e^- \longrightarrow [Ru(bpy^{\cdot -})(bpy)_2]^{+} \quad \textbf{(2.2)}$$

$$[Ru(bpy^{\cdot -})(bpy)_2]^{+} + e^- \longrightarrow [Ru(bpy^{\cdot -})_2(bpy)] \quad \textbf{(2.3)}$$

$$[Ru(bpy^{\cdot -})_2(bpy)] + e^- \longrightarrow [Ru(bpy^{\cdot -})_3]^{-} \quad \textbf{(2.4)}$$

The first two reductions, as well as the metal-centered oxidation, are reversible, where reversibility is defined by the difference in anodic and cathodic peak potentials (ideally 59 mV for a one-electron process, but more typically in the range of 70-80 mV in

non-aqueous media),[i] as well as a cathodic/anodic peak current ratio close to unity. By these metrics, the last reduction (eq 2.4) is quasi-reversible at best.

Using the description above, the energy of the ^{1}MLCT band can be thought of as the amount of energy necessary to reduce the ligand and oxidize the metal:

$$E(MLCT) = |E(Ru^{III}/Ru^{II})| + |E(bpy/bpy^{\cdot -})| \qquad \textbf{(2.5)}$$

Several aspects of equation 2.5 are worth noting: (a) this is an approximation: energetics associated with solvation as well as electron correlation effects are not accounted for in this simplified expression;[28] (b) the fact that there are two contributions to the MLCT energy −the oxidation potential of the metal and the reduction potential of the ligand− implies that the value of E(MLCT) alone is not sufficient to determine whether a chromphore's energetics are suitable for a given reaction. One can observe MLCT bands at roughly the same energy arising from a very strong reductant (i.e., very negative ligand reduction potential) coupled with a very weak oxidant, or vice-versa. The electrochemical data of the compound is one of the ways by which these important details can be deconvolved.

[i]The peak separation for a given redox couple may be affected by variables such as the solvent and the geometry of the electrode configuration. The ferrocene/ferrocenium couple is considered completely reversible in non-aqueous media. As such, its peak separation in a given experiment can be used as a criterion for reversibility for other redox processes as long as the experimental conditions are the same for all the measurements. See ref. 27 for further details.

2.3. Excited State Kinetics

We are ultimately interested in reactions between an excited donor and a ground-state acceptor. Before we can discuss these processes, however, it is necessary to understand the excited-state properties of the donor in the absence of a quencher, since the presence (or absence) of a reaction will ultimately be determined by referring back to the donor's intrinsic excited-state behavior.

In a one-electron approximation (e.g., Figure 2.5), the electronic configuration of the excited state is obtained by simply taking an electron from an occupied orbital in the ground state and placing it in an empty orbital of higher energy. Although this is useful as a first approximation - particularly with regard to developing chemical intuition concerning the potential reactivity of the excited state - this picture has a number of significant deficiencies. First, the geometry of the molecule in the excited state will be different from that of the ground state. Second, electronic correlation effects (e.g., electron-electron repulsion) significantly modulate both ground- and excited-state energetics in ways distinct from what is inferred from orbital energies. In other words, there is not a one-to-one correlation between differences in orbital energies and the energy of a given electronic excited state. Finally, this approximation does not account for spin, which, as explained in Chapter 1, is important for understanding electronic absorption spectra[24] as well as accounting for conservation of angular momentum for a given reaction.[29] So, while a molecular orbital diagram such as the one shown in Figure 2.5 is a useful construct in terms of understanding the chemical nature of an electronic excited state, electronic transitions and the photophysics of excited states are best viewed

in terms of potential energy surface diagrams. One such diagram is shown in Figure 2.7, where Morse-like[30] curves are used to represent the various electronic states that arise from Figure 2.5 coupled with consideration of electron-electron interactions and any changes in equilibrium geometry. The diagram shown in Figure 2.7 only includes MLCT transitions and is appropriate for Ru(II) polypyridyls, where the MLCT excited states are the ones relevant for photo-induced electron and energy transfer.

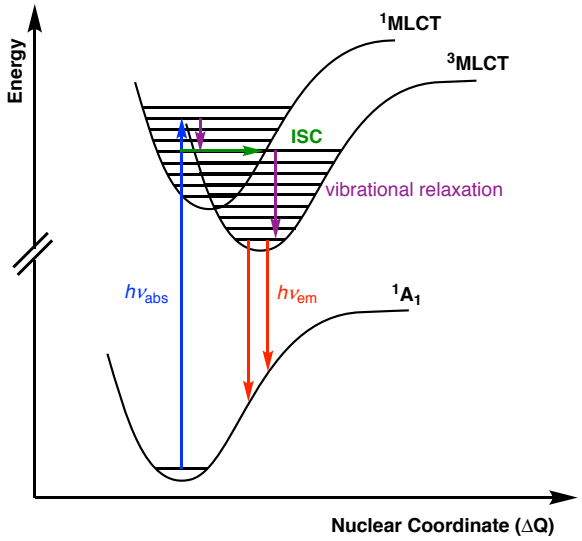


Figure 2.7. Simplified potential energy surface diagram for $[Ru(bpy)_3]^{2+}$.

2.3.1. Steady-State Emission

As shown in Figure 2.7, visible light excites $[Ru(bpy)_3]^{2+}$ into a ^{1}MLCT state; this short-lived state relaxes to a ^{3}MLCT state within ~100 fs via intersystem crossing (ISC, with rate constant k_{isc}).[31] The ^{3}MLCT state can relax back to the ground state either non-radiatively (with rate constant k_{nr}) or through luminescence (a radiative pathway with rate constant k_r). Equations 2.6 through 2.9 illustrate these processes. Photo-induced

reactions, such as ligand substitution, can also take place.[32] However, these are not observed in this dissertation, so they will not be discussed here.

$$[\mathrm{Ru^{II}(bpy)_3}]^{2+} + h\nu_{abs} \longrightarrow {}^1[\mathrm{Ru^{III}(bpy^{\cdot -})(bpy)_2}]^{2+*} \quad \textbf{(2.6)}$$

$${}^1[\mathrm{Ru^{III}(bpy^{\cdot -})(bpy)_2}]^{2+*} \xrightarrow{k_{isc}} {}^3[\mathrm{Ru^{III}(bpy^{\cdot -})(bpy)_2}]^{2+*} \quad \textbf{(2.7)}$$

$$[\mathrm{Ru^{III}(bpy^{\cdot -})(bpy)_2}]^{2+*} \xrightarrow{k_r} [\mathrm{Ru^{II}(bpy)_3}]^{2+} + h\nu_{em} \quad \textbf{(2.8)}$$

$$[\mathrm{Ru^{III}(bpy^{\cdot -})(bpy)_2}]^{2+*} \xrightarrow{k_{nr}} [\mathrm{Ru^{II}(bpy)_3}]^{2+} + heat \quad \textbf{(2.9)}$$

The solution-phase steady-state emission spectrum of $[Ru(bpy)_3]^{2+}$ at room temperature is shown in Figure 2.8: the emission maximum is at 620 nm. The same spectrum is obtained regardless of the excitation wavelength, consistent with the near-unit quantum yield of formation of the emissive ^{3}MLCT state.[14]

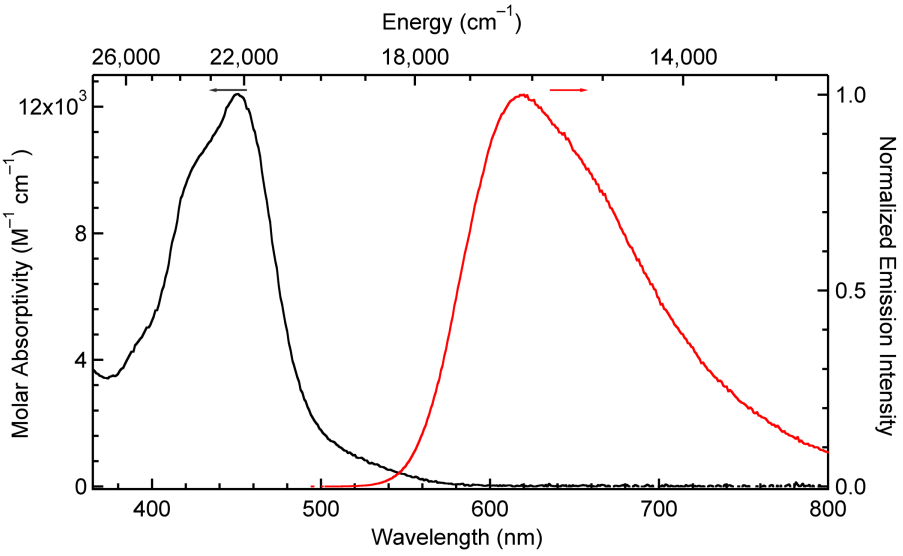


Figure 2.8. Electronic absorption spectrum (black trace) and steady state emission spectrum (red trace) of $[Ru(bpy)_3](PF_6)_2$ in acetonitrile solution at room temperature.

The emission maximum can be used as a first-order approximation of E_0, the energy difference between the triplet excited state (^{3}MLCT) and the ground state. The value of E_0 is an important quantity: in addition to quantifying the added free energy that light absorption affords, the zero-point energy of the excited state is needed in order to assess the thermodynamic viability of a given photo-induced reaction.

This value (E_0) is usually associated with the highest energy vibrational component of the emission spectrum at 77 K (which may or may not correspond to the observed emission maximum).[28] Regardless, E_0 can be accurately determined by a single mode fit of the steady-state emission spectrum as described by Claude and Meyer.[33] The spectrum should be corrected according to Parker and Rees when converting from wavelength to energy units.[34]

For an emissive substance, the simplest definition of the quantum yield (Φ) of emission (also called the radiative quantum yield) is the ratio between the number of photons emitted by a sample and the number of photons absorbed, as shown in eq 2.10.

$$\Phi = \frac{\#\ photons\ emitted}{\#\ photons\ absorbed} = \frac{I_{em}}{I_{abs}} \qquad \textbf{(2.10)}$$

The radiative quantum yield can also be described in terms of a kinetic competition, specifically the relative rate(s) of processes giving rise to emission versus the rates of all processes that serve to deplete the population of that emissive state. Using the rate constants from equations 2.8 and 2.9, in the absence of any species other than the chromophore, Φ can be expressed as:

$$\Phi_0 = \frac{k_r}{k_r + k_{nr}} = \frac{k_r}{k_0} \qquad \textbf{(2.11)}$$

where $k_0 = k_{nr} + k_r$, and the subscript 0 indicates that no quencher is present.

Experimental details regarding how to determine radiative quantum yields are included in the following chapters (see Experimental Section in Chapter 3).

2.3.2. Time-Resolved Emission

Both the radiative and non-radiative decay processes (equations 2.8 and 2.9 respectively) are first-order with respect to the excited state (ES) and give rise to the following expression for the rate at which that excited state is lost,

$$-\frac{d[\mathrm{ES}]}{dt} = k_r\,[\mathrm{ES}] + k_{nr}\,[\mathrm{ES}] = (k_r + k_{nr})[\mathrm{ES}] = k_0\,[\mathrm{ES}] \qquad \textbf{(2.12)}$$

this equation can be integrated to yield the rate law for a first-order reaction, shown in equation 2.13.

$$[\mathrm{ES}] = [\mathrm{ES}]_0\, e^{-k_0 t} \qquad \textbf{(2.13)}$$

The inverse of the observed rate constant, k_0^{-1}, is the lifetime (τ_0) of the excited state; for an emissive complex, this can be easily measured using time-resolved emission spectroscopy (for non-emissive compounds, excited-state lifetimes can be determined using time-resolved absorption methods).

In a time-resolved emission experiment, the sample is excited at a wavelength at or near its absorption maximum, with the emission collected at 90° with respect to the excitation beam in order to minimize scatter. A typical time-resolved emission trace for $[Ru(bpy)_3]^{2+}$ in acetonitrile is shown in Figure 2.9; τ_0 can be found by fitting the trace to a single exponential decay. For $[Ru(bpy)_3]^{2+}$, the lifetime ranges between 500 – 1000 ns, depending on a number of variables including solvent, oxygen concentration in the sample, and temperature.[8] In deoxygenated acetonitrile at room temperature, the lifetime of $[Ru(bpy)_3]^{2+}$ is 930 ± 40 ns (the error bars are obtained from the fitting of several datasets).

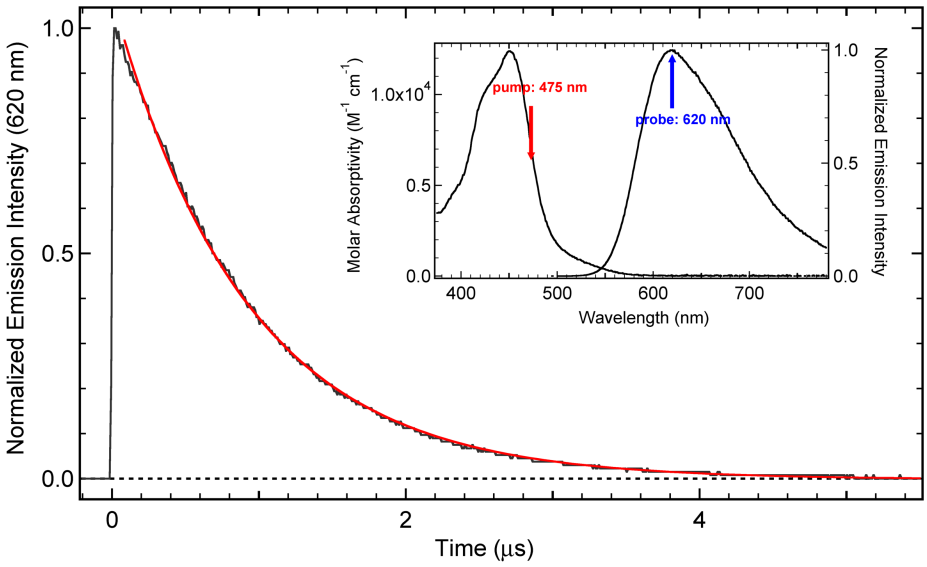


Figure 2.9. Time-resolved emission data (grey line) for $[Ru(bpy)_3]^{2+}$ in acetonitrile solution at room temperature. The sample was excited at 475 nm and emission was detected at 620 nm (as shown in the inset). The red trace shows the fit to a single exponential decay with τ = 930 ns.

Combining the excited-state lifetime and the radiative quantum yield, it is possible to calculate k_r and k_{nr}. Rearranging eq 2.11, we obtain:

$$k_r = \Phi_0 \times k_0 \quad \textbf{(2.14)}$$

$$k_{nr} = k_0 - (\Phi_0 \times k_0) = k_0 \times (1 - \Phi_0) \quad \textbf{(2.15)}$$

It is important to highlight that k_r is an intrinsic property of the luminophore and therefore remains constant no matter what reactions the excited state engages in (the value of k_r does, however, vary in different solvents[35]). On the other hand, k_{nr} varies when energy and/or electron transfer take place. All of the information that we will be interested in for a quenching reaction (in other words, the information about any processes competing with the emission) is contained in k_{nr}; in this regard, k_r can be viewed as a probe, providing insight into the dynamics of the system being manifested in k_{nr}. This concept will be revisited in later chapters.

2.4. Excited-State Reactivity of $[Ru(bpy)_3]^{2+}$

In its excited state, $[Ru(bpy)_3]^{2+}$ can act as an energy donor, an electron acceptor or an electron donor; thermodynamic and kinetic factors associated with a given reaction determine which process dominates.[12] In this dissertation, the Ru(II) polypyridyls always act as the donor, and both electron and energy transfer can take place; the energy transfer route can furthermore be subdivided according to the specific mechanism by which it proceeds. As a result, although determining that the excited state of the chromophore is reacting can be as straightforward as observing emission quenching, mechanistic determination of the nature of that reaction generally requires considerably more work, as will be described in the next few sections.

Figure 2.10 depicts the two most common mechanisms of energy transfer along with electron transfer. All of these are discussed below.

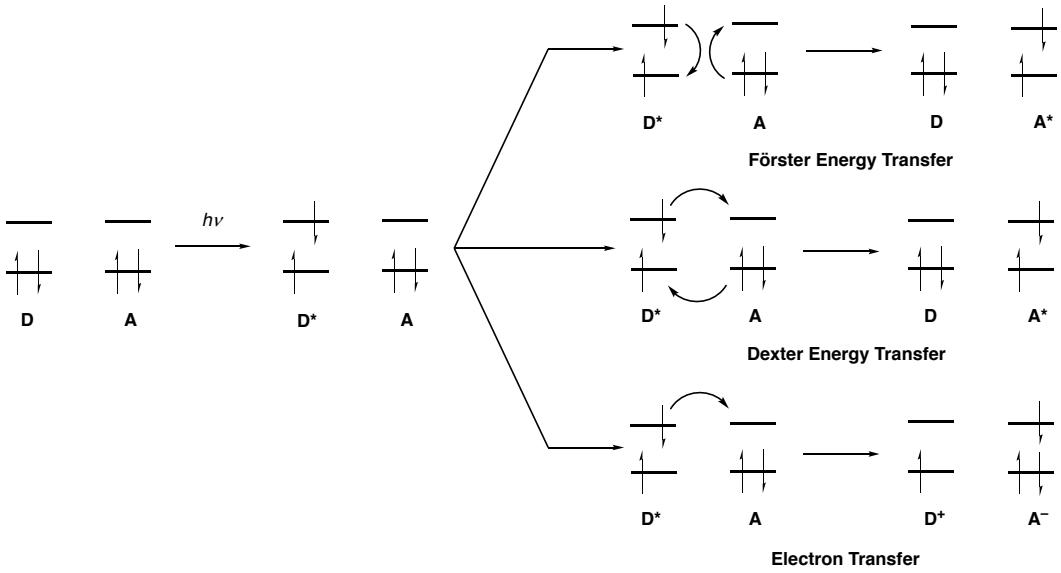


Figure 2.10. Electron and energy transfer mechanisms.

2.4.1. Energy Transfer: Förster and Dexter Mechanisms

Energy transfer is a process by which excess energy contained in one molecule (the donor) is transferred to another molecule (the acceptor). In the context of the chemical systems being discussed herein, that excess energy comes from the absorption of a photon by the donor to create an electronic excited state. The product of the reaction is an electronically excited acceptor molecule concomitant with reformation of the electronic ground state of the donor, as shown in eq 2.16.

$$D^* + A \xrightarrow{k_{EnT}} D + A^* \qquad \textbf{(2.16)}$$

Although energy transfer can occur as the result of emission from the donor and subsequent absorption of that emitted light by the acceptor (the so-called "trivial" mechanism), energy transfer more typically occurs via non-radiative processes (that is, the emission and reabsorption of light do not occur). The two most common mechanisms of non-radiative energy transfer are known as Förster (through-space) and Dexter (through-bond or "exchange") energy transfer. It should be noted that both Förster and Dexter transfer yield the same products (i.e. ground-state donor and excited-state acceptor), although the physical origins of the reaction are fundamentally different, as shown in Figure 2.10.[20]

Förster energy transfer (FRET)[36] is a dipolar mechanism that takes place through space: the transition moment dipole of the donor couples non-radiatively with the transition moment dipole of the acceptor (see Figure 2.11). Because of the dipolar nature of this mechanism, no orbital overlap is necessary between the donor and the acceptor. This makes Förster energy transfer operational over distances up to 100 Å.[37]

Overlap between the emission spectrum of the donor and the electronic absorption spectrum of the acceptor is necessary for the energy transfer to occur; this resonance condition (which in reality is simply a reflection of energy conservation for this process) is represented in Figure 2.12. Because of this condition, Förster transfer is often referred to as Fluorescence Resonance Energy Transfer (hence the acronym FRET).

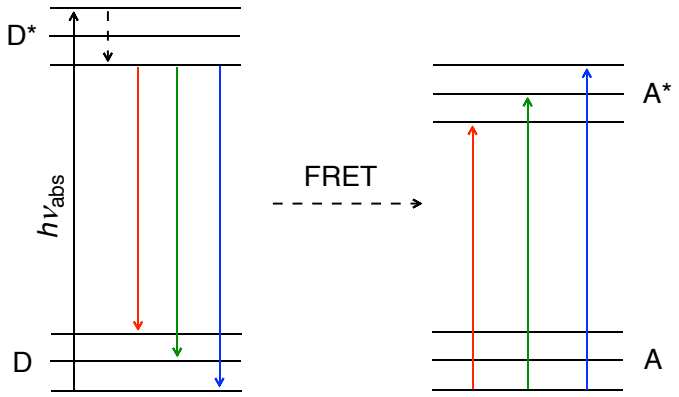


Figure 2.11. Simplified diagram showing the coupling of the donor (D) and acceptor (A) transition dipoles. Transitions represented in the same color are coupled together.

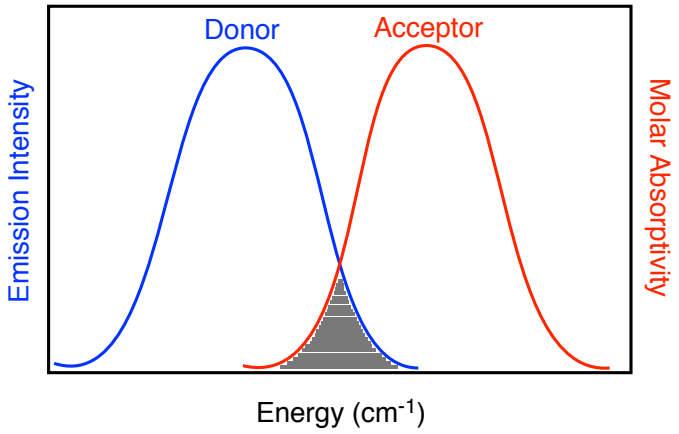


Figure 2.12. Schematic emission spectrum of the donor and absorption spectrum of the acceptor. The shaded region is the spectral overlap reflecting the resonance condition needed for Förster energy transfer to occur.

The rate constant for Förster energy transfer can be expressed as shown in equation 2.17,[38]

$$k_{FRET} = k_0^D \left(\frac{9(\ln 10)\kappa^2 \phi_D I}{128\pi^5 N \eta^4}\right) \frac{1}{R^6} \qquad \textbf{(2.17)}$$

where k_0^D and ϕ_D are the observed rate constant of the donor and its corresponding emission quantum yield (both in the absence of the acceptor), N is Avogadro's number,

η is the refractive index of the medium, I is the spectral overlap integral,[38] and R is the distance between the donor and the acceptor. The factor κ is related to the relative orientation of the dipoles associated with the donor's emission and the acceptor's absorption transitions. This orientation parameter can take any value between 0 and 4; for a bimolecular reaction between two freely rotating molecules in solution, a value of ⅔ is appropriate.[39]

Using the definition of radiative quantum yield (eq 2.11), equation 2.17 can be written as:

$$k_{FRET} = k_r^D \left(\frac{R_0}{R}\right)^6 \qquad \textbf{(2.18)}$$

where R_0 is the critical transfer distance (often called the Förster radius),[20] calculated as shown in (2.19). At such distance, both the relaxation of the donor and FRET are equally probable.

$$R_0^6 = \frac{9(\ln 10)\kappa^2}{128\pi^5 N\eta^4} I \qquad \textbf{(2.19)}$$

The Dexter mechanism,[40,41] on the other hand, is best thought of as two simultaneous electron transfer reactions (Figure 2.10). Except in rare cases, electron transfer is a through-bond process, meaning that Dexter energy transfer requires orbital overlap between the donor and the acceptor to occur: this limits its prevalence to reactions taking place at much shorter distances than the Förster mechanism (typically no more than 10 Å). In other words, for a bimolecular reaction the Dexter process requires physical contact between the excited donor and the acceptor. Conversely, since it is an

exchange process, "dark" states may be involved (i.e., the absorption or emission processes may be spin-forbidden, leading to a very small spectral overlap[5,42]). Only the relative energies of the electronic states involved in the reaction are relevant for defining a thermodynamically viable reaction. It is important to highlight that energy conservation is still a requirement.

Molecular oxygen can quench the excited state of many transition-metal polypyridyl compounds via Dexter energy transfer.[43,44] For this reason, most photophysical measurements involving $[Ru(bpy)_3]^{2+}$ and other transition-metal complexes are carried out in deoxygenated solutions.

Due to the fact that Dexter energy transfer is dependent upon orbital overlap, its distance dependence is exponential, as shown in (2.20).

$$k_{DET} = A \exp\left(-\beta(r - r_c)\right) \qquad \textbf{(2.20)}$$

where r is the D-A distance, r_c is the distance of closest approach at molecular contact, β is an attenuation factor (typically $\beta \leq 1$ Å^{-1}),[45] and A is on the order of 10^{10}–10^{13} s^{-1} for molecular systems.[42,45] Since it describes interactions between orbitals, which require short distances, equation 2.20 does not include the effect of diffusion in the energy transfer process.[42]

2.4.2. Electron Transfer

A generic electron transfer process can be represented as:

$$D + A \xrightarrow{k_{ET}} D^+ + A^- \qquad \textbf{(2.21)}$$

Although electron transfer can be accompanied by bond breaking and/or formation, the reactions in this dissertation are such that the structure and composition of both the donor and acceptor remain largely intact.

The kinetics of electron transfer can be described using Marcus theory,[46,47] where the rate constant for outer sphere electron transfer is shown in equation 2.22.

$$k_{ET} = \frac{2\pi}{\hbar}|H_{AB}|^2 \frac{1}{\sqrt{4\pi\lambda k_B T}} \exp\left[\frac{-(\Delta G_0 + \lambda)^2}{4\lambda k_B T}\right] \qquad \textbf{(2.22)}$$

In this expression, ΔG_0 is the driving force for electron transfer (which depends on the redox potentials of the donor and the acceptor[ii]), H_{AB} represents the electronic coupling between the donor and the acceptor, and λ is the reorganization energy. This latter term reflects energetics associated with the structural changes linked to oxidizing the donor and reducing the acceptor, as well as the reorganization of the solvent molecules due to the redistribution of charge that accompanies electron transfer. The magnitude of the electronic coupling (H_{AB}) depends on the distance and orientation of

[ii]For bimolecular reactions involving charged species, ΔG_0 includes work terms as well. These terms remain approximately constant within a series of closely related D-A systems (such as those considered in this dissertation) and will not be considered in subsequent chapters. See ref. 46 for further details.

donor and acceptor and therefore tends to be difficult to specify for bimolecular reactions in solution. Its determination, even for intramolecular D-A systems is not trivial.[48]

Even though electron transfer and Dexter energy transfer are closely related, two important differences should be noted. First, because two electrons are exchanged instead of one, Dexter energy transfer has a much steeper distance dependence than electron transfer (typically e^{-2r} as opposed to e^{-r} for electron transfer).[41] Second, since electron transfer leads to a new charge distribution, its reorganization energy (especially the solvent contribution) is much larger than that associated with Dexter (or for that matter Förster) energy transfer.[49]

Notwithstanding these details, the important point to appreciate is that the products formed following energy versus electron transfer are chemically distinct. This difference will provide a means for experimentally differentiating these two reaction pathways.

2.4.2.1 Redox Reactions in the Excited State: Redox Potentials

It was mentioned before that the redox activity of $[Ru(bpy)_3]^{2+}$ is enhanced in the excited state relative to the ground state: this circumstance arises due to the combined effects of charge separation (thereby creating chemical potential) as well as the increase in internal energy of the molecule due to the absorption of light. All the electron transfer reactions considered in this dissertation are photo-induced, which means it is the excited state of the donor that engages in a redox process. To assess whether these reactions are

thermodynamically favorable, the redox potentials of both the acceptor and the donor are necessary. In the case of the acceptor, those potentials are easily measured using cyclic voltammetry;[1,3,27] for the donor, more information must be taken into account, as described below.

Excited-state redox potentials cannot be directly measured, but can be calculated using the redox potentials for the ground state and the energy of the excited state. The relationship between these quantities is presented in Figure 2.13. Assuming that the all the excited state energy is available as free energy (i.e., the entropic contribution is neglected),[50] the excited state redox potentials can be calculated using equations 2.23 and 2.24.[12,19]

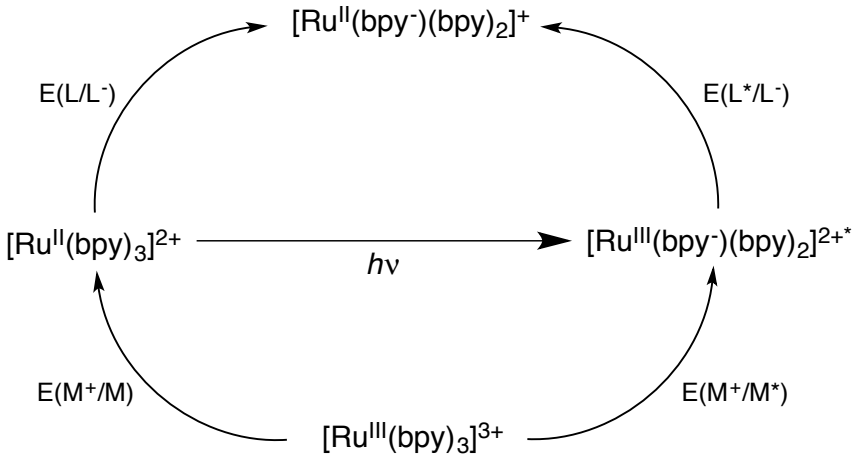


Figure 2.13. Thermodynamic cycle relating the excited and ground state redox potentials of $[Ru(bpy)_3]^{2+}$.

$$E(M^+/M^*) = E(M^+/M) - E_0 \quad \textbf{(2.23)}$$

$$E(L^*/L^-) = E(L/L^-) + E_0 \quad \textbf{(2.24)}$$

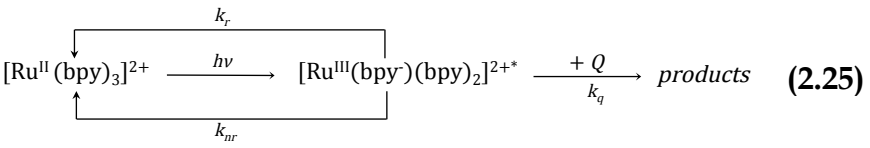
For the photo-induced reactions considered in this dissertation, the relevant quantity is $E(M^+/M^*)$, which will be combined with the reduction potential of the corresponding acceptor to calculate the driving force for the electron transfer. Several examples of this will be shown in the following chapters.

2.5. Stern-Volmer Quenching Studies

When investigating the kinetics of a given reaction like the ones in this dissertation, the simplest experiment that can be performed is a Stern-Volmer quenching study. This experiment allows one to determine whether a reaction is occurring between the excited state of the donor and the acceptor. While this is extremely useful information, it is important to stress that very little mechanistic information is afforded by a Stern-Volmer study, with the possible exception of identifying static versus dynamic contributions to the quenching (*vide infra*). As will become apparent in the discussion to follow, both energy and electron transfer reactions involving the excited state of the chromophore will yield experimentally indistinguishable results from a Stern-Volmer quenching study. It is only through the application of additional experiments (most notably time-resolved absorption spectroscopy) that further insight into the nature of the reaction responsible for the quenching can be gleaned.

In the context of an emissive species, the term "quenching" refers to any process that reduces the radiative quantum yield of a fluorophore. Not surprisingly, there is a wide variety of processes that could fall into this category, but only a few of which are relevant to this dissertation. Dynamic (or collisional) quenching is a bimolecular reaction between the excited chromophore and the quencher, whereas static quenching refers to process(es) that do not require diffusion of the reactants involved (e.g., a pre-association between the chromophore and the quencher prior to light absorption). Dynamic quenching can be quantified using time-resolved spectroscopic methods whereas static quenching is most clearly manifest using steady-state techniques (mainly, emission quantum yields). Ultimately, both methods should be employed in order to obtain a complete accounting of all of the contributions to quenching in a given system.

In section 2.3 the radiative and non-radiative pathways for the excited state were described. When a molecule other than the photoactive species is present in solution, the possibility of additional reactions (in this work, electron and/or energy transfer) is introduced. In a very general way, we can represent this situation in the following way:



(2.25)

where Q represents the quencher/substrate. In this scheme, the rate at which the excited state disappears is given by (2.26)

$$-\frac{d[\mathrm{ES}]}{dt} = k_0\,[\mathrm{ES}] + k_q\,[\mathrm{ES}][Q] \qquad \textbf{(2.26)}$$

"Quenching", then, refers to a situation in which k_q[Q] is sufficiently large relative to k_0 such that the observed lifetime of the excited state is measurably attenuated relative to its value in the absence of quencher. This condition is usually met provided the excited state lifetime is on the nanosecond time scale (or longer). Quantifying k_q is most easily done by carrying out measurements under pseudo first-order conditions: if the concentration of the quencher is at least one to two orders of magnitude larger than that of the chromophore,[iii] $[Q]$ can be assumed to be constant throughout the experiment. Under these conditions, equation 2.26 collapses to (2.27) and allows for the determination of k_q (eq 2.28).

$$-\frac{d[\mathrm{ES}]}{dt} = \left(k_0 + k_q[Q]\right)[\mathrm{ES}] = k_{obs}\,[\mathrm{ES}] \qquad \textbf{(2.27)}$$

$$k_{obs} = \left(k_0 + k_q[Q]\right) \qquad \textbf{(2.28)}$$

Based on equation 2.28, k_{obs} is now a concentration-dependent quantity reflecting both the intrinsic lifetime of the excited state and the extent to which the presence of the quencher introduces a kinetically competitive relaxation pathway. Since most Ru(II) polypyridyls are emissive, k_{obs} is most easily measured via time-resolved emission spectroscopy: by measuring the decay rate constant at several quencher concentrations,

[iii]Strictly, it must be [Q] >> [ES], but since evaluating the concentration of the excited state is not trivial, it is simpler to make [Q] >> [chromophore].

the quenching constant k_q can be determined by plotting k_{obs} as a function of quencher concentration as shown in the Stern-Volmer equation (eq 2.29).

$$\frac{k_{obs}}{k_0} = \frac{k_0 + k_q[Q]}{k_0} = 1 + \frac{k_q[Q]}{k_0} \qquad \textbf{(2.29)}$$

Thus, a plot of k_{obs}/k_0 versus [Q] should always yield a straight line with an intercept of 1 and a slope equal to k_q/k_0. Any significant deviations from linearity and/or an intercept value of 1 should be viewed as an indication of a problem with the data, the data workup, or, potentially, of a more complex reaction than represented by equation 2.27.[iv]

Alternatively, steady-state emission spectroscopy may be employed: the radiative quantum yield of the photocatalyst in the presence of a quencher depends on k_q and [Q] as shown in equation 2.30.

$$\Phi_q = \frac{k_r}{k_0 + k_q[Q]} \qquad \textbf{(2.30)}$$

Provided that the radiative quantum yields for the chromophore in the presence and absence of the quencher are determined under identical experimental conditions, their ratio can be related to the Stern-Volmer expression (eq 2.31).

[iv]Equation 2.27 is only valid in near-ideal scenarios. All the D-A systems studied in this dissertation can be reasonably represented by this model.

$$\frac{\Phi_0}{\Phi_q} = \frac{k_0 + k_q[Q]}{k_0} = 1 + \frac{k_q[Q]}{k_0} \qquad \textbf{(2.31)}$$

Assuming that the rate constant for excited-state decay of the chromophore (k_0) is known, k_q can be determined by measuring the radiative quantum yield as a function of quencher concentration. It is important to underscore that for the results of this experiment to be meaningful, quantum yields must be used in equation 2.31.

As was mentioned above, two kinds of quenching (static and dynamic) are possible. Figure 2.14 shows simulated Stern-Volmer plots using time-resolved and steady-state emission data for three different scenarios: 1) dynamic quenching (Figure 2.14*a*); 2) static quenching (Figure 2.14*b*); and 3) both dynamic and static quenching simultaneously present (Figure 2.14*c*).

In the case of dynamic quenching, the reaction with the acceptor provides additional pathways for the excited donor to disappear, which reduces its lifetime (because k_{nr} increases) and its quantum yield. Thus, if only dynamic quenching takes place, the Stern-Volmer plots derived from steady-state and time-resolved emission measurements will be indistinguishable from one another, as seen in Figure 2.14*a*. In other words, in this scenario equations 2.29 and 2.31 are equivalent and the ratio k_q/k_0 is typically denoted as K_D, the dynamic quenching constant.

Static quenching occurs when the chromophore and the quencher are associated in the ground state (i.e., prior to excitation); many authors refer to this situation as the formation of a "non-emissive complex".[42] In other words, there is an equilibrium between the free chromophore and the chromophore bound to the quencher, and the emission of

the latter is quenched. As a consequence, only emission from the free chromophore can be detected. This will typically not have an effect on the lifetime of the chromophore (that is, $k_{obs} = k_0$): the Stern-Volmer plot derived from time-resolved emission will therefore be a flat line (Figure 2.14*b*). This type of quenching will, nevertheless, manifest in the time-resolved data as a decrease in the initial amplitude of the signal. Conversely, measurements of the radiative quantum yield as a function of quencher concentration will yield a linear Stern-Volmer plot consistent with equation 2.31. In this case, k_q/k_0 is usually designated as K_S, the static quenching constant (note that this is an equilibrium constant, unlike K_D).

There are two possible explanations for the lack of emission from the D-A complex: a) its emission lifetime is faster than what can be measured with the instrument employed, or b) upon excitation, a different state is accessed in the free chromophore compared to the D-A complex. In the first scenario, using different instrumentation might reveal a faster kinetic component. In the second, the electronic absorption spectrum of the D-A complex will not be a simple linear combination of the individual spectra of the chromophore and the quencher.[42,51]

Finally, if static and dynamic contributions to the quenching are present, both the quantum yield and the lifetime of the excited state will be affected, albeit not in the same way. As shown in Figure 2.14*c*, the Stern-Volmer plot based on time-resolved emission data will yield a straight line, being only influenced by the dynamic contributions to the quenching. The plot based on radiative quantum yield data, on the other hand, will reflect

contributions from both static and dynamic processes and will display a quadratic relationship between Φ_0/Φ_q and [Q], as shown in Figure 2.14*c* and eq 2.32.

$$\frac{\Phi_0}{\Phi_q} = (1 + \mathrm{K_D[Q]})(1 + \mathrm{K_S[Q]}) \qquad \textbf{(2.32)}$$

where K_D and K_S are as previously defined.

As mentioned previously, K_D is the slope of the Stern- Volmer plot based on time-resolved experiments (eq 2.30), which allows K_S to be calculated using the quadratic fit of the steady-state Stern-Volmer plot and the value for K_D obtained from the linear fit of the time-resolved data.

It is important to notice that nowhere in the above discussion was the nature of the quenching mechanism considered. Stern-Volmer studies are helpful because the excited state lifetime is shortened if a reaction between the excited photocatalyst and a quencher is taking place. However, the only information these studies can provide is whether or not the excited state is engaging in a reaction. In Chapters 4 and 5, it will be described how these studies were used to determine that a bridge-exchange reaction was taking place between the donor and the acceptor. Nevertheless, even in that case, the reaction responsible for the quenching of the ^{3}MLCT of the donor was not identified based on steady-state or time-resolved emission results.

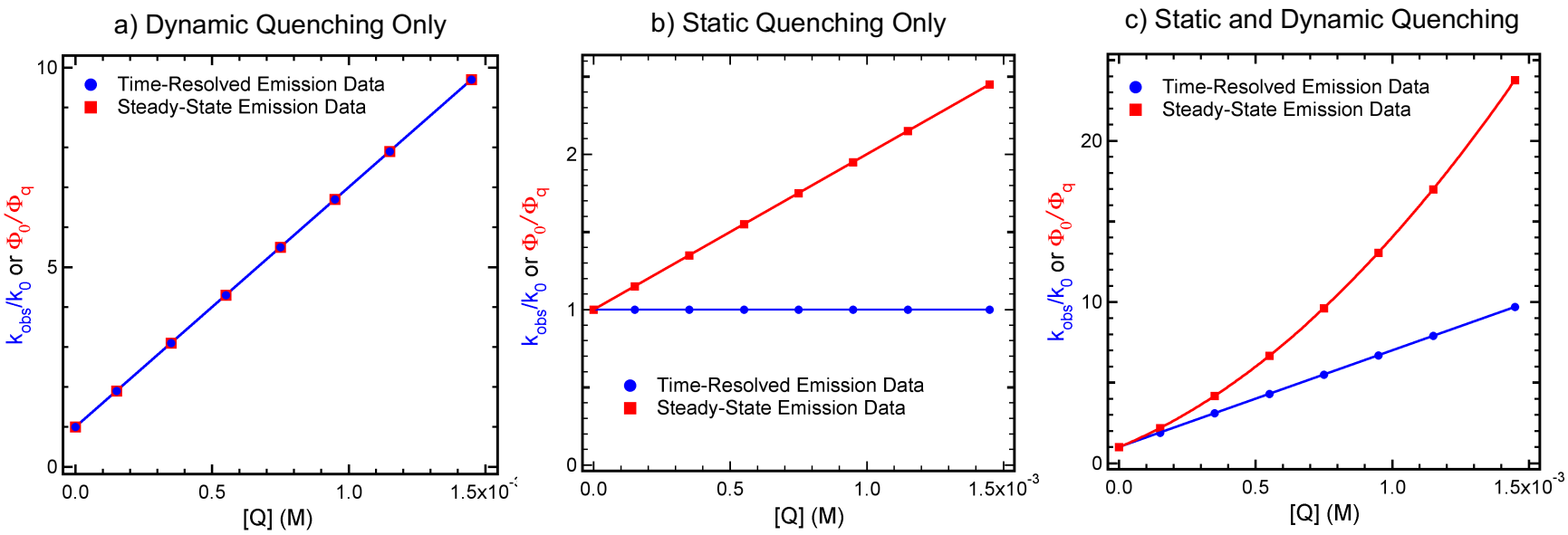


Figure 2.14. Simulated Stern-Volmer plots based on time-resolved (blue) and steady-state (red) emission experiments. The lines correspond to the fits according to equations 2.29, 2.31 or 2.32. For these simulations, K_D = 6000 M^{-1}, K_S = 1000 M^{-1}.

2.6. Identifying the Nature of the Excited State Reaction

The preceding discussion emphasized that a Stern-Volmer study does not provide any insight into the actual reaction the excited state of a sensitizer is engaging in. As any synthetic chemist knows, the disappearance of the starting material does not mean the formation of the desired product. Analogously, the observation of quenching of emission from the sensitizer in a Stern-Volmer quenching study is nothing more than evidence that the starting material (i.e., the excited state) is being consumed. In order to determine what reaction actually occurred, the product(s) of the reaction must be identified.

In this dissertation, dynamic quenching is far more prevalent than static quenching. For this reason, the latter will only be discussed when it is observed; the following sections will focus exclusively on dynamic quenching.

As mentioned previously, the two reaction pathways this work focuses on are electron and energy transfer between the excited donor and the acceptor/quencher. In the case of energy transfer, the donor will go back to the ground state, whereas electron transfer will result in its oxidation (with corresponding reduction of the acceptor). Direct detection of one (or more) of these products is the gold standard by which mechanistic pathways in these reactions must be established.

Time-resolved absorption spectroscopy, also known as transient absorption (TA), is a very useful tool in these cases. This technique uses a laser pulse to excite the sample and a white light source to probe the absorption of the transient species formed due to excitation. In many ways, one can think of transient absorption spectroscopy as taking a

UV-Vis spectrum of an excited state, using the absorption of the ground state as the blank. The TA signal, then, is the change in absorbance of the sample before and after excitation. This renders the technique more versatile than time-resolved emission because non-emissive molecules can be studied as well. Depending on the instrumentation available, difference spectra can be acquired at single wavelengths (yielding kinetic traces, as shown in Figure 2.15) or a full spectrum can be obtained.

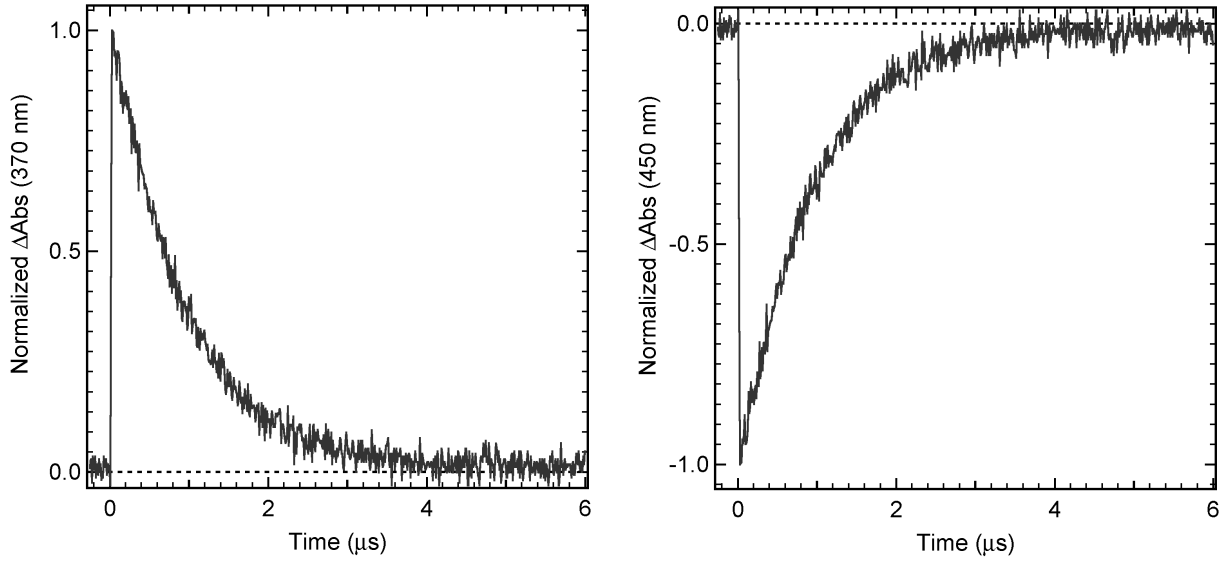


Figure 2.15. Kinetic traces for $[Ru(bpy)_3]^{2+}$ following MLCT excitation at 475 nm in acetonitrile solution. Left: λ_{probe} = 450 nm. The negative signal (i.e., "bleach") is due to the presence of Ru^{III} (loss of Ru^{II}) in the excited state relative to the ground state. Right: λ_{probe} = 370 nm. This positive feature arises due to the presence of the reduced ligand in the MLCT excited state.

For a TA experiment, an expression derived from Beer's law can be written for ΔA, the change in absorbance before and after excitation (i.e., excited state minus ground state):

$$\Delta A = \Delta\varepsilon \cdot b \cdot [GS] \cdot \eta^{ex} \quad \textbf{(2.33)}$$

Here, $\Delta\varepsilon$ is the change in molar absorptivity between the ground state and the excited state:

$$\Delta\varepsilon = \varepsilon_{ES} - \varepsilon_{GS} \quad \textbf{(2.34)}$$

Additionally, b is the optical path length, [GS] is the concentration of the ground state (i.e., the concentration of the sample) and η^{ex} is the fraction of molecules that are excited from the ground state to the excited state ($0 < \eta^{ex} < 1$). For a given experiment, b and [GS] are constant. η^{ex} depends on, among other factors, the cross-section between the pump and probe beams, but remains constant as long as the experimental conditions are not changed. When that is the case, any changes in the sign of ΔA are a direct reflection of the changes in $\Delta\varepsilon$.

Figure 2.16 presents a qualitative way to view the type of information obtained in a TA experiment. If at a certain wavelength the excited state absorbs more strongly than the ground state, a positive feature is observed. Conversely, if the ground state absorbs more than the excited state, a negative feature ("bleach") is obtained. The wavelengths at which the excited and ground states have the same absorbance are called isosbestic points.

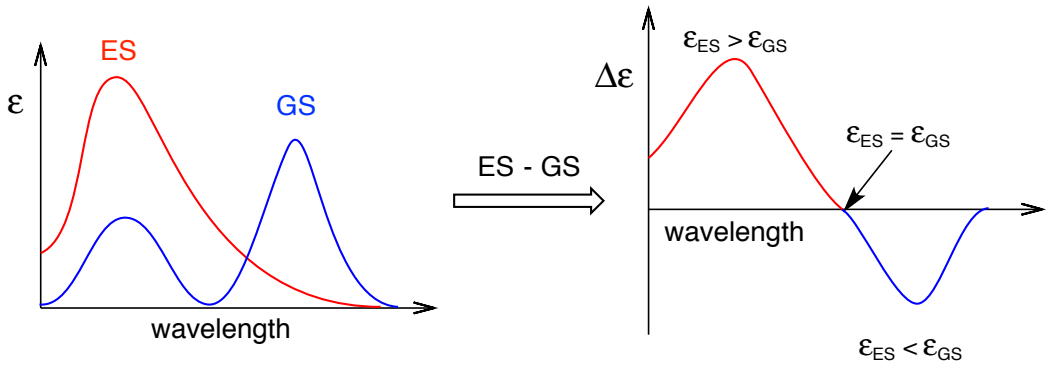


Figure 2.16. Left: schematic absorption spectra of the ground and excited states. Right: schematic representation of a transient absorption plot. The positive feature is shown in red, the bleach is in blue.

In the case of the MLCT excited state of $[Ru(bpy)_3]^{2+}$, the main diagnostic feature for the oxidized species is a bleach centered around 450 nm; this signal reflects the loss of Ru(II) in the excited state relative to the ground state (or the presence of Ru(III), depending how you look at it).[52] In contrast, the absorption centered around 370 nm indicates the presence of a bpy radical anion, and corresponds to the "reduced" portion of the excited state.[52] Kinetic traces for both of these features in the absence of any quencher are shown in Figure 2.15. It should be noted that as the excited molecules relax back to the ground state, both these signals decay simultaneously and their kinetic traces go back to zero, indicative of ground-state recovery.

Now let us consider what happens to the TA traces upon adding a quencher. To illustrate the different scenarios, several simulated TA traces are shown in Figure 2.17. For the unquenched chromophore, a lifetime of 700 ns was used. To make comparisons easier, a lifetime of 300 ns was assumed for the quenched chromophore, regardless of the reaction taking place. Upon photoexcitation, the excited state, $[Ru^{III}(bpy^{-})(bpy)_2]^{2+*}$, is

formed, leading to a positive feature at 370 nm (due to bpy^-) and a bleach at 450 nm (diagnostic for Ru^{III}). If no quencher is present, both traces go back to zero with the same rate constant.

In the presence of an energy acceptor, the product of the quenching reaction is $[Ru(bpy)_3]^{2+}$, the same species present before excitation (see Figure 2.10), so both the Ru^{III} and the bpy^- signals are lost at the same time, with an observed rate constant, k_{obs}, which is larger than k_0 (see equations 2.27 and 2.28). This illustrates what amounts to the most critical diagnostic for an energy transfer mechanism: the simultaneous, kinetically indistinguishable loss of both the bpy^- and Ru^{III} species. This occurs because both of these components comprise the reactive excited state, and therefore both are lost in an energy transfer process that returns the chromophore to the ground state.

In the case of an electron transfer, if $[Ru(bpy)_3]^{2+}$ acts as the donor (as in all the D-A systems in this dissertation), it is reduced to $[Ru(bpy^-)(bpy)_2]^+$ due to its reaction with the substrate. This has two consequences: (1) persistence of the absorption feature at 370 nm, concomitant with (2) a partial recovery of the bleach at 450 nm. The recovery of the bleach signal is only partial because, although reduction converts the Ru^{III} species present in the excited state to Ru^{II}, the ground-state MLCT absorption has three contributions (i.e., MLCT transitions to each of the three bpy ligands): the product of reductive quenching therefore only recovers ~⅔ of its original intensity due to the persistence of bpy^-. This situation is illustrated in Figure 2.17*e*. Oxidative quenching, on the other hand, results in the formation of $[Ru^{III}(bpy)_3]^{3+}$. This will result in the mirror image of the observables just described for reductive quenching wherein the bleach persists

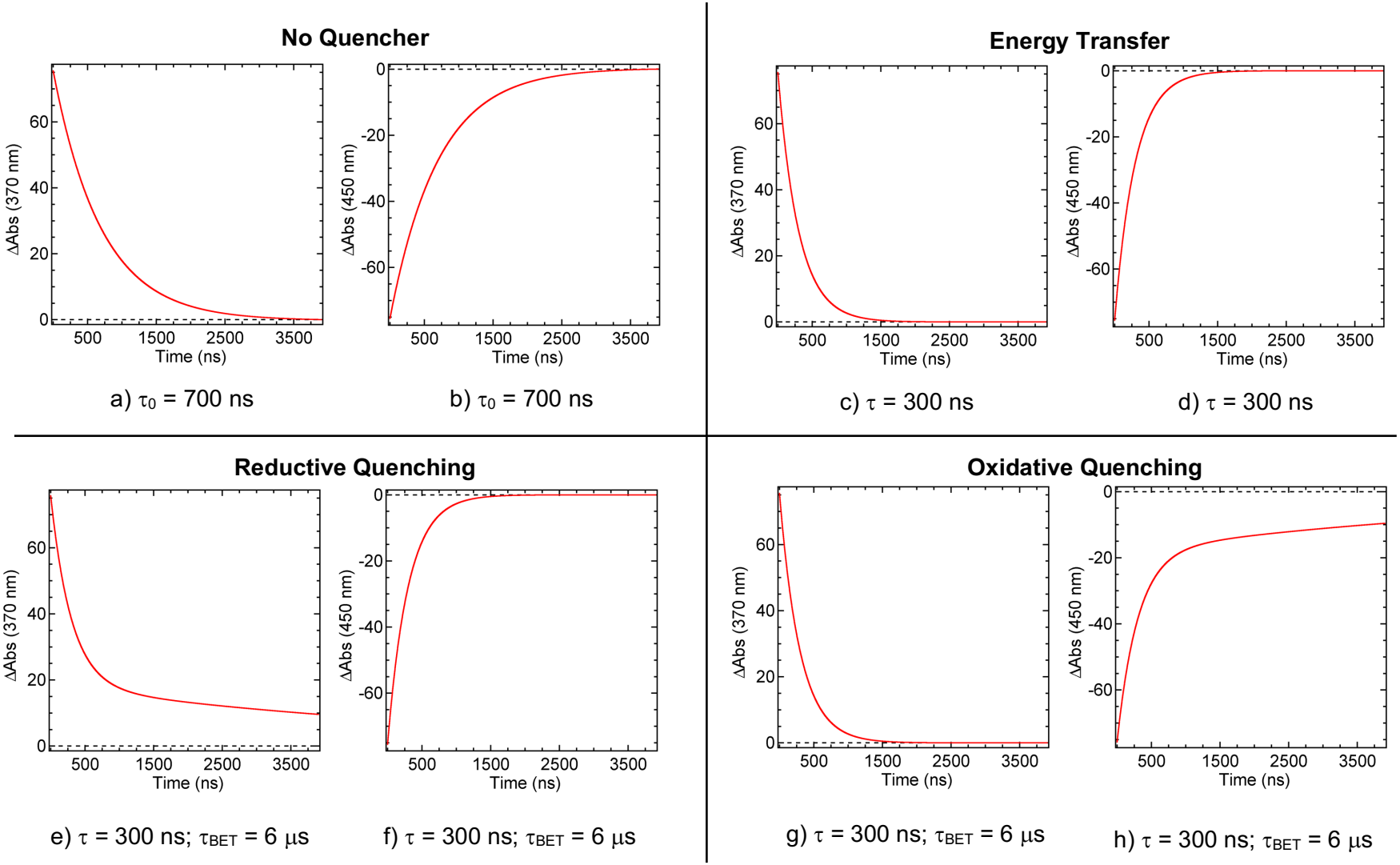


Figure 2.17. Simulated TA traces for $[Ru(bpy)_3]^{2+}$ following MLCT excitation with no quencher (a, b), in the presence of an energy transfer acceptor (c, d); in the presence of an electron donor (e, f); and in the presence of an electron acceptor (g, h).

concomitant with the loss of the bpy^- signal at 370 nm. This last scenario is included here for the sake of completion, despite not having any examples of Ru(II) polypyridyls as electron acceptors in this work.

Given these descriptions, the key qualitative differences between electron and energy transfer quenching processes lie in the wavelength dependence of the observed kinetics: for energy transfer one observes wavelength independent kinetics, whereas electron transfer results in qualitatively different kinetic traces depending on probe wavelength and the nature (i.e., oxidative or reductive) of the reaction.

It should be noted that this discussion was focused on the excited state of $[Ru(bpy)_3]^{2+}$ because its reduced and oxidized forms have easily distinguishable electronic absorption spectra. In a D-A system where the acceptor has clearly identifiable spectroscopic signatures, its changes could be monitored instead (or additionally). However, this is not the case for the compounds studied in this dissertation.

2.7. Concluding Remarks

The goal of this chapter has been to introduce the main concepts that will be employed to analyze the data obtained for the D-A systems throughout this dissertation. While many of these concepts will be revisited in later chapters, it is advantageous to compile all this information and connect these ideas in one place for easy reference.

As has been mentioned before, all of the donors used in this work are Ru(II) polypyridyls; their properties will be examined in comparison to other members of this

group and the reader is referred back to this chapter for a more detailed discussion of such properties. In a similar fashion, data from quenching studies will be presented in most chapters and will be analyzed as outlined in this chapter. When necessary, an additional theoretical framework will be presented, based on the specific system under consideration.

It is worth noting that the versatility of $[Ru(bpy)_3]^{2+}$ described here is not exclusive to Ru(II), as polypyridyl compounds of other transition metals behave similarly.[45,53,54] Furthermore, it is this behavior that has made these compounds the main focus of photoredox catalysis for several years,[55,56] even if new directions, employing metal-free catalysts, are presently being pursued by a large number of researchers.[57,58]

REFERENCES

REFERENCES

(1) Weldon, B. T.; Wheeler, D. E.; Kirby, J. P.; McCusker, J. K. *Inorg. Chem.* **2001**, *40*, 6802–6812.

(2) Picraux, L. B.; Weldon, B. T.; McCusker, J. K. *Inorg. Chem.* **2002**, *42*, 273–282.

(3) Picraux, L. B.; Smeigh, A. L.; Guo, D.; McCusker, J. K. *Inorg. Chem.* **2005**, *44*, 7846–7859.

(4) Kirby, J. P.; Weldon, B. T.; McCusker, J. K. *Inorg. Chem.* **1998**, *37*, 3658–3659.

(5) Soler, M.; McCusker, J. K. *J. Am. Chem. Soc.* **2008**, *130*, 4708–4724.

(6) Kouzelos, J. A. The Effect of Electronic Spin on the Reactivity of Spin-Coupled Transition Metal Complexes, Michigan State University, 2015.

(7) Armstrong, W. H.; Spool, A.; Papaefthymiou, G. C.; Frankel, R. B.; Lippard, S. J. *J. Am. Chem. Soc.* **1984**, *106*, 3653–3667.

(8) Juris, A.; Balzani, V.; Barigelletti, F.; Campagna, S.; Belser, P.; von Zelewsky, A. *Coord. Chem. Rev.* **1988**, *84*, 85–277.

(9) Lin, C. T.; Bottcher, W.; Chou, M.; Creutz, C.; Sutin, N. *J. Am. Chem. Soc.* **1976**, *98*, 6536–6544.

(10) Evans, I. P.; Spencer, A.; Wilkinson, G. *J. Chem. Soc. Dalt. Trans.* **1973**, 204–209.

(11) Kurtz, D. M. *Chem. Rev.* **1990**, *90*, 585–606.

(12) Creutz, C.; Sutin, N. *Inorg. Chem.* **1976**, *15*, 496–499.

(13) Balzani, V.; Bolletta, F.; Gandolfi, M.; Maestri, M. *Top. Curr. Chem.* **1978**, *75*, 1–64.

(14) Sutin, N.; Creutz, C. *Pure Appl. Chem.* **1980**, *52*, 2717–2738.

(15) Burstall, F. H. *J. Chem. Soc.* **1936**, 173.

(16) Lytle, F. E.; Hercules, D. M. *J. Am. Chem. Soc.* **1969**, *91*, 253–257.

(17) Knoll, J. D.; Turro, C. *Coord. Chem. Rev.* **2015**, *282–283*, 110–126.

(18) Boynton, A. N.; Marcélis, L.; McConnell, A. J.; Barton, J. K. *Inorg. Chem.* **2017**, *56*,

8381–8389.

(19) Rehm, D.; Weller, A. *Isr. J. Chem.* **1970**, *8*, 259–271.

(20) Arnaut, L.; Formosinho, S.; Burrows, H. *Chemical Kinetics. From Molecular Structure to Chemical Reactivity.*; Elsevier: Amsterdam, 2007.

(21) Carmieli, R.; Thazhathveetil, A. K.; Lewis, F. D.; Wasielewski, M. R. *J. Am. Chem. Soc.* **2013**, *135*, 10970–10973.

(22) Krzyaniak, M. D.; Kobr, L.; Rugg, B. K.; Phelan, B. T.; Margulies, E. A.; Nelson, J. N.; Young, R. M.; Wasielewski, M. R. *J. Mater. Chem. C* **2015**, *3*, 7962–7967.

(23) Sutin, N.; Creutz, C. *Adv. Chem. Ser.* **1978**, *168*, 1–27.

(24) Drago, R. S. *Physical Methods for Chemists*; Saunders College Pub.: Philadelphia, 1992.

(25) Mabbott, G. A. *J. Chem. Educ.* **1983**, *60*, 697.

(26) Bard, A. J.; Faulkner, L. R. *Electrochemical Methods Fundamentals and Applications*, 2nd ed.; Wiley & Sons: New York, 2001.

(27) Elgrishi, N.; Rountree, K. J.; McCarthy, B. D.; Rountree, E. S.; Eisenhart, T. T.; Dempsey, J. L. *J. Chem. Educ.* **2018**, *95*, 197–206.

(28) Vlcek, A. A.; Dodsworth, E. S.; Pietro, W. J.; Lever, A. B. P. *Inorg. Chem.* **1995**, *34*, 1906–1913.

(29) Guo, D.; Knight, T. E.; McCusker, J. K. *Science* **2011**, *334*, 1684–1687.

(30) McQuarrie, D. A.; Simon, J. D. *Physical Chemistry: a Molecular Approach*, 1st ed.; University Science Books, 1997.

(31) Damrauer, N. H.; Cerullo, G.; Yeh, A.; Boussie, T. R.; Shank, C. V; McCusker, J. K. *Science* **1997**, *275*, 54–57.

(32) White, J. K.; Schmehl, R. H.; Turro, C. *Inorg. Chim. Acta* **2017**, *454*, 7–20.

(33) Claude, J. P.; Meyer, T. J. *J. Phys. Chem.* **1995**, *99*, 51–54.

(34) Parker, C. A.; Rees, W. T. *Analyst* **1960**, *85*, 587–600.

(35) Caspar, J. V.; Meyer, T. J. *J. Am. Chem. Soc.* **1983**, *105*, 5583–5590.

(36) Förster, T. *Discuss. Faraday Soc.* **1959**, *27*, 7–17.

(37) Sahoo, H. *J. Photochem. Photobiol. C Photochem. Rev.* **2011**, *12*, 20–30.

(38) Scholes, G. D. *Annu. Rev. Phys. Chem.* **2003**, *54*, 57–87.

(39) Braslavsky, S. E.; Fron, E.; Rodríguez, H. B.; Román, E. S.; Scholes, G. D.; Schweitzer, G.; Valeur, B.; Wirz, J. *Photochem. Photobiol. Sci.* **2008**, *7*, 1444–1448.

(40) Dexter, D. L. *J. Chem. Phys.* **1953**, *21*, 836–850.

(41) Scandola, F.; Indelli, M. T.; Chiorboli, C.; Bignozzi, C. A. *Top. Curr. Chem.* **1990**, *158*, 73–149.

(42) Lakowicz, J. R. *Principles of Fluorescence Spectroscopy*, 3rd ed.; Springer US: Boston, 2006.

(43) Brunschwig, B.; Sutin, N. *J. Am. Chem. Soc.* **1978**, *100*, 7568–7577.

(44) Demas, J. N.; Harris, E. W.; McBride, R. P. *J. Am. Chem. Soc.* **1977**, *99*, 3547–3551.

(45) Barigelletti, F.; Flamigni, L. *Chem. Soc. Rev.* **2000**, *29*, 1–12.

(46) Marcus, R. A.; Sutin, N. *Biochim. Biophys. Acta - Rev. Bioenerg.* **1985**, *811*, 265–322.

(47) Marcus, R. A. *Angew. Chem. Int. Ed.* **1993**, *32*, 1111–1121.

(48) Wu, Q.; Van Voorhis, T. *J. Chem. Phys.* **2006**, *125*, 164105-1-164105–164109.

(49) Scandola, F.; Balzani, V. *J. Chem. Educ.* **1983**, *60*, 814–823.

(50) Balzani, V.; Bolletta, F.; Scandola, F.; Ballardini, R. *Pure Appl. Chem.* **1979**, *51*, 299–311.

(51) Welin, E. R.; Le, C.; Arias-Rotondo, D. M.; McCusker, J. K.; MacMillan, D. W. C. *Science* **2017**, *355*, 380–385.

(52) Brown, A. M.; McCusker, C. E.; McCusker, J. K. *Dalton Trans.* **2014**, *43*, 17635–17646.

(53) Dixon, I. M.; Collin, J.-P.; Sauvage, J.-P.; Flamigni, L.; Encinas, S.; Barigelletti, F. *Chem. Soc. Rev.* **2000**, *29*, 385–391.

(54) Sacksteder, L. A.; Brown, E. A.; Demas, J. N.; Zipp, A. P.; Streich, J.; DeGraff, B. A. *Inorg. Chem.* **1990**, *29*, 4335–4340.

(55) Prier, C. K.; Rankic, D. A.; MacMillan, D. W. C. *Chem. Rev*. **2013**, *113*, 5322–5363.

(56) Arias-Rotondo, D. M.; McCusker, J. K. *Chem. Soc. Rev.* **2016**, *45*, 5803–5820.

(57) Romero, N. A.; Nicewicz, D. A. *Chem. Rev.* **2016**, *116*, 10075–10166.

(58) Lim, C.-H.; Ryan, M. D.; McCarthy, B. G.; Theriot, J. C.; Sartor, S. M.; Damrauer, N. H.; Musgrave, C. B.; Miyake, G. M. *J. Am. Chem. Soc.* **2017**, *139*, 348–355.

Chapter 3. Synthesis and Characterization of a New Donor-Acceptor Pair in the Quest for a tren-Capped Intramolecular Assembly

"An expert is a person who has found out by his own painful experience all the mistakes that one can make in a very narrow field." –Niels Bohr

3.1. Introduction

Many factors can affect the reactivity of a given compound, some of them tied to its electronic structure, and while some have received much attention, the effect of spin polarization on reactivity has remained largely unexplored. The overarching goal of this dissertation is to explore the effect that the spin of a system has on its reactivity, with emphasis on electron and energy transfer. As was discussed in Chapter 1, Heisenberg spin-exchange can be used as a means to affect the spin distribution of a system without altering its geometry or composition. Thus, combining a spin-coupled acceptor with the appropriate donor gives us a platform to study the interplay between spin polarization and reactivity.

The ideal D-A system for this purpose would be one where every property (electronic and chemical structure, redox behavior, photophysics, etc.) remains exactly the same, except for the spin polarization, so that any changes in the reactivity can be attributed to such variation. On a feasible level, having a series of closely related compounds with different values of *J* (the strength of the spin coupling) is a realistic way to achieve this. In this context, the oxo/hydroxo-bridged diferric cores introduced in Chapter 1 are an attractive option for the acceptor, given their ease of synthesis,[1,2] their

well-characterized behavior,[1–3] their ability to quench the excited state of Ru(II) polypyridyls,[2,4] and the order-of-magnitude change in their coupling constant upon protonation.[2,5,6] Utilizing the same approach as Weldon et al.,[2] such a series of compounds may be designed. To overcome diffusion-limited kinetics, the objective is to prepare a series of covalently attached D-A systems with closely related properties.

Our first target was a relatively unadorned D-A intramolecular assembly. The use of tren (tris(2-aminoethyl)amine) as the capping ligand instead of Tp (1-hydrotris(pyrazolyl)borate) would simplify the spectroscopic and electrochemical properties of the system,[7] while only requiring one carboxylate bridge between the iron(III) centers. This capping ligand does not allow for protonation of the oxo bridge, which removed our ability to vary the strength of spin coupling in the acceptor. However, this D-A system was expected to be a relatively straightforward first step towards more complex ones. Regarding the donor, to localize its ^{3}MLCT excited state on the bridging ligand (closer to the diiron core), tmb (4,4',5,5'-tetramethyl-2,2'-bipyridine) was chosen as the ancillary ligand.

Initially, synthetic efforts were focused on preparing the donor and acceptor as separate molecules, which led to two new compounds, a tren-capped diiron(III) oxo-bridged core, and a heteroleptic Ru(II) polypyridyl complex; their syntheses and characterization are described in this chapter, along with bimolecular quenching studies involving them. Unfortunately, all attempts to synthesize the corresponding intramolecular assembly were unsuccessful. Those attempts and the possible reasons they did not work are also discussed here.

3.2. Experimental Section

General. All chemicals and solvents were obtained from Fisher Scientific or Sigma-Aldrich and used without purification unless otherwise stated. $RuCl_3 \cdot xH_2O$ was purchased from Strem Chemicals and Sephadex LH-20 from GE Life Sciences. 10% palladium on activated carbon paste type 487 (referred to as Pd/C throughout this dissertation) was purchased from Alfa Aesar. 2-acetylpyridine was freshly distilled under vacuum prior to use. Crotonaldehyde was distilled under N_2.[8] Anhydrous MeOH was purchased from Alfa Aesar and stored over 4Å molecular sieves. Diisopropylamine was distilled from NaOH, under nitrogen, then freeze–pump–thaw degassed and stored in the glovebox. Tren was distilled from activated carbon and KOH under nitrogen, then freeze–pump–thaw degassed and stored in the glovebox.

^1H NMR spectra were collected on Agilent DDR2 500 MHz NMR spectrometers equipped with 7600AS 96-sample autosamplers. Mass spectra were obtained at the Michigan State University Mass Spectrometry and Metabolomics Core. Elemental analyses were obtained through the analytical facilities at Michigan State University. Solvent included in calculated elemental analysis percentages was included to give the best fit based on solvents identified by NMR or XRD.

3.2.1. Syntheses

(2-Pyridacyl)pyridinium iodide.[9,10] Pyridine (60 mL) and I_2 (24 g) were stirred under a nitrogen atmosphere at 70 °C for 30 min. 2-acetylpyridine (10 mL, 0.089 mol) was then added and the reaction mixture was kept at 80 °C for 4 h. After that time, the reaction was

allowed to reach room temperature and the gray-green solid was collected by vacuum filtration and washed with pyridine and ethanol. That solid was recrystallized from hot ethanol using activated carbon to give the pure product as a glittery green solid. Yield: 16.6 g (52%). ^{1}H NMR (DMSO-d_6, 500 MHz) δ (ppm): 8.99 (dd, *J* = 6.7, 1.3 Hz, 2H), 8.86 (ddd, *J* = 4.7, 1.6, 1.0 Hz, 1H), 8.71 (tt, *J* = 7.8, 1.3 Hz, 1H), 8.26 (dd, *J* = 7.8, 6.7 Hz, 2H), 8.12 (td, *J* = 7.7, 1.7 Hz, 1H), 8.06 (dt, *J* = 7.8, 1.1 Hz, 1H), 7.82 (ddd, *J* = 7.6, 4.8, 1.4 Hz, 1H), 6.48 (s, 2H). HRMS (ESI-TOF) m/z: $[M-I]^+$ Calcd for $C_{12}H_{11}N_2O$ 199.0871; Found 199.0873. Anal. Calcd for $C_{12}H_{11}IN_2O \cdot 0.2\ H_2O$: C, 43.71; H, 3.48; N, 8.50. Found: C, 43.72; H, 3.45; N, 8.35.

4-methyl-2,2'-bipyridine (mmb).[10] (2-pyridacyl)pyridinium iodide (10.5 g, 0.032 mol), NH_4OH (33 g) and dry MeOH were bubble-degassed for 15 minutes and then crotonaldehyde (2.7 mL, 0.032 mol) was added with a syringe. The reaction was refluxed overnight under nitrogen. The resulting brown solution was cooled down to room temperature and then poured over ice. The crude product was extracted into hexanes until the organic layer tested negative with Fe(II).[i] The combined organic layers were dried with $MgSO_4$ and the solvent was then evaporated to yield a yellow oil. The product was purified with an alumina column (eluting with a hexanes/acetone 9:1 mixture); slow evaporation of the column fractions yielded colorless crystals suitable for X-ray diffraction. Yield: 1.74 g (32%). ^{1}H NMR ($CDCl_3$, 500 MHz) δ (ppm): 8.69 (ddd, *J* = 4.7, 1.7, 1.0 Hz, 1H), 8.55 (d, *J* = 4.9 Hz, 1H), 8.39 (dt, *J* = 8.0, 1.0 Hz, 1H), 8.24 (t, *J* = 0.8 Hz, 1H),

[i]In the presence of Fe(II), 2,2'-bipyridines form compounds of the general form $[Fe(bpy')_3]^{2+}$, usually pink-red colored.[56,57] This reaction was routinely used to test the presence of bipyridines in column fractions or extraction layers.

7.82 (td, *J* = 7.8, 1.8 Hz, 1H), 7.31 (ddd, *J* = 7.5, 4.8, 1.2 Hz, 1H), 7.14 (d, *J* = 4.9 Hz, 1H), 2.45 (s, 3H). HRMS (ESI-TOF) m/z: $[M+H]^+$ Calcd for $C_{11}H_{11}N_2$ 171.0922; Found 171.0921. Anal. Calcd for $C_{11}H_{10}N_2$: C, 77.62; H, 5.92; N, 16.46. Found: C, 77.40; H, 5.86; N, 16.46.

2,2'-bipyridine-4-acetic acid (bpyac).[11] Under a dinitrogen atmosphere, diisopropylamine (0.8 mL, 5.7 mmol) was dissolved in 2 mL of THF. The solution was brought to -78 °C using a dry ice-acetone bath and 1.6 M nBuLi in hexanes (3.6 mL, 5.7 mmol) was added with a syringe, turning the solution dark red. After 15 min, a solution of mmb (0.53 g, 3 mmol) in 20 mL of THF was added dropwise using an addition funnel. The reaction mixture was stirred at -78 °C for 2 h, after which it was poured over a mixture of dry ice and diethyl ether. The resulting pale yellow paste was allowed to sit overnight to sublime the excess CO_2 (s). The product was then extracted into 5 M NaOH. The combined aqueous layers were brought to approximately pH 4 with concentrated HCl, while keeping the solution on an ice bath. The acidified light pink solution was washed with Et_2O and the solvent was then evaporated. The solid obtained in this manner was a mixture of bpyac and NaCl, with minor Fe(II) contamination. The product was isolated using size-exclusion column chromatography in water. Evaporation of the solvent afforded the product as a pale pink solid. Yield: 0.57 g (85%). ^{1}H NMR (DMSO-d_6, 500 MHz) δ (ppm): 8.65 (ddd, *J* = 4.7, 1.7, 0.9 Hz, 1H), 8.48 (dd, *J* = 4.9, 0.5 Hz, 1H), 8.35 (dt, *J* = 8.0, 1.0 Hz, 1H), 8.26 (d, *J* = 0.9 Hz, 1H), 7.91 (td, *J* = 7.7, 1.8 Hz, 1H), 7.41 (ddd, *J* = 7.5, 4.8, 1.2 Hz, 1H), 7.28 (dd, *J* = 5.0, 1.7 Hz, 1H), 3.36 (s, 2H). HRMS (ESI-TOF) m/z: $[M+H]^+$ Calcd for $C_{12}H_{11}N_2O_2$ 215.0820; Found 215.0823.

4,4',5,5'-tetramethyl-2,2'-bipyridine (tmb).[12] 3,4-lutidine (100 mL, 0.89 mol) and Pd/C (10 g) were brought to reflux under a nitrogen atmosphere and maintained at such temperature for 8 days. After that time, 300 mL of $CHCl_3$/toluene 1:1 were added and the mixture was refluxed for 30 min. The catalyst was filtered off while the solution was still hot, and the solvent was evaporated. The crude product was recrystallized from hot toluene and the pure product was obtained as colorless crystals. Yield: 11.7 g (13%). ^{1}H NMR ($CDCl_3$, 500 MHz) δ (ppm): 8.37 (s, 2H), 8.14 (s, 2H), 2.35 (s, 6H), 2.29 (s. 6H).

Dichlorotetrakis(dimethylsulfoxide)ruthenium (II), $Ru(DMSO)_4Cl_2$. This compound was prepared by a modified version of the reported literature method.[13] $RuCl_3$ (3.6 g) and DMSO (45 mL) were bubbled degassed with nitrogen for 15 minutes and refluxed under nitrogen until the solution (originally brown) turned bright orange (30-60 minutes). The reaction mixture was cooled down to room temperature, 200 mL of acetone were added and then the flask was placed in the freezer overnight to facilitate crystallization of the product. The bright yellow solid was collected by vacuum filtration, rinsed with acetone and ether and dried under vacuum. Yield: 3.9 g. Anal. Calcd for $C_8H_{24}Cl_2O_4S_4Ru \cdot 0.25 (CH_3)_2SO$: C, 20.26; H, 5.10. Found: C, 20.19; H, 5.14.

Bis(4,4',5,5'-tetramethyl-2,2'-bipyridine)dichlororuthenium(II), $Ru(tmb)_2Cl_2$.[14,15] Reagent grade dimetylformamide (30 mL) was bubble-degassed with nitrogen for 15 minutes, and then $Ru(DMSO)_4Cl_2$ (1.03 g, 2.1 mmol), tmb (1.00 g, 4.7 mmol) and LiCl (12.7 g, 300 mmol) were added, and the mixture was bubble degassed for 5 more minutes. The reaction was shielded from light with aluminum foil and kept at 120 ^{o}C for 2 h. After this time, the dark purple solution was allowed cooled down for some minutes; 400 mL

of acetone were added, and the flask was left in the freezer overnight (still covered with foil). The product was collected by vacuum filtration and rinsed with water to remove the excess LiCl and any $[Ru(tmb)_3]Cl_2$ impurities. Once the aqueous filtrate was colorless, the purple microcrystalline solid was rinsed with ether and dried under vacuum. Yield: 0.34 g (27%). ^{1}H NMR (DMSO-d_6, 500 MHz) δ (ppm): 9.59 (s, 2H), 8.33 (s, 2H), 8.18 (s, 2H), 7.10 (s, 2H), 2.54 (s, 6H), 2.43 (s, 6H), 2.25 (s, 6H), 1.91 (s, 6H).

Bis(4,4',5,5'-tetramethyl-2,2'-bipyridine)bis(triflate)ruthenium(II), $Ru(tmb)_2(OTf)_2$.[16] Under a dinitrogen atmosphere, $Ru(tmb)_2Cl_2$ (0.65 g, 1.08 mmol) was dissolved in 45 mL of o-dichlorobenzene. Then, HOTf (0.33 mL, 3.73 mmol) was added, and the resulting solution was stirred for 1 hour at room temperature; during this time, a dark brick-red precipitate was formed. The solid was collected by vacuum filtration, washed with diethyl ether, and used without further purification. Yield: 0.67 g (75%).

Bis(2,2'-bipyridine)dichlororuthenium(II), $Ru(bpy)_2Cl_2$.[14,15] This synthesis was analogous to that for $Ru(tmb)_2Cl_2$, using 1.80 g of $Ru(DMSO)_4Cl_2$ (3.7 mmol), bpy (1.22 g, 7.8 mmol) and 10.9 g of LiCl (257 mmol) and heating to 140 °C for 4 h. Yield: 1.03 g (58%). ^{1}H NMR (DMSO-d_6, 500 MHz) δ (ppm): 9.96 (ddd, J = 5.7, 1.6, 0.7 Hz, 2H), 8.63 (dd, J = 8.1, 1.3 Hz, 2H), 8.48 (dd, J = 8.2, 1.3 Hz, 2H), 8.06 (ddd, J = 8.1, 7.5, 1.4 Hz, 2H), 7.76 (ddd, J = 7.2, 5.6, 1.3 Hz, 2H), 7.67 (ddd, J = 8.1, 7.4, 1.5 Hz, 2H), 7.51 (ddd, J = 5.8, 1.5, 0.7 Hz, 2H), 7.09 (ddd, J = 7.3, 5.8, 1.4 Hz, 2H).

Bis(4,4',5,5'-tetramethyl-2,2'-bipyridine) mono(2,2'-bipyridine-4-acetic acid) ruthenium(II) hexafluorophosphate, $[Ru(tmb)_2(bpyac)](PF_6)_2$ (1). Under a nitrogen atmosphere, $Ru(tmb)_2Cl_2$ (0.122 g, 0.21 mmol) and $TlPF_6$ (0.150 g, 0.43 mmol) were

dissolved in 10 mL of methanol and stirred in the dark at 0°C for 5 h. The reaction was allowed to reach room temperature over the course of 1 h and then it was cannula filtered into a round bottom flask containing bpyac (0.054 g, 0.25 mmol). The resulting mixture was shielded from light and stirred overnight under nitrogen. The reaction mixture was filtered through celite; the filtrate was a clear orange solution. The solvent was evaporated and the product was purified with a neutral alumina plug, using acetonitrile to remove $[Ru(tmb)_3](PF_6)_2$ had eluted, and then switching to acetonitrile/KNO_3 (aq, sat) 5:1. All the fractions containing the desired product were combined, the solvent was evaporated and the solid was dissolved in a minimum amount of water and re-precipitated with NH_4PF_6. Recrystallization by ethyl ether diffusion into acetonitrile yielded red crystals, suitable for XRD. Yield: 0.020 g (10%). ^{1}H NMR (CD_3CN, 500 MHz) δ (ppm): 8.41 (m, 2H), 8.22 (s, 2H), 8.21 (d, *J* = 6.3 Hz, 2H), 8.00 (td, *J* = 7.9, 1.5 Hz, 2H), 7.70 (ddd, *J* = 5.6, 1.3, 0.6 Hz, 1H), 7.61 (d, *J* = 5.8 Hz, 1H), 7.35 (ddd, *J* = 7.1, 5.6, 1.3 Hz, 1H), 7.30 (m, 4H), 7.21 (s, 1H), 3.85 (s, 2H), 2.43 (s, 9H), 2.42 (s, 3H), 2.17 (bs, 1H), 2.08 (s, 9H), 2.06 (s, 3H). HRMS (ESI-TOF) m/z: $[M–CO_2–2PF_6]^{2+}$ Calcd for $C_{39}H_{42}N_6Ru$ 348.1252; Found 348.1274; $[M–2PF_6]^{2+}$ Calcd for $C_{40}H_{42}N_6O_2Ru$ 370.1212; Found 370.1227; $[M-CO_2–PF_6]^+$ Calcd for $C_{39}H_{42}N_6RuPF_6$ 841.2151; Found 841.2191; $[M–PF_6]^+$ Calcd for $C_{40}H_{42}N_6O_2RuPF_6$ 885.2065; Found 885.2096. Anal. Calcd for $C_{40}H_{42}N_6O_2RuP_2F_{12}\cdot H_2O$: C, 45.85; H, 4.23; N, 8.02. Found: C, 45.75; H, 4.19; N, 8.00.

Tris (4,4',5,5'-tetramethyl-2,2'-bipyridine) ruthenium(II) hexafluorophosphate, $[Ru(tmb)_3](PF_6)_2$. $Ru(DMSO)_4Cl_2$ (0.32 g, 0.64 mmol) and tmb (0.47 g, 2.22 mmol) were suspended in degassed EtOH (45 mL). The mixture was bubble-degassed for 10 min and

heated to reflux under nitrogen for 24 h to give a dark orange solution. The solvent was removed under reduced pressure, the bright orange residue was dissolved in a small volume of water and filtered through a fine frit. $NaPF_6$ was added to precipitate the product, which was collected through vacuum filtration, and rinsed with water and ether. X-ray quality crystals were obtained via Et_2O diffusion into MeCN. Yield: 0.41 g (62%). ^1H NMR (CD_3CN, 500 MHz) δ (ppm): 8.22 (s, 6H), 8.32 (s, 6H), 2.45 (s, 18H), 2.10 (s, 18H). HRMS (ESI-TOF) m/z: $[M–2PF_6]^{2+}$ Calcd for $C_{42}H_{48}N_6Ru$ 369.1497; Found 369.1471; $[M–PF_6]^+$ Calcd for $C_{42}H_{48}N_6RuPF_6$ 883.2637; Found 883.2601. Anal. Calcd for $C_{42}H_{48}N_6RuP_2F_{12}\cdot 1.25\,H_2O$: C, 48.03; H, 4.84; N, 8.00. Found: C, 48.01; H, 4.67; N, 8.01.

(μ-Oxo)(μ-2,2'-bipyridine-4-acetato)bis(tris(2-aminoehtyl)amine)diiron(III) nitrate di(tetraphenylphosphate), $[(tren)_2Fe_2O(\mu\text{-bpyac})](NO_3)(BPh_4)_2$ (2).[7] In a nitrogen-filled glovebox, $Fe(NO_3)_3\cdot 9\,H_2O$ (0.414 g, 1.02 mmol) was dissolved in 30 mL of methanol and added dropwise to a rapidly stirring solution of tren (0.16 mL, 1.07 mmol) in 30 mL of methanol. To the resulting golden-brown solution, a mixture of bpyac (0.113 g, 0.53 mmol) and triethylamine (0.08 mL, 0.57 mmol) in 10 mL of methanol was added. $NaBPh_4$ (1.41 g, 4.1 mmol) in 10 mL of methanol was added to the reaction mixture to yield an orange precipitate and a green brown solution. The solid was filtered off and the filtrate was allowed to sit overnight. The product was obtained as copper-colored XRD-quality crystals, which were collected by vacuum filtration and washed with methanol and ether. Yield: 0.20 g (29%). HRMS (ESI-TOF) m/z: $[M\text{-}BPh_4]^+$ Calcd for $C_{48}H_{65}N_{11}BO_6Fe_2$ 1014.3922; Found 1014.3658. Anal. Calcd for $C_{72}H_{85}N_{11}B_2O_6Fe_2\cdot 2\,H_2O$: C, 63.13; H, 6.55; N, 11.25. Found: C, 63.12; H, 6.52; N, 11.55.

Caution: *Perchlorate salts may be explosive and must be handled very carefully.*

(μ-oxo)(μ-4-acetato)bis[tris(2-aminoehtyl)amine]diiron(III) perchlorate, [(tren)$_2$Fe$_2$O(μ-O$_2$CCH$_3$)](ClO$_4$)$_3$. To a solution of $Fe(ClO_4)_3$ (1.10 g, 2.00 mmol) in 20 mL of methanol, a solution of $NaO_2CCH_3 \cdot 3\ H_2O$ (0.14 g, 1.06 mmol) in 20 mL of methanol was added dropwise, giving a brown red solution. Then, 0.35 mL of tren (2.33 mmol) in 20 mL of methanol were added, and the solution turned green brown. After stirring for a minute, a green precipitate was obtained, which was collected by vacuum filtration. The solid was dissolved in a small amount of acetonitrile, excess ethanol was added, and the mixture was allowed to sit overnight. A green crystalline solid was obtained, which was filtered and washed with ethanol.

Attempted synthesis of [(tren)$_2$Fe$_2$O(μ-bpyac)Ru(tmb)$_2$]$^{5+}$.[7] In a dinitrogen-filled glovebox, $Fe(NO_3)_3 \cdot 9\ H_2O$ (0.027 g, 0.07 mmol) was dissolved in 1.75 mL of methanol and added dropwise to a solution of tren (8.7 μL, 0.06 mmol) in 1.75 mL of methanol. To this solution, $[Ru(tmb)_2(bpyac)](NO_3)_2$ (0.025 g, 0.03 mmol) and NEt_3 (4 μL, 0.03 mmol) in 0.5 mL of methanol were added. The solution was allowed to stir for several minutes, and then $NaBPh_4$ (0.079 g, 0.23 mmol) in 0.5 mL of methanol was added. An orange solid precipitated, and it was collected by vacuum filtration. ESI-MS results revealed the orange precipitate to be $[Ru(tmb)_2(bpyac)](BPh_4)_2$; no evidence of the desired product was observed in the ESI-MS spectra of the solid or the filtrate.

Attempted synthesis of [(tren)$_2$Fe$_2$O(μ-bpyac)Ru(tmb)$_2$]$^{5+}$.[7] In a dinitrogen-filled glovebox, $Ru(tmb)_2(OTf)_2$ (0.032 g, 0.04 mmol) was dissolved in 20 mL of acetonitrile and added dropwise to a solution of **(2)** (0.046 g, 0.04 mmol) in 20 mL of acetonitrile. The

reaction mixture was allowed to stir 48 h, and then the solvent was evaporated, yielding a red-orange solid. ESI-MS of this solid showed the formation of $[Ru(tmb)_3]^{2+}$ and $[Fe(tmb)_3]^{2+}$, along with other decomposition products. Ether diffusion into an acetonitrile solution of the solid yielded X-ray quality crystals of $[Fe(tmb)_3](PF_6)_2$.

Attempted synthesis of $[(tren)_2Fe_2O(\mu\text{-bpyac})Ru(bpy)_2]^{5+}$.[17] In a dinitrogen-filled glovebox, $Ru(bpy)_2Cl_2$ (0.034 g, 0.07 mmol) and $AgPF_6$ (0.053 g, 0.21 mmol) were dissolved in 50 mL of NMP and allowed to stir in the dark. The progress of the reaction was followed by UV-vis spectroscopy (the absorption maximum shifted from 560 nm to 500 nm). After 48 hours stirring, the spectrum stopped changing and the reaction mixture was filtered through celite to remove AgCl. The filtrate was added dropwise to a solution of **(2)** (0.10 g, 0.07 mmol) in NMP. The progress of the reaction was monitored by UV-vis spectroscopy; once the absorption spectrum stopped changing, the solvent was evaporated. ESI-MS results only showed the formation of $[Ru(bpy)_2(bpyac)]^{2+}$ and the decomposition of the diiron(III) core. No evidence of the desired product was obtained.

3.2.2. Physical Characterization

X-ray structure determination. Single-crystal X-ray diffraction data were acquired, and the structures were solved, by Dr. Richard Staples and/or Dr. Shannon Biros at the X-ray Facility of Michigan State University.

UV-visible absorption spectroscopy. All spectra were collected using spectrophotometric grade solvents, in 1 cm quartz cuvettes. The spectra were acquired using a Cary 50 spectrophotometer.

Electrochemistry and Spectroelectrochemistry. Both electrochemical and UV-visible spectroelectrochemical measurements were carried out in an argon-filled glovebox. All samples were prepared using spectrophotometric grade acetonitrile, which was freeze-pump-thaw degassed before using. 0.1 M tetrabutylammonium hexafluorophosphate ($TBAPF_6$) was used as the supporting electrolyte; it was recrystallized twice from hot ethanol before using.

For electrochemical experiments, a CHI 620B electrochemical analyzer was used, along with a three-electrode setup, consisting of a Pt or glassy carbon working electrode, a graphite counter electrode, and a Ag/AgCl reference electrode. Ferrocene was added as an internal standard; all potentials are reported versus the ferrocene/ferrocenium couple. Data were acquired by cyclic voltammetry (CV) and differential pulse voltammetry (DPV); the scan rate for the CV measurements was 50 mV/s and the scan rate and pulse width for the DPV measurements were 20 mV/s and 50 mV, respectively. Values for $E_{1/2}$ obtained by both techniques were comparable; the reported potentials were obtained from the DPV peak values.[18]

UV-visible spectroelectrochemical measurements were performed in a 1 mm pathlength spectroelectrochemical cell (CH Instruments). A three-electrode setup was employed, which consisted of a Pt mesh working electrode, a Ag wire counter electrode and a Ag/AgCl reference electrode. Samples were dissolved in the electrolyte solution to give an absorbance of 0.4–0.6 at the maximum of the MLCT band. Difference spectra were collected on a SI 440 CCD spectrometer every 30 seconds as the samples were oxidized or reduced. Oxidative spectra were collected at a potential ca. 100 mV more positive than

$E_{1/2}^{ox}$; reductive spectra were collected at a potential ca. 100 mV more negative than $E_{1/2}^{red1}$ or halfway between $E_{1/2}^{red1}$ and $E_{1/2}^{red2}$, whichever was less reducing. The potential was controlled using the same electrochemical analyzer that was used for CV and DPV experiments.

Steady-State Emission and Time-Resolved Emission and Absorption. All samples were prepared in an argon-filled glovebox, using spectrophotometric acetonitrile that was freeze-pump-thaw degassed prior to use. Air-free cells for these experiments were made in-house by attaching Kontes valves to 1 cm quartz cuvettes (FireflySci).

For both steady-state and time-resolved emission spectroscopy, the absorbance of the sample at the maximum of the MCLT band was kept between 0.1 and 0.2.

Steady-state emission spectra were collected using a Horiba Fluorolog-3 fluorimeter and corrected for instrumental response using a NIST standard of spectral irradiance (Optronic Laboratories, Inc., OL220 M tungsten quartz lamp). Relative quantum yields of emission (Φ_r) were calculated using $[Ru(bpy)_3](PF_6)_2$ in degassed acetonitrile as a standard ($\Phi = 0.095$).[19] Emission quantum yields were calculated using eq 3.1, where *x* refers to the molecule of interest and *std* to the standard; I_x and I_{std} are the integrated areas of the corrected emission spectra, A_x and A_{std} are the absorbances at the excitation wavelength, and η_x and η_{std} are the indices of refraction of the solutions (usually assumed to be equal to those of the neat solvents).

$$\Phi_x = \Phi_{std}\left(\frac{I_x/A_x}{I_{std}/A_{std}}\right)\left(\frac{\eta_x}{\eta_{std}}\right)^2 \qquad \textbf{(3.1)}$$

Alternatively, the absolute quantum yield of emission for **(1)** was measured using a Hamamatsu Photonic Quantaurus absolute PL QY spectrometer (C11347 series).

The zero-point energy gap (E_0) was estimated by a single mode fit of the steady–state emission spectrum as described by Claude and Meyer.[20] The spectrum was corrected according to Parker and Rees when converting from wavelength to energy units.[21]

Nanosecond time-resolved emission experiments were performed using an Nd:YAG laser spectrometer that has been described previously,[7,22] upgraded using an Opotek Vibrant 355 LD tunable pulsed laser system which generates nominally 5 ns laser pulses. Excitation energies were in the range of 1-3 mJ per pulse. All data were checked for linearity with respect to pump power. The data were fit to a single exponential decay to extract the observed rate constant (k_{obs}).

SQUID. Magnetic susceptibility data were collected using a Quantum Design MPMS SQUID magnetometer interfaced to a PC. Compounds were finely ground for sample preparation, and then packed in a plastic freezer bag and rolled into a drinking straw. Data were collected in applied fields of 1.00 and 2.50 T. Following each temperature change, the system was allowed to equilibrate at the new temperature for 5 minutes. Data were corrected for diamagnetism using Pascal's constants[23] and for the measured susceptibility of the sample holder, and are reported as effective magnetic moments (μ_{eff}). Data were fit to the van Vleck equation using Magfit.[24] When fitting, a paramagnetic impurity was included (5 mole% of an S = ½ compound) as well as temperature-independent paramagnetism (400 x10^{-6} cgsu).[25]

3.2.3. Bimolecular Quenching Studies

Samples for Stern-Volmer studies were prepared using varying volumes of a stock solution of **(2)** (~3.5 mM) and taking them to a final volume of 5.00 mL using a stock solution of the corresponding $[RuL_3]^{2+}$ (~6 μM, to ensure an absorbance of 0.1–0.2 of the Ru(II) donor at the excitation wavelength).[ii] All samples contained $TBAPF_6$ (0.075 M), added as a supporting electrolyte.[26,27]

Time-resolved emission experiments were carried out as described above. The laser power was periodically monitored to ensure constant pump power over the course of the experiment. The integrity of the samples was checked taking electronic absorption spectra before and after the time-resolved emission experiments.

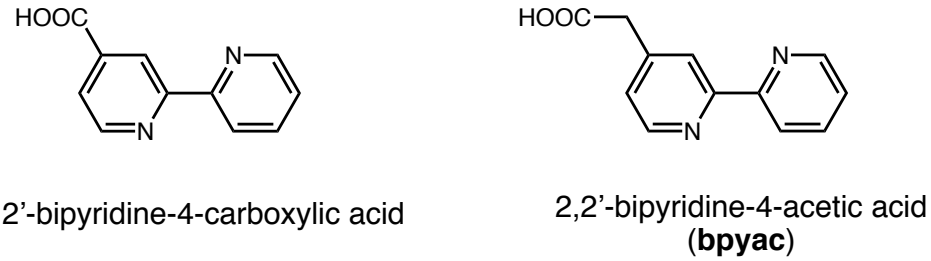
3.3. Results and Discussion

3.3.1. Syntheses

The research described herein builds upon previous work from our group using diiron(III) cores as energy and electron transfer acceptors, and Ru(II) polypyridyls as donors.[2,7,28] To avoid diffusion-limited kinetics,[2] the goal was to covalently link the donor and the acceptor moieties, using a modified bipyridine as the connecting ligand. While Tp-capped diiron(III) cores require two carboxylate bridges, the use of tren, a tetradentate ligand, left only one open coordination position on each Fe(III) center, and thus only one carboxylate bridge was necessary for the acceptor core. With this design in mind, the first

[ii]The concentration of the Ru(II) compound varied from one sample to the other. However, the lifetime (τ_0) of these compounds is not affected by their concentration under these experimental conditions.

synthetic challenge was to select the necessary bifunctional ligand. Such ligand was chosen to be a derivative of 2,2'-bipyridine that incorporated a carboxylate group *para*- with respect to the nitrogen atom of one of the pyridine rings; having the substituent in the 4- position should favor the direct coupling to the aromatic system.[15] To increase electronic communication between the donor and the acceptor, it would have been preferable to use 2,2'-bipyridine-4-carboxylic acid (shown in Figure 3.1). However, the extra methylene group in 2,2'-bipyridine-4-acetic acid ("bpyac", pictured on the right side of Figure 3.1) increases the distance between donor and acceptor, which should slow down Dexter energy transfer (or prevent it altogether);[29] in an attempt to simplify the photophysics of the system, bpyac was chosen as the bridging ligand.



2,2'-bipyridine-4-carboxylic acid

2,2'-bipyridine-4-acetic acid
(**bpyac**)

Figure 3.1. Two possible bifunctional bridging ligands for the tren-capped intramolecular assembly.

The synthesis of bpyac is shown in Figure 3.2; it was based on a procedure reported by Della Ciana et al. for the preparation of 4'-methyl-2,2'-bipyridine-4-acetic acid.[11] The choice of bpyac as opposed to the 4'-methylated version was driven by the need to localize the ^{3}MLCT excited state as close to the diiron(III) core in the intramolecular assembly as possible; removing that extra methyl group was expected to make bpyac even easier to reduce. The main difference between the synthesis of bpyac and the original procedure is the purification of the product: after the acid-base work up, bpyac

is obtained as a very pale pink solid (due to minor Fe(II) contamination) mixed with large amounts of NaCl, product of the neutralization. Della Ciana et al. use Cu(II) to extract the ligand and then sulfide to remove the Cu(II) and isolate the final product.[11] This procedure is cumbersome and potentially dangerous due to the use of H_2S which is highly toxic.[30] As an alternative, size-exclusion chromatography was found to be a convenient way to remove NaCl and most of the Fe(II) contamination from the product.

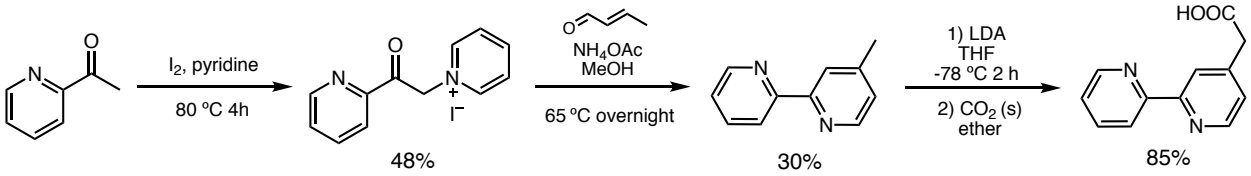


Figure 3.2. Synthetic route used to prepare 2,2'-bipyridine-4-acetic acid (bpyac). The yields for each individual step are shown below the corresponding molecule.

The Ru(II) polypyridyl compounds described in this chapter were prepared using previously reported techniques. As a starting material, $Ru(DMSO)_4Cl_2$ represents a cleaner alternative to $RuCl_3 \cdot xH_2O$;[15] this compound is also very easy to prepare and is stable under air.[13] Homoleptic tris-bipyridine Ru(II) compounds can be obtained by refluxing $Ru(DMSO)_4Cl_2$ in the presence of a slight excess of the ligand; this reaction is carried under inert atmosphere to prevent the oxidation of the metal to Ru(III).

The synthesis of heteroleptic Ru(II) polypyridyls is fairly straightforward, albeit more labor-intensive. These compounds can be obtained by simply refluxing a mixture of the RuL_2Cl_2 precursor (where L is a bipyridine ligand) and the second bipyridine to be added, yielding $[RuL_2L']Cl_2$.[15,31] However, at high temperatures, the ligands might "scramble" around the Ru(II) center, generating other compounds as byproducts (most commonly, $[RuL_3]^{2+}$). Ru(II) polypyridyls are amenable to column chromatography, but

depending on the identity of the ligands separation might not be feasible, which may make this a less desirable route in many cases.

A gentler, cleaner alternative is to react the RuL_2Cl_2 precursor with Ag(I) or Tl(I) to strip the chloride ligands before adding the second bipyridine, as schematized in Figure 3.3. The Ag(I) or Tl(I) sources are usually salts of weakly-coordinating anions,[32] such as AgOTf,[33] $AgClO_4$,[34] $AgNO_3$,[35] $AgPF_6$ or $TlPF_6$.[17] This strategy is not limited to Ru(II), as many Re(I) polypyridyls have been prepared in this way.[33,34] This is the preferred method when using less robust ligands that might decompose upon heating, because this route may be carried out at or below room temperature. Additionally, working at lower temperatures prevents the formation of other byproducts. This is particularly important when tmb is involved: this ligand binds very strongly to Ru(II), making $[Ru(tmb)_3]^{2+}$ which is very stable and is the major byproduct in the synthesis of $[Ru(tmb)_2(bpy')]^{2+}$ compounds.

The choice between silver and thallium is mainly based on redox properties: when $Ru(dmb)_2Cl_2$ or $Ru(tmb)_2Cl_2$ are employed, the metal center is electron-rich enough that Ag(I) can oxidize it; this difficulty can be circumvented by using Tl(I) instead. Regardless of the metal used, the product of this reaction step is most likely $[Ru(bpy')_2(solvent)_2]^{2+}$, which is very susceptible to ligand substitution as well as oxidation. For this reason, water and oxygen have to be carefully excluded from these reactions: in our case, these were carried out in a nitrogen-filled glovebox. Additionally, the bis-solvento species may undergo photo-induced ligand dissociation or substitution;[36] to prevent this, all the reaction flasks were wrapped with aluminum foil, shielding them from ambient light.

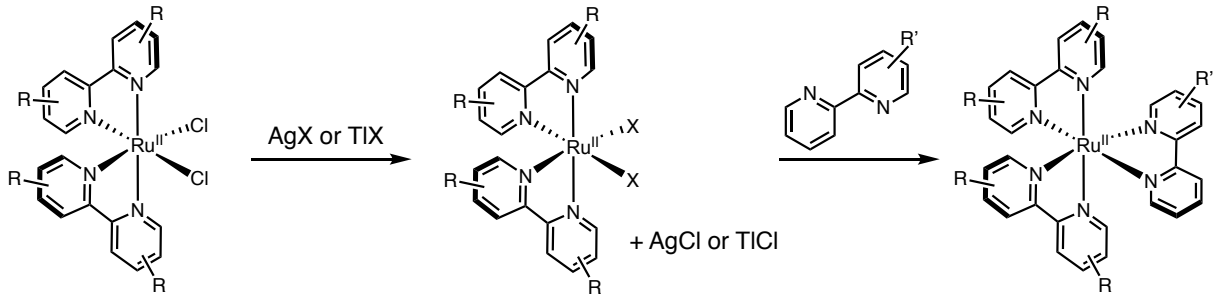
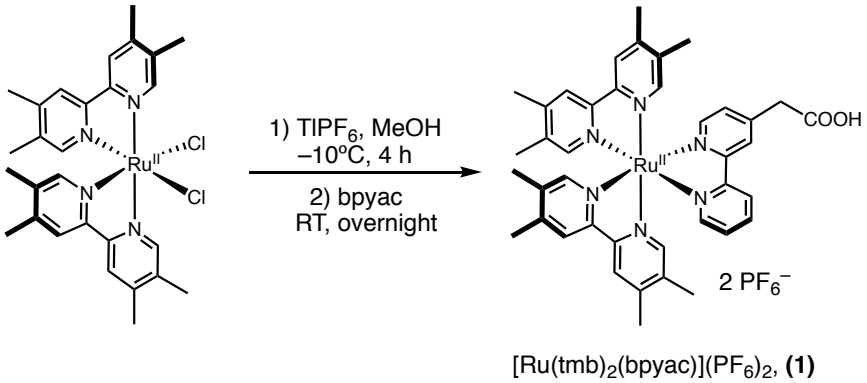


Figure 3.3. General strategy to make heteroleptic Ru(II) compounds in two steps. "X" may also be a solvent molecule.

A slight modification to the previous route is to synthesize and isolate a compound of the form $Ru(bpy')_2X_2$, where *X* is a weakly-coordinating anion. This strategy has been employed to make coordination compounds using a wide variety of transition metals, including Ru(II), Os(III), Ir(III), Re(I), Cr(III), Rh(III), Co(III) and Pt(IV).[37–40] A common choice for this purpose is triflate ion, which may be introduced using triflic acid,[16,37,38,40] or AgOTf.[40] An advantage of this approach over the one described above is the ability to purify triflate intermediate, ensuring that there are no other species present in the reaction mixture. For the compounds described in this dissertation, the one-pot Ag/Tl route gave satisfactory results and was employed routinely. However, as is discussed later in this chapter, $Ru(tmb)_2(OTf)_2$ was tested as a starting material to make the intramolecular assembly, mostly because of the possibility of the bis-solvento species to give $[Ru(tmb)_3]^{2+}$ if left in solution for a long time.

From the above discussion, it is no surprise that the first step in the synthesis of **(1)** (Figure 3.4) was carried out at 0°C, and the second, at room temperature. The low yield of this reaction is mainly attributed to the formation of the tris-tmb compound, although $[Ru(tmb)_2(mmb)]^{2+}$ was likely obtained as well, product of the loss of CO_2 from bpyac.[11] In either case, these impurities were separated from the desired product using a neutral

alumina plug, as both of them eluted with MeCN, while the product did not. When analyzing **(1)** by ESI-MS, $[Ru(tmb)_2(mmb)]^{2+}$ was consistently observed, and it was the only species (apart from **(1)**) detected. This was not seen as a problem, because of the tendency of some carboxylic acids[41] and other compounds[42] to lose CO_2 in the mass spectrometer. Added to this, the combination of a clean ^1H NMR spectrum, a satisfactory elemental analysis, and, more importantly, a crystal structure of the desired compound, were taken as evidence that **(1)** had been prepared and properly isolated. It is important to highlight that all the characterization experiments reported in this chapter were carried out using material from the same batch. The instability of **(1)** towards decarboxylation became apparent later on and is discussed in the next chapter.

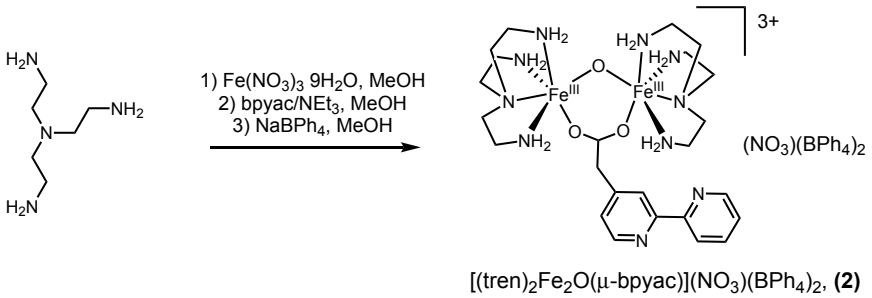


$[Ru(tmb)_2(bpyac)](PF_6)_2$, **(1)**

Figure 3.4. Synthesis of compound **(1)**, $[Ru(tmb)_2(bpyac)](PF_6)_2$.

The synthesis of the tren-capped diiron core was adapted from a procedure previously reported by our group (Figure 3.5).[7] The main byproduct generated in this reaction was an orange solid, possibly some Fe(III) hydroxide/oxide, due to the basic environment of the reaction. After the product crashed out overnight the supernatant was pink, coloration that seems to indicate the presence of a bpyac-Fe(II) complex. Both these byproducts were easily removed before isolating the final product. This compound was

obtained as a mixed salt of nitrate and tetraphenyl borate ions, as was the case for the previously reported naphthylacetic acid analog.[7]



[(tren)$_2$Fe$_2$O(μ-bpyac)](NO$_3$)(BPh$_4$)$_2$, **(2)**

Figure 3.5. Synthesis of compound **(2)**, [(tren)$_2$Fe$_2$O(μ-bpyac)](NO$_3$)(BPh$_4$)$_2$.

After successfully synthesizing and characterizing the donor and the acceptor individually, the synthesis of the intramolecular assembly was attempted. Two strategies were investigated for this purpose, as shown in Figure 3.6: in the first one, [Ru(tmb)$_2$(bpyac)]$^{2+}$ was used instead of bpyac in the synthesis of the diiron(III) core. No evidence of product formation was seen; it is unclear whether the coordinated bpyac was still protonated, preventing its binding to the Fe(III) centers, or if coulombic repulsion played a role instead. Another disadvantage of this reaction was its very small scale, which made any attempts to isolate a potential product extremely cumbersome.

The second approach was to use the already formed diiron(III) core as a "decorated bipyridine" in the method previously discussed. Because of the propensity of [Ru(tmb)$_2$(solvent)$_2$]$^{2+}$ to form [Ru(tmb)$_3$]$^{2+}$ if left in solution for too long, Ru(tmb)$_2$(OTf)$_2$ was used as an alternative starting material to prepare the assembly; this compound was expected to be more reactive towards the coordination of a third bipyridine, which might have reduced the necessary reaction time and generated a smaller amount of side products. Unfortunately, this was not the case, and after a couple of attempts using

$Ru(tmb)_2(OTf)_2$ to make the assembly, it became clear that this synthesis would be more challenging than initially anticipated.

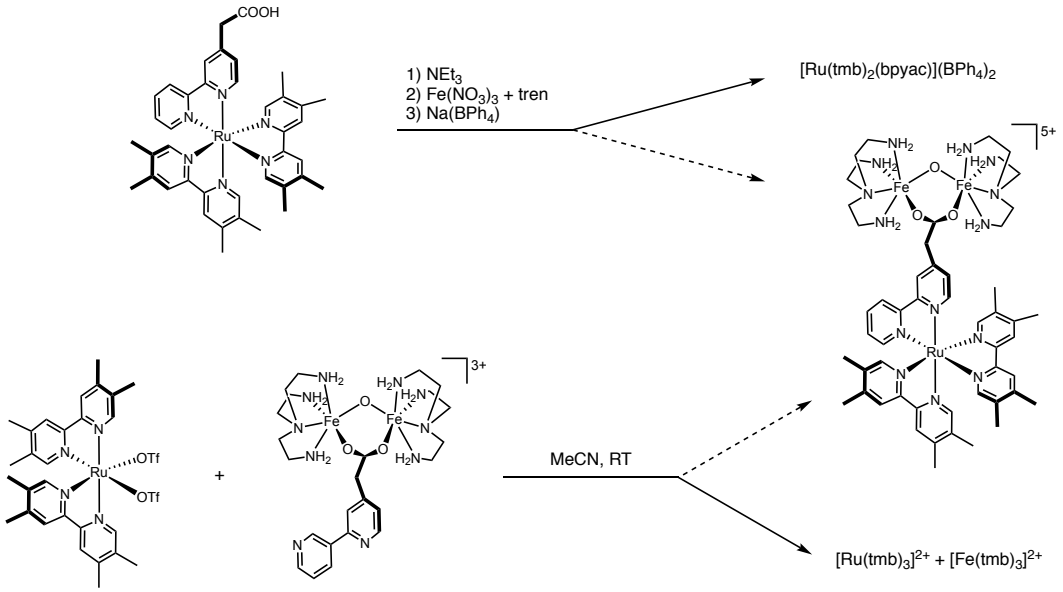


Figure 3.6. Representative examples of the many routes explored to synthesize a tren-capped D-A assembly.

Despite tmb being the desired ancillary ligand for the D-A assembly, its many disadvantages from a synthetic standpoint (i.e., higher cost, lower-yielding synthesis of $Ru(tmb)_2Cl_2$ and other heteroleptic compounds, need to use Tl(I), etc.) made us turn back to bpy when developing a synthetic route; once the reaction conditions to synthesize the intramolecular assembly had been optimized for $Ru(bpy)_2Cl_2$ or $Ru(bpy)_2(OTf)_2$ this would have been replaced with the corresponding tmb compounds. Unfortunately, this strategy did not pan out, as none of the attempts using $[Ru(bpy)_2(solvent)_2]^{2+}$ (using NMP, acetone or acetonitrile) resulted in the formation of the desired product.

A noteworthy disadvantage of this D-A system is that both the donor and acceptor moieties are highly charged, making Coulombic repulsion between the reactants

in solution a major obstacle for their coupling. This might have been overcome with the addition of $TBAPF_6$ as a supporting electrolyte, much like what is done for Stern–Volmer studies.[26] The presence of an inert electrolyte in high concentration could shield the charges and make it more favorable for the reactants to diffuse towards each other. This approach was not attempted, however, because the main problem encountered for these reactions was the instability of the tren-capped diiron(III) core, which lead to its rapid decomposition before the assembly could be formed. Ideally, the synthesis of the target assembly had to be run in a non-coordinating solvent, so that the intermediate species, $[RuL_2(solvent)_2]^{2+}$, would be as reactive as possible, favoring the formation of the desired product. However, **(2)** was not soluble in most common non-coordinating solvents (such as chloroform, dichloromethane, toluene or 2-methyltetrahydrofuran), and in many instances it decomposed shortly after being dissolved or suspended (decomposition was indicated by the change on the solution's color, from amber to pink). Finally, NMP was found to be a suitable choice, with the only potential caveat of its high boiling point; but, despite **(2)** being stable in solution under air for days, and having attempted all the reactions under nitrogen and in the dark, the ESI-MS spectra of the reaction mixtures only showed Ru(II) and Fe(II) polypyridyls as the products. In one instance, $[Fe(tmb)_3](PF_6)_2$ was crystallized from a reaction mixture (see Figure 3.7), showing how the decomposition of the diiron(III) core is even more favorable in the presence of bipyridines, because of how stable Fe(II) polypyridyls can be. In the structure shown below, most atoms were very disordered; however, the connectivity is confirmed. The low quality of the crystals obtained is likely due to the presence of other species in the original solution.

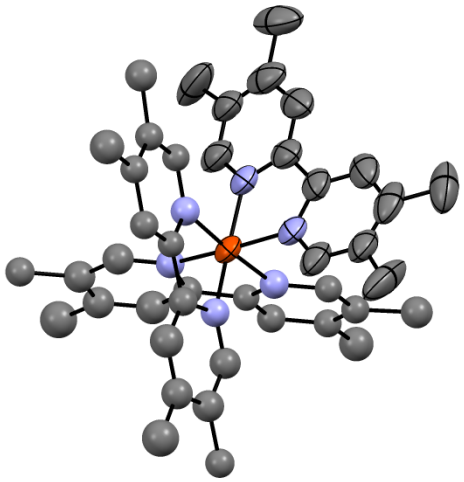


Figure 3.7. ORTEP drawing of $[Fe(tmb)_3]^{2+}$ obtained from a single-crystal X-ray structure determination. When possible, atoms are represented as 50% probability thermal ellipsoids. Only one possible molecule in the disorder is shown. Hydrogen atoms and anions are omitted for clarity. The full lists of bond lengths and angles are compiled in the appendix to this chapter.

3.3.2. Physical Characterization of the Donor and Acceptor

3.3.2.1. Crystal Structures

The crystallographic data for **(1)**, **(2)**, and $[Ru(tmb)_3](PF_6)_2$ are presented in Table 3.1; the crystal structure of the latter has not been reported before, despite the compound being known for decades. The empirical formulas shown in the table include any crystallization solvents found. In the case of **(1)**, the X-ray structure revealed 0.75 molecules of diethyl ether per molecule of the compound; most likely, part of the solvent was lost because the crystals had dried before mounting them.

Table 3.1. Crystallographic data for **(1)**, **(2)** and $[Ru(tmb)_3](PF_6)_2$.

	(1)	**(2)**	**$[Ru(tmb)_3](PF_6)_2$**
empirical formula	$C_{43}H_{49.5}N_6O_{2.75}F_{12}P_2Ru$	$C_{73}H_{89}B_2Fe_2N_{11}O_7$	$C_{42}H_{48}F_{12}N_6P_2Ru$
formula weight	1085.40	1365.87	1027.87
temperature (K)	173.15	173(2)	173(2)
crystal color, habit	red, blocks	orange, plates	red, needles
crystal system	triclinic	monoclininic	monoclinic
space group	P-1	I2/*a*	C2/*c*
cell dimensions:			
a (Å)	12.845(3)	29.662(4)	14.8999(10)
b (Å)	14.644(3)	10.2686(15)	22.7845(16)
c (Å)	14.656(3)	47.184(7)	13.5011(9)
Volume (Å^3)	2505.2(9)	14144(4)	4582.2(5)
Z	2	8	4
D_{calc} (g cm^{-3})	1.439	1.283	1.490
goodness of fit (F^2)	1.137	0.949	1.176
R_1 (I >2(I))	0.1050	0.2183	0.0594

The ORTEP drawings for the cations of **(1)** and **(2)** are shown in Figure 3.8; $[Ru(tmb)_3]^{2+}$ can be found in Figure 3.34. The structures of both Ru(II) compounds are comparable to other complexes of this class; Table 3.2 includes representative bond distances and angles for both these compounds and $[Ru(bpy)_3]^{2+}$.[43] It is clear that the substituents on the pyridine rings do not affect the geometry of the primary coordination sphere, even when comparing a heteroleptic complex with a homoleptic one. It is not surprising, however, that other characteristics, such as the symmetry of the molecule, the crystal system and space group, are affected by the identity of the ligands.

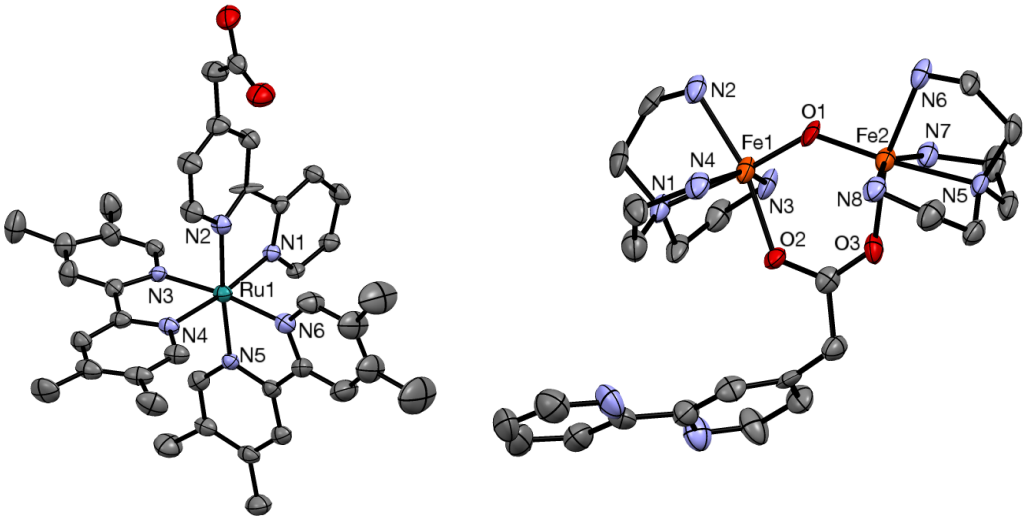


Figure 3.8. ORTEP drawings of $[Ru(tmb)_2(bpyac)]^{2+}$ **(1)** (left) and $[(tren)_2Fe_2O(\mu\text{-}bpyac)]^{3+}$ **(2)** (right) obtained from single-crystal X-ray structure determinations. Atoms are represented as 50% probability thermal ellipsoids. Hydrogen atoms and anions are omitted for clarity. The full lists of bond lengths and angles are compiled in the appendix to this chapter.

Table 3.2. Selected bond lengths and angles for **(1)**, $[Ru(tmb)_3](PF_6)_2$, and $[Ru(bpy)_3](PF_6)_2$ (from ref. 43).

	(1)	**$[Ru(tmb)_3]^{2+a}$**	**$[Ru(bpy)_3]^{2+}$**
		bond lengths (Å)	
Ru–N(1)	2.059(5)	2.047(4)	
Ru–N(2)	2.050(6)	2.058(4)	
Ru–N(3)	2.046(6)	2.061(4)	2.056
Ru–N(4)	2.056(5)		
Ru–N(5)	2.058(5)		
Ru–N(6)	2.074(6)		
		bond angles (°)	
N(1)–Ru–N(2)	78.7(2)	78.82(17)	78.6
N(2)–Ru–N(3)	88.5(2)	87.7(2)	89.1
N(1)–Ru–N(4)	173.2(2)	174.13(17)	173.0
N(1)–Ru–N(3)	96.8(2)	97.02(17)	96.3

[a]Only half the formula unit is present in the asymmetric unit; the other half are symmetry equivalent atoms.

The geometry of **(2)** is compared to $[(tren)_2Fe_2O(O_2CCH_2–C_{10}H_7)]^{3+}$ in Table 3.3: both cores are very similar, with most bond distances and angles within error of each other. These compounds' structures are similar to other molecules of this class, which helps explain why their optical, electrochemical and magnetic properties are also close related, as discussed in later sections.

Table 3.3. Selected bond lengths and angles for **(2)** and $[(tren)_2Fe_2O(O_2CCH_2\text{-}C_{10}H_7)]^{3+}$ (from ref. 7)

	(2)	**$[(tren)_2Fe_2O(O_2CCH_2\text{-}C_{10}H_7)]^{3+}$**
	bond lengths (Å)	
Fe(1)–O(1)	1.777(3)	1.773(3)
Fe(2)–O(1)	1.785(3)	1.790(3)
Fe(1)–O(2)	2.069(4)	2.036(4)
Fe(2)–O(3)	2.026(4)	2.054(3)
Fe(1)–N(1)	2.218(4)	2.238(4)
Fe(1)–N(2)	2.144(4)	2.179(4)
Fe(1)–N(3)	2.157(4)	2.149(4)
Fe(1)–N(4)	2.136(5)	2.149(4)
Fe(2)–N(5)	2.219(4)	2.266(4)
Fe(2)–N(6)	2.146(4)	2.150(4)
Fe(2)–N(7)	2.146(4)	2.147(4)
Fe(2)–N(8)	2.170(4)	2.162(4)
Fe(1)···Fe(2)	3.264	3.28
	bond angles (°)	
Fe(1)–O(1)–Fe(2)	132.7(2)	134.4(2)
O(1)–Fe(1)–O(2)	97.71(15)	96.3(2)
O(1)–Fe(2)–O(3)	99.48(15)	99.1(1)

3.3.2.2. Ground State Absorption Spectroscopy

The electronic absorption spectrum of $[Ru(tmb)_2(bpyac)](PF_6)_2$ in acetonitrile solution is shown in Figure 3.9: it closely resembles that of $[Ru(bpy)_3](PF_6)_2$ discussed in Chapter 2. The intense absorption at 289 nm corresponds to a ligand-centered transition

($\pi_L \rightarrow \pi_L^*$) and is comparable to the spectrum for bpyac seen in Figure 3.10. The analogous peak for $[Ru(tmb)_3](PF_6)_2$ shows up at 291 nm (see Figure 3.38 in the appendix), which is consistent with the identity of the substituents on the 4-position of a single ligand having little effect on the energy of this transition, as others have observerd.[44] The maximum of the MLCT absorption feature (λ_{max} = 445 nm) has a molar absorptivity of 17,000 $M^{-1}\,cm^{-1}$.

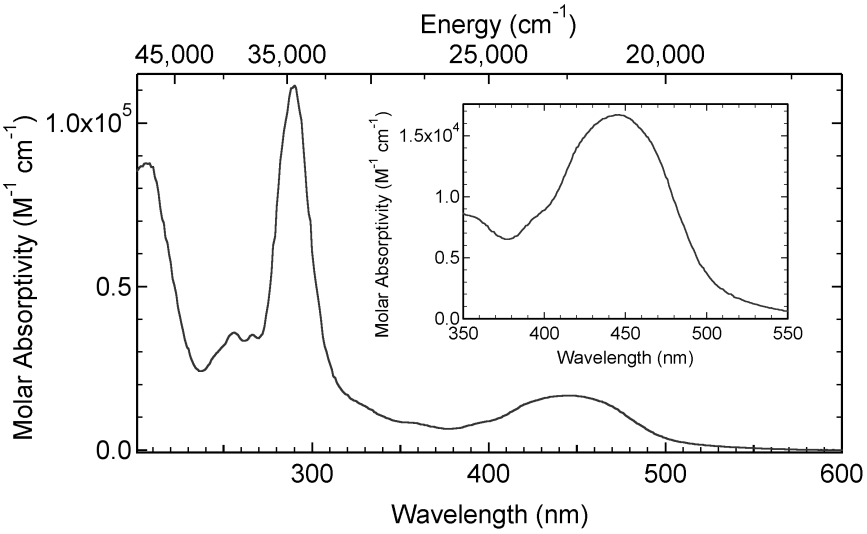


Figure 3.9. Electronic absorption spectrum of **(1)** in acetonitrile solution at room temperature. The inset shows the MLCT band. See text for details.

The most interesting feature of the UV-vis spectrum of **(1)** is the featureless, "rounded" MLCT band (cfr. Figure 2.3 and Figure 3.38). This may be due to the presence of the carboxylic acid group; it has been shown that the protonation/deprotonation of this group has an effect on the electronic absorption spectra of Ru(II) polypyridyls containing COOH groups.[45] Based on the crystal structure of this compound (Figure 3.8), the compound is fully protonated in the solid state; however, its acid-base properties have not been studied. Depending on the amount of water present in the spectroscopic grade MeCN used to obtain the spectrum in Figure 3.9, a fraction of the molecules of **(1)**

could have been deprotonated, which would have contributed to a broader, more featureless MLCT band.

The electronic absorption spectrum of **(2)** in acetonitrile solution at room temperature is shown in Figure 3.10, along with the spectra of $[(tren)_2Fe_2O(\mu\text{-}O_2CCH_3)_2](ClO_4)_3$ and bpyac; it is easy to see that the spectrum of **(2)** can be modeled as a linear combination of the two. The only difference between the spectra of the two diiron(III) cores is the very intense band below 300 nm for **(2)**, which corresponds to bpyac. The electronic absorption spectra of diiron(III) oxo complexes are well characterized and present several common features, regardless of the capping ligands utilized or the identities of other bridging groups;[3,46] the region between 300 and 400 nm is usually referred to as the "oxo dimer region", because the absorptive features in this range correspond to LMCT transitions between the oxo group and the metal centers.[3,46] For **(2)**, there are two features in this region: a band at 320 nm and a shoulder around 360 nm. Next, in the 400-550 nm range, three peaks can be seen (these are better displayed in the inset in Figure 3.10). Similar peaks are seen in other diiron(III) oxo complexes, which suggests that they are inherent to the Fe-O-Fe moiety and are not very sensitive to the capping ligands.[3] Some of these bands are assigned to ligand-field transitions of the Fe(III) centers and others are LMCT transitions.[46] Finally, the very weak band at 700 nm is assigned as a d-d transition, which in a mononuclear Fe(III) complex would be spin-forbidden, but gains intensity by mixing with the intense transitions in the oxo dimer region, as well as due to the relaxation of spin restrictions that arises because of Heisenberg spin exchange.[3,7,46,47]

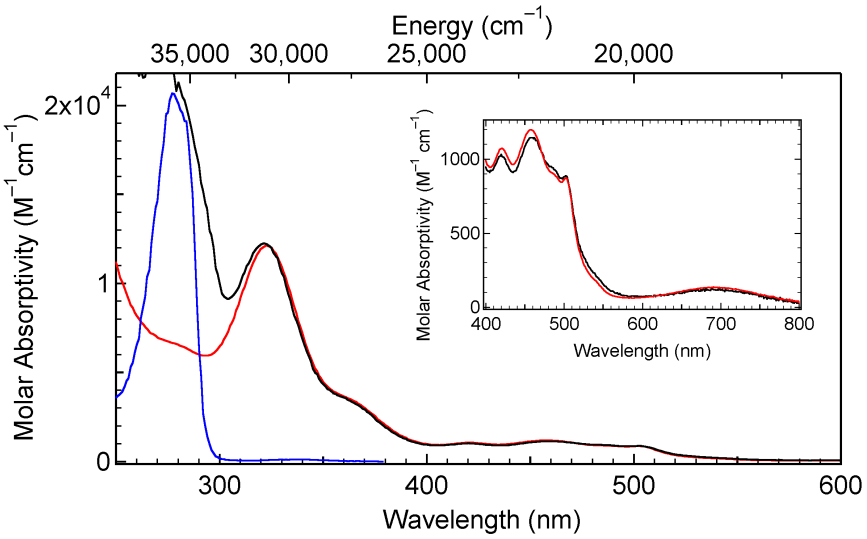


Figure 3.10. Electronic absorption spectrum of **(2)** (black trace) and $[(tren)_2Fe_2O(\mu\text{-}O_2CCH_3)_2](ClO_4)_3$ (red trace) in acetonitrile solution, and bpyac in aqueous solution (blue trace; its absorbance was normalized at 280 nm). All spectra were taken at room temperature. The inset shows the lower energy features. See text for details.

3.3.2.3. Electrochemistry

The cyclic voltammogram of **(1)** is presented in Figure 3.11. The redox processes observed here are analogous to those discussed for $[Ru(bpy)_3](PF_6)_2$ in Chapter 2 (Figure 2.6). As it was mentioned before, the choice of tmb as the ancillary ligand was driven by the need to localize the ^{3}MLCT excited state on the bpyac moiety.[17] The redox potentials for both **(1)** and $[Ru(tmb)_3](PF_6)_2$ are compiled in Table 3.4; the first reduction potential is 80 mV more positive for **(1)**, which suggests that bpyac is, indeed, easier to reduce than tmb and therefore the excited state will be localized in the former.

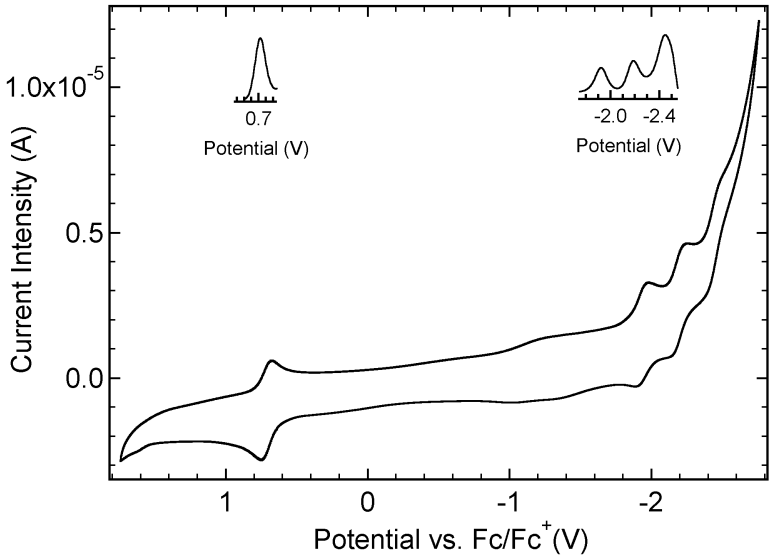


Figure 3.11. Cyclic voltammogram of **(1)** in acetonitrile with 0.1 M $TBAPF_6$ as supporting electrolyte. The insets show the DPV traces.

Table 3.4. Redox potentials for **(1)** and $[Ru(tmb)_3](PF_6)_2$ in acetonitrile. All values are referenced to the ferrocene/ferrocenium couple.

	$E(Ru^{III}/Ru^{II})$ (V)	$E(L/L^-)$ (V)	$E(L/L^-)$ (V)	$E(L/L^-)$ (V)
$[Ru(tmb)_2(bpyac)](PF_6)_2$ **(1)**	0.72	–1.93	–2.19	–2.43
$[Ru(tmb)_3](PF_6)_2$	0.64	–2.01	–2.20	–2.46

The cyclic voltammogram for **(2)** is seen in Figure 3.12. Only one wave is observed, at –0.84 V vs ferrocene, which corresponds to the irreversible reduction of one of the Fe(III) centers in the core, and may be assigned as such by comparison with other compounds of this type: for example, for $[(tren)_2Fe_2O(O_2CCH_2C_{10}H_7)](BPh_4)(NO_3)_2$, this reduction happens at –0.64 V vs ferrocene.[7] Successive scans during a cyclic voltammetry experiment resulted in the appearance of new peaks, which were probably due to decomposition products (after the CV scans, a thin pink layer could be seen coating the working electrode, suggesting that Fe(II) polypyridyls were among the compounds

formed upon reduction of the core). Other diiron(III) compounds present irreversible reductions as well.[1,2,7,28] The irreversibility of this reduction is consistent with the very few mixed-valent Fe^{II}-Fe^{III} oxo-bridged dimers that are known.[3]

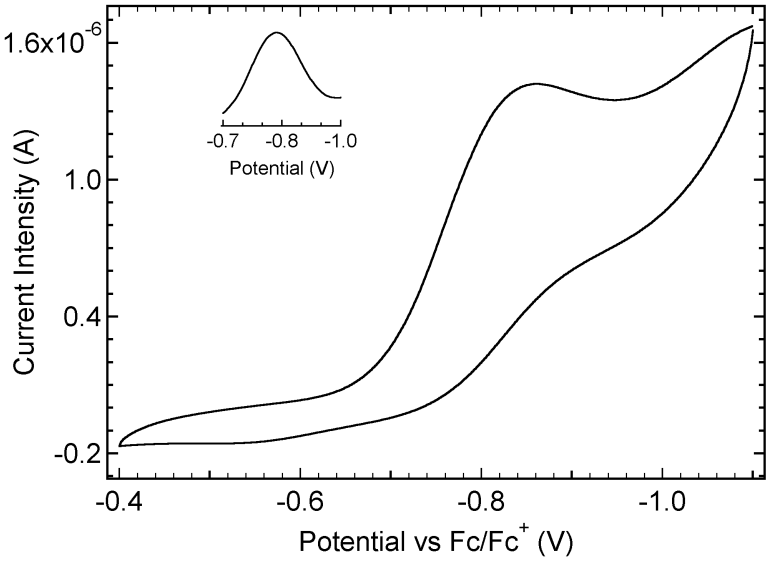


Figure 3.12. Cyclic voltammogram of **(2)** in acetonitrile with 0.1 M $TBAPF_6$ as supporting electrolyte. The inset shows the DPV trace.

3.3.2.4. Steady-State and Time-Resolved Emission of $[Ru(tmb)_2(bpyac)](PF_6)_2$

The steady-state emission spectra of **(1)** and $[Ru(tmb)_3](PF_6)_2$ in acetonitrile solution at room temperature are shown in Figure 3.13. The spectral profiles of both compounds are the same, consistent with emission from the ^{3}MLCT, characteristic of Ru(II) polypyridyls.[29] Their emission maxima, quantum yields and lifetimes are compiled in Table 3.5; the emission of **(1)** is red-shifted in comparison to $[Ru(tmb)_3](PF_6)_2$. Based on their electrochemical data, this difference (0.11 eV) may be attributed to the presence of bpyac instead of a third tmb, since the former is easier to reduce, which lowers the energy of the charge transfer excited state.

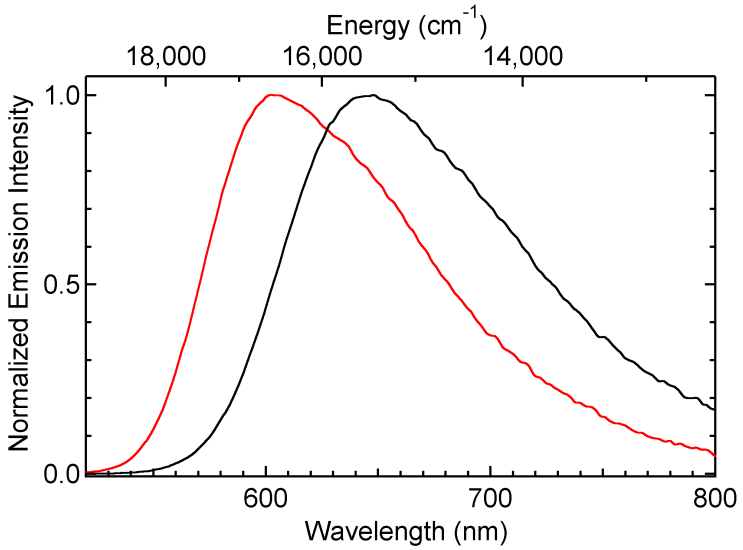


Figure 3.13. Steady-state emission spectra of **(1)** (black trace) and $[Ru(tmb)_3](PF_6)_2$ (red trace) in deoxygenated acetonitrile solution at room temperature.

Table 3.5. Photophysical properties of **(1)** and $[Ru(tmb)_3](PF_6)_2$. All measurements were done at room temperature, in deoxygenated acetonitrile solution.

	λ_{max} (nm)	Φ	E_0 (eV)	τ (ns)	k_r (10^5 s^{-1})	k_{nr} (10^5 s^{-1})
$[Ru(tmb)_2(bpyac)](PF_6)_2$	645	0.094[a]	1.94	850 ± 70	1.12 ± 0.06	10.8 ± 1.0
$[Ru(tmb)_3](PF_6)_2$	605	0.053[b]	2.05	470 ± 20	1.13 ± 0.05	20.1 ± 0.8

[a]Determined as an absolute value. [b]Determined as a relative value, using $[Ru(bpy)_3](PF_6)_2$ (Φ = 0.095) as the standard.

Representative time-resolved emission traces of both compounds are presented in Figure 3.14. The last two columns of Table 3.5 show the values for the radiative and non-radiative rate constants for the Ru(II) compounds under consideration, calculated using eq 2.12. It is noteworthy that both compounds have the same value of k_r, which is comparable to other Ru(II) polypyridyls;[22] their k_{nr} values, on the other hand, further support the claim that the ^{3}MLCT excited state is localized on a different ligand for each of these compounds. For a given series of related compounds of the form

$[Ru(bpy')_n(bpy'')_{3-n}]^{2+}$, the non-radiative rate constant decreases exponentially as E_0 increases, provided that the luminophore remains the same (i.e., the ^{3}MLCT excited state is localized on the same ligand).[48] In the case of **(1)** and $[Ru(tmb)_3](PF_6)_2$, both k_{nr} and E_0 are larger for the latter; since the excited state in the homoleptic compound involves a tmb, it follows that the ^{3}MLCT is localized on the bpyac in the case of **(1)**.

The effect of the carboxylic acid functionality on the emission properties of **(1)** is worth discussing. From the data on Table 3.5, the relative error for the lifetime of $[Ru(tmb)_3](PF_6)_2$ is ~4%, whereas for **(1)** it is ~8% (cfr. Chapter 2, ~4% for $[Ru(bpy)_3](PF)_2$). These lifetimes have been measured multiple times, and the errors are calculated as the standard deviation of those values. In other words, the lifetime measured for **(1)** is more variable than those of other Ru(II) compounds without carboxylic acid functionalities. The most likely explanation is, again, linked to the amount of water on the solvent used to make the emission samples.[iii] The COOH group can interact with water via hydrogen bonding, which increases the number of vibrational modes available to the molecule,[49] providing new pathways for the relaxation from the excited state to the ground state.[50] This, in turn, changes the value of k_{nr}; an increase in this rate constant will lead to a shortening of the lifetime (k_r is constant for a given compound[29] and is relatively insensitive to solvent variations[50]).

[iii]In some instances, water co-crystallized with the compounds used, which could have contributed to this. All compounds were dried in a desiccator overnight before transferring them to the glove box, but this may not have removed all the water in the crystal lattice.

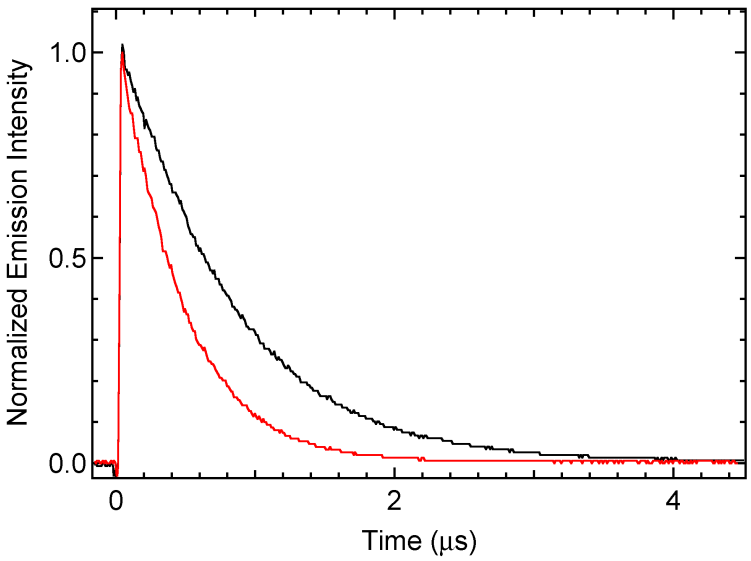


Figure 3.14. Time resolved emission traces for **(1)** (black trace) and $[Ru(tmb)_3](PF_6)_2$ (red trace) in deoxygenated acetonitrile solution at room temperature.

3.3.2.5. Magnetic Properties of $[(tren)_2Fe_2O(\mu\text{-}bpyac)](NO_3)(BPh_4)_2$

Variable temperature magnetic susceptibility data were collected for compound **(2)** in the solid state at applied fields of 1.00 T and 2.50 T. The results at both fields were the same within error; as a representative plot, the results for 2.50 T are presented in Figure 3.15 (other data can be found in the appendix to this chapter, Figure 3.40). The iron(III) centers are antiferromagnetically coupled; the effective magnetic moment for the compound at 350 K is ~3 μ_B, well below the value expected for an uncoupled iron(III) dimer (8.37 μ_B),[iv] and it decreases to ~0.3 μ_B at 2 K. At 0 K, only the lowest-energy spin state, S = 0 will be populated, and consequently, the effective magnetic moment for the system would be expected to be 0; the experimental discrepancy with this value may be

[iv]This was calculated as: $\mu_{eff} = \left[\sum_i (\mu_{eff})_i^2\right]^{\frac{1}{2}}$

explained by the combination of paramagnetic impurities and temperature-independent paramagnetism.[51] Both of these were included when fitting the data (as described in section 3.2.2).[24]

The exchange coupling constant, J, was obtained fitting the data to a spin Hamiltonian:

$$\widehat{H} = -2J\widehat{S}_1\widehat{S}_2 \qquad \textbf{(3.2)}$$

The red line in Figure 3.15 is a fit of the magnetic data to an operator-equivalent form of eq 3.2 with J = –124 cm^{-1}; this value is comparable to other diferric oxo-bridged compounds,[2,3] and is within experimental error of what was previously found for $[(tren)_2Fe_2O(\mu\text{-}O_2CCH_2C_{10}H_7)](NO_3)_2(BPh_4)$.[7] Our group has shown that most of the exchange coupling pathways are mediated by the oxo bridge, while the carboxylate group(s) and the capping ligands have little influence,[6] which explains these similarities.

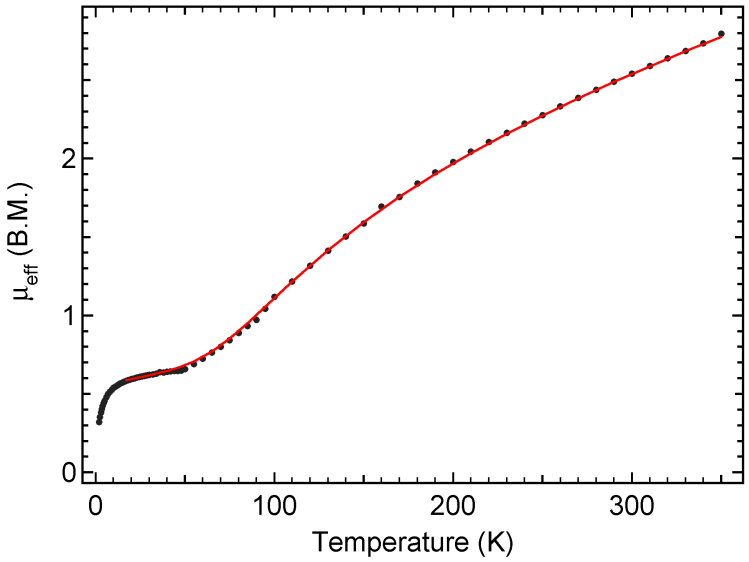


Figure 3.15. Effective magnetic moment as a function of temperature for **(2)** obtained with an applied magnetic field of 2.50 T. The black circles are the experimental data points, and the red trace is a fit to eq 3.2 with J = –124 cm^{-1}.

3.3.3. Bimolecular Quenching Studies

According to what was discussed in Chapter 2, the quenching studies presented here were performed under pseudo-first order conditions, keeping the concentration of **(2)** roughly two orders of magnitude larger than those of the Ru(II) donors. Stern-Volmer plots for **(1)** and $[Ru(tmb)_3](PF_6)_2$ using **(2)** as the quencher can be seen in Figure 3.16; the solid lines represent fits of the data to the Stern-Volmer equation, yielding k_q = 4.8 x 10^8 M^{-1} s^{-1} for $[Ru(tmb)_3](PF_6)_2$, and k_q = 2.9 x 10^8 M^{-1} s^{-1} for **(1)**.[v] These values have not been corrected for diffusion,[27,52] but because both Ru(II) donors have very similar structures, such corrections are not expected to affect the observed trend.[2]

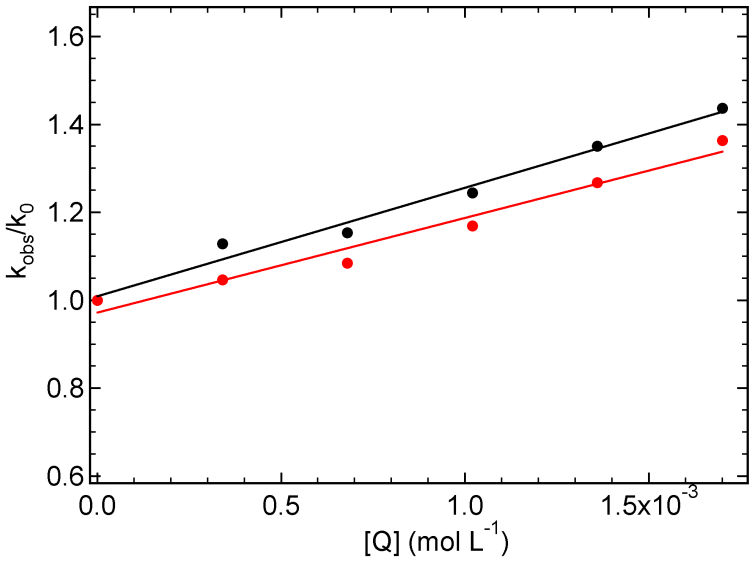


Figure 3.16. Quenching data for **(1)** (black circles) and $[Ru(tmb)_3](PF_6)_2$ (red circles) with varying concentrations of **(2)**. The lines correspond to fits to the Stern–Volmer equation.

For the D-A combinations presented in this chapter, both electron and energy transfer must be considered.[2] Figure 3.17 shows the overlap between the emission spectra of both Ru(II) chromophores and the absorption spectrum of **(2)**; the presence of spectral

[v]Based on multiple experiments, these values have an error of ~7%.

overlap between the emission of the donor and the absorption of the acceptor is necessary for FRET to take place, as described in Chapter 2. The values for the spectral overlap integral are shown in Table 3.6.

As shown by Rehm and Weller's work,[53] the driving force for electron transfer from an excited Ru(II) polypyridyl donor to a ground-state diiron(III) acceptor can be calculated using eq 3.3 and the values from Table 3.4 and 3.5. The values for the systems considered here are presented on Table 3.6.

$$\Delta G_0^{ET} = E^{(Ru^{II}/Ru^{III})} - E^{(Fe^{III}/Fe^{II})} - E_0 \qquad \textbf{(3.3)}$$

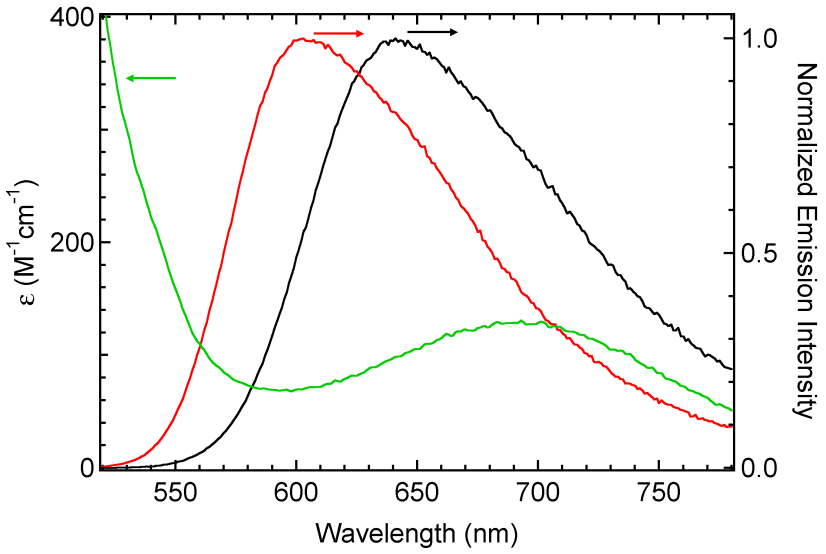


Figure 3.17. Overlay of the normalized emission spectra for **(1)** (black trace) and $[Ru(tmb)_3](PF_6)_2$ (red trace), and the electronic absorption spectrum of **(2)** (green trace). All spectra taken in acetonitrile.

For compounds in the Marcus normal region, a larger (more negative) driving force leads to a faster electron transfer.[54] Thus, it is expected that electron transfer will be faster for $[Ru(tmb)_3](PF_6)_2$. On the other hand, the rate for FRET, as discussed in Chapter 2, depends on k_r for the donor and R_0 (equations 2.18 and 2.19). R_0 depends on a number of constants and I, the spectral overlap integral. As presented on Table 3.6, the values of

R_0 for the Ru(II) donors are within ~2% of each other, and k_r is the same for both (see Table 3.5); consequently, k_{FRET} for both D-A pairs will be very similar. Additionally, recall that the absorptive feature of the diferric core involved in FRET with either of the donors is an inherently weak ligand-field transition,[49] which is consistent with this mechanism not being the main quenching pathway for these systems. Based on this semi-quantitative analysis, electron transfer (and, to a lesser extent, DET) is the main contributor to k_q; only in this way we can account for **(2)** quenching $[Ru(tmb)_3](PF_6)_2$ more efficiently than **(1)**.

Table 3.6. ΔG_0^{ET}, spectral overlap integral, Förster radius, and quenching rate constant for each donor, with **(2)** as the acceptor.

	ΔG_0^{ET} (eV)	I (10^{30} nm^6 mol^{-1})	R_0 (nm)	k_q (10^8 M^{-1} s^{-1})
$[Ru(tmb)_2(bpyac)](PF_6)_2$	–0.38	2.05	2.50	2.9 ± 0.2
$[Ru(tmb)_3](PF_6)_2$	–0.57	1.68	2.42	4.8 ± 0.2

Despite having the spectroscopic and electrochemical data for the donor and the acceptor, which indicated that **(2)** quenching the excited state of **(1)** was thermodynamically favorable, it was important to carry out the quenching studies anyway, to ensure that no unforeseen circumstances were preventing the expected reactions (for example, a process might be thermodynamically spontaneous but its kinetics might be unfavorable).[55] Only after it was confirmed that these compounds behaved as expected, the synthesis of the corresponding intramolecular assembly was attempted. As a general rule, for any D-A system, knowing how the individual components behave (separately and in bimolecular processes) is paramount to understand their behavior as part of a new compound, as a change in the properties of

either component may, in principle, be ascribed to its interaction with other parts of the system and as such, is worth investigating.

As will be discussed in the next two chapters, characterizing the donor and acceptor individually and then performing Stern-Volmer experiments are the first steps in the study of a new intramolecular D-A assembly.

3.4. Concluding Remarks

In this chapter, the synthesis and characterization of two new compounds, $[Ru(tmb)_2(bpyac)](PF_6)_2$ **(1)** and $[(tren)_2Fe_2O(\mu\text{-}bpyac)](NO_3)(BPh_4)_2$ **(2)** were presented. Their properties match what has been reported for other compounds of their kind, Ru(II) polypyridyls and iron(III) oxo-bridged dimers, respectively. As was expected, **(2)** quenches the ^{3}MLCT excited state of **(1)**, and both electron and energy transfer are favorable. The results of the Stern-Volmer quenching studies are in accordance with previous work from our group.[2]

Unfortunately, multiple attempts to prepare an intramolecular assembly using the donor and acceptor studied in this chapter were fruitless. Many factors contributed to this: in the first place, both the donor and acceptor were positively charged, leading to strong coulombic electrostatic repulsion forces which likely prevented them from getting close enough to react. While this repulsion could have been counteracted using a supporting electrolyte,[27] the intrinsic instability of the tren-capped diiron(III) oxo core lead to the decomposition of **(2)** before it could be bound to the donor. Finally, the formation of thermodynamically favorable Fe(II) polypyridyls was observed in most

cases; the formation of such stable products probably accelerated the decomposition of the dimer.

Given the instability of **(2)**, Tp was chosen instead of tren as the capping ligand for the acceptor moiety moving forward: the designs that were pursued are described in the following chapters. An added advantage of Tp-capped diiron(III) oxo cores is the possibility to protonate the oxo bridge, which decreases the strength of spin coupling.[2,5] The donor, however, appeared to be a good choice, and was further investigated; its ability to readily lose CO_2 in solution was discovered while in pursue of new intramolecular D-A assemblies, as is discussed in the next chapter.

APPENDIX

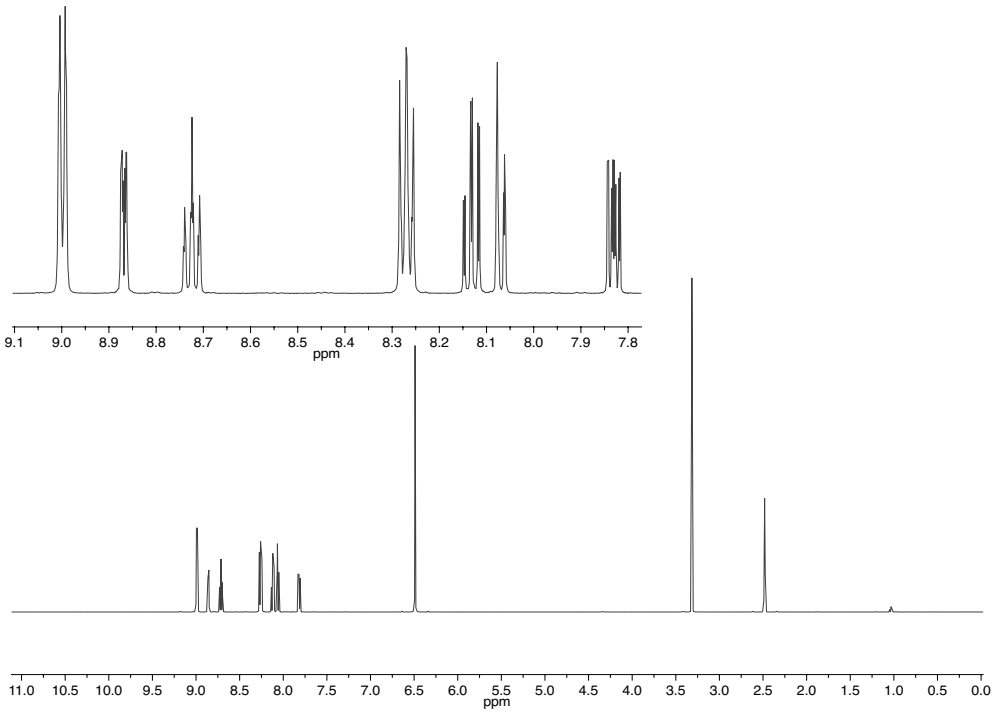


Figure 3.18. ^{1}H NMR of (2-pyridacyl)pyridinium iodide in DMSO-d_6.

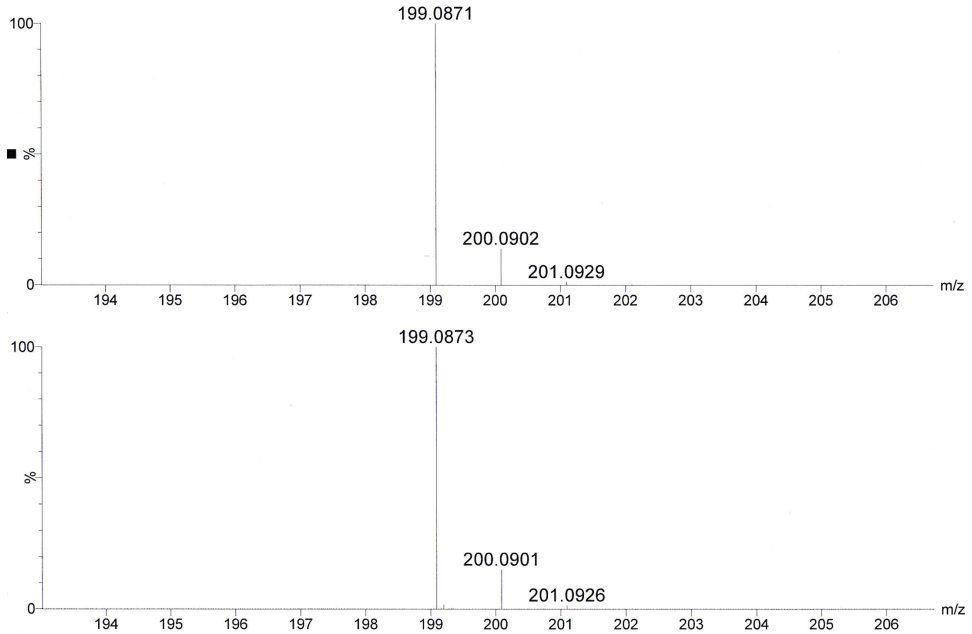


Figure 3.19. ESI-MS of (2-pyridacyl)pyridinium iodide. Top: calculated isotope pattern for $[M–I]^+$ ($C_{12}H_{11}N_2O$). Bottom: experimental result.

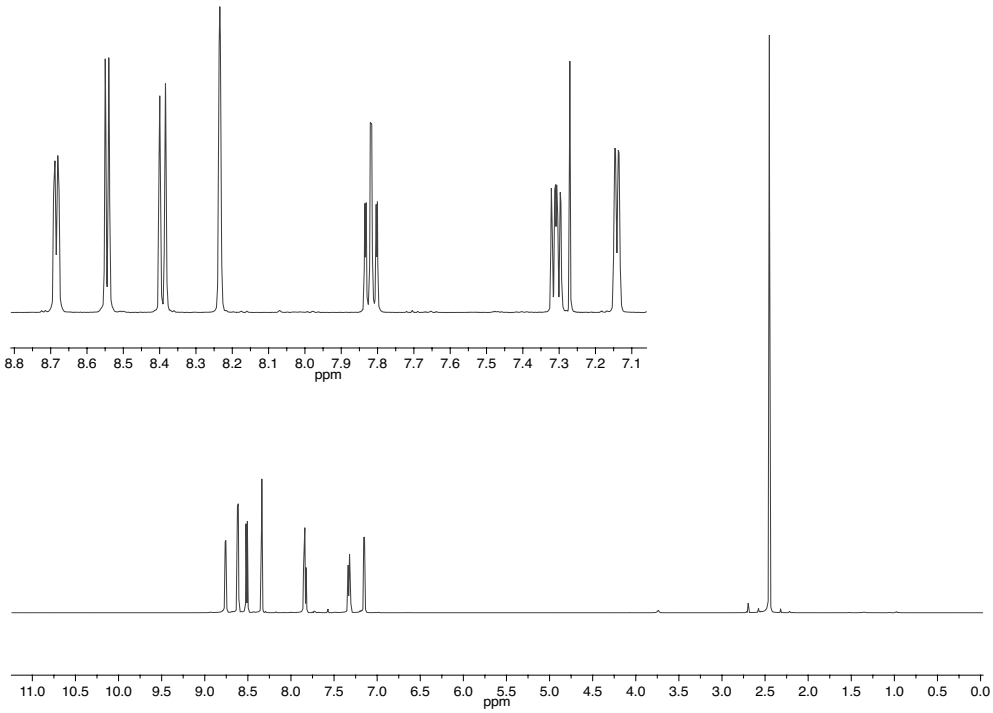


Figure 3.20. ^{1}H NMR of 4-methyl-2,2'-bipyridine in $CDCl_3$.

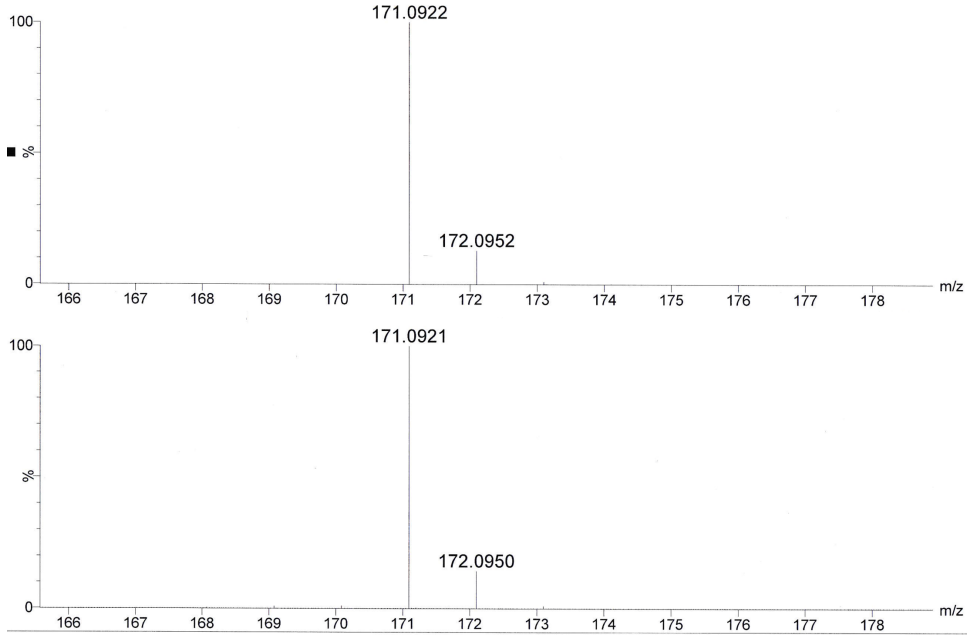


Figure 3.21. ESI-MS of 4-methyl-2,2′-bipyridine. Top: calculated isotope pattern for $[M+H]^+$ ($C_{11}H_{11}N_2$). Bottom: experimental result.

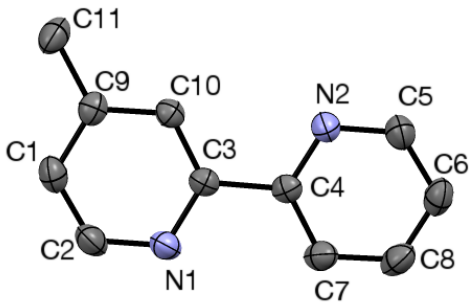


Figure 3.22. ORTEP drawing of 4-methyl-2,2'-bipyridine obtained from single-crystal X-ray structure determination. Atoms are represented as 50% probability thermal ellipsoids. Hydrogen atoms are omitted for clarity.

Table 3.7. Crystal data and structure refinement for 4-methyl-2,2'-bipyridine.

empirical formula	$C_{11}H_{10}N_2$
formula weight	170.21
temperature (K)	173
crystal color, habit	colorless, blocks
crystal system	orthorhombic
space group	Pbca
cell dimensions:	
a (Å)	11.3014(11)
b (Å)	7.4100(7)
c (Å)	21.656(2)
Volume (Å^3)	1813.6(3)
Z	8
D_{calc} (g cm^{-3})	1.247
goodness of fit (F^2)	1.064
R_1 ($I > 2(I)$)	0.0472

Table 3.8. Bond lengths for 4-methyl-2,2'-bipyridine.

Atoms	Length/Å	Atoms	Length/Å	Atoms	Length/Å
N1 C2	1.3376(18)	C1 C9	1.3879(19)	C6 C8	1.377(2)
N1 C3	1.3451(16)	C3 C4	1.4911(17)	C7 C8	1.383(2)
N2 C4	1.3415(16)	C3 C10	1.3917(17)	C9 C10	1.3913(18)
N2 C5	1.3390(17)	C4 C7	1.3899(18)	C9 C11	1.4982(19)
C1 C2	1.382(2)	C5 C6	1.378(2)		

Table 3.9. Bond angles for 4-methyl-2,2'-bipyridine.

Atoms	Angle/º	Atoms	Angle/º	Atoms	Angle/º
C2 N1 C3	116.86(11)	C10 C3 C4	121.19(11)	C8 C7 C4	119.19(13)
C5 N2 C4	117.45(12)	N2 C4 C3	116.43(10)	C6 C8 C7	119.09(13)
C2 C1 C9	119.27(13)	N2 C4 C7	122.12(12)	C1 C9 C10	117.15(12)
N1 C2 C1	124.12(13)	C7 C4 C3	121.45(12)	C1 C9 C11	121.41(13)
N1 C3 C4	116.24(11)	N2 C5 C6	124.11(14)	C10 C9 C11	121.44(13)
N1 C3 C10	122.57(11)	C8 C6 C5	118.02(13)	C9 C10 C3	120.03(12)

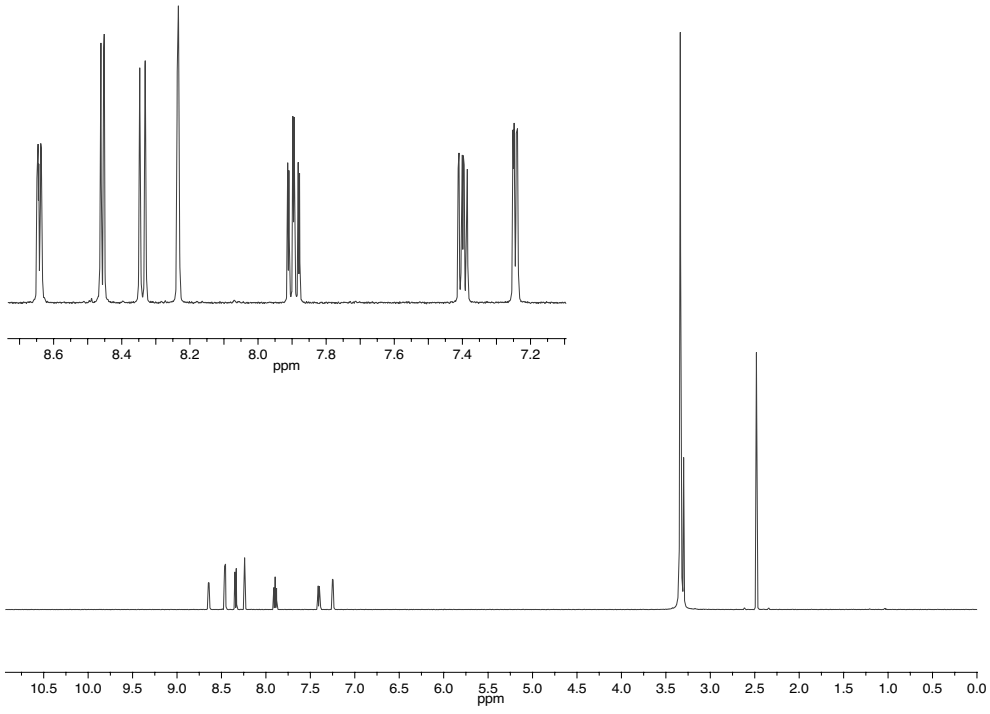


Figure 3.23. ^{1}H NMR of 2,2′-bipyridine-4-acetic acid in DMSO-d_6.

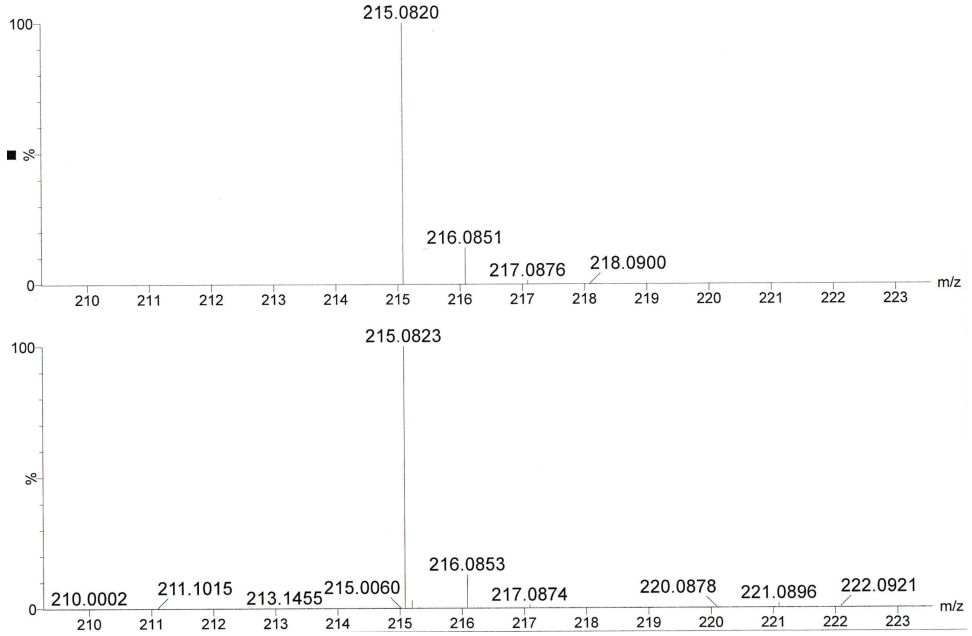


Figure 3.24. ESI-MS of 2,2′-bipyridine-4-acetic acid. Top: calculated isotope pattern for $[M+H]^+$ ($C_{12}H_{11}N_2O_2$). Bottom: experimental result.

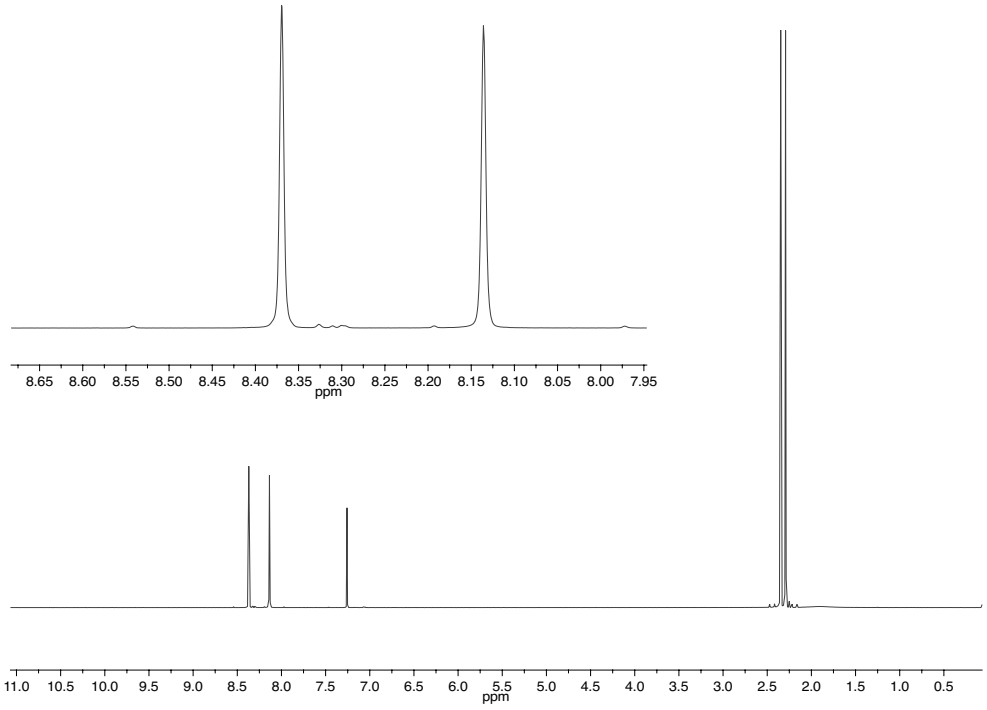


Figure 3.25. ^{1}H NMR of 4,4',5,5'-tetramethyl-2,2'-bipyridine in $CDCl_3$.

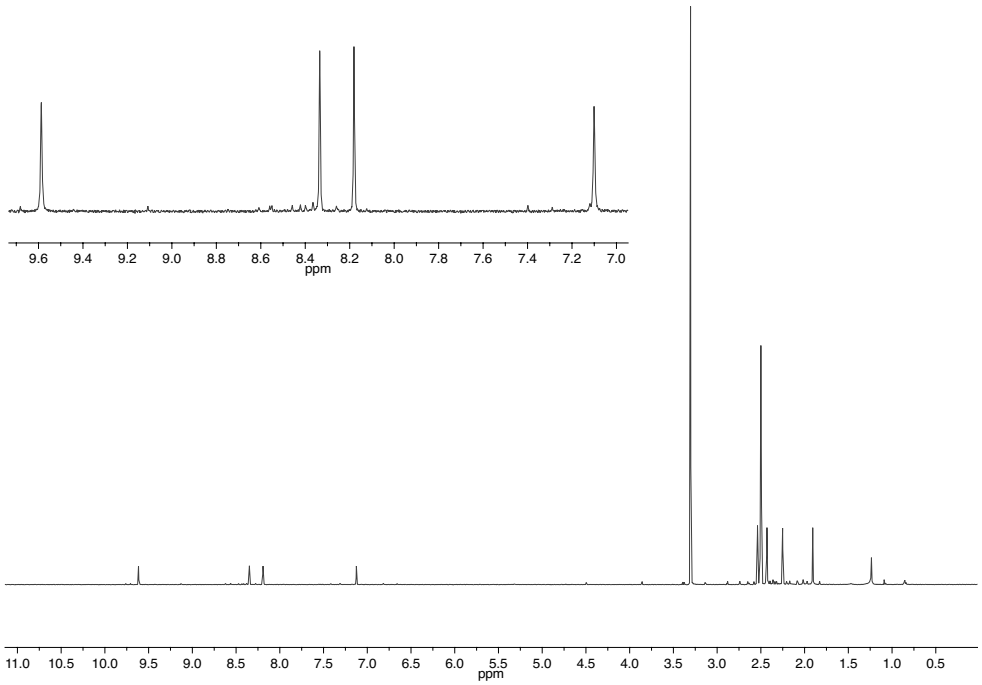


Figure 3.26. ^{1}H NMR spectrum of $Ru(tmb)_2Cl_2$ in DMSO-d_6.

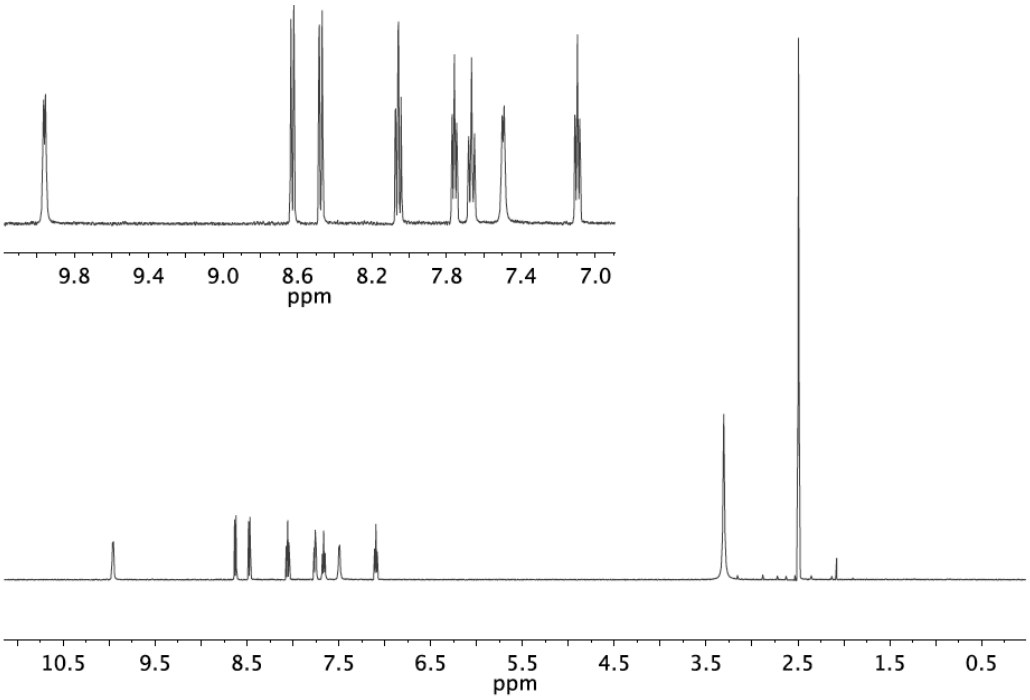


Figure 3.27. ^{1}H NMR spectrum of $Ru(bpy)_2Cl_2$ in DMSO-d_6.

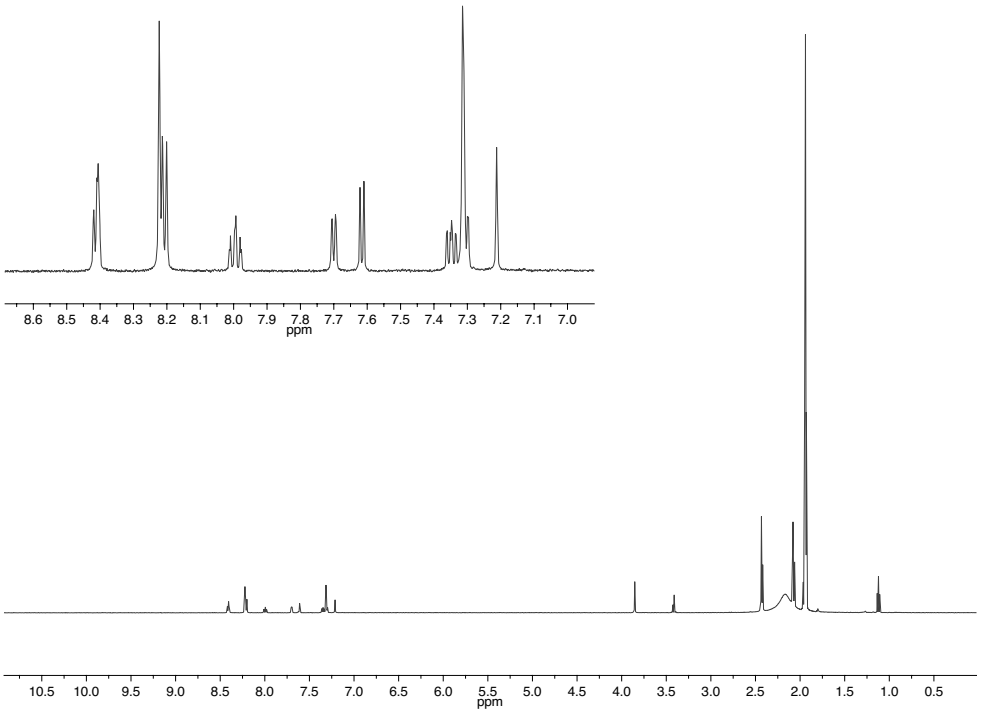


Figure 3.28. ^{1}H NMR spectrum of **(1)** in CD_3CN.

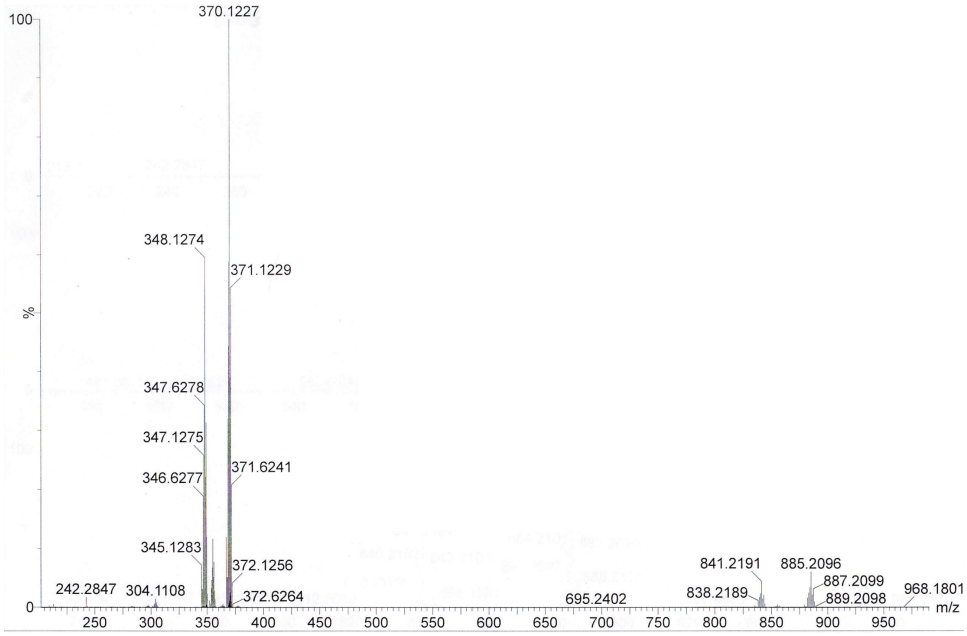


Figure 3.29. ESI-MS of **(1)**.

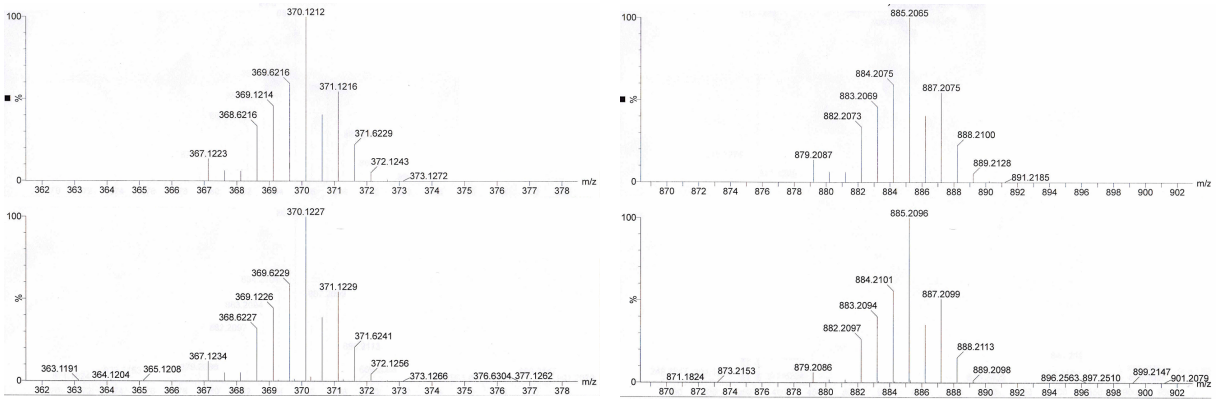


Figure 3.30. ESI-MS of **(1)**. Top left: calculated isotope pattern for $[M–2PF_6]^{2+}$ ($C_{40}H_{42}N_6O_2Ru$). Bottom left: experimental result. Top right: calculated isotope pattern for $[M–PF_6]^{+}$ ($C_{40}H_{42}N_6O_2RuPF_6$). Bottom right: experimental result.

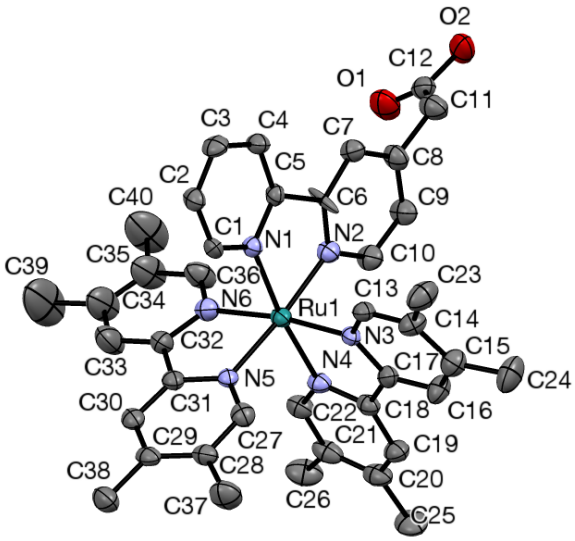


Figure 3.31. ORTEP drawing of $[Ru(tmb)_2(bpyac)]^{2+}$ obtained from single-crystal X-ray structure determination, showing all the atom labels. Atoms are represented as 50% probability thermal ellipsoids. Hydrogen atoms and anions are omitted for clarity.

Table 3.10. Bond lengths for the X-ray structure of compound **(1)**.

Atoms	Length/Å	Atoms	Length/Å	Atoms	Length/Å
Ru1 N1	2.059(5)	C19 C20	1.366(11)	C14 C15	1.415(11)
Ru1 N2	2.050(6)	C20 C21	1.398(12)	C14 C23	1.488(11)
Ru1 N3	2.046(6)	C20 C25	1.507(10)	C15 C16	1.382(11)
Ru1 N4	2.056(5)	C21 C22	1.386(10)	C15 C24	1.496(12)
Ru1 N5	2.058(5)	C21 C26	1.509(11)	C16 C17	1.378(10)
Ru1 N6	2.074(6)	C27 C28	1.381(10)	C17 C18	1.472(10)
O1 C12	1.212(10)	C28 C29	1.399(11)	C18 C19	1.386(10)
O2 C12	1.323(9)	C28 C37	1.481(11)	P2 F11	1.575(7)
N1 C1	1.339(8)	C29 C30	1.369(11)	P2 F12	1.563(7)
N1 C5	1.358(8)	C29 C38	1.496(10)	O1S C2S	1.55(3)
N2 C6	1.313(9)	C30 C31	1.398(10)	O1S C3S	1.53(3)
N2 C10	1.343(9)	C31 C32	1.461(11)	C1S C2S	1.36(4)
N3 C13	1.353(9)	C32 C33	1.382(12)	C3S C4S	1.45(4)
N3 C17	1.358(8)	C33 C34	1.391(14)		
N4 C18	1.352(9)	C34 C35	1.360(15)		
N4 C22	1.342(9)	C34 C39	1.532(15)		
N5 C27	1.338(9)	C35 C36	1.394(13)		
N5 C31	1.356(9)	C35 C40	1.527(14)		
N6 C32	1.353(9)	P1 F1	1.531(15)		
N6 C36	1.354(10)	P1 F2	1.543(13)		
C1 C2	1.369(9)	P1 F3	1.519(12)		
C2 C3	1.372(10)	P1 F4	1.531(12)		
C3 C4	1.394(10)	P1 F1B	1.547(14)		
C4 C5	1.386(9)	P1 F2B	1.496(13)		
C5 C6	1.496(9)	P1 F3B	1.535(15)		
C6 C7	1.406(9)	P1 F4B	1.572(13)		
C7 C8	1.389(10)	P1 F5	1.553(7)		
C8 C9	1.373(11)	P1 F6	1.565(6)		
C8 C11	1.505(10)	P2 F7	1.576(7)		
C9 C10	1.371(11)	P2 F8	1.534(8)		
C11 C12	1.504(12)	P2 F9	1.545(8)		
C13 C14	1.374(11)	P2 F10	1.545(8)		

Table 3.11. Bond angles for the X-ray crystal structure of **(1)**.

Atoms	Angle/º	Atoms	Angle/º	Atoms	Angle/º
N1 Ru1 N6	87.6(2)	C30 C29 C28	118.6(7)	C2 C3 C4	119.4(6)
N2 Ru1 N1	78.7(2)	C30 C29 C38	120.3(7)	C5 C4 C3	118.8(6)
N2 Ru1 N4	95.7(2)	C29 C30 C31	120.8(7)	F3 P1 F6	91.9(9)
N2 Ru1 N5	175.1(2)	N5 C31 C30	120.3(7)	F4 P1 F2	173.8(12)
N2 Ru1 N6	98.3(2)	N5 C31 C32	115.3(6)	N1 C5 C4	121.1(6)
N3 Ru1 N1	96.8(2)	C30 C31 C32	124.4(7)	N1 C5 C6	112.9(6)
N3 Ru1 N2	88.5(2)	N6 C32 C31	115.6(6)	C4 C5 C6	125.6(6)
N3 Ru1 N4	79.0(2)	N6 C32 C33	120.4(8)	N2 C6 C5	115.5(6)
N3 Ru1 N5	94.5(2)	C33 C32 C31	124.0(7)	N2 C6 C7	123.5(6)
N3 Ru1N6	172.5(2)	C32 C33 C34	120.7(9)	C7 C6 C5	119.9(6)
N4 Ru1 N1	173.2(2)	C33 C34 C39	119.1(11)	C8 C7 C6	118.4(7)
N4 Ru1 N5	88.7(2)	C35 C34 C33	119.2(9)	C7 C8 C11	121.0(7)
N4 Ru1 N6	97.2(2)	C35 C34 C39	121.7(10)	C9 C8 C7	116.8(7)
N5 Ru1 N1	97.0(2)	C34C35 C36	118.1(9)	C9 C8 C11	122.1(7)
N5 Ru1 N6	78.9(2)	C34 C35C40	124.2(9)	C10 C9 C8	121.0(7)
C1 N1 Ru1	125.7(4)	C36 C35 C40	117.6(10)	N2 C10 C9	122.6(7)
C1 N1 C5	118.8(5)	N6 C36 C35	123.1(8)	C12 C11 C8	113.0(7)
C5 N1 Ru1	115.5(4)	F1 P1 F2	87(2)	O1 C12 O2	123.2(8)
C6 N2 Ru1	115.9(4)	F1 P1 F4	91(2)	O1 C12 C11	125.7(7)
C6 N2 C10	117.1(6)	F1 P1 F1B	32(2)	O2 C12 C11	111.1(7)
C10 N2 Ru1	126.3(5)	F1P1 F3B	137(2)	N3 C13 C14	124.5(6)
C13 N3 Ru1	126.6(4)	F1 P1 F4B	50.9(19)	C13 C14 C15	118.1(7)
C13 N3 C17	117.3(6)	F1 P1 F5	90.9(12)	C13 C14 C23	120.8(7)
C17 N3 Ru1	116.1(5)	F1 P1 F6	86.5(12)	C15 C14 C23	121.1(7)
C18 N4 Ru1	115.2(4)	F2 P1 F1B	56.3(14)	C14 C15 C24	121.9(8)
C22 N4 Ru1	127.1(5)	F2 P1 F4B	134.1(13)	C16 C15 C14	116.8(7)
C22 N4 C18	117.6(6)	F2 P1 F5	84.6(9)	C16 C15 C24	121.4(7)
C27 N5 Ru1	126.1(5)	F2 P1 F6	94.8(9)	C17 C16 C15	122.1(7)
C27 N5 C31	118.6(6)	F3 P1 F1	178(2)	N3 C17 C16	120.9(7)
C31 N5 Ru1	115.3(5)	F3 P1 F2	91.7(14)	N3 C17 C18	114.0(6)
C32 N6 Ru1	114.6(5)	F3 P1 F4	89.8(18)	C16 C17 C18	125.1(6)
C32 N6 C36	118.4(7)	F3 P1 F1B	146.6(19)	N4 C1 C17	115.5(6)
C36 N6 Ru1	126.9(5)	F3 P1 F3B	44.0(13)	N4 C18 C19	120.6(7)
N1 C1 C2	122.9(6)	F3 P1 F4B	130.6(16)	C19 C18 C17	124.0(7)
C1 C2 C3	118.9(6)	F3 P1 F5	90.6(9)	C20 C19 C18	122.0(8)

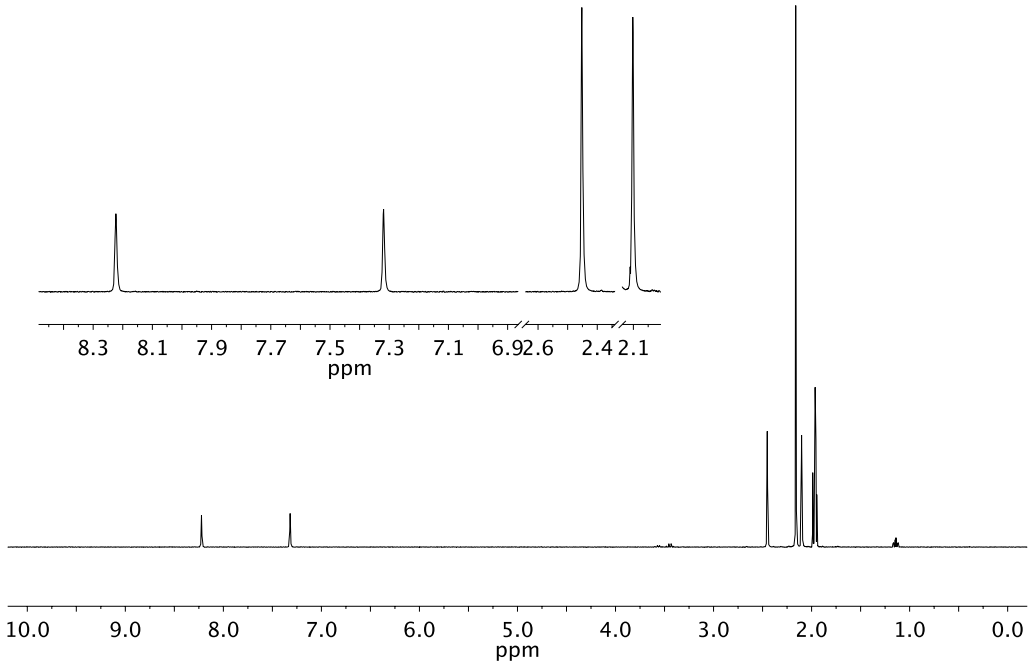


Figure 3.32. ^{1}H NMR of $[Ru(tmb)_3](PF_6)_2$ in CD_3CN.

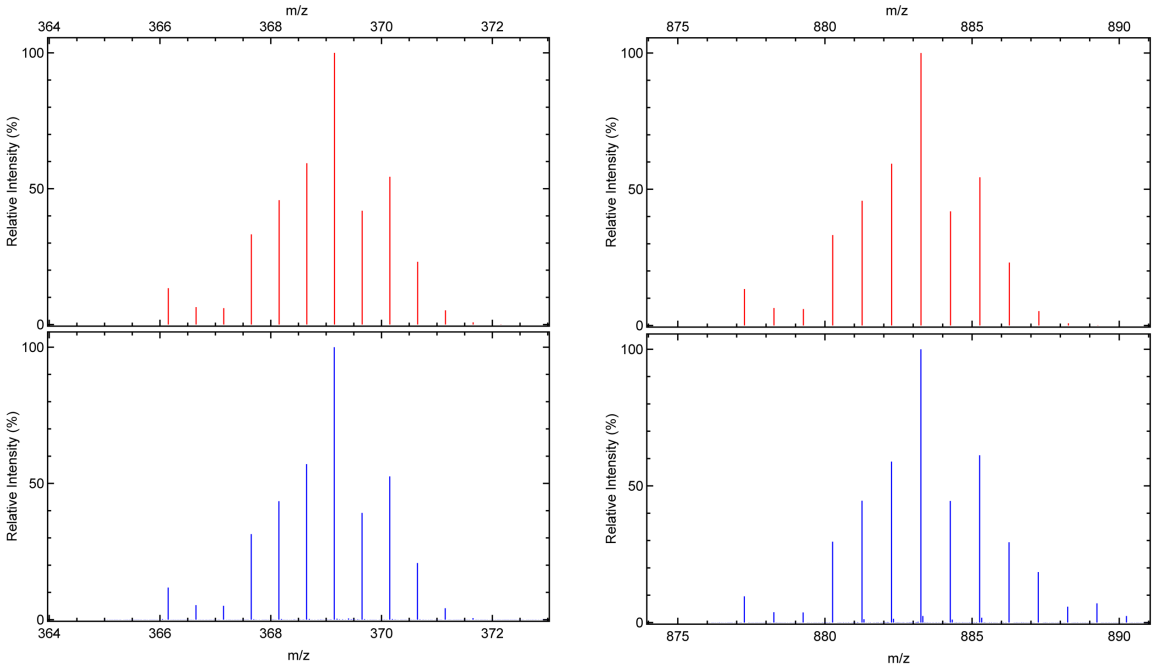


Figure 3.33. ESI-MS of $[Ru(tmb)_3](PF_6)_2$. Top left: calculated isotope pattern for $[M–2PF_6]^{2+}$ ($C_{42}H_{48}N_6Ru$). Bottom left: experimental result. Top right: calculated isotope pattern for $[M–PF_6]^{+}$ ($C_{42}H_{48}N_6RuPF_6$). Bottom right: experimental result.

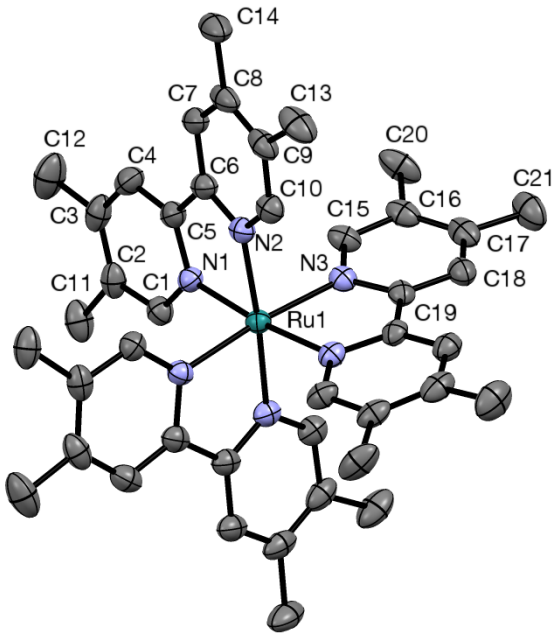


Figure 3.34. ORTEP drawing of $[Ru(tmb)_3]^{2+}$ obtained from single-crystal X-ray structure determination, showing the atom labels; half of the atoms are symmetry equivalent and their labels are not included. Atoms are represented as 50% probability thermal ellipsoids. Hydrogen atoms and anions are omitted for clarity.

Table 3.12. Bond lengths for the X-ray crystal structure of $[Ru(tmb)_3](PF_6)_2$.

Atoms	Length/Å	Atoms	Length/Å	Atoms	Length/Å
Ru1 N1[1]	2.047(4)	C3 C4	1.394(9)	C18 C19	1.386(7)
Ru1 N1	2.047(4)	C3 C12	1.496(8)	C19 C19[1]	1.459(11)
Ru1 N2[1]	2.058(4)	C4 C5	1.374(8)	P1 F1	1.569(13)
Ru1 N2	2.058(4)	C5 C6	1.470(8)	P1 F2	1.420(14)
Ru1 N3[1]	2.061(4)	C6 C7	1.388(7)	P1 F3	1.549(13)
Ru1 N3	2.061(4)	C7 C8	1.380(8)	P1 F4	1.549(12)
N1 C1	1.350(7)	C8 C9	1.403(9)	P1 F5	1.551(14)
N1 C5	1.361(7)	C8 C14	1.505(8)	P1 F6	1.554(12)
N2 C6	1.359(7)	C9 C10	1.379(8)	P2 F7	1.566(8)
N2 C10	1.340(7)	C9 C13	1.508(8)	P2 F8[2]	1.558(5)
N3 C15	1.344(7)	C15 C16	1.391(8)	P2 F8	1.558(5)
N3 C19	1.359(7)	C16 C17	1.392(9)	P2 F9	1.495(7)
C1 C2	1.385(8)	C16 C20	1.512(8)	P2 F10	1.587(4)
C2 C3	1.396(9)	C17 C18	1.393(8)	P2 F10[2]	1.587(4)
C2 C11	1.498(8)	C17 C21	1.491(8)		

[1]1–x, +y, ½–z; [2]1–x, +y, 3/2–z

Table 3.13. Bond angles for the X-ray crystal structure of $[Ru(tmb)_3](PF_6)_2$.

Atoms	Angle/º	Atoms	Angle/º	Atoms	Angle/º
N1[1] Ru1 N1	87.7(2)	C4 C3 C2	117.8(5)	F2 P1 F3	80.9(7)
N1[1] Ru1 N2[1]	78.82(17)	C4 C3 C12	120.7(6)	F2 P1 F4	172.9(9)
N1 Ru1 N2[1]	98.06(16)	C5 C4 C3	121.2(5)	F2 P1 F5	86.6(7)
N1[1] Ru1 N2	98.06(16)	N1 C5 C4	120.9(5)	F2 P1 F6	91.3(7)
N1 Ru1 N2	78.82(17)	N1 C5 C6	114.3(5)	F3 P1 F1	177.2(8)
N1[1] Ru1 N3[1]	174.13(17)	C4 C5 C6	124.7(5)	F3 P1 F5	88.8(9)
N1 Ru1 N3	174.13(17)	N2 C6 C5	115.0(4)	F3 P1 F6	90.2(7)
N1[1] Ru1 N3	97.08(17)	N2 C6 C7	120.4(5)	F4 P1 F1	90.5(8)
N1 Ru1 N3[1]	97.08(17)	C7 C6 C5	124.6(5)	F4 P1 F3	92.3(8)
N2[1] Ru1 N2	175.7(2)	C8 C7 C6	120.8(6)	F4 P1 F5	91.0(8)
N2 Ru1 N3	97.02(17)	C7 C8 C9	118.6(5)	F4 P1 F6	91.1(8)
N2[1] Ru1 N3	86.30(16)	C7 C8 C14	120.3(6)	F5 P1 F1	91.3(9)
N2[1] Ru1 N3[1]	97.02(16)	C9 C8 C14	121.1(6)	F5 P1 F6	177.7(7)
N2 Ru1 N3[1]	86.30(16)	C8 C9 C13	122.4(6)	F6 P1 F1	89.6(7)
N3[1] Ru1 N3	78.4(2)	C10 C9 C8	117.4(5)	F7 P2 F10[2]	89.7(2)
C1 N1 Ru1	125.9(3)	C10 C9 C13	120.2(6)	F7 P2 F10	89.7(2)
C1 N1 C5	118.0(4)	N2 C10 C9	124.3(5)	F8 P2 F7	87.7(4)
C5 N1 Ru1	116.0(3)	N3 C15 C16	123.3(5)	F8[2] P2 F7	87.7(4)
C6 N2 Ru1	115.2(3)	C15 C16 C17	118.7(5)	F8 P2 F8[2]	175.4(7)
C10 N2 Ru1	126.1(4)	C15 C16 C20	119.5(6)	F8 P2 F10	91.8(3)
C10 N2 C6	118.4(5)	C17 C16 C20	121.8(5)	F8[2] P2 F10	88.2(3)
C15 N3 Ru1	125.8(4)	C16 C17 C18	117.5(5)	F8 P2 F10[2]	88.2(3)
C15 N3 C19	118.4(4)	C16 C17 C21	121.4(6)	F8[2] P2 F10[2]	91.8(3)
C19 N3 Ru1	115.8(3)	C18 C17 C21	121.1(6)	F9 P2 F7	180.0
N1 C1 C2	123.7(5)	C19 C18 C17	121.2(5)	F9 P2 F8[2]	92.3(4)
C1 C2 C3	118.2(5)	N3 C19 C18	120.5(5)	F9 P2 F8	92.3(4)
C1 C2 C11	119.5(6)	N3 C19 C19[1]	114.9(3)	F9 P2 F10[2]	90.3(2)
C3 C2 C11	122.2(5)	C18 C19 C19[1]	124.6(3)	F9 P2 F10	90.3(2)
C2 C3 C12	121.4(6)	F2 P1 F1	96.3(8)	F10 P2 F10[2]	179.4(4)

[1]1–x, +y, ½–z; [2]1–x, +y, 3/2–z

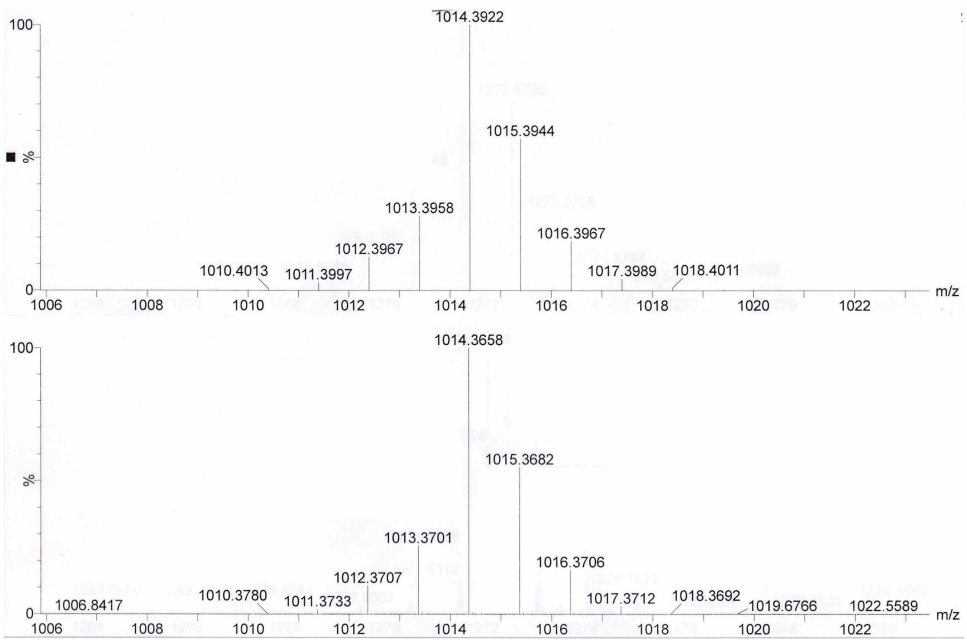


Figure 3.35. ESI-MS of **(2)**. Top: calculated isotope pattern for $[M–BPh_4]^+$ ($C_{48}H_{65}N_{11}BO_6Fe_2$). Bottom: experimental result.

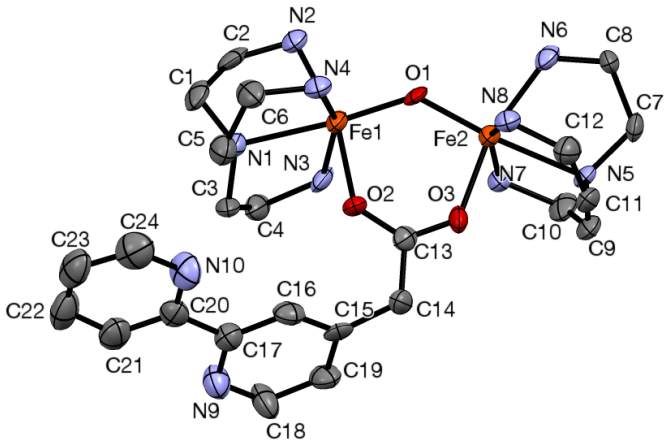


Figure 3.36. ORTEP drawing of $[(tren)_2Fe_2O(\mu\text{-bpyac})]^{3+}$ obtained from single-crystal X-ray structure determination. Atoms are represented as 50% probability thermal ellipsoids. Hydrogen atoms and anions are omitted for clarity.

Table 3.14. Bond lengths for the X-ray structure of compound **(2)**.

Atoms	Length/Å	Atoms	Length/Å	Atoms	Length/Å
Fe1 O1	1.777(3)	N10 C20	1.342(8)	C7B B1B	1.638(8)
Fe1 O2	2.069(4)	N10 C24	1.332(8)	C8B C9B	1.387(7)
Fe1 N1	2.218(4)	C1 C2	1.510(8)	C9B C10B	1.386(8)
Fe1 N2	2.144(4)	C3 C4	1.495(8)	C10B C11B	1.356(8)
Fe1 N3	2.157(4)	C5 C6	1.512(7)	C11B C12B	1.386(7)
Fe1 N4	2.136(5)	C7 C8	1.505(7)	C13B C14B	1.385(8)
Fe2 O1	1.785(3)	C9 C10	1.509(8)	C13B C18B	1.411(8)
Fe2 O3	2.026(4)	C11 C12	1.518(8)	C13B B1B	1.638(9)
Fe2 N5	2.219(4)	C13 C14	1.524(8)	C14B C15B	1.374(9)
Fe2 N6	2.146(4)	C14 C15	1.487(7)	C15B C16B	1.384(11)
Fe2 N7	2.146(4)	C15 C16	1.396(7)	C16B C17B	1.358(10)
Fe2 N8	2.170(4)	C15 C19	1.374(7)	C17B C18B	1.381(9)
O2 C13	1.257(6)	C16 C17	1.398(7)	C19B C20B	1.390(7)
O3 C13	1.252(6)	C17 C20	1.480(8)	C19B C24B	1.402(8)
N1 C1	1.480(7)	C18 C19	1.396(8)	C19B B1B	1.645(9)
N1 C3	1.471(6)	C20 C21	1.378(8)	C20B C21B	1.378(8)
N1 C5	1.487(7)	C21 C22	1.374(9)	C21B C22B	1.364(8)
N2 C2	1.481(6)	C22 C23	1.367(9)	C22B C23B	1.378(8)
N3 C4	1.492(6)	C23 C24	1.361(9)	C23B C24B	1.378(8)
N4 C6	1.484(6)	C1B C2B	1.391(7)	C1C C2C	1.393(7)
N5 C7	1.508(6)	C1B C6B	1.408(7)	C1C C6C	1.407(7)
N5 C9	1.468(6)	C1B B1B	1.624(8)	C1C B1C	1.638(8)
N5 C11	1.477(7)	C2B C3B	1.390(7)	C2C C3C	1.394(7)
N6 C8	1.484(6)	C3B C4B	1.373(7)	C3C C4C	1.375(7)
N7 C10	1.485(6)	C4B C5B	1.378(7)	C4C C5C	1.373(7)
N8 C12	1.496(6)	C5B C6B	1.382(7)	C5C C6C	1.383(7)
N9 C17	1.350(7)	C7B C8B	1.412(7)	C7C C8C	1.410(7)
N9 C18	1.326(7)	C7B C12B	1.396(7)	C7C C12C	1.399(7)
C7C B1C	1.644(8)	C14C C15C	1.374(8)	C21C C22C	1.375(7)
C8C C9C	1.388(7)	C15C C16C	1.384(8)	C22C C23C	1.374(7)
C9C C10C	1.376(7)	C16C C17C	1.366(8)	C23C C24C	1.387(7)
C10C C11C	1.374(7)	C17C C18C	1.380(8)	O1B N1B	1.248(6)
C11C C12C	1.383(7)	C19C C20C	1.401(7)	O2B N1B	1.228(6)
C13C C14C	1.407(7)	C19C C24C	1.393(7)	O3B N1B	1.243(6)
C13C C18C	1.407(7)	C19C B1C	1.644(8)	O1S C1S	1.413(9)
C13C B1C	1.635(9)	C20C C21C	1.391(7)		

Table 3.15. Bond lengths for the X-ray structure of compound **(2)**.

Atoms	Angle/º	Atoms	Angle/º	Atoms	Angle/º
O1 Fe1 O2	97.71(15)	C11 N5 Fe2	105.0(3)	C5B C6B C1B	123.7(5)
O1 Fe1 N1	175.25(17)	C11 N5 C7	112.3(4)	C8B C7B B1B	120.6(5)
O1 Fe1 N2	96.57(16)	C8 N6 Fe2	109.9(3)	C12B C7B C8B	113.3(5)
O1 Fe1 N3	103.49(16)	C10 N7 Fe2	112.5(3)	C12B C7B B1B	126.1(5)
O1 Fe1 N4	99.92(16)	C12 N8 Fe2	113.1(3)	C9B C8B C7B	123.6(5)
O2 Fe1 N1	86.89(16)	C18 N9 C17	117.0(5)	C10B C9B C8B	119.4(6)
O2 Fe1 N2	165.71(15)	C24 N10 C20	116.8(6)	C11B C10B C9B	119.1(6)
O2 Fe1 N3	83.81(16)	N1 C1 C2	112.9(5)	C10B C11B C12B	120.6(6)
O2 Fe1 N4	85.03(16)	N2 C2 C1	108.6(5)	C11B C12B C7B	123.7(6)
N2 Fe1 N1	78.84(17)	N1 C3 C4	110.0(5)	C14B C13B C18B	112.7(6)
N2 Fe1 N3	92.32(17)	N3 C4 C3	110.0(5)	C14B C13B B1B	125.9(6)
N3 Fe1 N1	78.10(17)	N1 C5 C6	110.1(5)	C18B C13B B1B	121.4(6)
N4 Fe1 N1	79.23(17)	N4 C6 C5	108.9(5)	C15B C14B C13B	124.9(7)
N4 Fe1 N2	93.08(18)	C8 C7 N5	111.1(4)	C14B C15B C16B	119.3(8)
N4 Fe1 N3	155.18(17)	N6 C8 C7	108.7(4)	C17B C16B C15B	119.3(8)
O1 Fe2 O3	99.48(15)	N5 C9 C10	110.5(5)	C16B C17B C18B	119.9(8)
O1 Fe2 N5	174.56(17)	N7 C10 C9	108.7(5)	C17B C18B C13B	123.9(7)
O1 Fe2 N6	96.33(16)	N5 C11 C12	111.3(5)	C20B C19B C24B	113.9(6)
O1 Fe2 N7	101.66(16)	N8 C12 C11	109.9(5)	C20B C19B B1B	123.9(6)
O1 Fe2 N8	100.93(16)	O2 C13 C14	117.8(5)	C24B C19B B1B	122.2(5)
O3 Fe2 N5	85.91(15)	O3 C13 O2	126.4(6)	C21B C20B C19B	123.1(7)
O3 Fe2 N6	163.98(15)	O3 C13 C14	115.8(5)	C22B C21B C20B	121.6(7)
O3 Fe2 N7	86.63(16)	C15 C14 C13	113.5(5)	C21B C22B C23B	117.0(6)
O3 Fe2 N8	82.32(16)	C16 C15 C14	120.6(5)	C24B C23B C22B	121.4(7)
N6 Fe2 N5	78.26(16)	C19 C15 C14	122.4(6)	C23B C24B C19B	122.7(6)
N6 Fe2 N8	92.18(17)	C19 C15 C16	117.0(5)	C1B B1B C7B	109.7(5)
N7 Fe2 N5	79.33(17)	C15 C16 C17	120.9(6)	C1B B1B C13B	107.3(5)
N7 Fe2 N6	92.74(17)	N9 C17 C16	121.3(6)	C1B B1B C19B	110.1(4)
N7 Fe2 N8	156.19(17)	N9 C17 C20	116.8(6)	C7B B1B C13B	110.0(4)
N8 Fe2 N5	78.90(17)	C16 C17 C20	122.0(6)	C7B B1B C19B	109.9(5)
Fe1 O1 Fe2	132.7(2)	N9 C18 C19	124.9(6)	C13B B1B C19B	109.8(5)
C13 O2 Fe1	130.6(4)	C15 C19 C18	118.7(6)	C2C C1C C6C	113.8(5)
C13 O3 Fe2	130.8(4)	N10 C20 C17	117.7(6)	C2C C1C B1C	125.1(5)
C1 N1 Fe1	110.4(3)	N10 C20 C21	122.3(6)	C6C C1C B1C	120.9(5)
C1 N1 C5	111.3(5)	C21 C20 C17	119.8(7)	C3C C2C C1C	123.6(5)
C3 N1 Fe1	105.8(3)	C22 C21 C20	119.5(7)	C4C C3C C2C	119.9(5)
C3 N1 C1	113.0(4)	C23 C22 C21	118.2(7)	C3C C4C C5C	118.9(5)
C3 N1 C5	109.7(5)	C24 C23 C22	119.1(7)	C4C C5C C6C	120.3(6)
C5 N1 Fe1	106.2(3)	N10 C24 C23	124.0(7)	C5C C6C C1C	123.4(5)
C2 N2 Fe1	110.4(3)	C2B C1B C6B	114.4(5)	C8C C7C B1C	125.6(5)
C4 N3 Fe1	113.3(3)	C2B C1B B1B	122.4(5)	C12C C7C C8C	113.9(5)
C6 N4 Fe1	113.6(3)	C6B C1B B1B	122.8(5)	C12C C7C B1C	120.4(5)
C7 N5 Fe2	111.1(3)	C3B C2B C1B	122.7(6)	C9C C8C C7C	122.8(5)
C9 N5 Fe2	106.3(3)	C4B C3B C2B	120.7(5)	C10C C9C C8C	120.4(6)
C9 N5 C7	110.8(4)	C3B C4B C5B	119.0(6)	C11C C10C C9C	119.0(5)

Table 3.15 (cont'd).

Atoms	Angle/°	Atoms	Angle/°	Atoms	Angle/°
C9 N5 C11	111.1(5)	C4B C5B C6B	119.5(6)	C10C C11C C12C	119.8(6)
C11C C12C C7C	123.9(6)	C20C C19C B1C	120.7(5)	C1C B1C C19C	110.0(4)
C14C C13C C18C	113.7(5)	C24C C19C C20C	114.5(5)	C13C B1C C1C	109.0(5)
C14C C13C B1C	123.6(5)	C24C C19C B1C	124.8(6)	C13C B1C C7C	109.7(4)
C18C C13C B1C	122.3(5)	C21C C20C C19C	123.5(6)	C13C B1C C19C	107.4(5)
C15C C14C C13C	124.0(6)	C22C C21C C20C	119.9(6)	C19C B1C C7C	108.5(5)
C14C C15C C16C	119.6(6)	C23C C22C C21C	118.3(6)	O2B N1B O1B	120.9(6)
C17C C16C C15C	118.8(6)	C22C C23C C24C	121.4(6)	O2B N1B O3B	120.0(6)
C16C C17C C18C	121.0(6)	C23C C24C C19C	122.4(6)	O3B N1B O1B	119.0(6)
C17C C18C C13C	122.8(6)	C1C B1C C7C	112.2(5)		

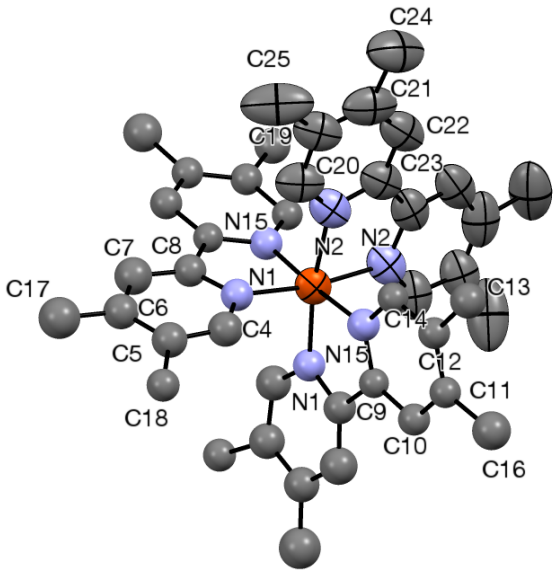


Figure 3.37. ORTEP drawing of $[Fe(tmb)_3]^{2+}$ obtained from a single-crystal X-ray structure determination. When possible, atoms are represented as 50% probability thermal ellipsoids. Only one possible molecule in the disorder is shown. Hydrogen atoms and anions are omitted for clarity.

Table 3.16. Crystallographic data for $[Fe(tmb)_3](PF_6)_2$.

empirical formula	$C_{42}H_{48}N_6FeP_2F_{12}$
formula weight	982.65
temperature (K)	173(2)
crystal color, habit	red, needles
crystal system	monoclininc
space group	*C*2/*c*
cell dimensions:	
a (Å)	14.1584(3)
b (Å)	23.2788(5)
c (Å)	14.0797(3)
Volume (Å^3)	4639.37(17)
Z	4
D_{calc} (g cm^{-3})	1.407
goodness of fit (F^2)	1.194
R_1 ($I > 2(I)$)	0.1146

Table 3.17. Bond lengths for the crystal structure of $[Fe(tmb)_3](PF_6)_2$.

Atoms	Length/Å	Atoms	Length/Å	Atoms	Length/Å
Fe1 N1[1]	1.964(10)	P2 F3[1]	1.548(8)	C14 N15	1.368(13)
Fe1 N1	1.964(10)	P2 F4[1]	1.565(6)	C19 C20	1.372(12)
Fe1 N2	1.980(6)	P2 F4	1.565(6)	C20 C21	1.332(14)
Fe1 N2[1]	1.980(6)	F1 F4AA	1.30(2)	C20 C25	1.518(14)
Fe1 N15[1]	1.940(10)	F3AA F4AA[2]	1.52(3)	C21 C22	1.412(14)
Fe1 N15	1.940(10)	N1 C4	1.327(15)	C21 C24	1.531(12)
Fe1 N1A	1.980(9)	N1 C8	1.361(14)	C22 C23	1.354(11)
Fe1 N1A[1]	1.980(9)	N2 C19	1.326(10)	C23 C23[1]	1.471(17)
Fe1 N15A[1]	2.025(9)	N2 C23	1.361(10)	C18A C5A	1.563(17)
Fe1 N15A	2.025(9)	F1AA F2	0.85(7)	C5A C4A	1.370(13)
P1 F1	1.64(2)	F4AA F5[2]	1.70(4)	C5A C6A	1.425(18)
P1 F1[2]	1.64(2)	C4 C5	1.368(15)	C4A N1A	1.333(13)
P1 F3AA[2]	1.57(3)	C5 C6	1.422(19)	N1A C8A	1.377(13)
P1 F3AA	1.57(3)	C5 C18	1.556(18)	C8A C7A	1.354(16)
P1 F1AA	1.44(3)	C6 C7	1.38(2)	C8A C9A	1.472(18)
P1 F1AA[2]	1.44(3)	C6 C17	1.491(16)	C7A C6A	1.381(18)
P1 F2[2]	1.74(2)	C7 C8	1.353(17)	C6A C17A	1.483(15)
P1 F2	1.74(2)	C8 C9	1.479(19)	C9A C10A	1.404(12)
P1 F4AA[2]	1.82(2)	C9 C10	1.404(13)	C9A N15A	1.348(15)
P1 F4AA	1.82(2)	C9 N15	1.359(17)	C10A C11A	1.430(17)
P1 F5[2]	1.72(4)	C10 C11	1.422(18)	C11A C16A	1.526(14)
P1 F5	1.72(4)	C11 C12	1.379(18)	C11A C12A	1.373(17)
P2 F0AA	1.478(11)	C11 C16	1.544(16)	C12A C13A	1.549(14)
P2 F2AA	1.559(10)	C12 C13	1.546(16)	C12A C14A	1.413(13)
P2 F3	1.548(8)	C12 C14	1.418(15)	C14A N15A	1.373(12)

[1]–x, +y, ½–z; [2]1–x, –y, 1–z

Table 3.18. Bond angles for the crystal structure of $[Fe(tmb)_3](PF_6)_2$.

Atoms	Angle/°	Atoms	Angle/°	Atoms	Angle/°
N1[1] Fe1 N1	95.4(13)	F1AA[2] P1 F1[2]	102.2(16)	N1 C4 C5	125.6(16)
N1 Fe1 N2	171.4(6)	F1AA P1 F1	102.2(16)	C4 C5 C6	115.3(14)
N1[1] Fe1 N2[1]	171.4(6)	F1AA[2] P1 F1	77.8(16)	C4 C5 C18	119.1(15)
N1[1] Fe1 N2	91.6(7)	F1AA P1 F3AA	81(2)	C6 C5 C18	125.3(14)
N1 Fe1 N2[1]	91.6(7)	F1AA[2] P1 F3AA[2]	81(2)	C5 C6 C17	118.1(17)
N1[1] Fe1 N1A[1]	7.5(9)	F1AA[2] P1 F3AA	99(2)	C7 C6 C5	118.9(13)
N1 Fe1 N1A[1]	88.3(7)	F1AA P1 F3AA[2]	99(2)	C7 C6 C17	122.9(17)
N1[1] Fe1 N15A[1]	74.9(5)	F1AA[2] P1 F1AA	180(3)	C8 C7 C6	121.3(16)
N1 Fe1 N15A[1]	98.7(5)	F1AA[2] P1 F2[2]	29(3)	N1 C8 C9	113.4(11)
N2[1] Fe1 N2	81.9(4)	F1AA[2] P1 F2	151(3)	C7 C8 N1	120.1(16)
N2 Fe1 N15A	99.2(4)	F1AA P1 F2	29(3)	C7 C8 C9	126.4(14)
N2[1] Fe1 N15A	87.9(4)	F1AA P1 F2[2]	151(3)	C10 C9 C8	120.6(15)
N2[1] Fe1 N15A[1]	99.2(4)	F1AA P1 F4AA[2]	79.4(18)	N15 C9 C8	117.7(9)
N2 Fe1 N15A[1]	87.9(4)	F1AA[2] P1 F4AA[2]	100.6(18)	N15 C9 C10	121.7(14)
N15[1] Fe1 N1	96.4(6)	F1AA[2] P1 F4AA	79.4(18)	C9 C10 C11	117.1(15)
N15 Fe1 N1	85.9(5)	F1AA P1 F4AA	100.6(18)	C10 C11 C16	118.0(16)
N15 Fe1 N1[1]	96.4(6)	F1AA[2] P1 F5[2]	87.1(19)	C12 C11 C10	120.3(11)
N15[1] Fe1 N1[1]	85.9(5)	F1AA P1 F5[2]	92.9(19)	C12 C11 C16	121.7(14)
N15 Fe1 N2	88.4(4)	F1AA[2] P1 F5	92.9(19)	C11 C12 C13	122.6(12)
N15[1] Fe1 N2	89.0(5)	F1AA P1 F5	87.1(19)	C11 C12 C14	120.8(12)
N15 Fe1 N2[1]	89.0(5)	F2 P1 F2[2]	180.0	C14 C12 C13	116.6(15)
N15[1] Fe1 N2[1]	88.4(4)	F2[2] P1 F4AA[2]	72.0(17)	N15 C14 C12	118.1(13)
N15 Fe1 N15[1]	176.6(9)	F2 P1 F4AA[2]	108.0(17)	C9 N15 Fe1	110.3(8)
N15[1] Fe1 N1A[1]	89.1(5)	F2 P1 F4AA	72.0(17)	C9 N15 C14	122.0(11)
N15 Fe1 N1A[1]	93.5(6)	F2[2] P1 F4AA	108.0(17)	C14 N15 Fe1	127.0(9)
N15 Fe1 N15A[1]	170.4(6)	F4AA P1 F4AA[2]	180.0	N2 C19 C20	124.7(9)
N15[1] Fe1 N15A[1]	11.1(4)	F5[2] P1 F2	81.9(18)	C19 C20 C25	119.5(10)
N1A[1] Fe1 N2	98.4(6)	F5[2] P1 F2[2]	98.1(18)	C21 C20 C19	118.4(9)
N1A Fe1 N2	177.5(4)	F5 P1 F2[2]	81.9(18)	C21 C20 C25	122.1(10)
N1A[1] Fe1 N1A	81.4(11)	F5 P1 F2	98.1(18)	C20 C21 C22	118.2(9)
N1A[1] Fe1 N15A	94.5(5)	F5[2] P1 F4AA[2]	122.7(17)	C20 C21 C24	122.1(10)
N1A Fe1 N15A[1]	94.5(5)	F5 P1 F4AA	122.7(17)	C22 C21 C24	119.8(11)
N1A Fe1 N15A	78.3(4)	F5 P1 F4AA[2]	57.3(17)	C23 C22 C21	121.0(10)
N1A[1] Fe1 N15A[1]	78.3(4)	F5[2] P1 F4AA	57.3(17)	N2 C23 C23[1]	114.2(4)
N15A Fe1 N15A[1]	170.6(7)	F5[2] P1 F5	180(3)	C22 C23 N2	120.0(8)
F1[2] P1 F1	180.0(17)	F0AA P2 F2AA	180.0	C22 C23 C23[1]	125.7(6)
F1 P1 F2	78.0(15)	F0AA P2 F3	89.4(5)	F4AA[2] F5 P1	64.4(13)
F1[2] P1 F2[2]	78.0(15)	F0AA P2 F3[1]	89.4(5)	C4A C5A C18A	119.5(14)
F1[2] P1 F2	102.0(15)	F0AA P2 F4	89.9(4)	C4A C5A C6A	119.0(13)
F1 P1 F2[2]	102.0(15)	F0AA P2 F4[1]	89.9(4)	C6A C5A C18A	121.5(12)
F1 P1 F4AA[2]	136.3(8)	F2AA P2 F4	90.1(4)	N1A C4A C5A	125.3(13)
F1[2] P1 F4AA	136.3(8)	F2AA P2 F4[1]	90.1(4)	C4A N1A Fe1	128.0(9)
F1[2] P1 F4AA[2]	43.7(8)	F3 P2 F2AA	90.6(5)	C4A N1A C8A	113.8(11)
F1 P1 F4AA	43.7(8)	F3[1] P2 F2AA	90.6(5)	C8A N1A Fe1	118.0(10)
F1[2] P1 F5[2]	79.1(17)	F3[1] P2 F3	178.8(9)	N1A C8A C9A	112.7(11)

Table 3.18 (cont'd).

Atoms	Angle/°	Atoms	Angle/°	Atoms	Angle/°
F1 P1 F5	79.1(17)	F3^{1} P2 F4^{1}	94.2(4)	C7A C8A N1A	125.7(15)
F1 P1 F5^{2}	100.9(17)	F3 P2 F4	94.2(4)	C7A C8A C9A	121.2(13)
F1^{2} P1 F5	100.9(17)	F3^{1} P2 F4	85.8(4)	C8A C7A C6A	119.3(12)
F3AA P1 F1^{2}	95.8(15)	F3 P2 F4^{1}	85.8(4)	C5A C6A C17A	123.0(15)
F3AA P1 F1	84.2(15)	F4^{1} P2 F4	179.7(7)	C7A C6A C5A	116.7(11)
F3AA^{2} P1 F1	95.8(15)	F4AA F1 P1	75.6(12)	C7A C6A C17A	120.2(13)
F3AA^{2} P1 F1^{2}	84.2(15)	F4AA^{2} F3AA P1	72.3(13)	C10A C9A C8A	125.2(14)
F3AA^{2} P1 F3AA	180(3)	C4 N1 Fe1	128.6(11)	N15A C9A C8A	112.9(9)
F3AA^{2} P1 F2	86.1(17)	C4 N1 C8	118.4(13)	N15A C9A C10A	121.8(14)
F3AA P1 F2	93.9(17)	C8 N1 Fe1	111.9(10)	C9A C10A C11A	117.7(14)
F3AA P1 F2^{2}	86.1(17)	C19 N2 Fe1	127.9(6)	C10A C11A C16A	120.0(13)
F3AA^{2} P1 F2^{2}	93.9(17)	C19 N2 C23	117.5(7)	C12A C11A C10A	120.9(10)
F3AA P1 F4AA^{2}	52.7(15)	C23 N2 Fe1	114.5(6)	C12A C11A C16A	119.2(12)
F3AA^{2} P1 F4AA	52.7(15)	F2 F1AA P1	95(6)	C11A C12A C13A	125.3(10)
F3AA P1 F4AA	127.3(15)	F1AA F2 P1	56(3)	C11A C12A C14A	118.0(10)
F3AA^{2} P1 F4AA^{2}	127.3(15)	F1 F4AA P1	60.8(15)	C14A C12A C13A	116.7(13)
F3AA P1 F5^{2}	173(2)	F1 F4AA F3AA^{2}	115(2)	N15A C14A C12A	121.9(11)
F3AA^{2} P1 F5^{2}	7(2)	F1 F4AA F5^{2}	119(2)	C9A N15A Fe1	117.6(7)
F3AA P1 F5	7(2)	F3AA^{2} F4AA P1	55.0(13)	C9A N15A C14A	119.7(9)
F3AA^{2} P1 F5	173(2)	F3AA^{2} F4AA F5^{2}	7(2)	C14A N15A Fe1	122.7(7)
F1AA P1 F1^{2}	77.8(16)	F5^{2} F4AA P1	58.3(18)		

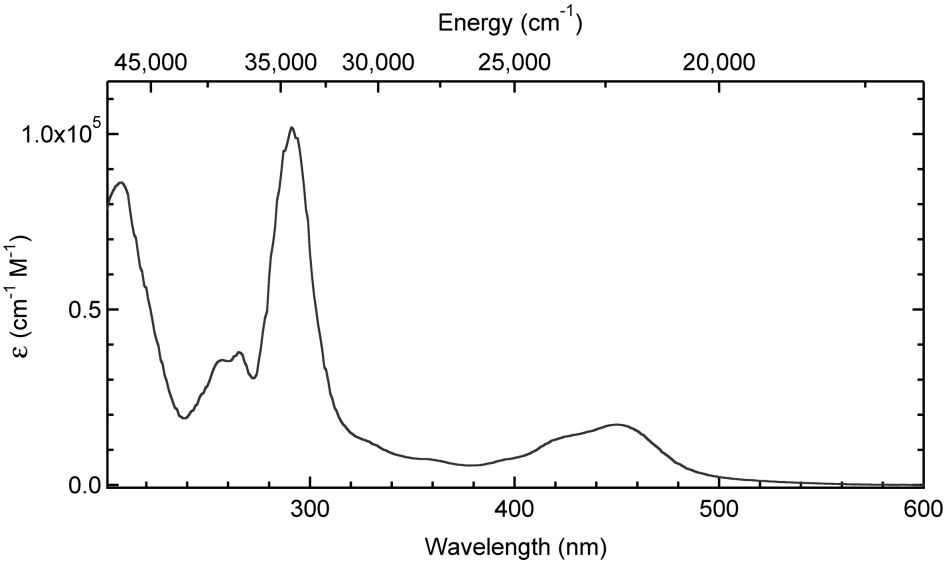


Figure 3.38. Electronic absorption spectrum of $[Ru(tmb)_3](PF_6)_2$ in acetonitrile solution at room temperature.

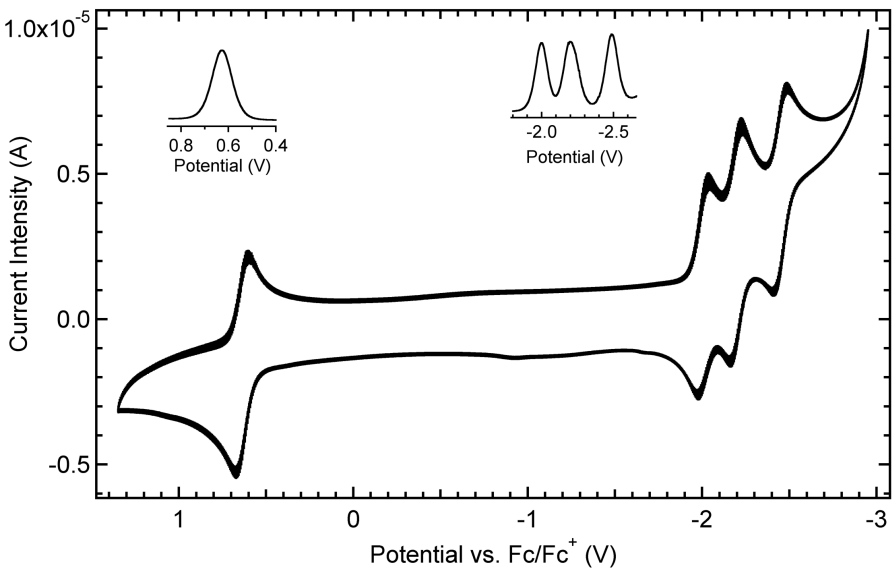


Figure 3.39. Cyclic Voltammogram for $[Ru(tmb)_3](PF_6)_2$ in acetonitrile with 0.1 M $TBAPF_6$ as supporting electrolyte. The insets show the DPV traces.

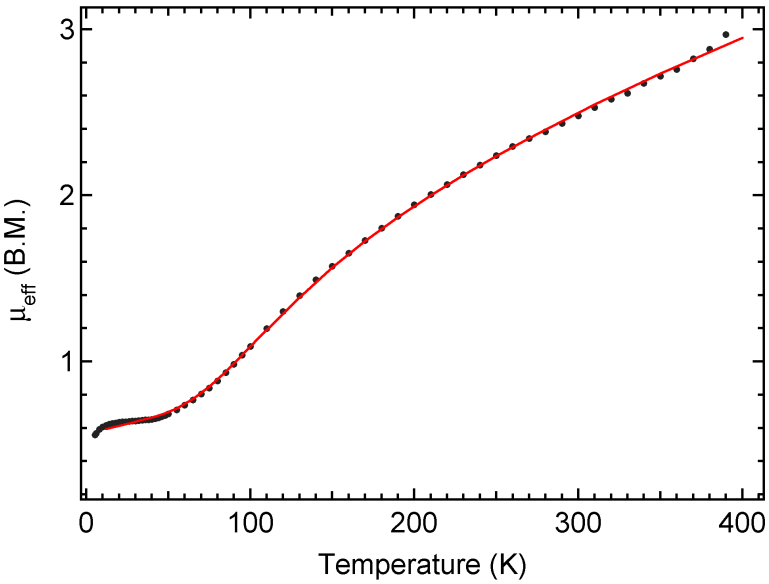


Figure 3.40. Effective magnetic moment (black circles) as a function of temperature for **(2)** measured at 1.00 T. The red trace is a fit to eq 3.2 with J = –128 cm^{-1}.

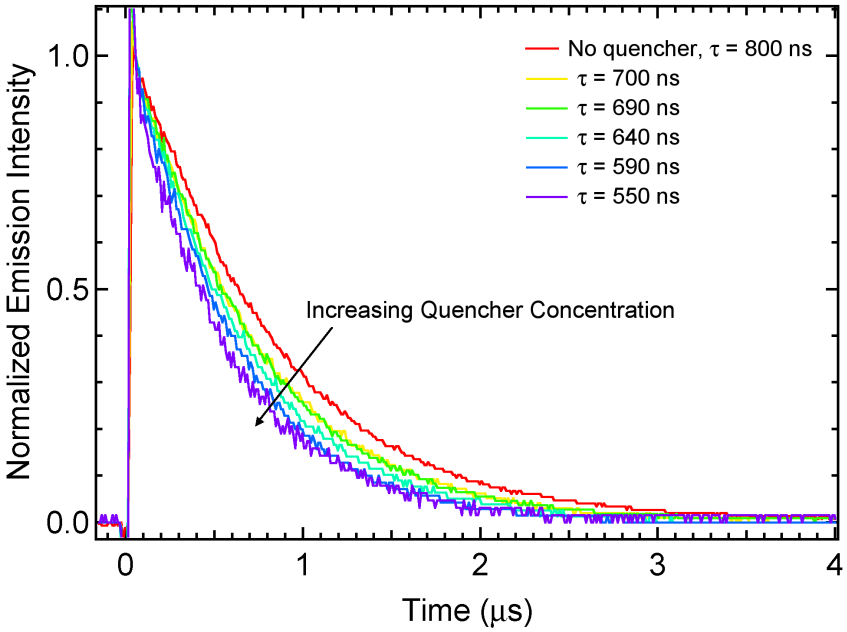


Figure 3.41. Time-resolved emission traces for **(1)** in the presence of increasing concentrations of **(2)**. The data points up to 0.055 μs were omitted when fitting the data to an exponential decay.

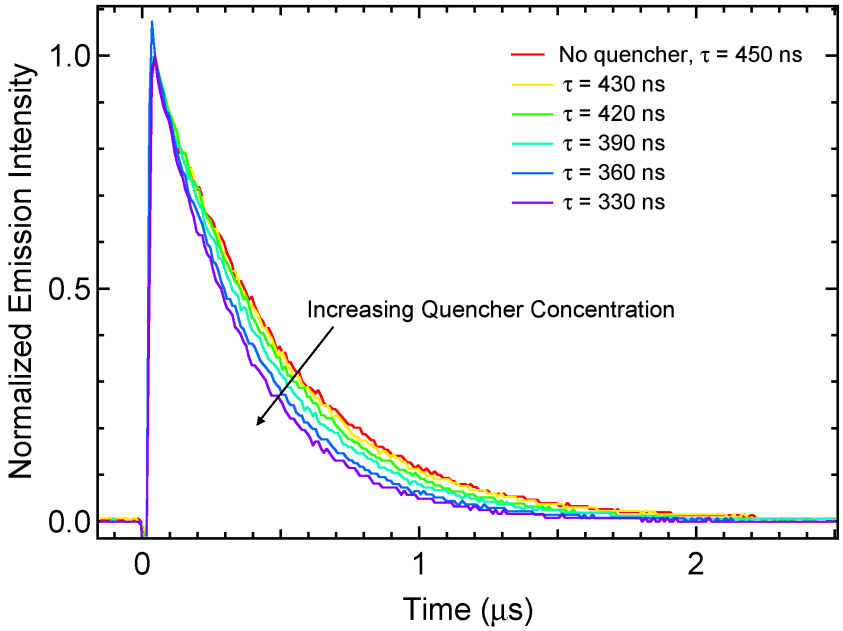


Figure 3.42. Time-resolved emission traces for $[Ru(tmb)_3](PF_6)_2$ in the presence of increasing concentrations of **(2)**. The data points before 0.045 μs were omitted when fitting the data to an exponential decay.

REFERENCES

REFERENCES

(1) Armstrong, W. H.; Spool, A.; Papaefthymiou, G. C.; Frankel, R. B.; Lippard, S. J. *J. Am. Chem. Soc.* **1984**, *106*, 3653–3667.

(2) Weldon, B. T.; Wheeler, D. E.; Kirby, J. P.; McCusker, J. K. *Inorg. Chem.* **2001**, *40*, 6802–6812.

(3) Kurtz, D. M. *Chem. Rev.* **1990**, *90*, 585–606.

(4) Kirby, J. P.; Weldon, B. T.; McCusker, J. K. *Inorg. Chem.* **1998**, *37*, 3658–3659.

(5) Armstrong, W. H.; Lippard, S. J. *J. Am. Chem. Soc.* **1984**, *106*, 4632–4633.

(6) Rodriguez, J. H.; McCusker, J. K. *J. Chem. Phys.* **2002**, *116*, 6253–6270.

(7) Picraux, L. B.; Smeigh, A. L.; Guo, D.; McCusker, J. K. *Inorg. Chem.* **2005**, *44*, 7846–7859.

(8) Armarego, W. L. F.; Chai, C. L. L. *Purification of Organic Chemicals*, 6th ed.; Elsevier, 2009.

(9) Fan, C.; Wang, X.; Ding, P.; Wang, J.; Liang, Z.; Tao, X. *Dyes Pigments* **2012**, *95*, 757–767.

(10) Ballardini, R.; Balzani, V.; Clemente-León, M.; Credi, A.; Gandolfi, M. T.; Ishow, E.; Perkins, J.; Stoddart, J. F.; Tseng, H.-R.; Wenger, S. *J. Am. Chem. Soc.* **2002**, *124*, 12786–12795.

(11) Della Ciana, L.; Hamachi, I.; Meyer, T. J. *J. Org. Chem.* **1989**, *54*, 1731–1735.

(12) Mines, G. A.; Bjerrum, M. J.; Hill, M. G.; Casimiro, D. R.; Chang, I.; Winkler, J. R.; Gray, H. B. *J. Am. Chem. Soc.* **1996**, *118*, 1961–1965.

(13) Evans, I. P.; Spencer, A.; Wilkinson, G. *J. Chem. Soc. Dalt. Trans.* **1973**, 204–209.

(14) Sullivan, B. P.; Salmon, D. J.; Meyer, T. J. *Inorg. Chem.* **1978**, *17*, 3334–3341.

(15) McCusker, C. E.; McCusker, J. K. *Inorg. Chem.* **2011**, *50*, 1656–1669.

(16) Hoertz, P. G.; Staniszewski, A.; Marton, A.; Higgins, G. T.; Incarvito, C. D.; Rheingold, A. L.; Meyer, G. J. *J. Am. Chem. Soc.* **2006**, *128*, 8234–8245.

(17) Soler, M.; McCusker, J. K. *J. Am. Chem. Soc.* **2008**, *130*, 4708–4724.

(18) Richardson, D. E.; Taube, H. *Inorg. Chem.* **1981**, *20*, 1278–1285.

(19) Suzuki, K.; Kobayashi, A.; Kaneko, S.; Takehira, K.; Yoshihara, T.; Ishida, H.; Shiina, Y.; Oishi, S.; Tobita, S. *Phys. Chem. Chem. Phys.* **2009**, *11*, 9850–9860.

(20) Claude, J. P.; Meyer, T. J. *J. Phys. Chem.* **1995**, *99*, 51–54.

(21) Parker, C. A.; Rees, W. T. *Analyst* **1960**, *85*, 587–600.

(22) Damrauer, N. H.; Boussie, T. R.; Devenney, M.; McCusker, J. K. *J. Am. Chem. Soc.* **1997**, *119*, 8253–8268.

(23) Bain, G. A.; Berry, J. F. *J. Chem. Educ.* **2008**, *85*, 532–536.

(24) Schmitt, E. A. Characterization of Tetranuclear Manganese Complexes and Thermochromic Copper(II) and Nickel(II) Complexes, University of Illinois at Urbana-Champaign, 1995.

(25) Guo, D.; McCusker, J. K. *Inorg. Chem.* **2007**, *46*, 3257–3274.

(26) Bock, C. R.; Connor, J. A.; Gutierrez, A. R.; Meyer, T. J.; Whitten, D. G.; Sullivan, B. P.; Nagle, J. K. *J. Am. Chem. Soc.* **1979**, *101*, 4815–4824.

(27) Clark, C. D.; Hoffman, M. Z. *Coord. Chem. Rev.* **1997**, *159*, 359–373.

(28) Picraux, L. B.; Weldon, B. T.; McCusker, J. K. *Inorg. Chem.* **2002**, *42*, 273–282.

(29) Arias-Rotondo, D. M.; McCusker, J. K. *Chem. Soc. Rev.* **2016**, *45*, 5803–5820.

(30) Smith, R. P.; Gosselin, R. E. *J. Occup. Med.* **1979**, *21*, 93–97.

(31) Mabrouk, P. A.; Wrighton, M. S. *Inorg. Chem.* **1986**, *25*, 526–531.

(32) Krossing, I.; Raabe, I. *Angew. Chem. Int. Ed.* **2004**, *43*, 2066–2090.

(33) Chen, P.; Duesing, R.; Graff, D. K.; Meyer, T. J. *J. Phys. Chem.* **1991**, *95*, 5850–5858.

(34) Sacksteder, L. A.; Brown, E. A.; Demas, J. N.; Zipp, A. P.; Streich, J.; DeGraff, B. A. *Inorg. Chem.* **1990**, *29*, 4335–4340.

(35) Baron, A.; Herrero, C.; Quaranta, A.; Charlot, M.-F.; Leibl, W.; Vauzeilles, B.; Aukauloo, A. *Inorg. Chem.* **2012**, *51*, 5985–5987.

(36) Balzani, V.; Barigelletti, F.; De Cola, L. *Top. Curr. Chem.* **1990**, *158*, 31–71.

(37) Dixon, N. E.; Lawrance, G. A.; Lay, P. A.; Sargeson, A. M. *Inorg. Chem.* **1983**, *22*, 846–847.

(38) Dixon, N. E.; Lawrance, G. A.; Lay, P. A.; Sargeson, A. M. *Inorg. Chem.* **1984**, *23*, 2940–2947.

(39) Sullivan, B. P.; Meyer, T. J. *J. Chem. Soc., Chem. Commun.* **1984**, 403–405.

(40) Hino, J. K.; Della Ciana, L.; Dressick, W. J.; Sullivan, B. P. *Inorg. Chem.* **1992**, *31*, 1072–1080.

(41) Benoit, F.; Holmes, J. L.; Isaacs, N. S. *Org. Mass Spectrom.* **1969**, *2*, 591–601.

(42) Rose, M. E.; Johnstone, R. A. W. *Mass Spectrometry for Chemists and Biochemists*, 2nd ed.; Cambridge University Press: Cambridge, 1996.

(43) Biner, M.; Burgi, H. B.; Ludi, A.; Rohr, C. *J. Am. Chem. Soc.* **1992**, *114*, 5197–5203.

(44) Zhou, M.; Robertson, G. P.; Roovers, J. *Inorg. Chem.* **2005**, *44*, 8317–8325.

(45) Badaeva, E.; Albert, V. V.; Kilina, S.; Koposov, A.; Sykora, M.; Tretiak, S. *Phys. Chem. Chem. Phys.* **2010**, *12*, 8902.

(46) Brown, C. A.; Remar, G. J.; Musselman, R. L.; Solomon, E. I. *Inorg. Chem.* **1995**, *34*, 688–717.

(47) McCarthy, P. J.; Güdel, H. U. *Coord. Chem. Rev.* **1988**, *88*, 69–131.

(48) McClanahan, S. F.; Dallinger, R. F.; Holler, F. J.; Kincaid, J. R. *J. Am. Chem. Soc.* **1985**, *107*, 4853–4860.

(49) Drago, R. S. *Physical Methods for Chemists*; Saunders College Pub: Philadelphia, 1992.

(50) Caspar, J. V.; Meyer, T. J. *J. Am. Chem. Soc.* **1983**, *105*, 5583–5590.

(51) Kahn, O. *Molecular Magnetism*; VCH Publishers: New York, 1993.

(52) Crowley, C. E.; Clark, C. D.; Hoffman, M. Z. *Inorg. Chem.* **1998**, *37*, 5704–5706.

(53) Rehm, D.; Weller, A. *Isr. J. Chem.* **1970**, *8*, 259–271.

(54) Marcus, R. A. *Angew. Chem. Int. Ed.* **1993**, *32*, 1111–1121.

(55) Arnaut, L.; Formosinho, S.; Burrows, H. *Chemical Kinetics. From Molecular Structure to Chemical Reactivity.*; Elsevier: Amsterdam, 2007.

(56) Krumholz, P. *J. Am. Chem. Soc.* **1953**, *75*, 2163–2166.

(57) Nakamoto, K. *J. Phys. Chem.* **1960**, *64*, 1420–1425.

Chapter 4. "First Generation" of Donor-Acceptor Assemblies: Synthesis, Characterization and Challenges.

"Above all, don't fear difficult moments. The best comes from them." -Rita Levi-Montalcini.

4.1. Introduction

The results discussed in the previous chapter made us turn away from a tren-capped D-A assembly: not only all the attempts to synthesize such an assembly had failed, but the instability of the tren-capped core itself had become apparent. We then focused on a more desirable, albeit potentially more challenging, target: an assembly using a Tp-capped acceptor (Tp is hydrotris(pyrazolyl)borate). The remainder of this dissertation focuses on assemblies of that kind, using a variety of synthetic strategies.

Tp-capped diiron(III) cores are more prevalent in literature than tren-capped ones, likely due to their greater stability.[1] Additionally, tris-pyrazolyl borate as the capping ligand allows for protonation of the oxo bridge, which leads to an order-of-magnitude decrease in the strength of the coupling between the two metal centers.[2–4] As a consequence, these dimers are very attractive tunable platforms to study the effect of spin polarization on reactivity, as our group has previously shown.[2]

Oxo-bridged diiron(III) cores are prepared using "spontaneous self-assembly" reactions:[1,5,6] the Fe(III) source and the ligands are mixed in solution, and the product precipitates, leaving behind all or most of the impurities. The insolubility of the dimers in the reaction mixture drives the equilibrium towards their formation. While this is a straightforward synthetic strategy, it is not always clean or easy to adapt; based on the

attempts described in Chapter 3, we were looking for a synthetic route that left less to chance. The inspiration for our new approach came from a paper by the prolific Lippard Group: they showed that it is possible to cleanly exchange both carboxylate bridges simply by stirring a mixture of a diiron(III) core and the incoming bridge at room temperature.[7]

The simplicity of Lippard's approach was quite appealing; if we could swap one (or two) of the bridges by $[Ru(tmb)_2(bpyac)]^{2+}$, then we would have the assembly we were after. Based on previous work by our group,[8] we wished to only attach one Ru(II) donor per diiron(III) core. This was not a major concern, because we expected coulombic electrostatic repulsion to work on our favor, preventing the incorporation of a second Ru(II) unit.

In this chapter, the syntheses of two D-A assemblies using a carboxylate bridge swapping reaction are presented. Their photophysical properties are also discussed; as mentioned before, bimolecular quenching studies using the corresponding donor and acceptor are included as a stepping stone in the path to interpreting the new behavior of the new systems.

4.2. Experimental Section

General. All chemicals and solvents were obtained from Fisher Scientific or Sigma-Aldrich and used without purification unless otherwise stated. $RuCl_3 \cdot xH_2O$ was purchased from Strem Chemicals, and Sephadex LH-20 from GE Life Sciences. Anhydrous MeOH was purchased from Alfa Aesar and stored over 4Å molecular sieves.

^{1}H NMR spectra were collected on Agilent DDR2 500 MHz NMR spectrometers equipped with 7600AS 96-sample autosamplers. Mass spectra were obtained at the Michigan State University Mass Spectrometry and Metabolomics Core using a Waters G2-XS Qtof mass spectrometer interfaced to a Waters Aquity UPLC.

The syntheses of $Ru(DMSO)_4Cl_2$, 4,4',5,5'-tetramethyl-2,2'-bipyridine, 2,2'-bipyridine-4-acetic acid, $Ru(tmb)_2Cl_2$, $Ru(bpy)_2Cl_2$ and $[Ru(tmb)_2(bpyac)](PF_6)_2$ **(1)**, are described in Chapter 3 of this dissertation. Potassium hydrotris(1-pyrazolyl)borate (KTp),[9] $(Tp)_2Fe_2O(O_2CCH_3)_2$ and $(Tp)_2Fe_2O(O_2CCF_3)_2$[2] were prepared following literature procedures. $[(Tp)_2Fe_2(OH)(O_2CCH_3)_2](ClO_4)$ was graciously donated by Dr. Dong Guo.

4.2.1. Syntheses

(μ-oxo)bis(μ -2,2'-bipyridine-4-acetato)bis(tri-1-pyrazolylborato)diiron(III), $(Tp)_2Fe_2O(bpyac)_2$.[7] $(Tp)_2Fe_2O(O_2CCF_3)_2$ (0.17 g, 0.22 mmol) was dissolved in 75 mL of CH_2Cl_2; bpyac (0.1 g, 0.46 mmol) was dissolved in 8 mL of MeOH and added dropwise into the first solution. The reaction mixture was stirred at room temperature for 1.5 h, then the solvent was evaporated under reduced pressure and a dark red/orange residue was obtained. The solid was treated with CH_2Cl_2 and the soluble fraction was analyzed by mass spectroscopy. HRMS (ESI-TOF) m/z: $[M+H]^+$ Calcd for $C_{42}H_{39}N_{16}O_5B_2Fe_2$ 981.2190; Found 981.2217.

Bis(2,2'-bipyridine) mono(2,2'-bipyridine-4-acetic acid) ruthenium(II) hexafluorophopshpate, $[Ru(bpy)_2(bpyac)](PF_6)_2$ (3). In a nitrogen-filled glovebox, $Ru(bpy)_2Cl_2$ (0.20 g, 0.42 mmol) and $AgPF_6$ (0.32 g, 1.26 mmol) were dissolved in 60 mL of MeOH and stirred in the dark, at room temperature, for 3.5 h. The mixture was then filtered through a celite pad to remove AgCl, and it was added to a solution of bpyac (0.13 g, 0.62 mmol) in a small volume of MeOH. The solution was heated to 60°C under nitrogen, in the dark, overnight; after this time, the solvent was removed under reduced pressure, and the solid was purified with a neutral alumina plug, using neat MeCN to remove an orange band, and then switching to MeCN/KPF_6 (aq, sat) 5:1 to elute the product. The resulting solution was evaporated to dryness, the residue dissolved in MeCN and re-precipitated by addition of Et_2O. Yield: 0.14 g (36%, if pure). ^1H NMR (CD_3CN, 500 MHz) δ (ppm): 8.51 (m, 5H), 8.45 (d, *J* = 1.5 Hz, 1H), 8.06 (m, 5H), 7.75 (m, 5H), 7.60 (d, *J* = 5.8 Hz, 1H), 7.41 (m, 5H), 7.33 (dd, *J* = 5.8, 1.8 Hz, 1H), 7.30 (m, 4H), 7.21 (s, 1H), 3.63 (s, 2H). HRMS (ESI-TOF) m/z: $[M–2PF_6]^{2+}$ Calcd for $C_{32}H_{26}N_6O_2Ru$ 314.0585; Found 314.0550.

$[(Tp)_2Fe_2O(\mu\text{-}O_2CCH_3)(\mu\text{-bpyac})Ru(bpy)_2](PF_6)_2$ (4).[7] Solid $(Tp)_2Fe_2O(O_2CCH_3)_2$ (53 mg, 0.08 mmol) was added to a solution of **(3)** in CH_2Cl_2 (50 mL, 1.2 mM), and the mixture was stirred at room temperature for 5 days. The solvent was evaporated, and the crude was purified by size-exclusion chromatography on a glass column using acetone as the eluent. Complete isolation was not achieved, so no yield was calculated. HRMS (ESI-TOF) m/z: $[M–2PF_6]^{2+}$ Calcd for $C_{52}H_{48}N_{18}B_2O_5Ru$ 620.1008; Found 620.1099; $[M–PF_6]^+$ Calcd for $C_{52}H_{48}N_{18}B_2O_5RuPF_6$ 1385.1658; Found 1385.1770.

[(Tp)$_2$Fe$_2$O(μ-O$_2$CCH$_3$)(μ-bpyac)Ru(tmb)$_2$](PF$_6$)$_2$, (5).[7] Solid (Tp)$_2$Fe$_2$O(O$_2$CCH$_3$)$_2$ (9 mg, 0.01 mmol) was added to a solution of **(1)** in MeCN (25 mL, 0.5 mM), and the mixture was stirred at room temperature overnight. The solvent was evaporated, and the crude was purified by size-exclusion chromatography on a glass column using acetone as the eluent. Complete isolation was not achieved, so no yield was calculated. HRMS (ESI-TOF) m/z: [M–2PF$_6$]$^{2+}$ Calcd for $C_{60}H_{64}N_{18}B_2O_5Fe_2Ru$ 676.1635; Found 676.1631; [M–PF$_6$]$^{2+}$ Calcd for $C_{60}H_{64}N_{18}B_2O_5Fe_2RuPF_6$ 1497.2913; Found 1497.2860.

Methyl (2,2'-bipyridine)-4-acetate (bpyester).[10] bpyac (0.27 g, 1.26 mmol) was dissolved in 20 mL of freshly distilled MeOH and cooled down in an ice bath. SOCl$_2$ (15 mL) was added to the cold solution in small portions. Once the addition was completed, the ice bath was removed, and the reaction was put under nitrogen and stirred at room temperature overnight. Then, the mixture was refluxed for 3 h, still under nitrogen; after that time, it was allowed to cool down and the solvent and excess SOCl$_2$ were removed.[i] Slowly, NaHCO$_3$ (aqueous saturated solution) was added to the obtained solid until no bubbling was observed. The product was then extracted into CH$_2$Cl$_2$ until the organic layer tested negative with Fe(II). The combined organic extracts were dried with MgSO$_4$ and the solvent was evaporated, yielding a brown oil that was purified using a basic alumina plug, eluting with CH$_2$Cl$_2$. The product was obtained as a colorless oil. Yield: 0.16 g (56%). ^{1}H NMR (CDCl$_3$, 500 MHz) δ (ppm): 8.68 (ddd, *J* = 4.9, 1.8, 0.9 Hz, 1H), 8.64 (dd, *J* = 4.9, 0.5 Hz, 1H), 8.41 (dt, *J* = 7.9, 1.0 Hz, 1H), 8.33 (dd, *J* = 1.8, 0.7 Hz, 1H), 7.83 (td, *J* = 7.7, 1.8 Hz, 1H), 7.32 (ddd, *J* = 7.5, 4.8, 1.0 Hz, 1H), 7.28 (dd, *J* = 4.9, 1.8 Hz, 1H), 3.75

[i]Never use a rotovap to remove SOCl$_2$: it can hydrolyze to form acids that might corrode parts of the instrument.

(s, 2H), 3.74 (s, 3H). HRMS (ESI-TOF) m/z: $[M+H]^+$ Calcd for $C_{13}H_{13}N_2O_2$ 229.0977; Found 229.0991.

Bis(4,4',5,5'-tetramethyl-2,2-bipyridine) mono(methyl (2,2'-bipyridine)-4-acetate) ruthenium(II) hexafluorophosphate, $[Ru(tmb)_2(bpyester)](PF_6)_2$, (6). Under a nitrogen atmosphere, $Ru(tmb)_2Cl_2$ (0.11 g, 0.19 mmol) and $TlPF_6$ (0.16 g, 0.45 mmol) were dissolved in 40 mL of MeOH and stirred in the dark, at –10°C for 3 h. The mixture was filtered through a celite pad and added to a solution of bpyester (68 mg, 0.30 mmol) in a small volume of CH_2Cl_2. The reaction was stirred overnight at room temperature and in the darkness. The solvent was removed under reduced pressure and the solid was purified using a neutral alumina column, eluting with MeCN until the first band eluted, and then switching to 7:1 MeCN/KPF_6 (aqueous saturated solution) to elute the product. The combined fractions that had the product were evaporated to dryness, redissolved in a minimum amount of MeCN and precipitated by addition of Et_2O. ^1H NMR (CD_3CN, 500 MHz) δ (ppm): 8.45 (d, *J* = 8.1 Hz, 1H), 8.38 (d, *J* = 1.0 Hz, 1H), 8.24 (m, 4H), 7.99 (td, *J* = 8.0, 1.5 Hz, 1H), 7.72 (d, *J* = 5.4 Hz, 1H), 7.58 (d, *J* = 5.9 Hz, 1H), 7.36 (ddd, *J* = 7.6, 5.8, 1.1 Hz, 1H), 7.32 (m, 4H), 7.27 (s, 1H), 3.67 (s, 2H), 2.42 (s, 3H).

4.2.2. Physical Characterization

X-ray structure determination. Single-crystal X-ray diffraction data were acquired, and the structures were solved, by Dr. Richard Staples at the X-ray Facility of Michigan State University.

UV-visible absorption spectroscopy. All spectra were collected using spectrophotometric grade solvents, in 1 cm quartz cuvettes. The spectra were acquired using a Cary 50 spectrophotometer.

Steady-State Emission and Time-Resolved Emission and Absorption. All samples were prepared in an argon-filled glovebox, using spectrophotometric acetonitrile that was freeze-pump-thaw degassed prior to use. Air-free cells for these experiments were made in-house by attaching Kontes valves to 1 cm quartz cuvettes (FireflySci).

For both steady-state and time-resolved emission spectroscopy, the absorbance of the sample at the maximum of the MCLT band was kept between 0.1 and 0.2. This was not the case for Stern-Volmer quenching studies (*vide infra*).

Steady-state emission spectra were collected using a Horiba Fluorolog-3 fluorimeter and corrected for instrumental response using a NIST standard of spectral irradiance (Optronic Laboratories, Inc., OL220 M tungsten quartz lamp). To attenuate the inner-filter effect, spectra were further corrected as shown in eq 4.1,[11] where $Abs_{\lambda,exc}$ is the absorbance of the sample at the excitation wavelength, and $Abs_{\lambda,em}$ is the absorbance of the sample at each wavelength of the emission spectrum.

$$I_{corr} = I_{obs} \times 10^{\left(\frac{Abs_{\lambda,exc}+Abs_{\lambda,em}}{2}\right)} \qquad \textbf{(4.1)}$$

Relative quantum yields of emission (Φ_r) were calculated using $[Ru(bpy)_3](PF_6)_2$ in degassed acetonitrile as a standard (Φ = 0.095).[12] Emission quantum yields were calculated using eq 4.2, as described in Chapter 3.

$$\Phi_x = \Phi_{std}\left(\frac{I_x/A_x}{I_{std}/A_{std}}\right)\left(\frac{\eta_x}{\eta_{std}}\right)^2 \qquad \textbf{(4.2)}$$

For ease of comparing emission spectra, in many instances the corrected intensity (from eq 4.1) is further divided by the absorbance of the sample at the excitation wavelength, analogously to what is done in (4.2); the last term in this equation is ignored because all the spectra presented in this chapter were taken in acetonitrile.

Nanosecond time-resolved emission experiments were performed using an Nd:YAG laser spectrometer that has been described previously,[13,14] upgraded using an Opotek Vibrant 355 LD tunable pulsed laser system which generates nominally 5 ns laser pulses. Excitation energies were in the range of 1-3 mJ per pulse. All data were checked for linearity with respect to pump power. The data were fit to a single exponential decay to extract the observed rate constant (k_{obs}).

4.2.3. Bimolecular Quenching Studies

Samples for Stern-Volmer studies were prepared in an argon-filled glovebox, using spectrophotometric acetonitrile that was freeze-pump-thaw degassed prior to use. A variable volume of a stock solution of $[(Tp)_2Fe_2(OH)(\mu\text{-}O_2CCH_3)_2](ClO_4)$ (~3 mM) was combined with 1.00 mL of a stock solution of **(1)** (with an absorbance ~0.5 at the excitation wavelength) and the mixture was taken to a final volume of 5.00 mL. All samples contained $TBAPF_6$ (0.075 M), added as a supporting electrolyte.[15,16]

4.2.4. Geometry Optimizations[ii]

Calculations were performed using Gaussian 03.[17] Geometry optimizations were done on the ground state using a spin unrestricted formalism at the B3LYP/LANL2DZ level of theory.[18] No symmetry restrictions were placed on the geometry optimizations.

The input file was prepared using the x-ray crystal structures of $(Tp)_2Fe_2O(O_2CCH_3)_2$ (as reported by Weldon et al.)[2] and of $[Ru(tmb)_2(bpyac)]^{2+}$, shown in Chapter 3.

4.3. Results and Discussion

4.3.1. Syntheses

Our goal was to prepare a Tp-capped D-A assembly, using $[Ru(tmb)_2(bpyac)]^{2+}$ as the donor, as described in Chapter 3. Following the work of Armstrong and Lippard,[7] we explored the possibility of exchanging the carboxylate bridges on an already prepared diiron(III) oxo-bridged core. Initially, the starting material used was $(Tp)_2Fe_2O(O_2CCF_3)_2$; of all the carboxylate bridges that Weldon et al. had utilized,[2] trifluoroacetate was the weakest base and the least nucleophilic, so it was expected to be the easiest bridge to replace. To test the feasibility of this strategy, bpyac was reacted with $(Tp)_2Fe_2O(O_2CCF_3)_2$, following the published procedure,[7] as shown in Figure 4.1. The crude reaction product was analyzed by ESI-MS, and the expected product was observed, which was taken as confirmation that this was a sound route to pursue. Additionally, attempts to prepare $(Tp)_2Fe_2O(\mu\text{–bpyac})_2$ "from scratch", following Weldon's route[2]

[ii]Jon Yarranton's help with all things Gaussian is gratefully acknowledged.

yielded pink solids and solutions, indicating the formation of Fe(II) polypyridyl compounds (analogously to what was described in the previous chapter). The bridge exchange route not only allowed us to obtain the desired product, but also seemed to preserve the diiron(III) core, preventing the coordination of bpyac through its N atoms.

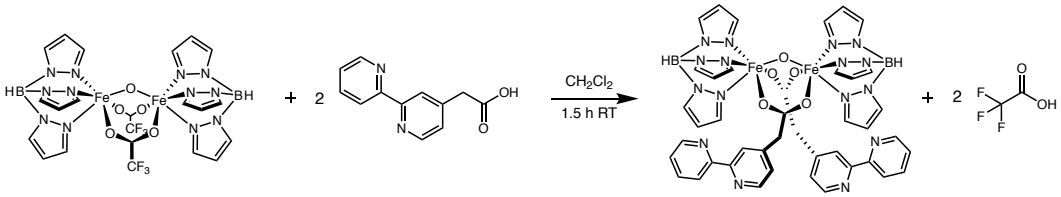
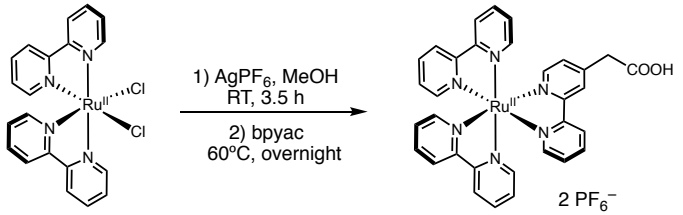


Figure 4.1. Bridge-exchange reaction to prepare $(Tp)_2Fe_2O(\mu\text{–}bpyac)_2$.

Perusing the literature, several examples of carboxylate bridge exchange were found; all of them used the conjugate acid of the incoming bridge instead of the deprotonated form.[19–21] Moreover, in his extensive review of diiron complexes, Kurtz mentions that a proton donor is necessary for such bridge exchanges to proceed, because the displaced bridge leaves as the protonated acid.[1] Consequently, a stronger conjugated base appeared to be a better option for the leaving carboxylate, because it will be easier to protonate. Thus, $(Tp)_2Fe_2O(O_2CCH_3)_2$ was instead used as the starting material from that point on.

Considering the low yield reported for the synthesis of $[Ru(tmb)_2(bpyac)](PF_6)_2$ **(1)** in the previous chapter, it was decided to use $[Ru(bpy)_2(bpyac)](PF_6)_2$ **(3)** instead; this compound was expected to be easier to prepare (its synthesis is shown in Figure 4.2), and would be used to find the right reaction conditions for the bridge exchange and study the feasibility of this approach. The new donor was prepared using the strategies outlined in

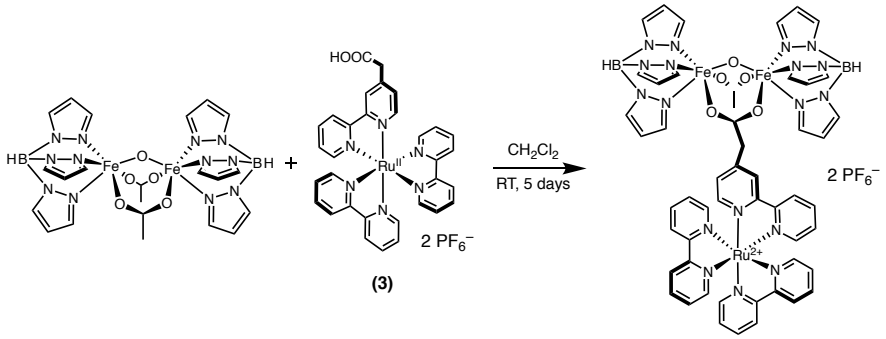
Chapter 3, in a two-step reaction. Its marked tendency to decarboxylate is discussed in section 4.3.2.



[Ru(bpy)$_2$(bpyac)](PF$_6$)$_2$, **(3)**

Figure 4.2. Synthesis of compound **(3)**, [Ru(bpy)$_2$(bpyac)](PF$_6$)$_2$.

The bridge exchange using (Tp)$_2$Fe$_2$O(μ-O$_2$CCH$_3$)$_2$ and **(3)** is shown in Figure 4.3. The reaction conditions were adapted from Lippard's work,[7] but longer times were necessary for the desired product to form (after 24 h stirring at room temperature, no assembly was detected in ESI-MS): after 5 days its molecular ion was observed (see Figure 4.4).



[(Tp)$_2$Fe$_2$O(μ-O$_2$CCH$_3$)(μ-bpyac)Ru(bpy)$_2$](PF$_6$)$_2$, **(4)**

Figure 4.3. Bridge exchange reaction to synthesize [(Tp)$_2$Fe$_2$O(μ-O$_2$CCH$_3$)(μ-bpyac)Ru(bpy)$_2$](PF$_6$)$_2$ **(4)**.

The lability of the carboxylate bridges becomes quite evident in mass spectroscopy experiments. In Figure 4.4, the ESI-MS data for **(4)** are displayed; the expected peak for [(Tp)$_2$Fe$_2$O(μ-O$_2$CCH$_3$)(μ-bpyac)Ru(bpy)$_2$](PF$_6$)$^+$ is observed (m/z = 1385.1770), along

with one that matches $[(Tp)_2Fe_2O(\mu\text{-}O_2CH)(\mu\text{-}bpyac)Ru(bpy)_2](PF_6)^+$ (m/z = 1371.1606). This observation might be baffling at first, but it can be rationalized considering that one of the main solvent systems used in the ESI-TOF instrument is a formic acid/formate buffer solution. If the column is not properly rinsed after using this buffer, some formic acid will linger and can readily react with any diiron(III) cores that are introduced in the instrument. In one of their early reports, Lippard and coworkers prepared and characterized $(Tp)_2Fe_2O(\mu\text{-}O_2CH)_2$, which further supports this hypothesis.[5] Analogous results were obtained for **(5)** (see Figure 4.22, appendix) and by other group members.[22] Unfortunately, it was not always possible to remove all the formic acid present in the instrument.

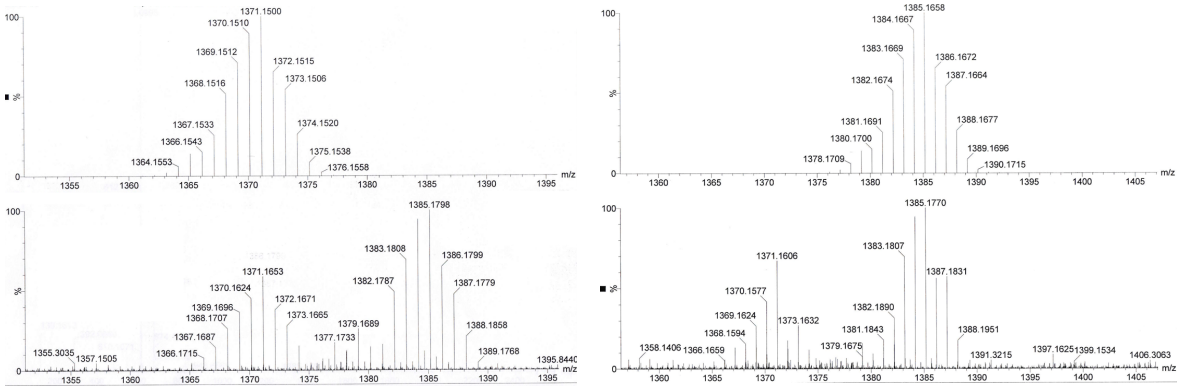


Figure 4.4. ESI-MS of **(4)**. Top left: predicted isotope pattern for $[M–PF_6]^+$ for a formate-bridged assembly ($C_{51}H_{46}N_{18}O_5B_2Fe_2RuPF_6$). Top right: predicted pattern for $[M–PF_6]^+$ ($C_{52}H_{48}N_{18}O_5B_2Fe_2RuPF_6$). Bottom: Experimental results.

It is worth pointing out that, while it was possible to replace both carboxylate bridges when using bpyac (and the same was observed by Lippard and coworkers[7]), no evidence of the presence of two Ru(II) units was observed for any of the D-A assemblies discussed in this chapter. Considering the geometry of the system, it should have been possible to append two Ru(II) donors per diiron(III) core: Figure 4.5 shows the result of a

geometry optimization for such a compound. The incorporation of only one Ru(II) polypyridyl, then, may be explained based on electrostatic repulsion: the product of the reaction shown in Figure 4.1 has no net charge, whereas **(4)** (see Figure 4.3) and **(5)** are cationic species. The incorporation of a second Ru(II) donor is likely unfavorable, especially in the absence of supporting electrolyte (see Chapter 3).

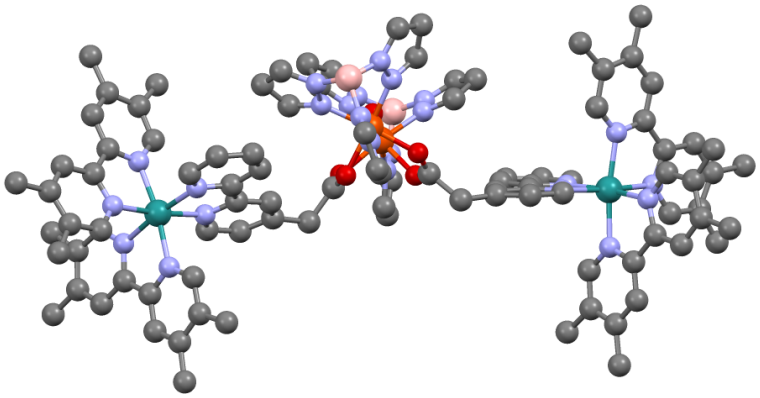


Figure 4.5. Geometry optimization of a possible assembly incorporating two Ru(II) donors. See text for details.

Several purification methods were tested to isolate the D-A assembly, most of them column chromatography options (recrystallization attempts were unsuccessful, yielding only starting materials). Unfortunately, diferric cores do not withstand most common stationary phases, such as silica gel or alumina; even using RP-18 silica gel led to the formation of $[Fe(Tp)_2]^+$, the main decomposition product for these compounds.[1] Alternatively, size-exclusion chromatography (SEC) yielded more promising results: indeed, other bimetallic carboxylate-bridged compounds have been purified in this fashion.[21,23]

In a size-exclusion (also known as gel filtration or gel permeation) chromatography column, molecules are separated not only based on their weight, but

also their shape. In layman terms, SEC can be thought of as a "molecular colander": molecules do not interact with the stationary phase as they do on silica gel, but instead they traverse different paths as they pass through the SEC medium.[24] Typically, the larger/heavier molecules have access to a smaller fraction of the pores of the Sephadex matrix, and so they elute before other compounds. As their size/weight decrease, the molecules can enter more of those pores, and as a result they are retained in the column for longer (i.e., they elute more slowly). Finally, very small species (inorganic salts such as NaCl, for example) have full access to the pores and take the longest time to leave the column; as a result, this technique is commonly used to desalt solutions.[24]

Both the starting materials and the product are soluble and stable in acetonitrile, but this is not a good solvent to use with Sephadex LH-20, because it does not properly swell the material, causing very poor separation.[24] Methanol was used in Chapter 2 with good results for bpyac, but the limited solubility of the compounds of interest in this solvent prevented its use. Finally, acetone was found to be a suitable option: it dissolved all the compounds of interest and provided sufficient separation. Great care was taken not to overload the SEC column, but even then, the sample ran as one long band. Consequently, numerous fractions of 5 mL or less were collected each time, and analyzed by UV-vis spectroscopy and ESI-MS. Figure 4.6 contains electronic absorption spectra representative of the different fractions obtained from a SEC column. To rationalize the different spectra obtained, the expected spectrum of the assembly was modelled as the sum of the spectra for **(3)** and $(Tp)_2Fe_2O(\mu\text{-}O_2CCH_3)_2$. The electronic coupling between

donor and acceptor in the assembly was expected to be fairly weak, which justified this approximation.

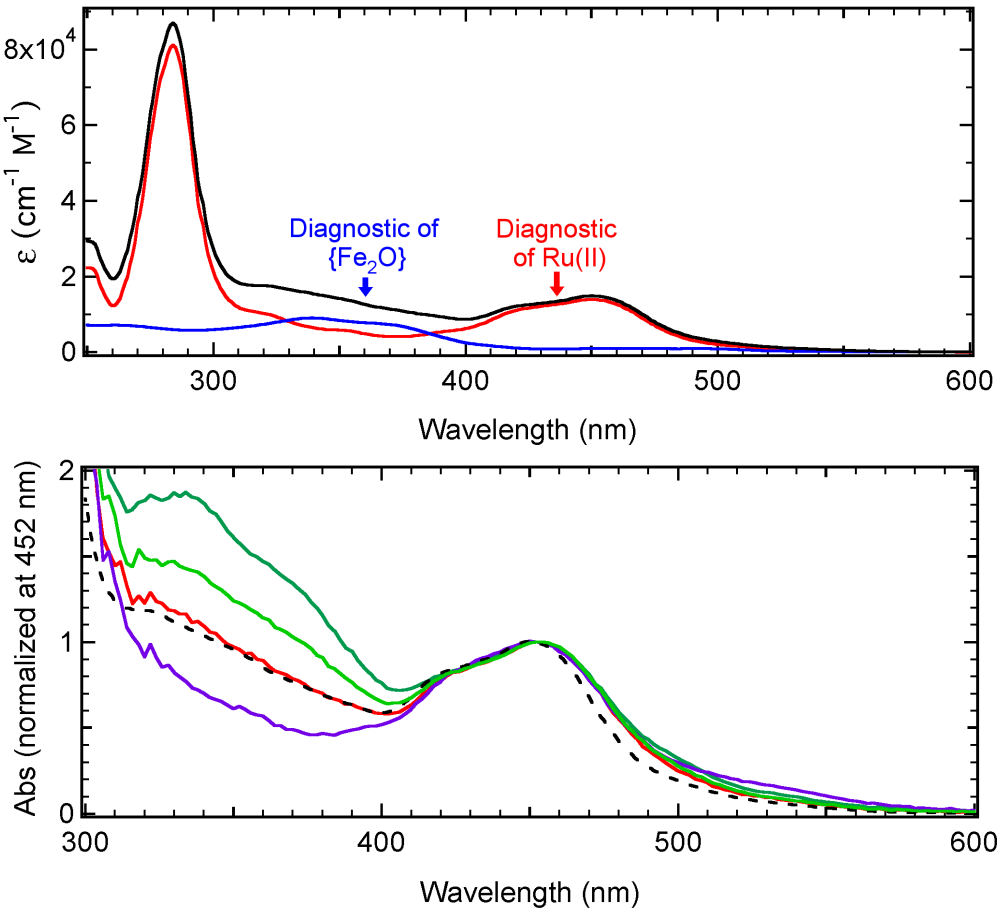


Figure 4.6. Top: Simulated electronic absorption spectrum of **(4) (**black trace), generated by adding the spectra of **(3)** (red trace) and $(Tp)_2Fe_2O(O_2CCH_3)_2$ (blue trace). Bottom: Representative electronic absorption spectra for SEC fractions in the synthesis of **(4).** The dashed black trace is the simulated spectrum of the assembly; the red trace corresponds to early column fractions; the green traces, to intermediate ones. Later fractions are shown in purple.

In the present case, the D-A assembly was the largest species present, and it eluted in the first place. The red trace in Figure 4.6 (bottom) is representative of what earlier fractions in a SEC column looked like: it closely matches the spectrum modelled for the assembly. All fractions with similar spectra were combined; ESI-MS results showed the

expected isotope pattern for **(4)**. Unfortunately, no fraction contained only the D-A assembly; this was likely due to decomposition of the sample, although it is unclear whether such decomposition took place during SEC or afterwards.

Intermediate fractions (the green traces in Figure 4.6) show increasing amounts of $(Tp)_2Fe_2O(\mu\text{-}O_2CCH_3)_2$, while the later fractions seem to only contain **(3)**[iii] (these results matched what was observed using ESI-MS). If the separation was based solely on molecular weight, the Ru(II) starting material would be expected to leave the column before the diiron(III) core (M = 917.60 vs. 671.80). However, two factors must be taken into account: a) molecular shape, and b) the decarboxylation of **(3)**. Regarding their shape, **(3)** is a "rounder" molecule, while $(Tp)_2Fe_2O(\mu\text{-}O_2CCH_3)_2$ is more elongated; despite their sizes being similar, the more elongated molecule may not be able to access as many of the matrix's pores and elute earlier. This argument becomes much more plausible when the tendency of bpyac to lose CO_2 is considered (*vide infra*): if **(3)** decarboxylated while in the column to form $[Ru(bpy)_2(mmb)]^{2+}$ (mmb is 4-methyl-2,2'-bipyridine), its diameter would be reduced by ca. 0.8 Å, making it rounder and smaller than the diferric core, and thus more likely to elute in the last place. Ball-and-stick pictures showing the shapes of all three species can be seen in Figure 4.7.

[iii]Actually, a mixture of $[Ru(bpy)_2(bpyac)]^{2+}$ and predominantly $[Ru(bpy)_2(mmb)]^{2+}$ was obtained, although this only became apparent in the ESI-MS data.

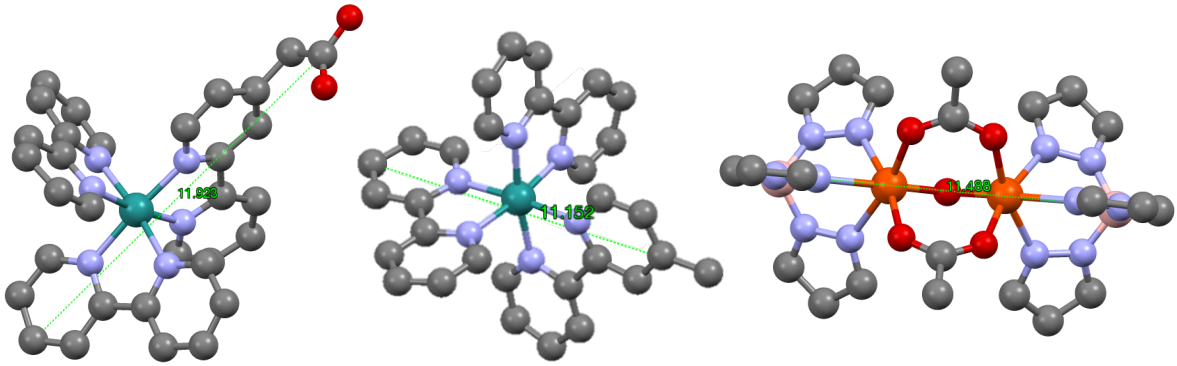


Figure 4.7. Ball-and-stick renderings of $[Ru(bpy)_2(bpyac)]^{2+}$ (left), $[Ru(bpy)_2(mmb)]^{2+}$ (center; these two are based on the crystal structure of **(1)**) and $(Tp)_2Fe_2O(\mu\text{-}O_2CCH_3)_2$ (right, from its crystal structure). Shown in green are the longest atom-to-atom distances in each molecule (in Å).

Unfortunately, **(4)** was unstable and dissociated readily in solution; this was probably worsened by the decarboxylation of **(3)** in a subsequent step. As a result, it was impossible to isolate **(4)**, and its characterization became challenging. We turned our attention back to $[Ru(tmb)_2(bpyac)](PF_6)_2$, **(1)**, as the donor, which was expected to be more robust. For the bridge exchange reaction, acetonitrile was used instead of dichloromethane, which lead to shorter reaction times. This is most likely due to its larger dielectric constant (37.5 for MeCN vs. 9.1 for CH_2Cl_2):[25] its ability to shield electric charges from each other lessened the electrostatic repulsions between the intervening species, speeding up the reaction.

Initially, the tmb-based assembly seemed to be a well-behaved system. However, it was found to also be quite unstable, noticeably decomposing after 24 h in solution, as described in section 4.3.3.

Attempts to prepare a hydroxo-bridged D-A assembly, either by bridge exchange or protonation of an oxo-bridge assembly were unsuccessful. In the first case, the only signals observed in ESI-MS corresponded to $[Fe(Tp)_2]^+$ or the hydroxo-bridged staring

material. Alternatively, when **(4)** or **(5)** were treated with HOTf, the solutions lost their orange coloration, and usually a red precipitate was formed, which was found to contain mostly $[Fe(Tp)_2]^+$. While it was expected that the synthesis of a hydroxo-bridged assembly would be more challenging, we had not envisioned as many obstacles as we encountered. This approach led to a new road block; unexpectedly, Stern-Volmer studies suggested new possibilities to study these systems, as described in section 4.3.5.

To understand the photophysics of the tmb-based assembly, the aforementioned bimolecular quenching experiments were performed using both **(1)** and $[Ru(tmb)_2(bpyester)](PF_6)_2$ **(6)**. The bpyester ligand had not been reported before; perhaps because its synthesis was less straightforward than anticipated: Fisher esterification conditions,[26,27] using anhydrous MeOH, afforded very small amounts of the ester, with the main product being mmb as a result of the loss of CO_2 at reflux temperatures.[28] Alternatively, a literature procedure for methyl (4'-methyl-2,2'-bipyridine)-4-acetate[29] employed methyl chloroformate as the nucleophile in a reaction analogous to that used to make bpyac; the yield of this reaction was low as well, with ~15% of the starting material recovered during the purification steps. Finally, reaction of bpyac with $SOCl_2$ and MeOH (Figure 4.8)[10] afforded the desired pure product in good yield, with no decarboxylated side products.

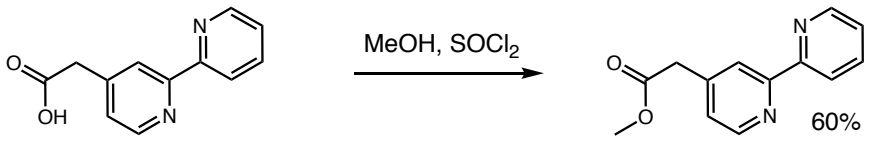


Figure 4.8. Synthesis of bpyester.

With the ligand in hand, the same strategy used to prepare **(1)** was used for **(6)**, as shown in Figure 4.9.

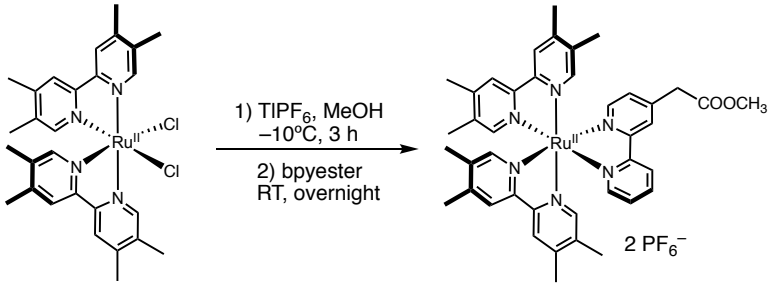


Figure 4.9. Synthesis of compound **(6),** $[Ru(tmb)_2(bpyester)](PF_6)_2$.

4.3.2. The Instability of $[RuL_2(bpyac)]^{2+}$ Towards Decarboxylation

In Chapter 3, the tendency of bpyac to lose CO_2 was briefly mentioned. Della Ciana et al. reported such a reaction for 4'-methyl-2,2'-bipyridine-4-acetic acid upon heating;[28] however, when working with **(1)** this instability did not seem to be a problem: obtaining good quality crystals of the intact product was taken as a good sign, even though decarboxylation was observed when using ESI-MS (this phenomenon has been reported before[30,31]). The synthesis of **(1)** was performed at or below room temperature, which prevented the decomposition of bpyac to a certain extent as well, even though this was not the main consideration when choosing the reaction conditions.

As previously mentioned, the choice of tmb as the ancillary ligand was driven by the need to localize the ^{3}MLCT of the donor as close to the acceptor as possible; the disadvantage of this choice was that **(1)** was obtained in very low yield, although this was not entirely unexpected. At the time, it was assumed that the only side product was $[Ru(tmb)_3]^{2+}$, but we now know that $[Ru(tmb)_2(mmb)]^{2+}$ probably formed during the reaction as well. Separating these compounds from the desired product was easily done

using an alumina plug, since both of them eluted with acetonitrile, while **(1)** required KNO_3 as well. Indeed, freshly obtained fractions from such a separation showed **(1)** as the only species on ESI-MS.

As mentioned above, considering the disadvantages of working with tmb, it was decided to use bpy instead, at least to optimize the bridge exchange conditions (using the same rationale discussed in Chapter 3). More product was obtained in the synthesis of **(3)** (36% yield vs. 10% yield), but the latter appeared to be even more prone to decomposing than **(1)**, with the ESI-MS signals for $[Ru(bpy)_2(mmb)]^{2+}$ being much more intense or even the only ones present in some cases, as seen in Figure 4.10. This instability was a bigger problem when studying the donor on its own, because in the bridge swapping reactions, only intact **(3)** could react, and the largest part of the remaining Ru(II) species, decarboxylated or not, were removed using SEC. It is likely, however, that the instability of **(3)** made **(4)**, in turn, even less stable; that, together with the lack of success when trying to protonate the oxo bridge in **(4)** made the bpy-based assembly quite unappealing, despite its interesting photophysics (discussed in the following section). In contrast, going back to tmb as the ancillary ligand was expected to a) increase the stability of the donor, and consequently, of the assembly, and b) favor the protonation of the oxo bridge, because the assembly overall would be more electron-rich.

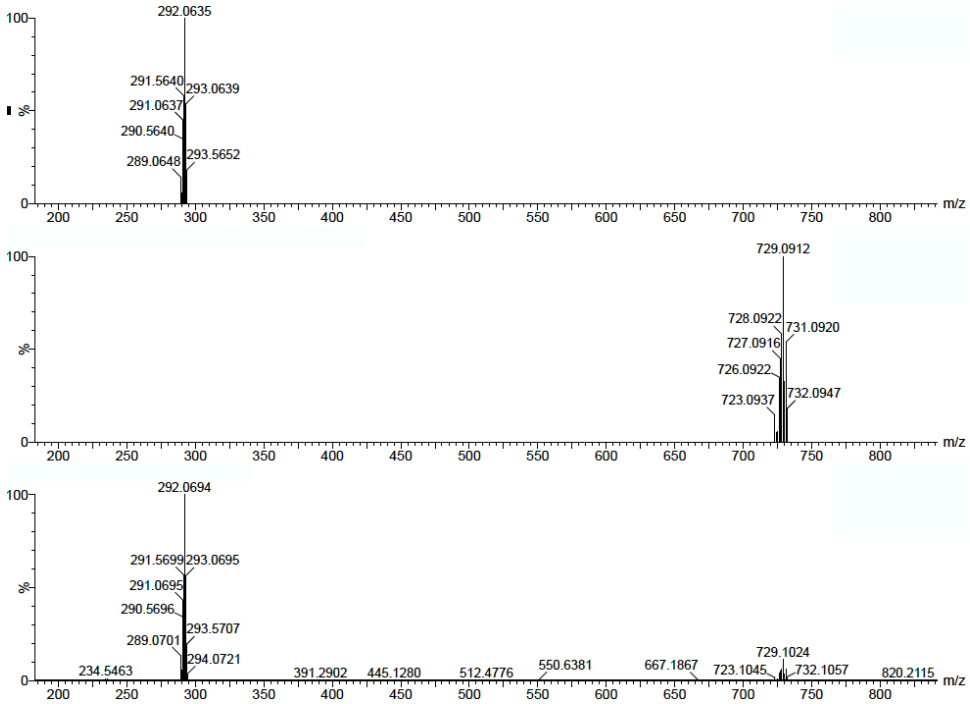


Figure 4.10. ESI-MS of "**(3)**". Top: predicted isotope pattern for $[M\text{-}CO_2\text{–}2PF_6]^{2+}$ ($[Ru(bpy)_2(mmb)]^{2+}$). Middle: isotope pattern for $[M\text{-}CO_2\text{–}PF_6]^{+}$ ($[Ru(bpy)_2(mmb)](PF_6)^{+}$). Bottom: spectrum obtained.

Unfortunately, while the photophysics of **(5)** were intriguing, its observed instability, as discussed in section 4.3.4, suggested that other D-A systems would be better platforms for our studies. On the other hand, the bimolecular quenching results using **(1)** and **(6)** (section 4.3.5) provided us with a slightly different avenue to explore, namely the in-situ bridge swapping. This strategy required the synthesis of pure **(1)** and **(6)**, which was rendered nearly impossible by the instability of both bpyac and bpyester. It was surprising to find that bpyester could decarboxylate as well: the crystals obtained from ether diffusion into an acetonitrile solution of **(6)** yielded $[Ru(tmb)_2(mmb)](PF_6)_2$ instead of the expected compound (Figure 4.11). The same decarboxylation phenomenon has been reported for diethyl 2,2'-bipyridine-4,4'-dicarboxylate, albeit under harsher conditions: this ligand can lose CO_2 in a microwave reactor.[32] Considering that any

intermediates in the decarboxylation of **(1)** and **(6)** are probably aromatic (whereas for carboxylate groups directly attached to a pyridine ring this may not be true), it would be expected for bpyester to decarboxylate more readily than diethyl 2,2'-bipyridine-4,4'-dicarboxylate.

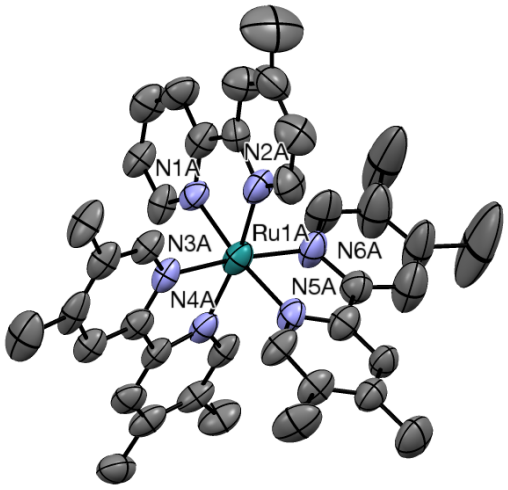


Figure 4.11. ORTEP drawing of $[Ru(tmb)_2(mmb)]^{2+}$ obtained from single-crystal X-ray structure determinations. Atoms are represented as 50% probability thermal ellipsoids. Anions are omitted for clarity. All bond lengths and angles are compiled in the appendix to this chapter.

Up to this point, we were under the impression that **(3)** was very unstable, but **(1)** was not. Observing that even the ester analog could decompose in solution at room temperature brought our assumptions into question. HPLC-MS provided further evidence of the fragility of **(1)**, since it was possible to separate it from $[Ru(tmb)_2(mmb)]^{2+}$ present in a sample of "**(1)**" using a C18 HPLC column and a water/acetonitrile gradient (Figure 4.12); this would have not been possible if the decarboxylation was taking place in the QTOF trap. These results confirmed that the decarboxylation process was more pervasive than originally believed.

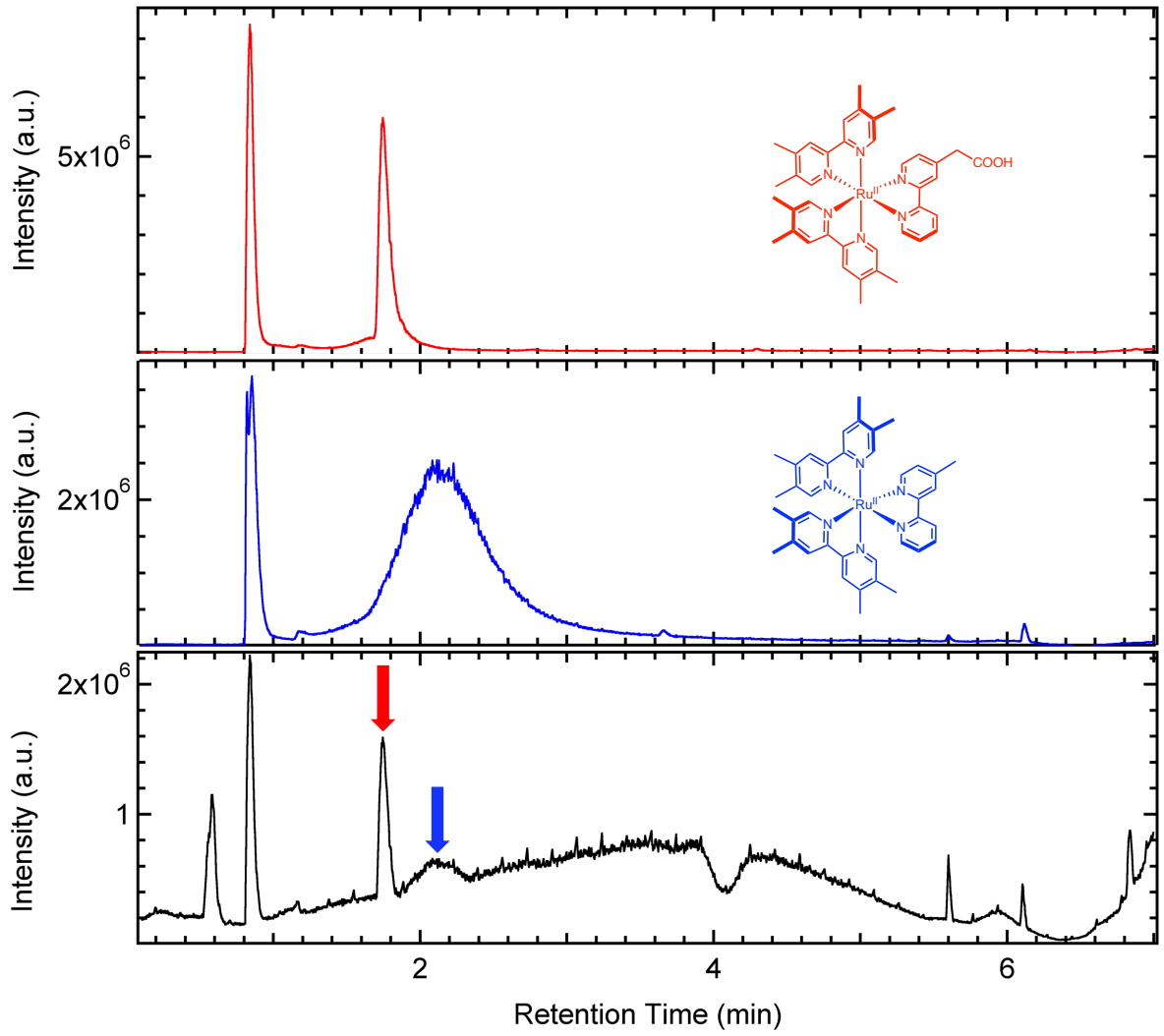


Figure 4.12. HPLC-MS results for **(1)**. Bottom: full elution profile for the sample; the arrows indicate the relevant peaks. Center: elution profile for $[Ru(tmb)_2(mmb)]^{2+}$, extracted from the full profile. Top: elution profile for $[Ru(tmb)_2(bpyac)]^{2+}$, extracted from the full profile. The peak at ~0.8 min corresponds to a portion of the sample that did not interact with the HPLC column material and was eluted with the solvent front. The identity of other peaks is unclear.

The chromatogram shown in Figure 4.12 is informative, but rather coarse, because this technique was not optimized for this system: initially, the possibility of using preparative scale HPLC to purify **(1)** was considered, but this idea was abandoned due to the instability of this compound in solution.

The systems described in this chapter taught us much about the feasibility of bridge swapping as a means to covalently attach the donor and the acceptor. Additionally, the photophysics of the resulting assemblies seemed worth investigating. However, the instability of the donors (and as a consequence, of the corresponding assemblies) turned out to be a significant obstacle. The need to use more robust molecules steered this work in a slightly different direction, as will be described in Chapter 5.

4.3.3. Photophysics of $[(Tp)_2Fe_2O(\mu\text{-}O_2CCH_3)(\mu\text{-}bpyac)Ru(bpy)_2](PF_6)_2$

The photophysical properties of the D-A assembly **(4)** were studied using time-resolved and steady-state emission spectroscopy and were compared to the unquenched donor **(3)** and to bimolecular D-A mixtures (using **(3)** and $(Tp)_2Fe_2O(\mu\text{-}O_2CCH_3)_2$). The time-resolved emission results are compiled in Figure 4.28 (appendix) and in Table 4.1: the lifetime for the 100:1 A/D sample is much shorter than for the other two, whereas the values for the free donor and **(4)** are within experimental error of each other (~4%), which suggests that there is no quenching taking place in the D-A assembly compared to the free donor. The pronounced quenching in the bimolecular sample is not surprising, considering the results discussed in Chapter 3.

Table 4.1. Time-resolved and steady-state emission results for samples used in the study of **(4)**.

	λ_{em} (nm)	Φ	τ (ns)
$[Ru(bpy)_2(bpyac)](PF_6)_2$, **(3)**[a]	620	0.090[b]	870
Assembly **(4)**	655	0.042[b]	910
100:1 A/D sample[c]	620	N/A	400

[a]Labeled as the bpyac compound despite being a mixture of the intact and decarboxylated complexes. [b]Determined as a relative value, using $[Ru(bpy)_3](PF_6)_2$ as the standard. [c]0.1 M $TBAPF_6$ was used as the supporting electrolyte. See text for details.

In contrast, the steady-state emission results are quite different from one sample to the other, as shown in Figure 4.13 and Table 4.1. The emission intensity of the assembly is roughly 50% lower than that of **(3)**; moreover, the emission maximum in the case of the assembly is red shifted by ca. 30 nm with respect to the unquenched donor, while for a mixture of the donor and acceptor, no such shift is seen. These data demand careful consideration: in the first place, the shift of the emission maximum for **(4)** compared to **(3)** indicates that the energetics of the luminophore have changed. Such a change could be explained in two ways: a) the identity of the emissive species could have drastically changed (for example, the ^{3}MLCT excited stated could be localized on a different ligand than in **(3)**), or b) the emissive species could be very similar to that of **(3)**, but its energetics have been tweaked. In either case, it seems clear that the change in the emission spectrum must have been brought about by the formation of a D-A assembly.

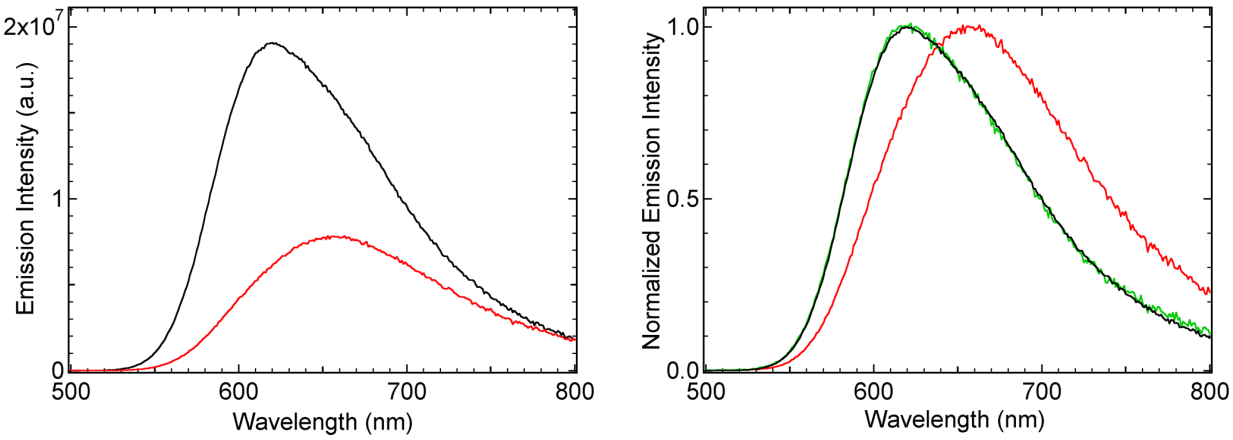


Figure 4.13. Steady-state emission spectra for **(3)** (black trace), **(4)** (red trace) and a 100:1 mixture of $(Tp)_2Fe_2O(\mu\text{-}O_2CCH_3)_2$ and **(3)** (green trace). Left: the emission intensity at each point was divided by the absorbance of that sample at the excitation wavelength. Right: all traces normalized to their emission maximum.

The SSEm spectra of **(3)** and $[Ru(bpy)_3]^{2+}$ (see Figure 2.8) are almost identical, which suggests that the ^{3}MLCT excited state is located on a bpy in either case (or that, at least, the reduction potential of bpy and bpyac are very similar, and the excited state could be localized on either). This discussion is, of course, muddled by the fact that what we call **(3)** is in reality a mixture of **(3)** and $[Ru(bpy)_2(mmb)]^{2+}$. When the assembly **(4)** is formed, part of the electron density of bpyac is shifted towards the Fe(III) centers, making this ligand's reduction potential more positive, and therefore more likely for the ^{3}MLCT excited state to be localized there. So, as mentioned above, there are two possible scenarios: a) the excited state (ES) in **(3)** was bpy-based, and now in **(4)** it is on the bridging ligand, which completely changes the identity of the luminophore, or b) the ES is localized on bpyac in either case, but the coordination to the diferric core has lowered the reduction potential of the ligand, which in turn lowers the energy of the excited state. Both these possibilities satisfactorily explain the shift in the emission maximum. Based on the results for **(5)** (*vide infra*), a change in the luminophore from **(3)** to **(4)** seems more

plausible. Regardless, as shown in Figure 4.13 (right side), the emission spectrum of the assembly is not only red-shifted, but it is also broader, so the presence of free donor in addition to the assembly cannot be dismissed.

On the other hand, the decreased emission quantum yield for the assembly seems to contradict the lack of quenching observed with time-resolved emission spectroscopy. This apparent contradiction may be ascribed to static quenching (see Chapter 2) or explained considering the likely composition of the sample: as was mentioned before, the assembly seems to decompose, either during or after the SEC purification step. If that is the case, then there is a non-negligible amount of unbound Ru(II) in any sample.[iv] The emission intensity of any free Ru(II) species will be much more intense than that of the assembly, and it will therefore be the main contribution to the signal recorded in either time-resolved or steady-state emission experiments. In the first case, this will lead to the observed lifetime being the same as that of **(3)**; in the second case, the radiative quantum yield will decrease because some of the Ru(II) in the sample is quenched.

In a way, invoking the notion of "static quenching" to explain this system's behavior is simplifying the problem. The data suggest that the donor and the acceptor are associated in solution, which agrees with the definition of static quenching as presented in Chapter 2. However, since the presence of unquenched donor in the sample cannot be ruled out, there seem to be many contributions to the observed photophysics. Additionally, as was mentioned in Chapter 2, what seems static at a given timescale may be dynamic when the appropriate time resolution is used. Due to the instability of these

[iv]This could be **(3)** or the decarboxylation product, $[Ru(bpy)_2(mmb)]^{2+}$; the photophysics of these two compounds are likely to be hard to distinguish from one another.

assemblies (*vide infra*), the study of their photophysics at shorter timescales was not pursued. This idea is revisited in Chapter 5, using more robust systems than those described here.

4.3.4. Photophysics of $[(Tp)_2Fe_2O(\mu\text{-}O_2CCH_3)(\mu\text{-}bpyac)Ru(tmb)_2](PF_6)_2$

Analogously to the study of **(4)**, the photophysics of **(5)** were compared to those of the unquenched donor **(1)** and also to a bimolecular D-A mixture. In this case, none of the solutions had supporting electrolyte, to ensure that any quenching observed was not facilitated by its presence (i.e., to ensure only intramolecular quenching was studied). Much as before, the time-resolved emission studies (see Figure 4.29 and Table 4.2) showed no dynamic quenching for the assembly compared to the free donor. Steady-state emission, however, paints a different picture (Figure 4.14): the emission intensity of **(5)** is much weaker than that of **(1)**. Under the same conditions, a 1:1 D/A sample shows no quenching of the emission, indicating that the quenching observed for **(5)** does not arise from bimolecular processes. Contrary to what happened with **(4)**, there is no shifting of the emission spectrum of **(5)** compared to **(1)**: this suggests that the only luminophore in all of these samples is $\{Ru^{III}(bpyac^-)\}^*$, either as part of the assembly or in the free donor.

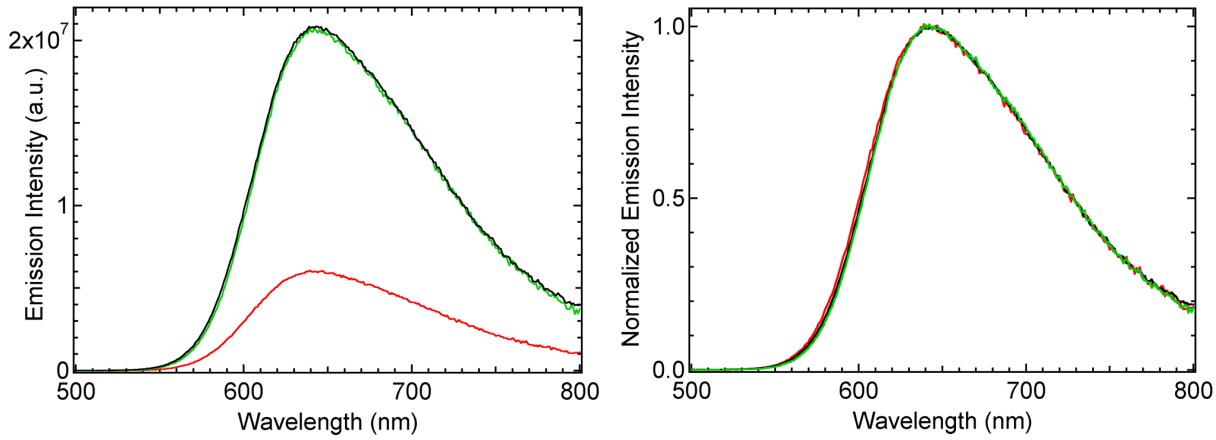


Figure 4.14. Steady-state emission spectra for **(1)** (black trace), **(5)** (red trace) and a 1:1 mixture of $(Tp)_2Fe_2O(\mu\text{-}O_2CCH_3)_2$ and **(1)** (green trace). Left: the emission intensity at each point was divided by the absorbance of that sample at the excitation wavelength. Right: all traces normalized to their emission maximum.

Table 4.2. Time-resolved and steady-state emission results for samples used in the study of **(5)**.

	λ_{em} (nm)	Φ	τ (ns)
$[Ru(tmb)_2(bpyac)](PF_6)_2$ **(1)**	640	0.094[a]	860
Assembly **(5)**	640	0.026[b]	890
Assembly **(5)** after 24 h	640	0.070[b]	880

[a]Determined as a relative value, using $[Ru(bpy)_3](PF_6)_2$ as the standard. [b]Determined relative to **(1)**. See text for details.

Comparing the data in Tables 4.1 and 4.2, the emission quantum yield is lower for **(5)** compared to **(4)**, which means that the quenching in the tmb-assembly is more efficient than in the bpy-assembly. This can be attributed to the identity of the ancillary bipyridines in either case: the Ru(II) center in **(1)** is more electron-rich, and therefore easier to oxidize, than that of **(3)**; no electrochemical data are available for the latter, due to its tendency to lose CO_2, but based on data for other compounds,[33] this is a reasonable assumption (see the data for $[Ru(bpy)_3](PF_6)_2$ in Chapter 2 and for $[Ru(tmb)_3](PF_6)_2$ in

Chapter 3 as an example). This difference in the oxidation potential of the donors translates into a larger (more negative) ΔG_0^{ET} for **(5)**, leading to a more efficient quenching by electron transfer.[v] On the other hand, the spectral overlap seems to be larger for **(4)** (see Figure 4.15), although the integral cannot be properly calculated for these assemblies because of the uncertainty in the composition of the samples. If the spectral overlap integral is indeed larger for **(4)**, this would mean that the contribution of FRET to the quenching is larger for this assembly. Just as was observed for the systems presented in Chapter 3, these results suggest that electron transfer is the main quenching mechanism at play for these assemblies, which was expected based on how weak is the ligand-field absorption of the diiron(III) core that is involved in FRET.[34]

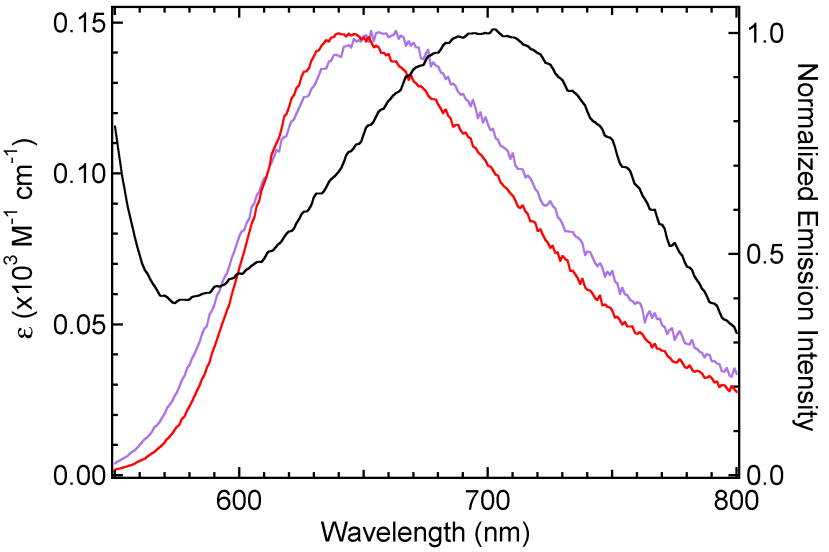


Figure 4.15. Overlay of the steady-state emission spectra for **(4)** (purple trace) and **(5)** (red trace), and the absorption spectrum for $(Tp)_2Fe_2O(\mu\text{-}O_2CCH_3)_2$ (black trace).

As promising as these results were, the stability of this new assembly posed a challenge as well. In Figure 4.16, the steady-state emission spectrum of **(1)** is compared

[v]Electron transfer for these D-A systems is in the normal region of the Marcus curve. See ref. 2.

to the spectrum of a freshly prepared sample of **(5)**, and that of the same sample, 24 hours after being made (the sample was kept in a sealed air-free cuvette during this time); the quantum yields are compiled in Table 4.2. The emission of this old sample is at least twice as intense as it originally was, which can only be explained if the assembly is falling apart in solution (recall that a 1:1 sample under identical conditions shows no quenching of the emission). In contrast, a sample of **(1)** in acetonitrile under the same conditions maintained its emissive properties for over 24 h. It should also be mentioned that had any oxygen leaked into either of the cuvettes, the emission of either sample would have decreased, not increased (recall that O_2 engages in DET with excited Ru(II) polypyridyls, Chapter 2).

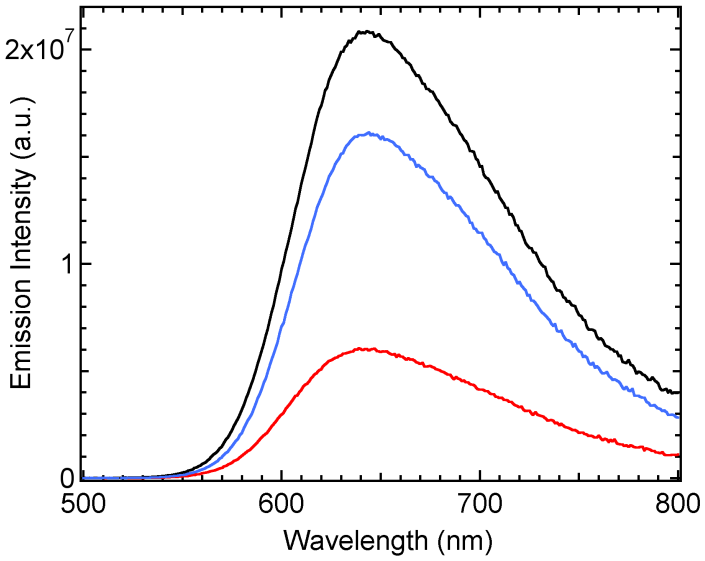


Figure 4.16. Steady-state emission spectra for **(1)** (black trace), **(5)** (red trace) and the same sample of **(5)** 24 hours after being prepared, kept under argon (blue trace).

4.3.5. In-Situ Bridge Exchange?

As mentioned in Chapter 3, bimolecular quenching studies using the donor and acceptor may aid the study of the photophysics of a covalently attached D-A system. To that end, Stern-Volmer quenching studies were performed using **(1)** and **(6)** with some diferric cores as the acceptors. The results when using $[(Tp)_2Fe_2(OH)(\mu\text{-}O_2CCH_3)_2]^+$ as the acceptor are collected in the left half of Figure 4.17. A "zoomed in" version of this plot is presented on the right half of the figure.

In most cases, it is convenient to use an ester as the model compound instead of an acid,[10] partly because of the interactions of the carboxylate group with the solvent (see Chapter 3). However, in this case, one of the goals of the Stern-Volmer studies was to gain insight on the role of the carboxylic acid in the quenching process; to this end, the free acid analog was used in addition to the ester.

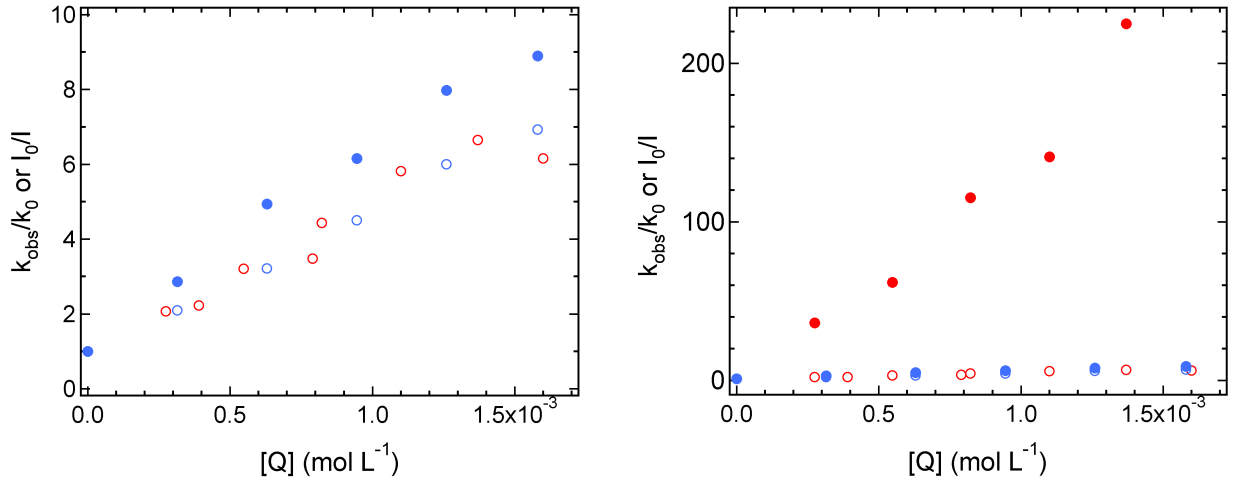


Figure 4.17. Quenching data for **(1)** (red) and **(6)** (blue) in the presence of increasing concentrations of $[(Tp)_2Fe_2(OH)(\mu\text{-}O_2CCH_3)_2]^+$. The open circles correspond to time-resolved emission results, and the full circles, to steady-state emission. Left: all datasets shown. Right: the steady-state data for **(1)** are omitted.

The time-resolved emission data for **(1)** and **(6)** are within error of each other, which is consistent with their closely related structures and very similar electronic properties. These data are also comparable to the steady-state emission data for **(6)**; the most likely cause of discrepancies between both datasets for the ester analog arising from the high absorbances of the samples. For emission experiments, it is advisable to work with optically dilute samples (i.e., those with absorbances below 0.2 at the excitation wavelength), to avoid the so-called inner filter effect.[11,35] Essentially, if a solution is too concentrated, the sample will absorb part of the light it emits before it can reach the detector, and the emission will appear quenched, even if only the luminophore is present in solution. While this effect is very important in steady-state measurements, optically dense samples do not present a major challenge for time-resolved emission, because the inner filter effect does not affect the observed lifetime of the sample. Having to work under pseudo-first order conditions with respect to the acceptor (see Chapter 2) and using a concentration of the donor such that emission can be observed leads to fairly dark samples, which makes the steady-state emission results less reliable.

A very different situation arises when comparing the SSEm data for **(1)** and **(6)**: the extent of the quenching is much larger for the acid than for the ester. This seems to be a textbook-worthy example of dynamic and static quenching combined (recall Figure 2.14). It is important to highlight that for any quencher concentration, the UV-vis absorption spectrum of the "acid" sample and that of the "ester" sample are almost identical. A consequence of this is that the extra quenching observed for **(1)** cannot be ascribed to inner-filter effects: there must be another quenching mechanism that is

operative when bpyac is used in the donor. From an electronic and a geometric point of view, **(1)** and **(6)** should be equivalent, with the main difference between these two molecules being the presence of a free carboxylate group in one of them. These results strongly suggest that the same bridge exchange that was used to prepare **(4)** and **(5)** can take place in the Stern-Volmer samples, and that the formation of a D-A assembly is responsible for the lower emission intensity measured for the "acid" samples.[vi]

More importantly, these results suggest that the synthesis and isolation of a D-A assembly based on the donors and acceptors described in this chapter may not be necessary: it should be possible to study the photophysics of such assemblies by simply preparing suitable bimolecular samples. Furthermore, the data from Figure 4.17 were obtained using a hydroxo-bridged acceptor: recall that the only assemblies that could be prepared in this chapter were oxo-bridged, and that attempts to synthesize the OH- analogs were unsuccessful. This new approach should allow for the study of both kinds of acceptors without much of the hassle of synthesis.

4.4. Concluding Comments

In this chapter, the synthesis and characterization of the first covalently linked D-A systems were presented. The ease of preparation of such assemblies belied the many difficulties encountered when their isolation was attempted, and the instability observed

[vi]Based on the discussion in this chapter, it is highly likely that the samples of **(1)** and **(6)** contain some amount of decarboxylated Ru(II) species. Those would contribute to the emission intensity observed, not to the quenching, and it is unlikely that only the ester would have decomposed. The uncertainty in the samples' composition prevents us from quantitatively analyzing these data but does not invalidate the possibility of bridge exchange happening in-situ.

afterward. The photophysics of the assemblies showed that the ^{3}MLCT excited state of the donor was quenched, but no short-time TREm components were observed. Whether this was due to static quenching or if our time resolution was not fast enough for these compounds was not clear: the instability of these assemblies discouraged any further studies.

The bimolecular quenching results using **(1)** and **(6)** were unexpected, and led to a new strategy: if the desired bridge swapping can take place under Stern-Volmer conditions, then it is not necessary to prepare and isolate the assemblies beforehand. While this approach is in principle less "clean", considering that we were unable to obtain pure assemblies before, and their photophysics were interspersed with those of the free donor, attaching donor and acceptor in situ has the benefit of sparing us some trouble. Given that only one bridge is swapped when using a Ru-bpyac moiety, this method has the added appeal of leaving one carboxylate bridge intact, which could be used to tweak the redox potential of the diiron(III) core. While this did not seem viable when trying to prepare and isolate the D-A assemblies, it is still an avenue worth exploring.

The main caveat to these bimolecular quenching experiments came from the instability of the donors themselves; studying the in-situ D-A system and deconvolving its photophysics from those of the bimolecular donor and acceptor interactions is cumbersome enough, so it is really important to ensure that the donor and acceptor are clean and stable in solution. With this in mind, the donor design was reassessed; the next chapter describes the systems employed instead, and their photophysical properties.

APPENDIX

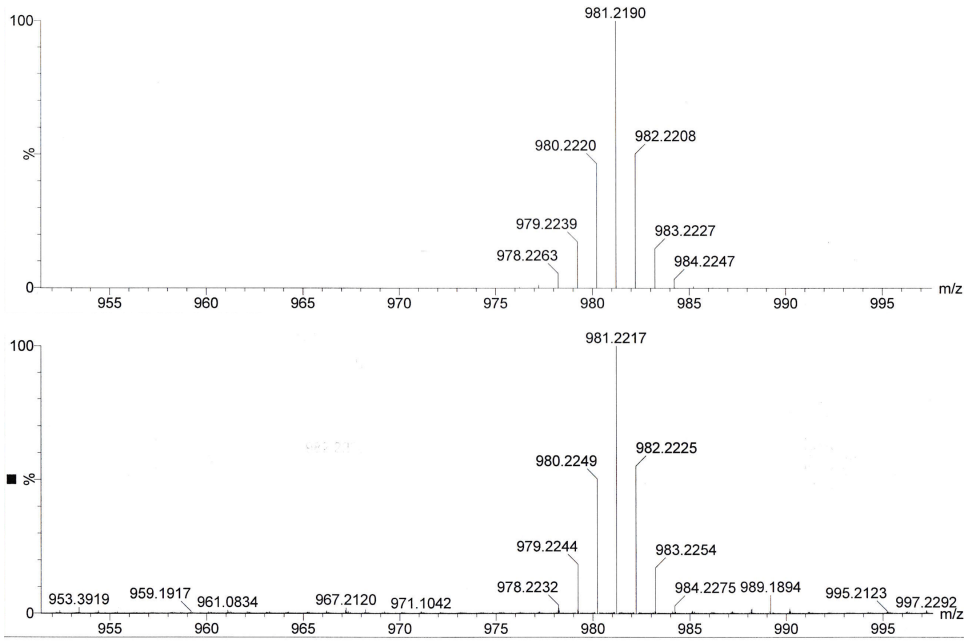


Figure 4.18. ESI-MS of $(Tp)_2Fe_2O(bpyac)_2$. Top: predicted isotope pattern for $[M+H]^+$ ($C_{42}H_{39}N_{16}O_5B_2Fe_2$). Bottom: experimental result.

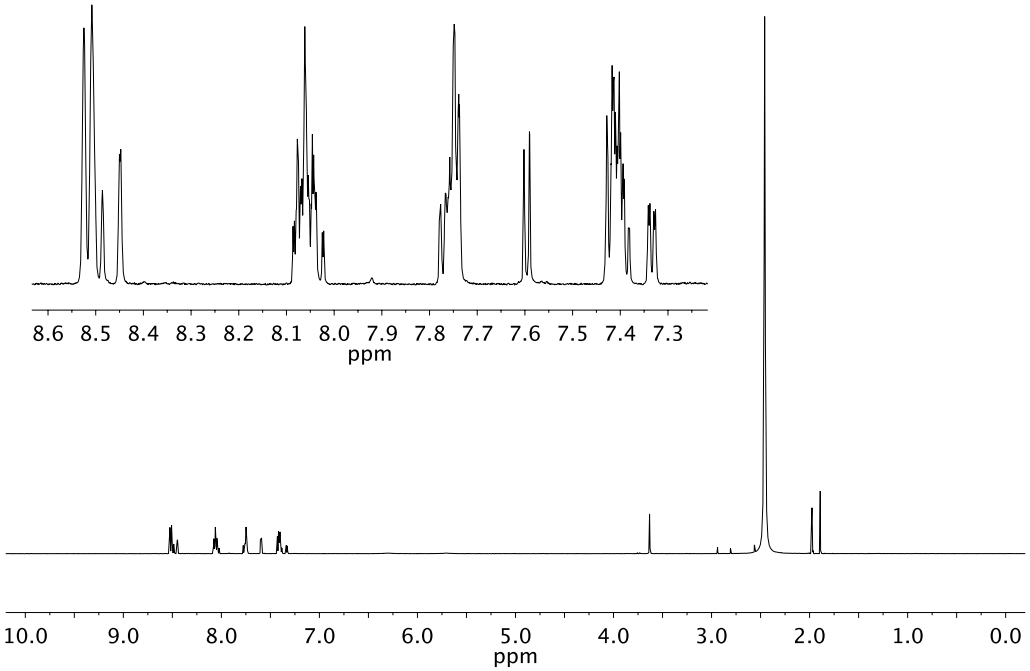


Figure 4.19. ^1H NMR of (presumed) **(3)** in CD_3CN.

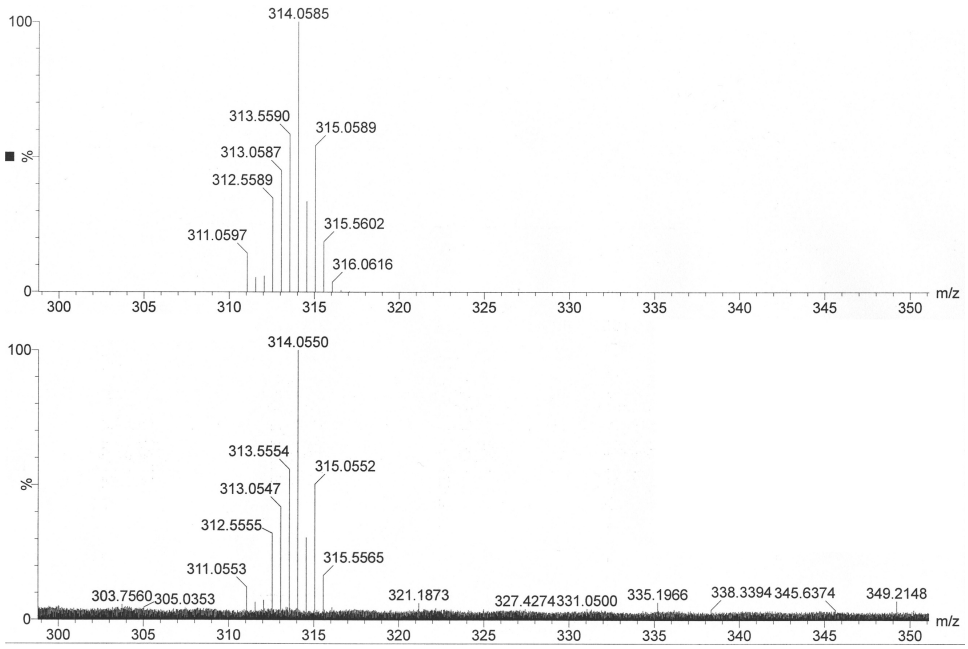


Figure 4.20. ESI-MS of **(3)**. Top: predicted isotope pattern for $[M–2PF_6]^{2+}$ ($C_{32}H_{26}N_6O_2Ru$). Bottom: experimental result.

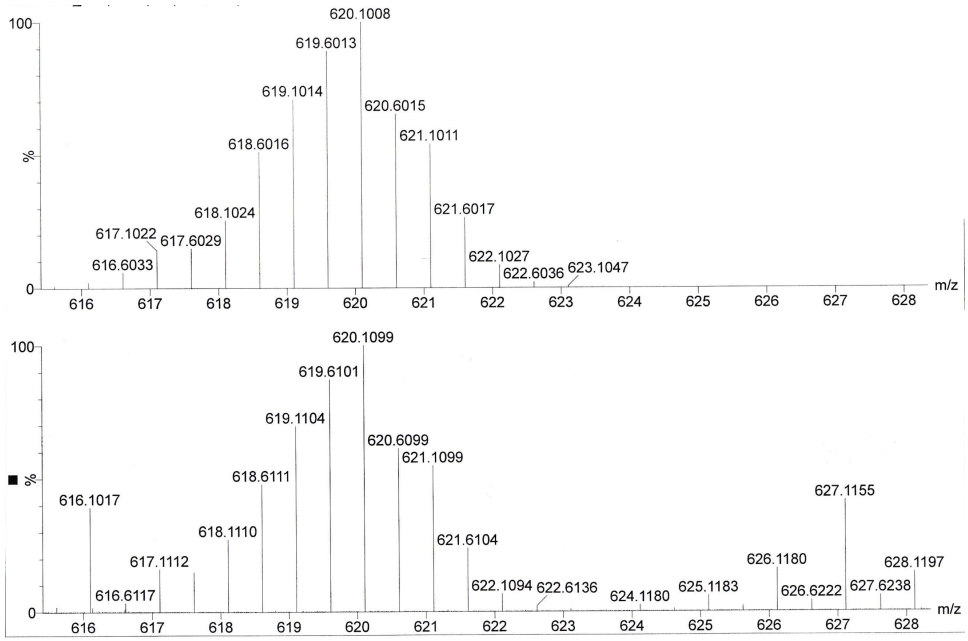


Figure 4.21. ESI-MS of **(4)**. Top: predicted isotope pattern for $[M–2PF_6]^{2+}$ ($C_{52}H_{48}N_{18}O_5B_2Fe_2Ru$). Bottom: experimental result.

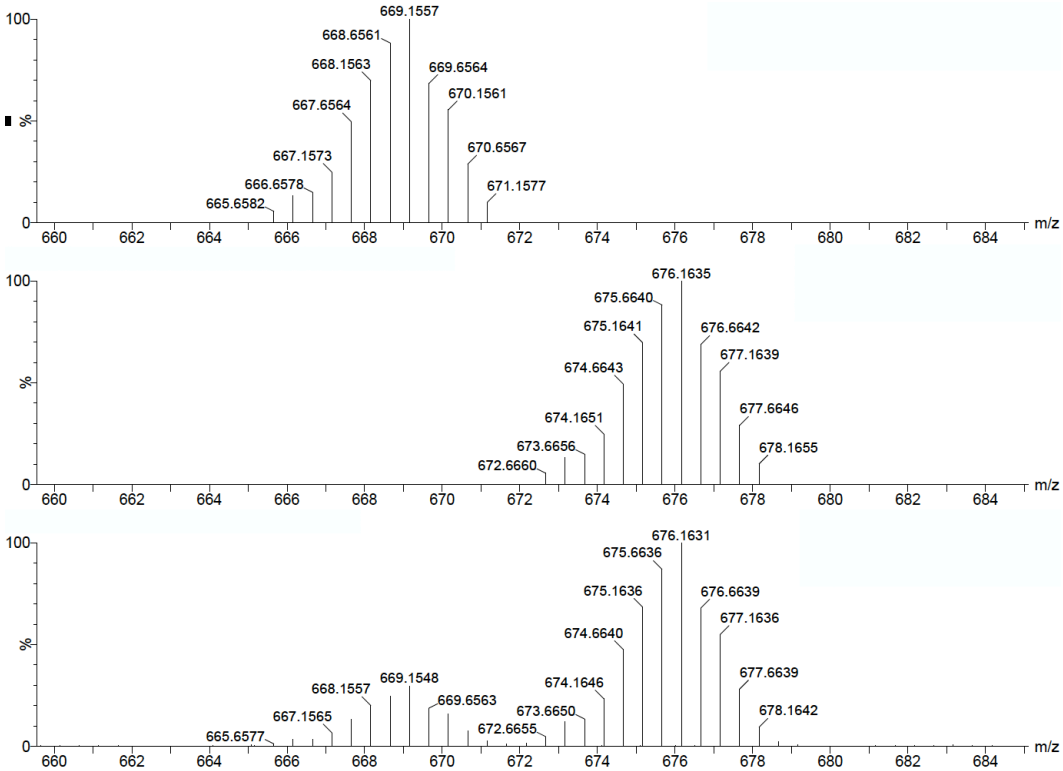


Figure 4.22. ESI-MS of **(5)**. Top: predicted isotope for $[M–2PF_6]^{2+}$ of the formate-bridged assembly ($C_{59}H_{62}N_{18}O_5B_2Fe_2Ru$). Middle: predicted isotope pattern for $[M–2PF_6]^{2+}$ ($C_{60}H_{64}N_{18}O_5B_2Fe_2Ru$). Bottom: experimental results.

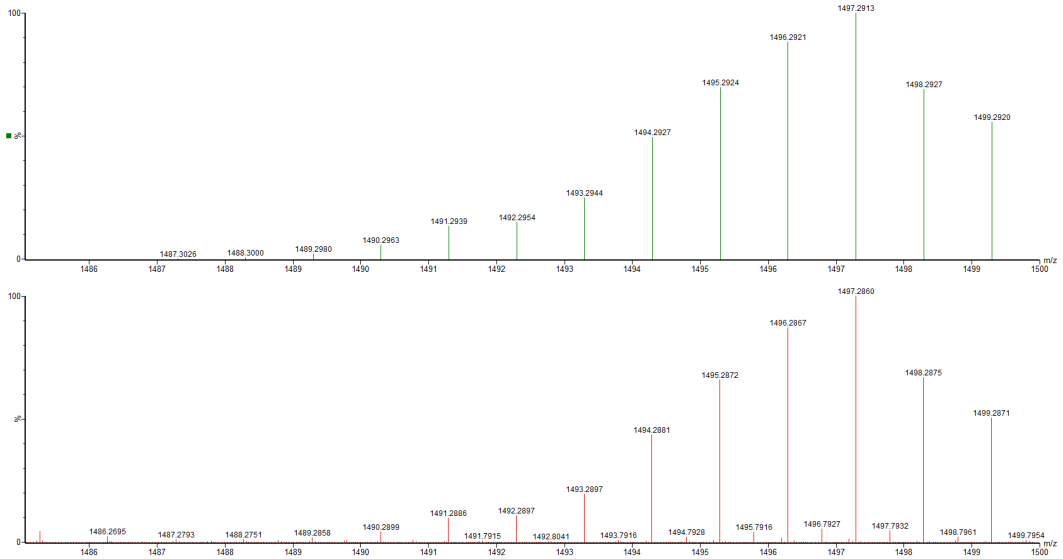


Figure 4.23. ESI-MS of **(5)**. Top: predicted isotope for $[M–PF_6]^{2+}$ ($C_{60}H_{64}N_{18}O_5B_2Fe_2RuPF_6$). Bottom: experimental result.

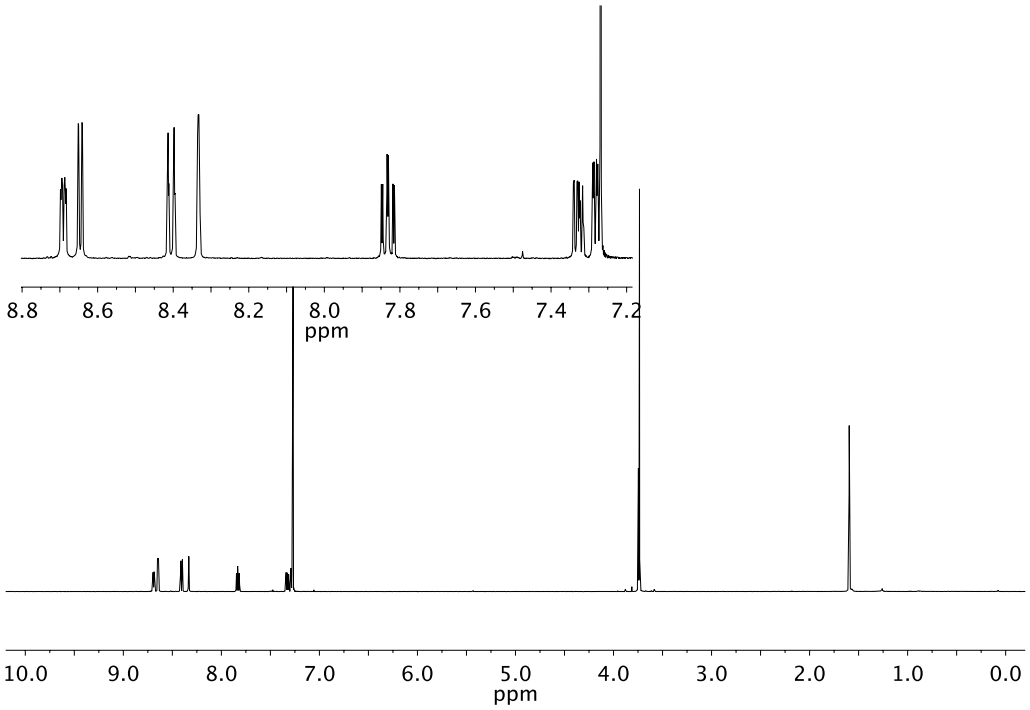


Figure 4.24. ^{1}H NMR of bpyester in $CDCl_3$.

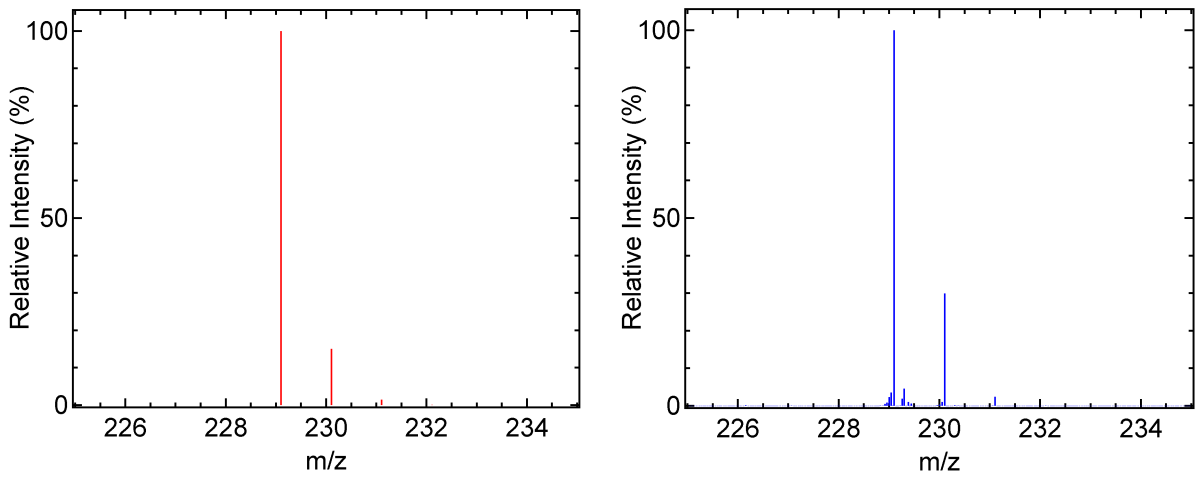


Figure 4.25. ESI-MS of bpyester. Left: predicted isotope pattern for $C_{13}H_{13}N_2O_2$. Right: experimental result.

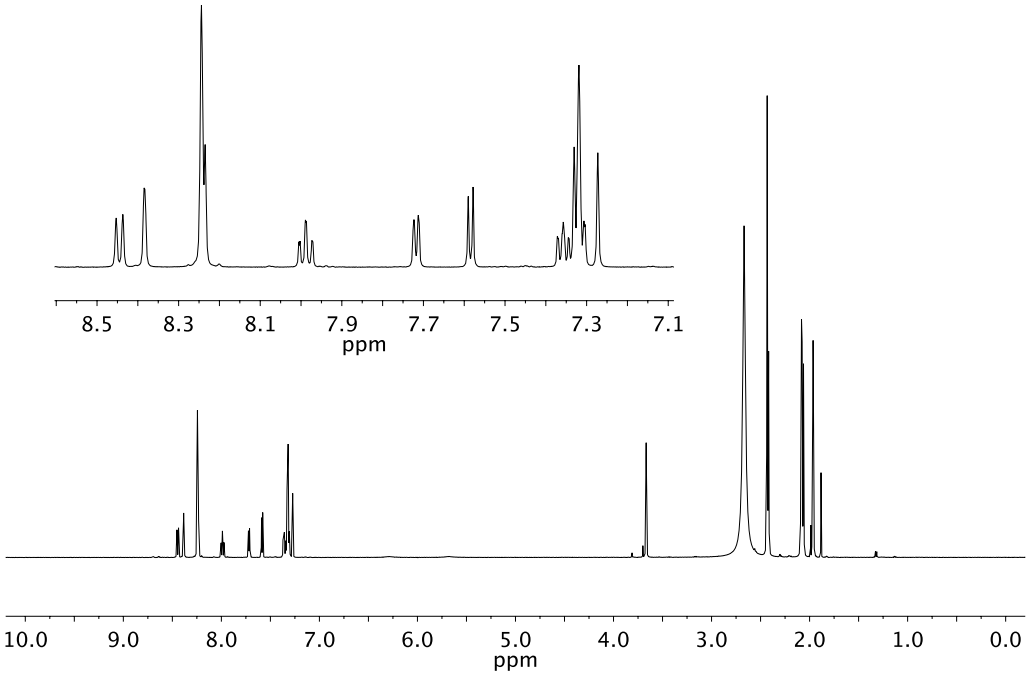


Figure 4.26. ^{1}H NMR of **(6)** in CD_3CN. The peaks at $\delta < 3$ ppm correspond to solvents used when working up the reaction.

Table 4.3. Crystallographic data for $[Ru(tmb)_2(mmb)](PF_6)_2$.

empirical formula	$C_{42}H_{46.5}N_{7.5}F_{12}P_2Ru$
formula weight	1047.3
temperature (K)	173(2)
crystal color, habit	red, plates
crystal system	triclinic
space group	*P*-1
cell dimensions:	
a (Å)	13.954(3)
b (Å)	16.924(3)
c (Å)	20.182(4)
Volume (Å^3)	4668.1(15)
Z	4
D_{calc} (g cm^{-3})	1.490
goodness of fit (F^2)	1.028
R_1 (I >2(I))	0.1070

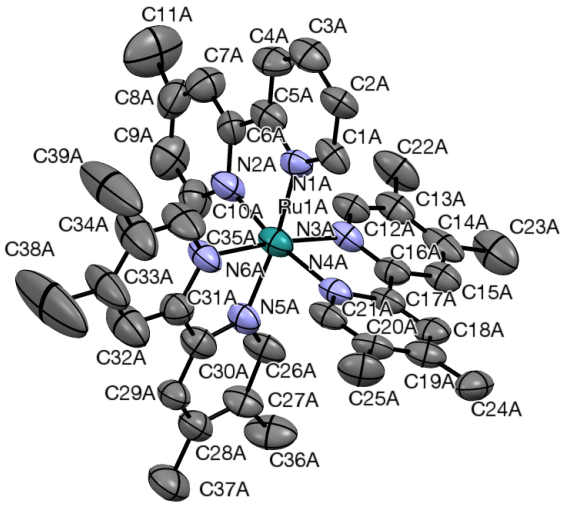


Figure 4.27. ORTEP drawing of $[Ru(tmb)_2(mmb)]^{2+}$ obtained from single-crystal X-ray structure determinations, showing the labelling system. Atoms are represented as 50% probability thermal ellipsoids. Anions are omitted for clarity.

Table 4.4. Bond lengths for the crystal structure of $[Ru(tmb)_2(mmb)](PF_6)_2$.

Atoms	Length/Å	Atoms	Length/Å	Atoms	Length/Å
Ru1A N1A	2.053(8)	C12A C13A	1.348(14)	P2 F9	1.573(8)
Ru1A N2A	2.030(10)	C13A C14A	1.430(17)	P2 F10	1.542(11)
Ru1A N3A	2.056(8)	C13A C22A	1.507(14)	P2 F11	1.465(11)
Ru1A N4A	2.061(9)	C14A C15A	1.422(16)	P2 F12	1.563(12)
Ru1A N5A	2.058(9)	C14A C23A	1.517(15)	P3 F13	1.664(11)
Ru1A N6A	2.070(9)	C15A C16A	1.418(14)	P3 F14	1.585(7)
N1A C1A	1.357(13)	C16A C17A	1.500(14)	P3 F15	1.502(10)
N1A C5A	1.359(14)	C17A C18A	1.380(15)	P3 F16	1.571(8)
N2A C6A	1.392(14)	C18A C19A	1.361(14)	P3 F17	1.552(9)
N2A C10A	1.353(14)	C19A C20A	1.384(16)	P3 F18	1.557(8)
N3A C12A	1.324(12)	C19A C24A	1.482(15)	P1 F1	1.604(9)
N3A C16A	1.352(13)	C20A C21A	1.411(15)	P1 F2	1.530(11)
N4A C17A	1.365(12)	C20A C25A	1.490(14)	P1 F3	1.517(12)
N4A C21A	1.374(12)	C26A C27A	1.399(15)	P1 F4	1.595(10)
N5A C26A	1.328(13)	C27A C28A	1.389(16)	P1 F5	1.579(12)
N5A C30A	1.354(13)	C27A C36A	1.509(15)	P1 F6	1.563(12)
N6A C31A	1.390(14)	C28A C29A	1.413(15)	P4A F19A	1.609(17)
N6A C35A	1.335(14)	C28A C37A	1.488(16)	P4A F20A	1.537(17)
C1A C2A	1.372(15)	C29A C30A	1.381(15)	P4A F21A	1.529(16)
C2A C3A	1.369(16)	C30A C31A	1.456(15)	P4A F22A	1.599(17)
C3A C4A	1.370(16)	C31A C32A	1.407(17)	P4A F23A	1.575(17)
C4A C5A	1.392(15)	C32A C33A	1.381(19)	P4A F24A	1.572(18)
C5A C6A	1.464(16)	C33A C34A	1.38(2)	N1S C2S	1.12(4)

Table 4.4 (cont'd)

Atoms	Length/Å	Atoms	Length/Å	Atoms	Length/Å
C6A C7A	1.383(16)	C33A C38A	1.57(2)	C1S C2S	1.50(4)
C7A C8A	1.391(18)	C34A C35A	1.382(18)	N2S C4S	1.03(2)
C8A C9A	1.388(19)	C34A C39A	1.54(2)	C3S C4S	1.43(3)
C8A C11A	1.49(2)	P2 F7	1.556(9)	N15 C11	1.16(3)
C9A C10A	1.358(17)	P2 F8	1.475(9)	C03C C11	1.40(3)

Table 4.5. Bond angles for the crystal structure of $[Ru(tmb)_2(mmb)](PF_6)_2$.

Atoms	Angle/º	Atoms	Angle/º	Atoms	Angle/º
N1A Ru1A N3A	91.1(3)	C14A C13A C22A	121.2(11)	F11 P2 F9	89.3(7)
N1A Ru1A N4A	96.5(3)	C13A C14A C23A	122.5(12)	F11 P2 F10	79.1(10)
N1A Ru1A N5A	172.5(3)	C15A C14A C13A	120.2(10)	F11 P2 F12	174.7(12)
N1A Ru1A N6A	94.1(3)	C15A C14A C23A	117.4(13)	F12 P2 F9	90.7(6)
N2A Ru1A N1A	79.1(4)	C16A C15A C14A	116.6(11)	F14 P3 F13	87.9(5)
N2A Ru1A N3A	93.2(4)	N3A C16A C15A	123.0(9)	F15 P3 F13	176.6(8)
N2A Ru1A N4A	171.0(3)	N3A C16A C17A	115.5(9)	F15 P3 F14	90.1(5)
N2A Ru1A N5A	97.8(4)	C15A C16A C17A	121.5(11)	F15 P3 F16	91.9(6)
N2A Ru1A N6A	90.5(4)	N4A C17A C16A	112.8(10)	F15 P3 F17	95.2(8)
N3A Ru1A N4A	78.9(3)	N4A C17A C18A	121.4(9)	F15 P3 F18	92.3(7)
N3A Ru1A N5A	95.9(3)	C18A C17A C16A	125.6(10)	F16 P3 F13	90.0(6)
N3A Ru1A N6A	174.1(4)	C19A C18A C17A	121.9(11)	F16 P3 F14	177.1(6)
N4A Ru1A N6A	97.7(4)	C18A C19A C20A	118.7(11)	F17 P3 F13	87.4(6)
N5A Ru1A N4A	87.5(3)	C18A C19A C24A	120.4(12)	F17 P3 F14	86.7(5)
N5A Ru1A N6A	79.1(3)	C20A C19A C24A	120.8(10)	F17 P3 F16	95.4(6)
C1A N1A Ru1A	125.7(8)	C19A C20A C21A	118.2(9)	F17 P3 F18	172.0(7)
C1A N1A C5A	117.7(10)	C19A C20A C25A	122.8(11)	F18 P3 F13	84.9(6)
C5A N1A Ru1A	116.4(7)	C21A C20A C25A	119.0(11)	F18 P3 F14	90.7(5)
C6A N2A Ru1A	115.6(7)	N4A C21A C20A	122.8(10)	F18 P3 F16	87.0(5)
C10A N2A Ru1A	127.5(9)	N5A C26A C27A	126.0(10)	F2 P1 F1	95.3(7)
C10A N2A C6A	116.8(10)	C26A C27A C36A	121.3(11)	F2 P1 F4	177.2(8)
C12A N3A Ru1A	127.7(8)	C28A C27A C26A	118.0(10)	F2 P1 F5	93.0(7)
C12A N3A C16A	116.5(9)	C28A C27A C36A	120.7(11)	F2 P1 F6	89.5(8)
C16A N3A Ru1A	115.5(6)	C27A C28A C29A	116.5(10)	F3 P1 F1	91.0(7)
C17A N4A Ru1A	116.6(7)	C27A C28A C37A	123.7(11)	F3 P1 F2	91.6(8)
C17A N4A C21A	116.8(9)	C29A C28A C37A	119.7(11)	F3 P1 F4	88.7(7)
C21A N4A Ru1A	126.6(7)	C30A C29A C28A	121.2(10)	F3 P1 F5	173.1(9)
C26A N5A Ru1A	127.7(7)	N5A C30A C29A	122.2(10)	F3 P1 F6	89.5(8)
C26A N5A C30A	116.2(9)	N5A C30A C31A	115.2(10)	F4 P1 F1	81.9(6)
C30A N5A Ru1A	116.1(7)	C29A C30A C31A	122.6(11)	F5 P1 F1	93.6(7)
C31A N6A Ru1A	114.1(7)	N6A C31A C30A	115.4(10)	F5 P1 F4	87.0(7)
C35A N6A Ru1A	128.0(8)	N6A C31A C32A	120.4(11)	F6 P1 F1	175.2(8)

Table 4.5 (cont'd)

Atoms	Angle/°	Atoms	Angle/°	Atoms	Angle/°
C35A N6A C31A	118.0(10)	C32A C31A C30A	124.0(12)	F6 P1 F4	93.3(8)
N1A C1A C2A	121.6(11)	C33A C32A C31A	119.3(13)	F6 P1 F5	85.5(8)
C3A C2A C1A	120.6(11)	C32A C33A C38A	119.6(14)	F20A P4A F19A	94.2(12)
C2A C3A C4A	118.9(12)	C34A C33A C32A	119.9(13)	F20A P4A F22A	178.2(15)
C3A C4A C5A	119.0(12)	C34A C33A C38A	120.5(14)	F20A P4A F23A	91.6(14)
N1A C5A C4A	122.1(11)	C33A C34A C35A	118.7(13)	F20A P4A F24A	84.0(13)
N1A C5A C6A	114.0(10)	C33A C34A C39A	121.6(13)	F21A P4A F19A	88.8(12)
C4A C5A C6A	123.8(12)	C35A C34A C39A	118.8(14)	F21A P4A F20A	89.5(11)
N2A C6A C5A	114.6(10)	N6A C35A C34A	123.7(12)	F21A P4A F22A	91.1(14)
C7A C6A N2A	121.5(11)	F7 P2 F9	177.4(8)	F21A P4A F23A	176.8(15)
C7A C6A C5A	123.6(11)	F7 P2 F12	87.3(6)	F21A P4A F24A	91.8(13)
C6A C7A C8A	120.5(13)	F8 P2 F7	88.7(6)	F22A P4A F19A	84.1(11)
C7A C8A C11A	119.0(14)	F8 P2 F9	92.8(6)	F23A P4A F19A	94.1(13)
C9A C8A C7A	116.8(13)	F8 P2 F10	178.8(11)	F23A P4A F22A	87.9(15)
C9A C8A C11A	123.8(14)	F8 P2 F12	83.2(9)	F24A P4A F19A	178.1(14)
C10A C9A C8A	121.5(13)	F10 P2 F7	91.5(6)	F24A P4A F22A	97.6(13)
N2A C10A C9A	122.7(13)	F10 P2 F9	87.0(5)	F24A P4A F23A	85.4(10)
N3A C12A C13A	128.8(12)	F10 P2 F12	95.6(11)	N1S C2S C1S	177(4)
C12A C13A C14A	115.0(10)	F11 P2 F7	92.5(7)	N2S C4S C3S	176(3)
C12A C13A C22A	123.8(12)	F11 P2 F8	102.1(12)	N15 C11 C03C	177(5)

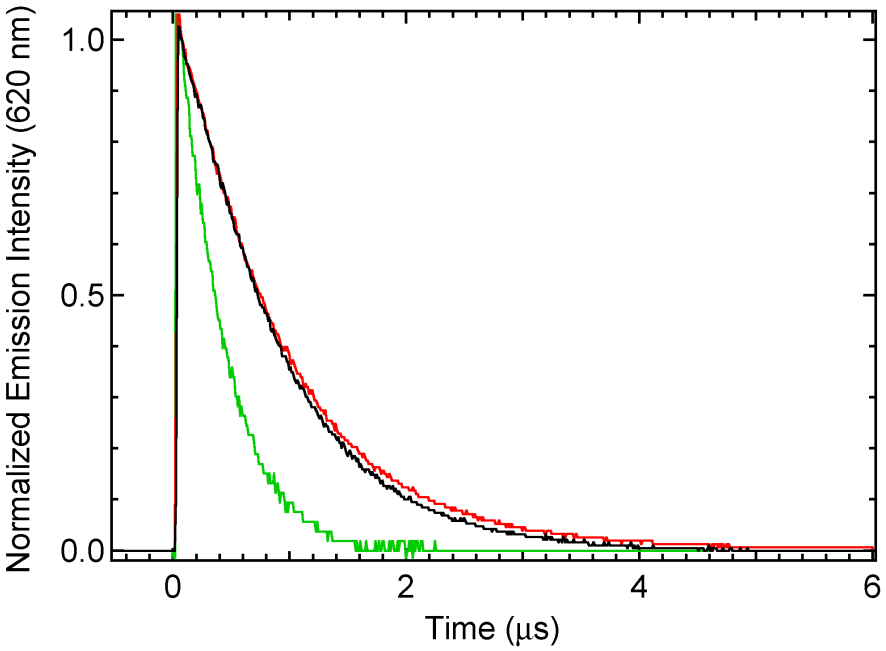


Figure 4.28. Time-resolved emission traces for **(3)** (black), **(4)** (red), and a 100:1 mixture of $(Tp)_2Fe_2O(\mu\text{-}O_2CCH_3)_2$ and **(3)** (green). All samples prepared in deoxygenated acetonitrile, all spectra collected at room temperature.

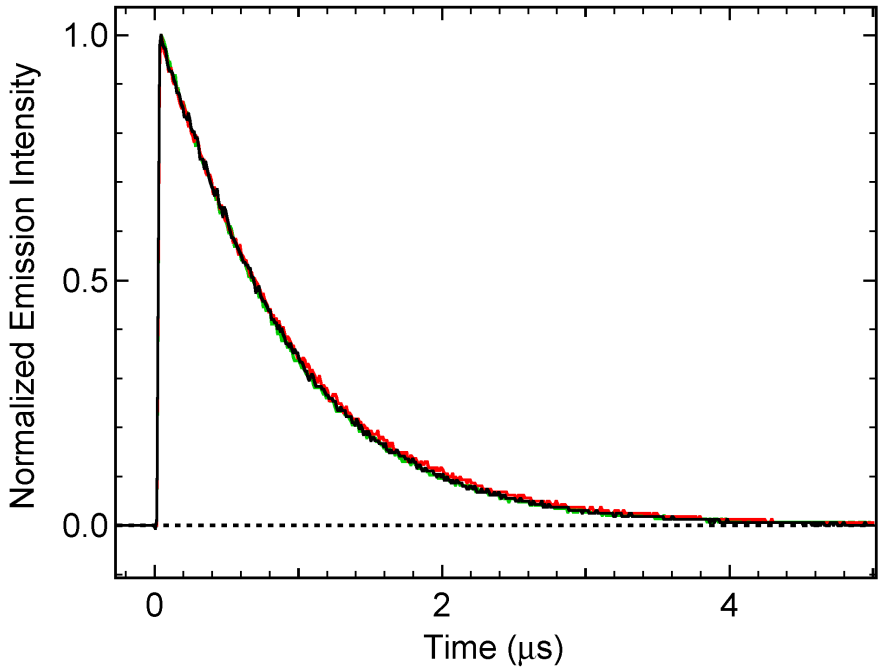


Figure 4.29. Time-resolved emission traces for **(1)** (black), **(5)** (red), and a 1:1 mixture of $(Tp)_2Fe_2O(\mu\text{-}O_2CCH_3)_2$ and **(1)** (green). All samples prepared in deoxygenated acetonitrile, spectra collected at room temperature.

REFERENCES

REFERENCES

(1) Kurtz, D. M. *Chem. Rev.* **1990**, *90*, 585–606.

(2) Weldon, B. T.; Wheeler, D. E.; Kirby, J. P.; McCusker, J. K. *Inorg. Chem.* **2001**, *40*, 6802–6812.

(3) Armstrong, W. H.; Lippard, S. J. *J. Am. Chem. Soc.* **1984**, *106*, 4632–4633.

(4) Rodriguez, J. H.; McCusker, J. K. *J. Chem. Phys.* **2002**, *116*, 6253–6270.

(5) Armstrong, W. H.; Spool, A.; Papaefthymiou, G. C.; Frankel, R. B.; Lippard, S. J. *J. Am. Chem. Soc.* **1984**, *106*, 3653–3667.

(6) Armstrong, W. H.; Lippard, S. J. *J. Am. Chem. Soc.* **1983**, *105*, 4837–4838.

(7) Armstrong, W. H.; Lippard, S. J. *J. Am. Chem. Soc.* **1985**, *107*, 3730–3731.

(8) Picraux, L. B.; Weldon, B. T.; McCusker, J. K. *Inorg. Chem.* **2002**, *42*, 273–282.

(9) Trofimenko, S. *J. Am. Chem. Soc.* **1967**, *89*, 3170–3177.

(10) Soler, M.; McCusker, J. K. *J. Am. Chem. Soc.* **2008**, *130*, 4708–4724.

(11) Lakowicz, J. R. *Principles of Fluorescence Spectroscopy*, 3rd ed.; Springer US: Boston, 2006.

(12) Suzuki, K.; Kobayashi, A.; Kaneko, S.; Takehira, K.; Yoshihara, T.; Ishida, H.; Shiina, Y.; Oishi, S.; Tobita, S. *Phys. Chem. Chem. Phys.* **2009**, *11*, 9850–9860.

(13) Picraux, L. B.; Smeigh, A. L.; Guo, D.; McCusker, J. K. *Inorg. Chem.* **2005**, *44*, 7846–7859.

(14) Damrauer, N. H.; Boussie, T. R.; Devenney, M.; McCusker, J. K. *J. Am. Chem. Soc.* **1997**, *119*, 8253–8268.

(15) Bock, C. R.; Connor, J. A.; Gutierrez, A. R.; Meyer, T. J.; Whitten, D. G.; Sullivan, B. P.; Nagle, J. K. *J. Am. Chem. Soc.* **1979**, *101*, 4815–4824.

(16) Clark, C. D.; Hoffman, M. Z. *Coord. Chem. Rev.* **1997**, *159*, 359–373.

(17) Frisch, M. J.; Trucks, G. W.; Schlegel, H. B.; Scuseria, G. E.; Robb, M. A.; Cheeseman, J. R.; Montgomery, Jr., J. A.; Vreven, T.; Kudin, K. N.; Burant, J. C.; Millam, J. M.;

Iyengar, S. S.; Tomasi, J.; Barone, V.; Mennucci, B.; Cossi, M.; Scalmani, G.; Rega, N.; Petersson, G. A.; Nakatsuji, H.; Hada, M.; Ehara, M.; Toyota, K.; Fukuda, R.; Hasegawa, J.; Ishida, M.; Nakajima, T.; Honda, Y.; Kitao, O.; Nakai, H.; Klene, M.; Li, X.; Knox, J. E.; Hratchian, H. P.; Cross, J. B.; Bakken, V.; Adamo, C.; Jaramillo, J.; Gomperts, R.; Stratmann, R. E.; Yazyev, O.; Austin, A. J.; Cammi, R.; Pomelli, C.; Ochterski, J. W.; Ayala, P. Y.; Morokuma, K.; Voth, G. A.; Salvador, P.; Dannenberg, J. J.; Zakrzewski, V. G.; Dapprich, S.; Daniels, A. D.; Strain, M. C.; Farkas, O.; Malick, D. K.; Rabuck, A. D.; Raghavachari, K.; Foresman, J. B.; Ortiz, J. V.; Cui, Q.; Baboul, A. G.; Clifford, S.; Cioslowski, J.; Stefanov, B. B.; Liu, G.; Liashenko, A.; Piskorz, P.; Komaromi, I.; Martin, R. L.; Fox, D. J.; Keith, T.; Al-Laham, M. A.; Peng, C. Y.; Nanayakkara, A.; Challacombe, M.; Gill, P. M. W.; Johnson, B.; Chen, W.; Wong, M. W.; Gonzalez, C.; Pople, J. A. *Gaussian 03, Revision D.01. Gaussian, Inc., Wallingford CT, 2004*.

(18) Monat, J. E.; Rodriguez, J. H.; McCusker, J. K. *J. Phys. Chem. A* **2002**, *106*, 7399–7406.

(19) Drüeke, S.; Wieghardt, K.; Nuber, B.; Weiss, J.; Fleischhauer, H. P.; Gehring, S.; Haase, W. *J. Am. Chem. Soc.* **1989**, *111*, 8622–8631.

(20) Turowski, P. N.; Armstrong, W. H.; Roth, M. E.; Lippard, S. J. *J. Am. Chem. Soc.* **1990**, *112*, 681–690.

(21) Tanihara, N.; Obata, M.; Harada, M.; Mikata, Y.; Hamazawa, A.; Kinoshita, I.; Isobe, K.; Ichimura, A.; Hoshino, M.; Mikuriya, M.; Yano, S. *Inorg. Chem. Commun.* **2003**, *6*, 447–450.

(22) Kouzelos, J. A. The Effect of Electronic Spin on the Reactivity of Spin-Coupled Transition Metal Complexes, Michigan State University, 2015.

(23) Nakai, M.; Funabiki, T.; Ohtsuki, C.; Harada, M.; Ichimura, A.; Tanaka, R.; Kinoshita, I.; Mikuriya, M.; Benten, H.; Ohkita, H.; Ito, S.; Obata, M.; Yano, S. *Inorg. Chem.* **2006**, *45*, 3048–3056.

(24) GE Healthcare Life Sciences. *Size Exclusion Chromatography: Principles and Methods*; 2012.

(25) Smallwood, I. M. *Handbook of Organic Solvent Properties*; Arnold, 1996.

(26) Elliott, C. M.; Hershenhart, E. J. *J. Am. Chem. Soc.* **1982**, *104*, 7519–7526.

(27) Picraux, L. B. Studies of Intramolecular Electron and Energy Transfer in Donor-Acceptor Assemblies Incorporating a Heisenberg Spin Coupled Metal Center, University of California, Berkeley, 2003.

(28) Della Ciana, L.; Hamachi, I.; Meyer, T. J. *J. Org. Chem.* **1989**, *54*, 1731–1735.

(29) Aranyos, V.; Grennberg, H.; Tingry, S.; Lindquist, S. E.; Hagfeldt, A. *Sol. Energy Mater. Sol. Cells* **2000**, *64*, 97–114.

(30) Benoit, F.; Holmes, J. L.; Isaacs, N. S. *Org. Mass Spectrom.* **1969**, *2*, 591–601.

(31) Rose, M. E.; Johnstone, R. A. W. *Mass Spectrometry for Chemists and Biochemists*, 2nd ed.; Cambridge University Press: Cambridge, 1996.

(32) Anderson, T. J.; Scott, J. R.; Millett, F.; Durham, B. *Inorg. Chem.* **2006**, *45*, 3843–3845.

(33) Arias-Rotondo, D. M.; McCusker, J. K. *Chem. Soc. Rev.* **2016**, *45*, 5803–5820.

(34) Drago, R. S. *Physical Methods for Chemists*; Saunders College Pub.: Philadelphia, 1992.

(35) Crosby, G. A.; Demas, J. N. *J. Phys. Chem.* **1971**, *75*, 991–1024.

Chapter 5. In Situ Bridge Exchange: Bimolecular vs. Intramolecular Quenching Mechanisms

"(…) my dear Watson, how dangerous it always is to reason from insufficient data."

–Sherlock Holmes[1]

5.1. Introduction

The Stern-Volmer quenching studies using $[Ru(tmb)_2(bpyac)]^{2+}$ and $[Ru(tmb)_2(bpyester)]^{2+}$ with variable concentrations of the hydroxo-bridged acceptor $[(Tp)_2Fe_2(OH)(O_2CCH_3)_2](ClO_4)$ were discussed in Chapter 4. The marked difference in the steady-state emission data for these Ru(II) donors was ascribed to a bridge-swapping reaction that led to a covalently linked D-A assembly. This observation opened the door to a simpler approach to such intramolecular D-A systems. This was particularly advantageous considering how challenging the purification of the assemblies described in Chapter 4 was. However, the donors we had used up to that point were fairly unstable, losing CO_2 in solution to yield $[RuL_2(mmb)]^{2+}$ (L = bpy or tmb).

To avoid such decarboxylation of the ligands, we modified the design of the donors, using 4'-methyl-2,2'-bipyridine-4-carboxylic acid as the carboxylate-containing ligand; both the free acid and the ester analogues were used, in an effort to parse out the different contributions to the quenching, in the same way as was described in Chapter 4. The choice of the acceptors was based on the same strategy that Weldon et al.[2] used to decouple the effects of the driving force and Heisenberg spin exchange. In other words,

we sought to keep ΔG_0^{ET} constant for the D-A pairs, or, if that was not possible, we chose an oxo-bridged acceptor with a larger ΔG_0^{ET} value than its hydroxo-bridged counterpart.

In this chapter, the photophysics of the resulting D-A pairs are studied, and the bimolecular and intramolecular quenching processes are considered.

5.2. Experimental Section

General. All chemicals and solvents were obtained from Fisher Scientific or Sigma-Aldrich and used without purification unless otherwise stated. $RuCl_3 \cdot xH_2O$ was purchased from Strem Chemicals. 4-picoline was treated with KOH and activated carbon, and then vacuum distilled over CaH_2 prior to use.

^1H NMR spectra were collected on Agilent DDR2 500 MHz NMR spectrometers equipped with 7600AS 96-sample autosamplers. Mass spectra were obtained at the Michigan State University Mass Spectrometry and Metabolomics Core using a Waters G2-XS Qtof mass spectrometer interfaced to a Waters Aquity UPLC.

The syntheses of $Ru(DMSO)_4Cl_2$ and $Ru(bpy)_2Cl_2$ are described in Chapter 3 of this dissertation. $(Tp)_2Fe_2O(O_2CCH_3)_2$, $(Tp)_2Fe_2O(O_2CCHCl_2)_2$ and $(Tp)_2Fe_2O(O_2CCF_3)_2$ were prepared following a reported procedure.[2] 4'-methyl-4-ethylcarboxy-2,2'-bipyridine (mcbEt), 4,4'-bis(trifluoromethyl)-2,2'-bipyridine (btfmb), $[Ru(bpy)_2(mcbEt)](PF_6)_2$ (RumcbEt), and $[Ru(btfmb)_2(mcbEt)](PF_6)_2$ (Ru^FmcbEt) were generously donated by Dr. Monica Soler, $Ru(btfmb)_2Cl_2$ by Dr. John-Andrew Kouzelos, and $[(Tp)_2Fe_2(OH)(O_2CCH_2Cl)_2](ClO_4)$ by Dr. Dong Guo. $[Ru(bpy)_2(mcbEt)](PF_6)_2$ was recrystallized by ether diffusion into a solution of the compound in acetonitrile.

5.2.1. Syntheses

4,4'-dimethyl-2,2'-bipyridine (dmb).[3] Freshly distilled 4-picoline (400 mL, 4.11 mol) and Pd/C (11 g) were combined and refluxed under nitrogen for 6 days, after which time 200 mL of benzene were added, and the mixture was refluxed again for 30 minutes. The reaction mixture was filtered warm to remove the Pd/C, and the crude product precipitated as the filtrate cooled down. The filtrate was concentrated to about half its initial volume using vacuum distillation to obtain more solid. The solid was collected and recrystallized from hot ethyl acetate. Yield: 17.20 g (5%). ^{1}H NMR ($CDCl_3$, 500 MHz) δ (ppm): 8.53 (d, *J* = 4.9 Hz, 2H), 8.22 (s, 2 H), 7.13 (dd, *J* = 4.9, 0.7 Hz, 2H), 2.44 (s, 6H).

4'-methyl-2,2'-bipyridine-4-carboxaldehyde (dmb-CHO).[4,5] Anhydrous 1,4-dioxane (100 mL) was bubble-degassed with nitrogen for 5 min. Under a positive nitrogen pressure, dmb (5.10g, 27.7 mmol) and SeO_2 (3.66g, 33.0 mmol) were added, the mixture was bubble-degassed for 30 min, and then refluxed under nitrogen for 24 h. After that time, it was cooled down, and the insoluble solids were filtered off. The yellow filtrate was evaporated to dryness, then 500 mL of ethyl acetate were added, the suspension was refluxed for 1 h, filtered while hot and then allowed to reach room temperature. The solution was washed with 0.1 M Na_2CO_3 (2 x 130 mL) and then the product was extracted into 0.3 M $Na_2S_2O_5$ (3x 100 mL). The pH of the combined aqueous layers was adjusted to ~9 with solid Na_2CO_3, and the product was extracted into CH_2Cl_2. The organic layers were dried over $MgSO_4$ and the solvent was evaporated under reduced pressure to give the product as a white solid. Yield: 2.99 g (54%). ^{1}H NMR ($CDCl_3$, 500 MHz) δ (ppm):

10.20 (s, 1H), 8.91 (d, *J* = 4.9 Hz, 1H), 8.84 (dd, *J* = 1.5, 0.9 Hz, 1H), 8.59 (d, *J* = 4.9 Hz, 1H), 8.29 (bs, 1H), 7.74 (dd, *J* = 4.9, 1.6 Hz, 1H), 7.21 (ddd, *J* = 4.9, 1.7, 0.8 Hz, 1H), 2.48 (s, 3H).

4'-methyl-2,2'-bipyridine-4-carboxylic acid (mcb).[5] dmb-CHO (0.51 g, 2.59 mmol) was suspended in 95% EtOH (21 mL), and $AgNO_3$ (0.49 g, 2.87 mmol) dissolved in 5.5 mL of water was then added to it. 1 M NaOH (11.5 mL) was added dropwise over 15 min, forming a black precipitate (Ag_2O) and a metallic silver coating on the walls of the flask. The reaction was stirred at room temperature for 24 h, and then the EtOH was evaporated under reduced pressure. The remaining solution was filtered to remove Ag and Ag_2O, and the solid was washed with 2 M NaOH and water. The filtrate was washed with CH_2Cl_2 (2x 80 mL), its pH was taken to ~3 with HCl, when a fine white solid began to precipitate. The suspension was cooled down overnight, and the product was collected by vacuum filtration. Yield: 0.15 g (27%). ^{1}H NMR (d_6-DMSO, 500 MHz) δ (ppm): 13.8 (bs, 1H), 8.89 (dd, *J* = 4.9, 0.7, 1H), 8.82 (dd, *J* = 1.6, 0.8 Hz, 1H), 8.57 (dd, *J* = 4.9, 0.5, 1H), 8.26 (bs, 1H), 7.85 (dd, *J* = 5.0, 1.6 Hz, 1H), 7.32 (ddd, *J* = 5.0, 1.7, 0.8 Hz, 1H), 2.42 (s, 3H).

Bis(2,2'-bipyridine) mono(4'-methyl-2,2'-bipyridine-4-carboxylic acid) ruthenium(II) hexafluorophosphate, $[Ru(bpy)_2(mcb)](PF_6)_2$ (Rumcb). In a nitrogen-filled glovebox, $Ru(bpy)_2Cl_2$ (97 mg, 0.2 mmol) was dissolved in 20 mL of MeOH, and a solution of AgOTf (0.11 g, 0.42 mmol) in 3 mL of MeOH was added to it. The mixture was stirred in the dark at room temperature for 4 h; after this time, it was filtered through celite and solid mcb (54 mg, 0.25 mmol) was added. The solution was refluxed under nitrogen overnight. After cooling down, the mixture was filtered through celite again and the solvent was removed at reduced pressure. The solid was purified using a neutral alumina column:

the product eluted with MeCN/KNO_3 (aq, sat) 5:1. The solvent was evaporated, the residue taken up in a small volume of water, and KPF_6 (aq, sat) was added to precipitate the product. The solid was collected by vacuum filtration, washed with water and ether, and recrystallized by ether diffusion into acetonitrile or acetone (this procedure gave X-ray quality crystals). ^{1}H NMR (d_3-MeCN, 500 MHz) δ (ppm): 8.89 (d, *J* = 1.2 Hz, 1H), 8.54 (bs, 1H), 8.51 (dt, *J* = 8.2, 0.9 Hz, 4H), 8.07 (m, 4H), 7.91 (dd, *J* = 5.8, 0.6 Hz, 1H), 7.78 (dd, *J* = 5.8, 1.7 Hz, 1H), 7.73 (m, 4H), 7.58 (d, *J* = 5.8 Hz, 1H), 7.42 (m, 4H), 7.29 (ddd, *J* = 5.8, 1.7, 0.6, 1H), 2.57 (s, 3H). HRMS (ESI-TOF) m/z: $[M–2PF_6]^{2+}$ Calcd for $C_{32}H_{26}N_6O_2Ru$ 314.0585; Found 314.0595; $[M–PF_6]^+$ Calcd for $C_{32}H_{26}N_6O_2RuPF_6$ 773.0811; Found 773.0818.

Bis(4,4'-bis(trifluoromethyl)-2,2'-bipyridine) mono(4'-methyl-2,2'-bipyridine-4-carboxylic acid) ruthenium(II) hexafluorophosphate, $[Ru(btfmb)_2(mcb)](PF_6)_2$ (Ru^Fmcb). In a nitrogen-filled glovebox, $Ru(btfmb)_2Cl_2$ (99 mg, 0.13 mmol) was dissolved in MeOH (20 mL), and AgOTf (80 mg, 0.31 mmol) were added. The mixture was shielded from light and stirred at room temperature for 24 h. After this time, it was filtered through a celite pad and combined with mcb (38 mg, 0.18 mmol). The solution was refluxed under nitrogen, in the dark, for 48 h. After it cooled down, the reaction mixture was filtered through a celite pad, and the solvent was removed at reduced pressure. The residue was loaded onto a neutral alumina column, initially eluting with MeCN, then adding a saturated solution of KNO_3; the product eluted with MeCN/KNO_3 (aq, sat) 5:1. The fractions containing the product were combined, the solvent was evaporated and the solid taken up in a small volume of water. KPF_6 (aq, sat) was added to precipitate the

product. The solid was collected by vacuum filtration, washed with water and ether. ^{1}H NMR (d_3-MeCN, 500 MHz) δ (ppm): 9.00 (s, 5H), 8.60 (bs, 1H), 8.05 (m, 3H), 8.01 (d, *J* = 5.9 Hz, 1H), 7.84 (dd, *J* = 5.6, 1.5 Hz, 1H), 7.72 (m, 4H), 7.64 (dd, *J* = 5.6, 0.4 Hz, 1H), 7.51 (d, *J* = 5.9 Hz, 1H), 7.28 (dd, *J* = 5.9, 1.0 Hz, 1H), 2.58 (s, 3H). HRMS (ESI-TOF) m/z: [M–2PF_6]$^{2+}$ Calcd for $C_{36}H_{22}N_6O_2F_{12}Ru$ 450.0333; Found 450.0337; [M–PF_6]$^+$ Calcd for $C_{36}H_{22}N_6O_2F_{12}RuPF_6$ 1045.0308; Found 1045.0334.

(μ-hydroxo)bis(μ-acetato)bis[hydrotris(1-pyrazolyl)borato]diiron(III) triflate, [(Tp)$_2$Fe$_2$(OH)(μ-O$_2$CCH$_3$)$_2$])(OTf).[2] $(Tp)_2Fe_2(\mu\text{-}O_2CCH_3)_2$ (0.48 g, 0.71 mmol) was dissolved in 250 mL of diethyl ether, and to it, 0.25 M HOTf in diethyl ether[i] was added dropwise, while stirring. The solution went from golden-brown to yellow, and a yellow precipitate formed, which was collected by vacuum filtration and washed with copious amounts of ether. The solid was recrystallized by ether diffusion into acetone, to give X-ray quality crystals. Anal. Calcd for $C_{23}H_{27}N_{12}B_2O_8Fe_2F_3S \cdot (CH_3)_2CO$: C, 35.41; H, 4.00; N, 19.06. Found: C, 35.44; H, 3.77; N, 19.22.

5.2.2. Physical Characterization

X-ray structure determination. Single-crystal X-ray diffraction data were acquired, and the structures were solved, by Dr. Richard Staples at the X-ray Facility of Michigan State University.

[i]Diethyl ether was cooled in an ice bath, and HOTf was added dropwise, while stirring. The solution was dried over $MgSO_4$ before using.

UV-visible absorption spectroscopy. All spectra were acquired using a Cary 50 spectrophotometer. The samples were prepared using spectrophotometric grade solvents, and placed in 1 cm quartz cuvettes.

Steady-State Emission and Time-Resolved Emission and Absorption. All samples were prepared in an argon-filled glovebox, using spectrophotometric acetonitrile that was freeze-pump-thaw degassed prior to use. Air-free cells for these experiments were made in-house by attaching Kontes valves to 1 cm quartz cuvettes (FireflySci).

For both steady-state and time-resolved emission spectroscopy, the absorbance of the sample at the maximum of the MCLT band was kept between 0.1 and 0.2. This was not the case for Stern-Volmer quenching studies (*vide infra*).

Steady-state emission spectra were collected using a Horiba Fluorolog-3 fluorimeter and corrected for instrumental response using a NIST standard of spectral irradiance (Optronic Laboratories, Inc., OL220 M tungsten quartz lamp). To compensate for the inner-filter effect, spectra were further corrected as shown in eq 4.1.[6] Zero-point energies (E_0) were calculated using eq 3.2, as previously described.

Nanosecond time-resolved emission experiments were performed using an Nd:YAG laser spectrometer that has been described previously,[7,8] upgraded using an Opotek Vibrant 355 LD tunable pulsed laser system which generates nominally 5 ns laser pulses. Excitation energies were in the range of 1-3 mJ per pulse. All data were checked for linearity with respect to pump power. The data were fit to a single or double exponential decay to extract the observed rate constant(s) (k_{obs}).

The aforementioned pulsed laser system was also used for transient absorption experiments, coupled to an LP980 laser flash photolysis system (Edinburgh Instruments).

Time-resolved emission experiments in the picosecond to nanosecond timescale were carried out using a time-correlated single photon counting (TCSPC) instrument.[ii] The light source is a CW passively mode-locked, diode-pumped Nd:YVO_4 laser (Spectra Physics Vanguard) with 13 ps pulses; this laser's output pumps a cavity-dumped dye laser (Coherent 702-2), which generates 5 ps pulses in the 430-850 nm range. A detailed description of this setup has been previously reported.[9]

Electrochemistry. A CHI 620B electrochemical analyzer was used, along with a three-electrode setup, consisting of a Pt working electrode, a Pt wire counter electrode, and a Ag wire reference electrode. Ferrocene was added as an internal standard; all potentials are reported versus the ferrocene/ferrocenium couple. Data were acquired by cyclic voltammetry (CV) and differential pulse voltammetry (DPV); the scan rate for the CV measurements was 50 mV/s and the scan rate and pulse width for the DPV measurements were 20 mV/s and 50 mV, respectively. Values for $E_{1/2}$ obtained by both techniques were comparable; the reported potentials were obtained from the DPV peak values.[10]

5.2.3. Geometry Optimizations

Calculations were performed using Gausian 03.[11] Geometry optimizations were done on the ground state using a spin unrestricted formalism at the B3LYP/LANL2DZ

[ii]Big Thanks to Prof. Gary Blanchard for his assistance in the collection of these data.

level of theory.[12] No symmetry restrictions were placed on the geometry optimizations.

The input files were prepared using the x-ray crystal structures of $(Tp)_2Fe_2O(O_2CCF_3)_2$, $(Tp)_2Fe_2O(O_2CCHCl_2)_2$ (as reported by Weldon et al.)[2] or $[(Tp)_2Fe_2(OH)(O_2CCH_3)_2](OTf)$ (shown in this chapter) and of $[Ru(bpy)_2(mcb)]^{2+}$, (shown in this chapter).

5.2.4. Bimolecular Quenching Studies

Samples for Stern-Volmer studies were prepared in an argon-filled glovebox, using spectrophotometric acetonitrile that was freeze-pump-thaw degassed prior to use. Variable volumes of a stock solution of each acceptor were combined with 1.00 mL of a stock solution of the Ru(II) donor (with an absorbance ~0.5 at the excitation wavelength) and the mixture was taken to a final volume of 5.00 mL. All samples contained $TBAPF_6$ (0.075 M), added as a supporting electrolyte.[13,14]

5.3. Results and Discussion

5.3.1. Syntheses

In Chapter 4, the results of Stern-Volmer studies using $[Ru(tmb)_2(bpyac)](PF_6)_2$ and $[Ru(tmb)_2(bpyester)](PF_6)_2$ with varying concentrations of $[(Tp)_2Fe_2(OH)(O_2CCH_3)_2](ClO_4)$ were discussed. The most interesting feature of these data (Figure 4.17) was the static quenching observed in the case of the acid, which was strongly suggestive of a carboxylate bridge swapping taking place in the samples. Due to the instability of the carboxylate group on bpyac and bpyester, it was necessary to find a

different bipyridyl ligand to attach the donor and the acceptor. The most straightforward option was to use 4'-methyl-2,2'-bipyridine-4-carboxylic acid (mcb) and 4'-methyl-4-ethylcarboxy-2,2'-bipyridine (mcbEt), which are known, stable molecules.[4,5,15,16] The main concern regarding these ligands was whether mcb would allow for the formation of the D-A assembly: a geometry optimization of such assembly, using the X-ray crystal structures of $[Ru(bpy)_2(mcb)]^{2+}$ and $(Tp)_2Fe_2O(O_2CCH_3)_2$, showed that the sterics of the system would not be a concern, and thus the syntheses were pursued.

The structures of all four donors used in this chapter are presented in Figure 5.1. The synthesis and characterization of Ru^FmcbEt[16] and Rumcb[15] were previously reported. These compounds were prepared following the same methods that were discussed in Chapter 3. It is worth mentioning that the CF_3 groups in 4,4'-bis(trifluoromethyl)-2,2'-bipyridine (btfmb) make the metal center in the $\{Ru(btfmb)_2\}$ fragment very electron deficient, and it takes a longer time to remove the chlorides coordinated to the starting material (RuL_2Cl_2) than it does when bpy is used instead. The CF_3 groups also increase the solubility of Ru^Fmcb and Ru^FmcbEt in most solvents, which has prevented us from obtaining X-ray quality crystals of these compounds. Oils have been obtained in most cases, with some solvent combinations yielding very fine powders. Efforts to grow crystals are still ongoing.

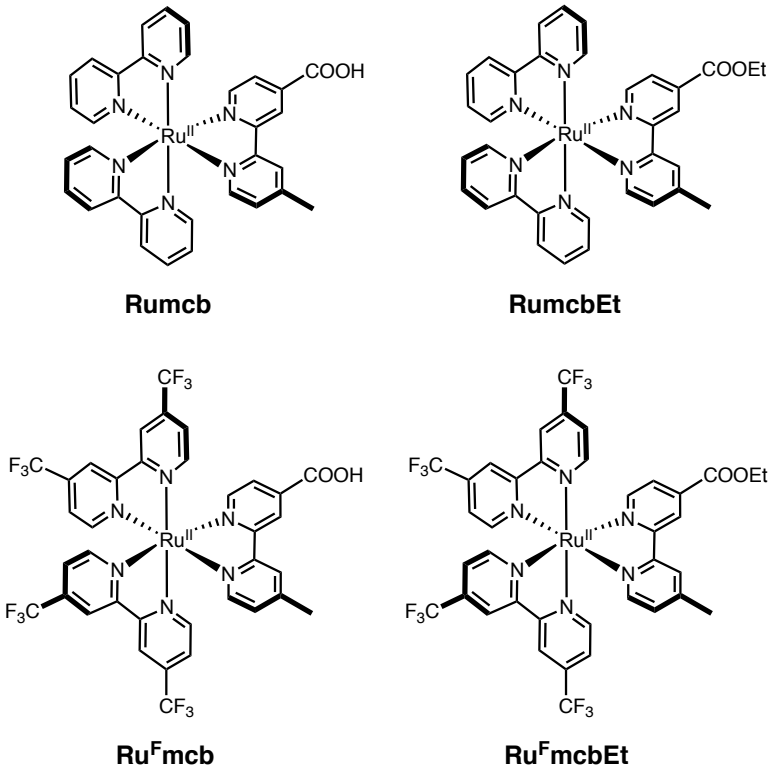


Figure 5.1. Donors used in this chapter, both in their acid and ester forms.

The structures of the acceptors used in this chapter are shown in Figure 5.2. For the first set of Stern-Volmer studies, we used a legacy sample of $[(Tp)_2Fe_2(OH)(O_2CCH_2Cl)_2](ClO_4)$. After that, it was necessary to synthesize more of this compound

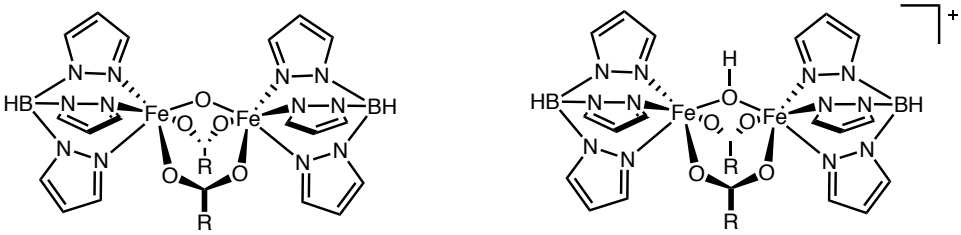


Figure 5.2. Diiron(III) cores used as acceptors in this chapter.

The hydroxo-bridged dimers, $[(Tp)_2Fe_2(OH)(O_2CR)_2]^+$, have previously been prepared as the perchlorate salt, by reacting $(Tp)_2Fe_2(OH)(O_2CR)_2$ with perchloric acid.[2,17] However, perchlorate salts may be explosive, and the use of $HClO_4$ requires a specially-rated fume hood, due to its toxicity.[18] To circumvent these issues, a different strong acid, also containing a weakly-coordinating anion, was necessary. Both HPF_6 and HOTf were tested: HPF_6 was the preferred option, because all the Ru(II) donors in this dissertation are PF_6^- salts. Unfortunately, this acid is sold as an aqueous solution (~55% by weight) by most vendors, and water must be excluded from the protonation reaction for it to work. Triflic acid, on the other hand, may be purchased in 98% (or higher) purity, and the ethereal solution is easily dried with $MgSO_4$.

Adapting the published procedure to these new conditions, $[(Tp)_2Fe_2(OH)(O_2CCH_3)_2](OTf)$ was satisfactorily obtained. Conversely, it was not possible to isolate $[(Tp)_2Fe_2(OH)(O_2CCH_2Cl)_2](OTf)$; upon addition of a few drops of HOTf, the initially yellow precipitate turned red/orange almost immediately. It was attempted to collect the solid as soon as it was formed, washing it with large volumes of diethyl ether, but it changed color after a couple of minutes. The UV-vis spectra of all these batches revealed that only $[Fe(Tp)_2]^+$ had formed. After several failed reactions, it was decided to use $[(Tp)_2Fe_2(OH)(O_2CCH_3)_2](OTf)$ as the acceptor for all the remaining quenching studies.

5.3.2. Crystal Structures

Using ether diffusion into solutions of the compounds in acetonitrile or acetone, X-ray quality crystals of $[Ru(bpy)_2(mcb)](PF_6)_2$, $[Ru(bpy)_2(mcb)](PF_6)_2$ and $[(Tp)_2Fe_2(OH)(O_2CCH_3)_2](OTf)$ were obtained. The crystallographic data for all three compounds are compiled in Table 5.1.

For Rumcb, two molecules of water were found; one of them was at 100% occupancy, while the other one, and an acetonitrile molecule were refined as 0.23:0.77 occupancy. The presence of water in the crystal structure is not surprising, considering the carboxylic acid functionality.

Table 5.1. Crystallographic data for Rumcb, RumcbEt, and $[(Tp)_2Fe_2(OH)(O_2CCH_3)_2](OTf)$.

	Rumcb	**RumcbEt**	**$[(Tp)_2Fe_2(OH)(O_2CCH_3)_2](OTf)$**
empirical formula	$C_{33.56}H_{30.78}N_{6.78}O_{3.22}F_{12}P_2Ru$	$C_{40}H_{43}N_7O_3F_{12}P_2Ru$	$C_{26}H_{33}B_2F_3Fe_2N_{12}O_9S$
formula weight	971.57	1060.82	880.02
temperature (K)	173(2)	173(2)	173(2)
crystal color, habit	red, chunks	orange, plates	orange, blocks
crystal system	monoclinic	orthorhombic	orthorhombic
space group	$P2_1/c$	$Pna2_1$	$P2_12_12_1$
cell dimensions:			
a (Å)	11.3225(7)	38.063(2)	12.3365(8)
b (Å)	24.7802(15)	9.7328(6)	15.2091(10)
c (Å)	13.6503(8)	12.1829(7)	19.9748(14)
Volume (Å^3)	3814.9(4)	4513.2(5)	3747.8(4)
Z	4	4	4
D_{calc} (g cm^{-3})	1.692	1.561	1.560
goodness of fit (F^2)	1.045	1.047	1.037
R_1 ($I > 2(I)$)	0.0523	0.0616	0.0461

The crystal structure of Rumcb has been previously reported,[15] with those metrics matching ours (interestingly, despite having obtained their crystals from a water/acetonitrile solution, Nickita et al. obtained a trihydrate, with no acetonitrile co-crystalized). The structure of RumcbEt had not been reported before. Its bond lengths and angles (see appendix) are well within error of those of Rumcb, and these two compounds are also comparable with other Ru(II) polypyridyls (see Chapter 3). ORTEP drawings of both these compounds are shown in Figure 5.3.

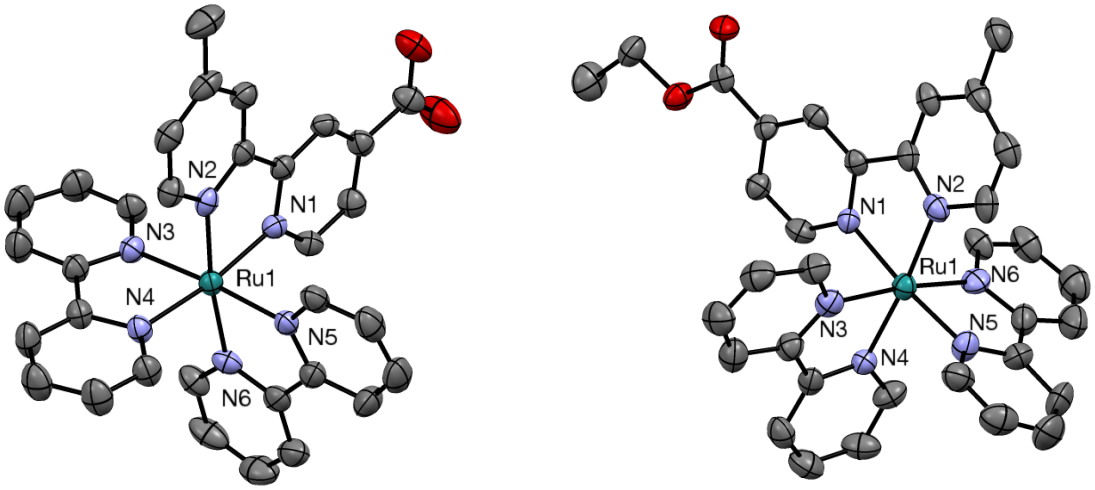


Figure 5.3. ORTEP drawings of $[Ru(bpy)_2(mcb)]^{2+}$ (left) and $[Ru(bpy)_2(mcbEt)]^{2+}$ (right) obtained from single-crystal X-ray structure determinations. Hydrogens, counterions, and solvent molecules are omitted for clarity. Atoms are represented as 50% probability ellipsoids. The lists of bond lengths and angles are compiled in the appendix to this chapter.

The crystal structure of $[(Tp)_2Fe_2(OH)(O_2CCH_3)_2](OTf)$ is shown in Figure 5.4; the bond lengths and angles of the core are within experimental error of those for $[(Tp)_2Fe_2(OH)(O_2CCH_3)_2](ClO_4)$,[17] as was expected.

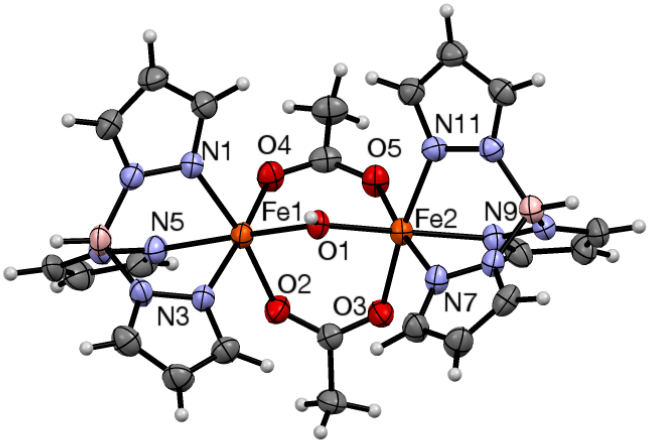


Figure 5.4. ORTEP drawing of $[(Tp)_2Fe_2(OH)(O_2CCH_3)_2]^+$ obtained from single-crystal X-ray structure determination. Atoms are represented as 50% probability ellipsoids. Hydrogen positions were calculated geometrically, except for the H on O1, which was found by difference Fourier methods and refined isotropically. The triflate ion and crystallization solvent are omitted for clarity. The full list of bond lengths and angles is included in the appendix to this chapter.

5.3.3. Bimolecular Quenching Studies

In their work on electron and energy transfer between Tp-capped diferric cores and Ru(II) polypyridyls, Weldon et al. showed that the hydroxo-bridged cores are faster quenchers than the oxo-bridged ones, even at constant ΔG_0^{ET}.[2] Based on this, we wanted to work with two D-A pairs that had the same driving force for electron transfer. When this was not possible, we chose to have a larger ΔG_0^{ET} for the D-A system with the oxo-bridged dimer, to see if the quenching was still more efficient for the D-A pair with a hydroxo-bridged acceptor.

Initially, the acceptors used for these studies were $[(Tp)_2Fe_2(OH)(O_2CCH_2Cl)_2](ClO_4)$ and $(Tp)_2Fe_2O(O_2CCHCl_2)_2$; the reduction potential for $Fe^{III/II}$ in either of these cores is the same,[2] which in turn means that the driving force for electron transfer from a Ru(II) donor to these acceptors would be the same. Using the

same rationale as Weldon et al., we wanted to keep ΔG_0^{ET} constant, in an effort to simplify the analysis of these systems' photophysics. Unfortunately, we only had a small legacy sample of $[(Tp)_2Fe_2(OH)(O_2CCH_2Cl)_2](ClO_4)$, and attempts to prepare more were unsuccessful (*vide supra*). Instead, we used $[(Tp)_2Fe_2(OH)(O_2CCH_3)_2](OTf)$ for most of the quenching experiments; the reduction potential of this core is more negative than that of $(Tp)_2Fe_2O(O_2CCHCl_2)_2$ (see Table 5.2), which means that ΔG_0^{ET} is larger for the oxo-bridged acceptor (provided that the donor remains the same).

Table 5.2. Driving forces for electron transfer for the D-A pairs studied in this chapter.

bridges (acceptor)	$E(Fe^{III/II})$ (V)	ΔG_0^{ET} Rumcb (eV)	ΔG_0^{ET} Ru^Fmcb (eV)
OH/O_2CCH_2Cl	–0.89	–0.33	--
OH/O_2CCH_3	–1.09	–0.13	0.44
O/O_2CCHCl_2	–0.87	–0.31	0.22
O/O_2CCF_3	–0.68	--	0.03

Bimolecular quenching studies using Rumcb and RumcbEt as the donors, and $[(Tp)_2Fe_2(OH)(O_2CCH_2Cl)_2](ClO_4)$ and $(Tp)_2Fe_2O(O_2CCHCl_2)_2$ as the acceptors were carried out to investigate if the same static quenching component that was observed in Chapter 4 manifested itself in these systems. The data in Figure 5.5 confirm that there is only dynamic quenching taking place between RumcbEt and the diiron(III) cores: the results for SSEm and TREm are within error of each other for each D-A pair, which indicates that the quenching is dynamic (see Chapter 2). In contrast, the data on Figure 5.6 show a drastic difference between the free acid and the ester analogues: just as was seen in Chapter 4, the SSEm data for Rumcb is noticeably different from both the TREm

data for Rumcb and all the data for RumcbEt. This is strong evidence of static quenching[iii] taking place when Rumcb interacts with the iron(III) dimers.

At high concentrations of the quencher, the SSEm data in Figures 5.5 and 5.6 become less reliable, due to the high absorbances of the samples. These samples were very optically dense, and some of the light emitted was reabsorbed before it could reach the detector, to an extent that could not be corrected for using eq 4.1. As a result, the Stern-Volmer plots show significant scatter, which prevented us from quantitatively analyzing the data. Nevertheless, the observed trends can be interpreted qualitatively.

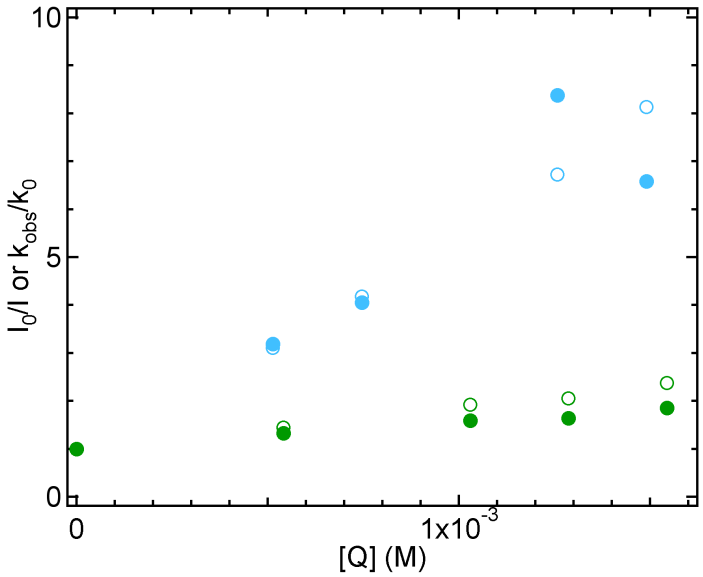


Figure 5.5. Stern-Volmer data for RumcbEt in the presence of $[(Tp)_2Fe_2(OH)(O_2CCH_2Cl)_2](ClO_4)$ (blue) and with $(Tp)_2Fe_2O(O_2CCHCl_2)_2$ (green). Full circles: SSEm data, open circles: TREm data.

On the other hand, the fact that the TREm data for Rumcb and RumcbEt are comparable suggests that the only processes observed in this timescale are bimolecular.

[iii]Given its similarities with what is described by Lakowicz and other authors (see ref. 6), this type of quenching will be referred to as "static" for most of this chapter. TREm experiments with shorter time resolution showed that this is a misnomer, as will be discussed later.

The TREm data for Rumcb in the presence of $[(Tp)_2Fe_2(OH)(O_2CCH_2Cl)_2](ClO_4)$ and $(Tp)_2Fe_2O(O_2CCHCl_2)_2$ are presented in Figure 5.7; Tables 5.2 and 5.3 compile the relevant parameters for quenching in these systems. These results agree with those obtained by Weldon et al.:[2] the driving force for electron transfer is almost the same for both D-A pairs, and the oxo-bridged core can also engage in FRET with the donor, whereas the hydroxo-bridged core cannot. However, the quenching is faster for the latter, despite having only two available quenching mechanisms (DET and electron transfer). Parsing out the contribution of each mechanism to the quenching process is not trivial; this chapter describes our efforts towards this end.

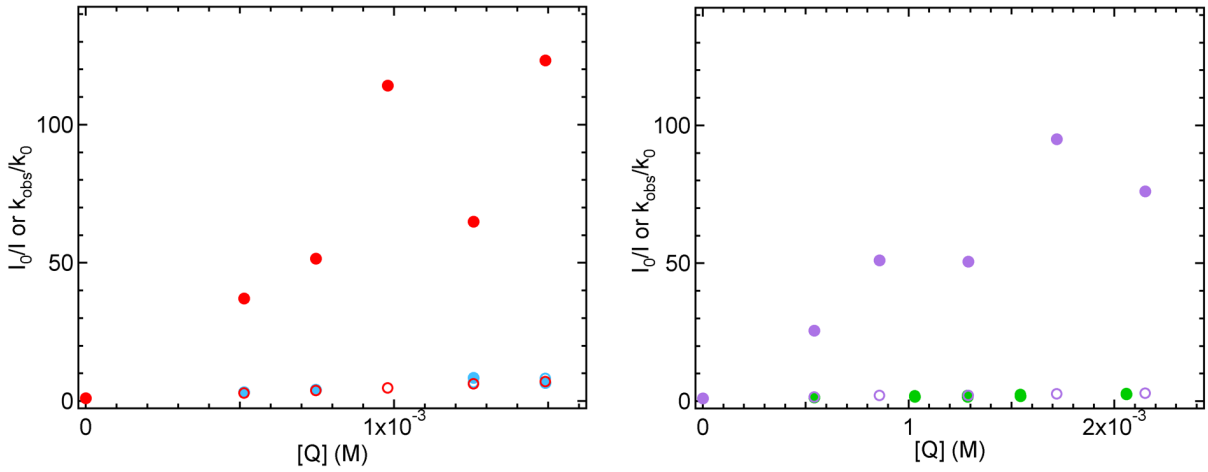


Figure 5.6. Left: Stern-Volmer plots for $[(Tp)_2Fe_2(OH)(O_2CCH_2Cl)_2](ClO_4)$ quenching RumcbEt (blue) and Rumcb (red). Right: data for $(Tp)_2Fe_2O(O_2CCHCl_2)_2$ quenching RumcbEt (green) and Rumcb (purple). Full circles: SSEm data, open circles: TREm data.

Table 5.3. Values of k_q for Rumcb and RumcbEt obtained from Stern-Volmer quenching studies.

	$[(Tp)_2Fe_2(OH)(O_2CCH_2Cl)_2]^+$ k_q (10^9 s^{-1} M^{-1})	$(Tp)_2Fe_2O(O_2CCHCl_2)_2$ k_q (10^9 s^{-1} M^{-1})
Rumcb	3.90	0.85
RumcbEt	3.95	0.71

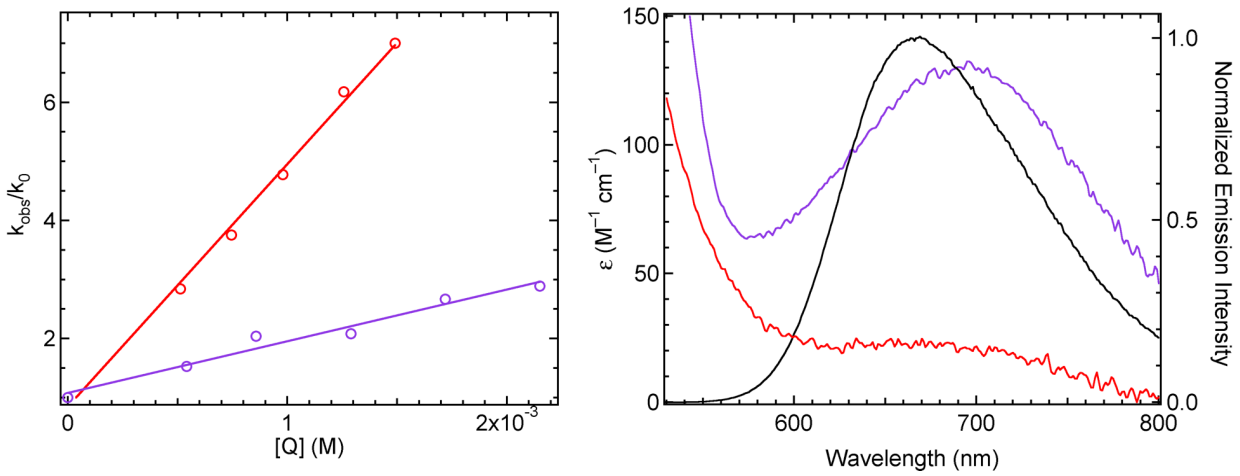


Figure 5.7. Left: Time-resolved emission results for Rumcb with variable concentrations of $[(Tp)_2Fe_2(OH)(O_2CCH_2Cl)_2](ClO_4)$ (red circles) and $(Tp)_2Fe_2O(O_2CCHCl_2)_2$ (purple cirlces). The solid lines are fits to the Stern-Volmer equation. Right: Overlay of the steady-state emission spectrum of RumcbEt (black trace) and the electronic absorption spectra of $(Tp)_2Fe_2O(O_2CCHCl_2)_2$ (purple trace) and $[(Tp)_2Fe_2(OH)(O_2CCH_2Cl)_2](ClO_4)$ (red trace).

These data were very informative with respect to the possibility of bridge swapping taking place under Stern-Volmer conditions. Additionally, the time-resolved emission data for these systems allowed us to study the bimolecular quenching for each D-A pair. However, working under pseudo-first order conditions (see Chapter 2) led to optically dense solutions, which intensified the inner filter effect past what can be corrected using eq 4.1.[19] Considering that we are interested in the unimolecular processes (i.e., those that take place after the bridge exchange), it is not necessary to use such high concentrations of the quencher. The rest of our studies were then carried out using acceptor concentrations that kept the absorbance of the samples below 0.5. Additionally, $[(Tp)_2Fe_2(OH)(O_2CCH_3)_2](OTf)$ was used, as previously explained. The different concentration ranges used in either set of experiments can be seen in the Stern-Volmer plots of Figure 5.8. While the concentrations are much lower for the second experiment,

the OH-core still seems to be a more efficient quencher than its oxo counterpart, despite having a smaller driving force for electron transfer. This agrees with the results reported by Weldon et al.[2]

The normalized steady-state emission data for Rumcb with and without the quenchers are shown in Figure 5.9. In the presence of the OH-bridged quencher, the emission spectrum maximum shifts red ~20 nm, which is consistent with the formation of a D-A assembly (see Chapter 4). Furthermore, the emission spectrum of this assembly is very similar to that of RumcbEt (see Figure 5.36, appendix), suggesting that the carboxylate group is responsible for this shift of the emission maximum. Surprisingly, no shift is observed for Rumcb when combined with the oxo-bridged quencher, which suggests that either the energetics of the luminophore are not affected by the formation of the assembly, or that the observed emission is predominantly due to the unquenched donor.

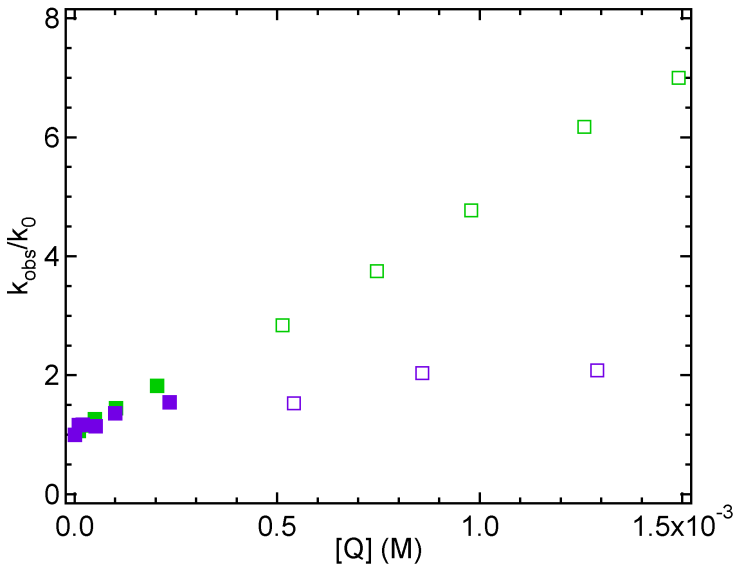


Figure 5.8. Time-resolved emission data for Rumcb in the presence of $(Tp)_2Fe_2O(O_2CCHCl_2)_2$ (purple), $[(Tp)_2Fe_2(OH)(O_2CCH_2Cl)_2]^+$ (green, open squares), and $[(Tp)_2Fe_2(OH)(O_2CCH_3)_2]^+$ (green, full squares). See text for details.

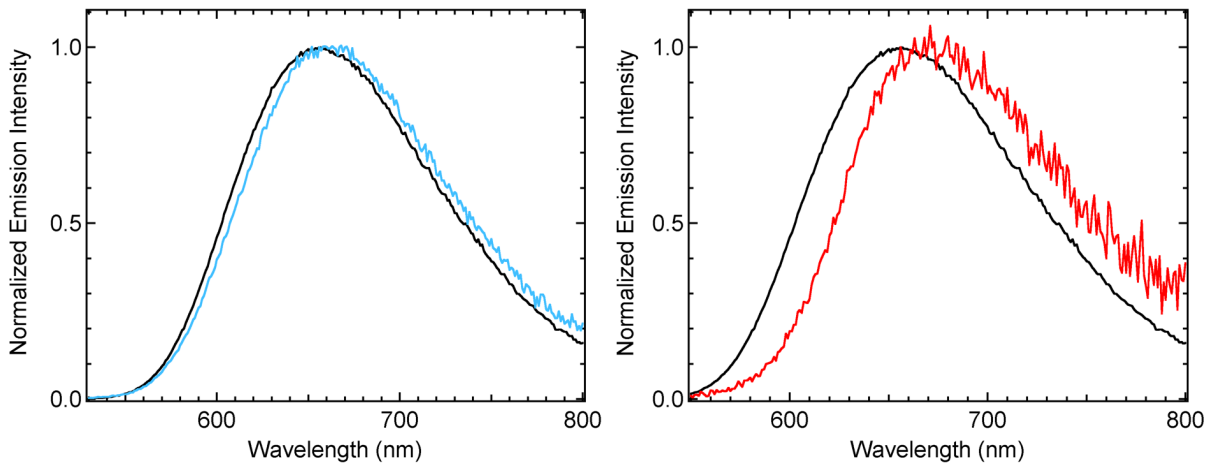


Figure 5.9. Normalized steady-state emission spectra for Rumcb without quencher (black trace). Left: in the presence of $(Tp)_2Fe_2O(O_2CCHCl_2)_2$ 51 μM (blue trace). Right: in the presence of $[(Tp)_2Fe_2(OH)(O_2CCH_3)_2](OTf)$ 41 μM (red trace).

After the bridge exchange takes place, part of the electronic density on the carboxylate group (and consequently, on the mcb ligand) is claimed by the diiron(III) core, which will alter the energetics of the ^{3}MLCT excited state that is localized on the mcb. One would expect that the diferric core that is easier to reduce (i.e., is more electronegative) will affect the energetics of the donor's excited state more. In our case, since the oxo-bridged acceptor has a more positive reduction potential than the hydroxo-bridged one, a larger shift of the emission spectrum would be expected in the presence of the former, which does not seem to be the case, based on the spectra in Figure 5.9. The reason for the red shift observed in the presence of $[(Tp)_2Fe_2(OH)(O_2CCH_3)_2](OTf)$ must lie elsewhere. The most reasonable explanation is that the hydroxo-bridged acceptor quenches the emission from free Rumcb (i.e., that which did not take part on the bridge exchange) further than the oxo-bridged dimer does. Thus, the emission observed for the latter is dominated by the signal from unbound Ru(II), whereas for the former, a larger

contribution from the D-A assembly is observed. The steady-state emission traces in Figure 5.10 lend credence to this argument: even when the concentration of either acceptor is the same, the emission from Rumcb is quenched to a larger extent in the presence of $[(Tp)_2Fe_2(OH)(O_2CCH_3)_2](OTf)$.[iv] The same effect can be seen in the TCSPC traces from Figure 5.11, where the emission from the long-lived component is more intense for the oxo-bridged system.

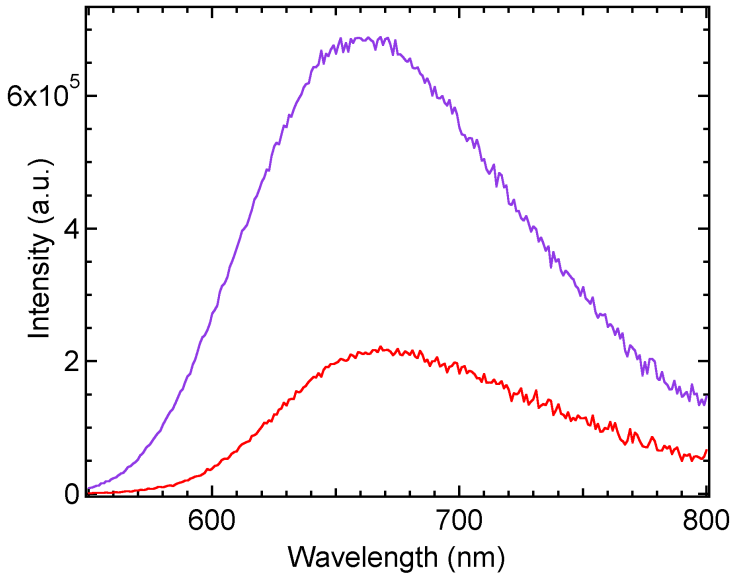


Figure 5.10. Steady-state emission data for Rumcb in the presence of 20 μM $(Tp)_2Fe_2O(O_2CCHCl_2)_2$ (purple trace), and 21 μM $[(Tp)_2Fe_2(OH)(O_2CCH_3)_2](OTf)$ (red trace).

The TREm traces for Rumcb in the presence of the acceptors showed a sharp feature at very short times, which we suspected was due to intramolecular processes, but was too fast to be studied with our instrument. Using TCSPC, it was possible to observe the time-resolved emission traces for these D-A systems at shorter times, as seen in Figure

[iv]The absorbances of both samples at the excitation wavelength were comparable, so inner filter effects cannot account for such a large difference as observed here.

5.11. Unfortunately, the observed signal was very weak, likely because of the low emission quantum yield of the assembly, and this made any lifetime determinations very inaccurate. It may be possible to study the photophysics of these systems using ultrafast transient absorption spectroscopy; work along these lines is underway.

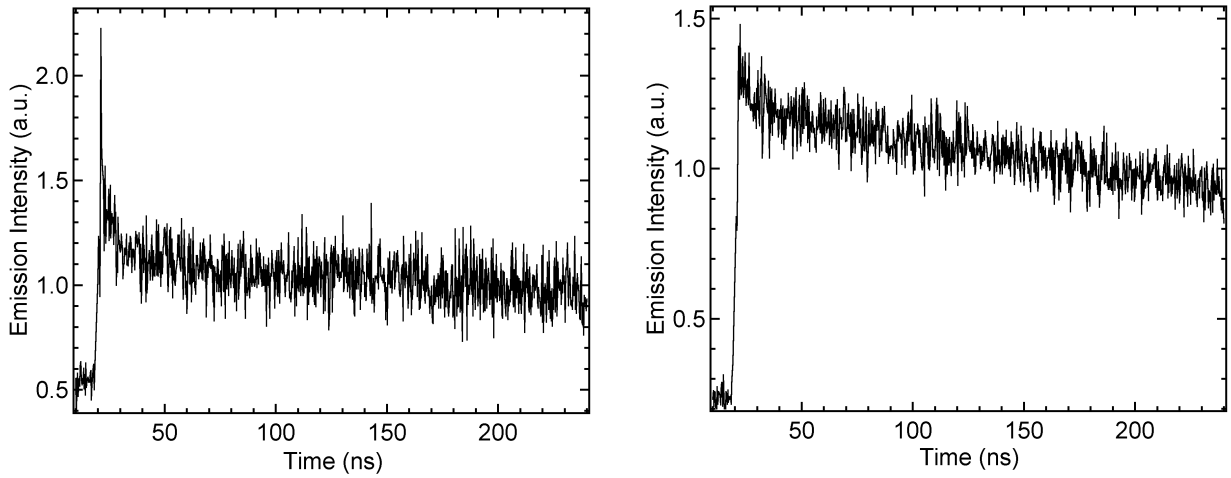


Figure 5.11. TCSPC data for Rumcb with 0.17 mM $[(Tp)_2Fe_2(OH)(O_2CCH_3)_2](OTf)$ (left) and 0.23 mM $(Tp)_2Fe_2O(O_2CCHCl_2)_2$ (right).

While Rumcb was able to replace one of the carboxylate bridges in both the oxo- and hydroxo-bridged acceptors, the quenching was too fast to be studied with the instrumentation readily available to us. It was necessary to modify the donor to slow down the quenching. Soler and McCusker[16] had faced a similar situation when working with $[Ru(dmb)_2(mcb)]^{2+}$ and $[Ru(btfmb)_2(mcb)]^{2+}$: the trifluoromethyl groups in btfmb are strongly electron-withdrawing, making the ligand much easier to reduce, and localizing the ^{3}MLCT excited state on that ligand, whereas the methyl groups in dmb make it more electron rich, which in turn localizes the excited state on mcb instead. In their work, the authors observed that the lifetime of a D-A assembly where the donor is $[Ru(dmb)_2(mcb)]^{2+}$ had a lifetime 100 times shorter than the btfmb-based analogue. Based

on the close similarities between their systems and the ones herein, it was decided to use btfmb instead of bpy as the ancillary ligand.

Just as it was the case with Rumcb and RumcbEt, comparing the steady-state emission data for Ru^{F}mcb and Ru^{F}mcbEt suggest that static quenching is taking place in these systems as well (see Figure 5.12 and Figure 5.37, appendix).

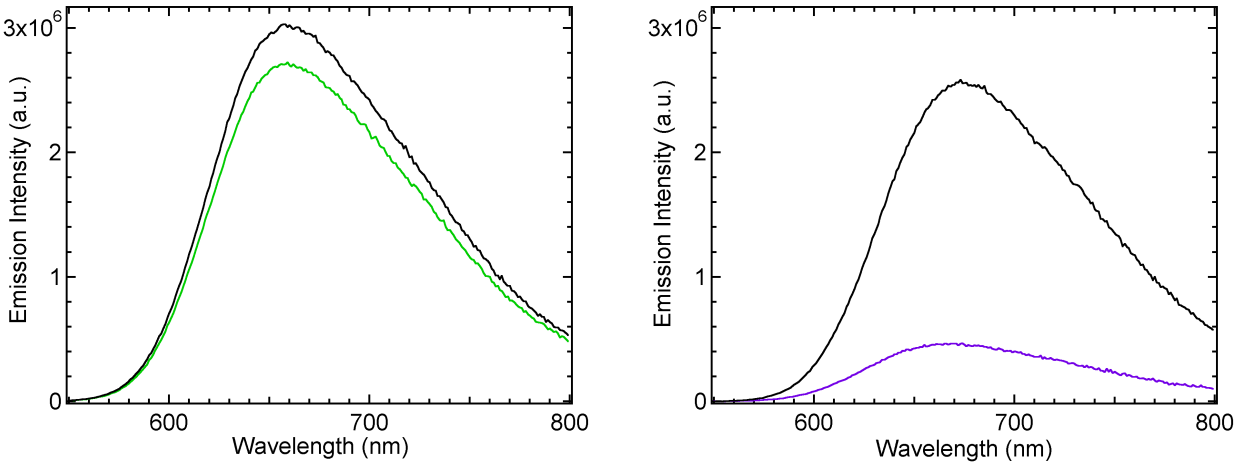


Figure 5.12. Left: Steady-state emission spectrum of Ru^{F}mcbEt alone (black trace) and in the presence of $(Tp)_2Fe_2O(O_2CCHCl_2)_2$ (green trace). Right: Ru^{F}mcb without quencher (black trace) and combined with $(Tp)_2Fe_2O(O_2CCHCl_2)_2$ (purple trace). The concentration of the quencher is the same in both cases.

The steady-state emission spectra of Ru^{F}mcb in the presence of each of the quenchers are shown in Figure 5.13. In the case of $(Tp)_2Fe_2O(O_2CCHCl_2)_2$, there is a blue shift (~10 nm) of the emission maximum; a similar, more pronounced (~20 nm) shift is observed of the hydroxo-bridged quencher. As it happened for the Rumcb-based systems, the spectra of the quenched samples are more similar to the emission spectrum of ester analogue (see Figure 5.38, appendix), again pointing at the carboxylic acid functionality being involved in the shift. In the case of Ru^{F}mcb, as opposed to Rumcb, the SSEm spectra shift to higher energies when the COOH group is not free.

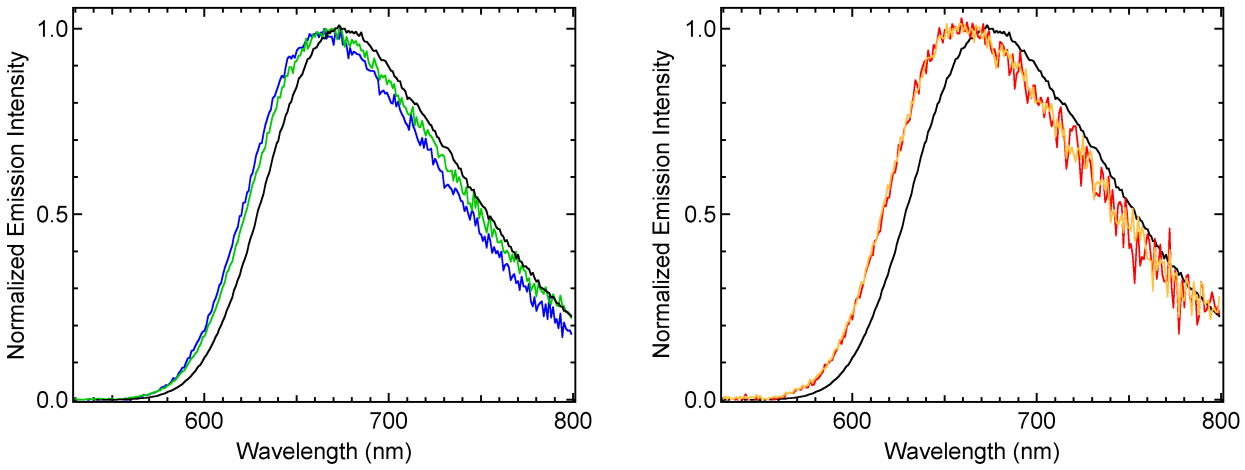


Figure 5.13. Normalized steady-state emission spectra for Ru^{F}mcb without quencher (black trace). Left: in the presence of: $(Tp)_2Fe_2O(O_2CCHCl_2)_2$ 51 μM (green trace) and 0.20 mM (blue trace). Right: in the presence of: $[(Tp)_2Fe_2(OH)(O_2CCH_3)_2](OTf)$ 41 μM (orange trace) and 0.17 mM (red trace).

Analogously to what happened for the Rumcb-based systems, if the hydroxo-bridged acceptor is a more efficient quencher, the SSEm spectrum will have less contribution from free Ru(II) than for the D-A pair with the oxo-bridged core, which could explain the larger shift.

The TREm data require closer inspection. In Figure 5.14, the TREm traces for Ru^{F}mcbEt on its own, and in the presence of both quenchers can be seen. There is no effect on the lifetime in the presence of the oxo-bridged quencher, while the hydroxo-bridged dimer quenches the excited state of Ru^{F}mcbEt, albeit not very efficiently. Considering that ΔG_0^{ET} is positive for both D-A pairs (i.e., electron transfer is not favorable), the lack of quenching is not entirely unexpected. These results will be discussed in sections 5.3.5 and 5.3.6.

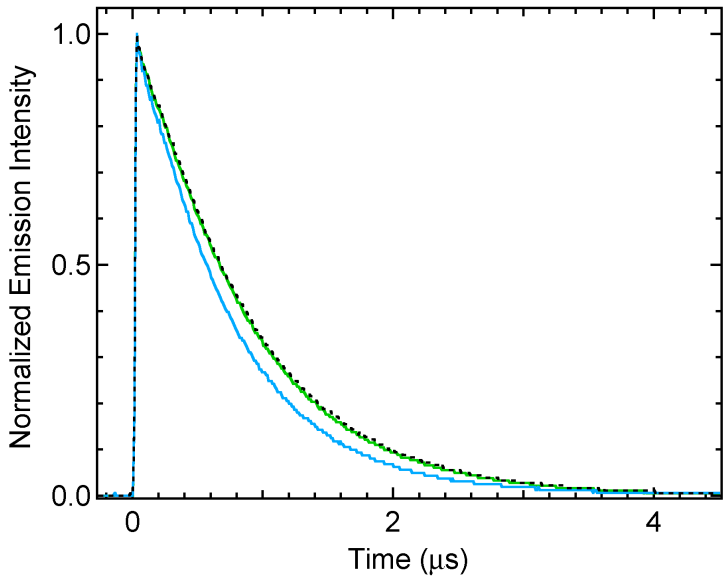


Figure 5.14. Time-resolved emission traces for Ru^{F}mcbEt without quenchers (black, dashed), and in the presence of $[(Tp)_2Fe_2(OH)(O_2CCH_3)_2]^+$ (blue) and $(Tp)_2Fe_2O(O_2CCHCl_2)_2$ (green). The quencher concentrations are comparable in both cases. See text for details.

The data in Figure 5.15 are more surprising: in the presence of $(Tp)_2Fe_2O(O_2CCHCl_2)_2$, the lifetime of Ru^{F}mcb increases, approaching that of Ru^{F}mcbEt. This effect is even more pronounced when $[(Tp)_2Fe_2(OH)(O_2CCH_3)_2]^+$ is used. Additionally, for Ru^{F}mcb in the presence of either quencher there is an extra component at very short times, which is discussed below.

As was discussed in Chapter 4, the free COOH group in Ru^{F}mcb may interact with the solvent, and more importantly, with any trace of water that is present in it. This interaction increases k_{nr}, shortening the lifetime of the excited state. In contrast, Ru^{F}mcbEt does not have such a COOH group, which takes away some vibrational relaxation pathways, lengthening the lifetime of its ^{3}MLCT excited state. In a similar way, when Ru^{F}mcb is combined with one of the diiron(III) cores, bridge swapping takes place, effectively blocking the COOH group. Furthermore, appending the acceptor moiety may

restrict some of the non-radiative relaxation pathways, because the molecule is now larger and more "sluggish". As a consequence, the lifetime of Ru^{F}mcb in the presence of the acceptors is longer, instead of being shortened. Conversely, Ru^{F}mcbEt is quenched by the diferric cores, and thus its lifetime is shortened, albeit much less so than in the case of RumcbEt, which is consistent with the difference in electron transfer driving forces (see Table 5.2). It is unclear if at larger concentrations of the quenchers the lifetime of Ru^{F}mcb would decrease. Stern-Volmer quenching studies for this donor are underway.

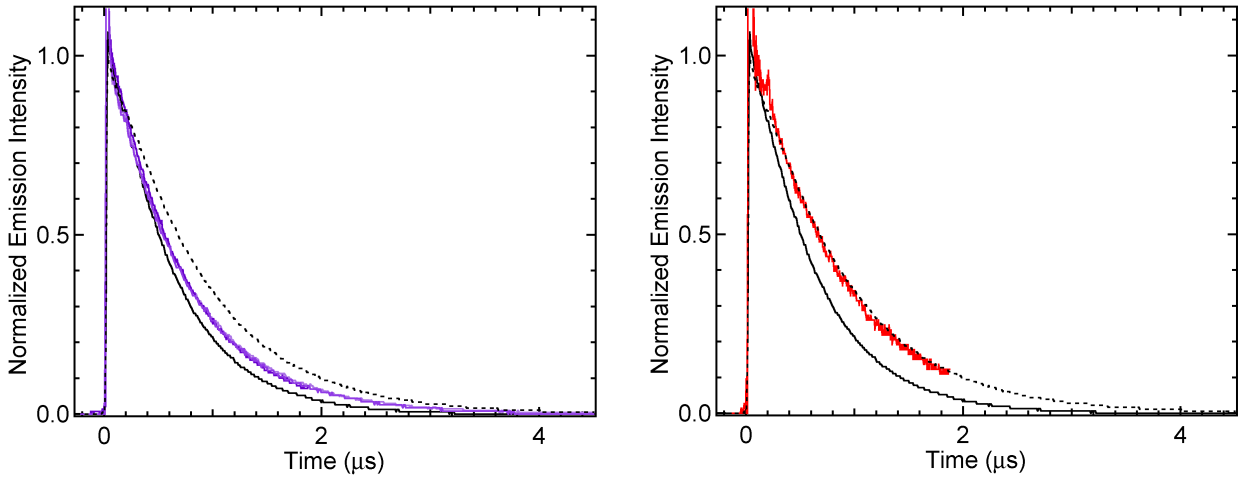


Figure 5.15. TREm data for Ru^{F}mcb in the presence of increasing concentrations of $(Tp)_2Fe_2O(O_2CCHCl_2)_2$ (purple) and $[(Tp)_2Fe_2(OH)(O_2CCH_3)_2]^+$ (red, right). The full black line corresponds to Ru^{F}mcb in the absence of quenchers, and the black dashed trace is for Ru^{F}mcbEt.

Summarizing our findings so far, the SSEm data suggest that bridge exchange is taking place for Rumcb and Ru^{F}mcb in these samples, resulting in the formation of a D-A assembly. Bimolecular quenching is observed; it is more efficient for the bpy-based donors, mainly due to electron transfer and DET being more favorable (see Table 5.2). For both RumcbEt and Ru^{F}mcbEt, the hydroxo-bridged acceptor is a better quencher than its oxo counterpart, just as Weldon et al. had observed.[2] Based on the driving force for

electron transfer, the oxo-acceptors should be better quenchers; moreover, these compounds can also engage in FRET, which is not favorable for the hydroxo-bridged dimers. As a result, it is intriguing that the quenching is more efficient when hydroxo-bridged acceptors are used.

Turning our attention to faster processes, the TREm data for Ru^{F}mcb vs Ru^{F}mcbEt differ noticeably at short times: there is a sharp peak in the traces for Ru^{F}mcb, which is not present for the ester analogue (see Figure 5.16). It is important to highlight that this sharp feature is not merely due to scatter (and it only happens in the Ru^{F}mcb samples). The inset in Figure 5.16 compares the signal with the instrument response function (IRF) of our setup:[v] while it is clear that the signal and the IRF are in the same timescale, which prevents us from extracting a lifetime, it is also easy to see that the two traces are different. In short, in the Ru^{F}mcb samples there is a faster component, but it is too fast to be studied with this instrument.

[v]This trace was obtained by suspending a small amount of powdered coffee creamer in water and measuring the lifetime of such a sample.

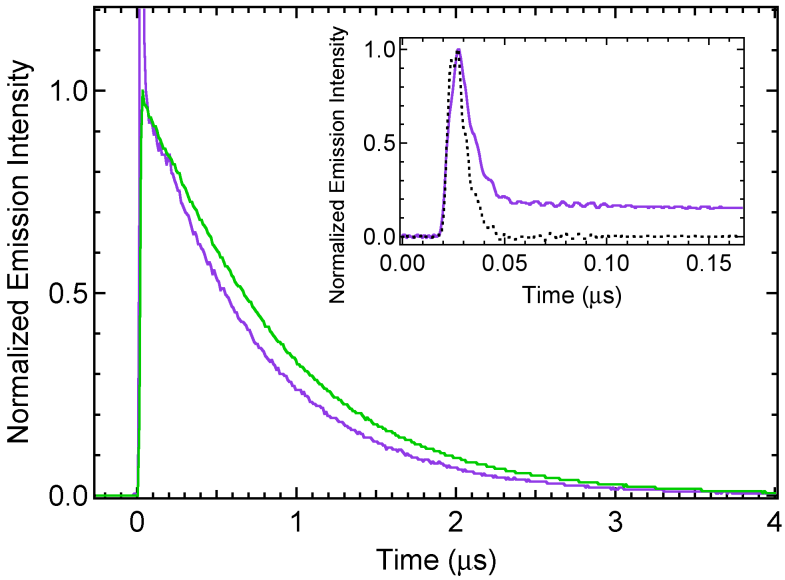


Figure 5.16. TREm traces for Ru^{F}mcb (purple) and Ru^{F}mcbEt (green), both in the presence of 0.24 mM $(Tp)_2Fe_2O(O_2CCHCl_2)_2$. The inset shows the trace at shorter times (purple trace), along with the IRF of the instrument (dashed black line).

5.3.4. Intramolecular Processes

To gain insight on the photophysics of the D-A assemblies formed upon bridge exchange, these systems were studied using TCSPC, which has a shorter time resolution than our nanosecond TREm setup. Since Ru^{F}mcbEt did not show any short-lived components (Ru^{F}mcb in the absence of quenchers did not exhibit any short-lived processes either, Figure 5.39), only Ru^{F}mcb was used; this donor was combined with three different acceptors: $(Tp)_2Fe_2O(O_2CCF_3)_2$, $(Tp)_2Fe_2O(O_2CCHCl_2)_2$ and $[(Tp)_2Fe_2(OH)(O_2CCH_3)_2](OTf)$. The concentration of the acceptors varied between samples, but that of the donor remained the same. The lifetime of the fast process did not change with the concentration of the acceptor (see Figure 5.40), which is consistent with an intramolecular process.

Representative time-resolved emission traces for all three D-A pairs are shown in Figure 5.17. The lifetimes in this case are noticeably longer than those of the Rumcb-based assemblies (Figure 5.11). The explanation for this difference is tied to the localization of the ^{3}MLCT excited state in either donor. In Rumcb, the ES is localized on the mcb ligand (which is the easiest to reduce in this compound); upon excitation of the chromophore, the electron is already on the ligand that is closest to the diferric core, and thus the quenching reaction(s) takes place immediately. On the other hand, the ES of Ru^{F}mcb is localized in one of the peripheral ligands (i.e., btfmb); as a result, the electron must be relocated to the mcb to then be transferred into the core, which slows down the quenching. Soler and McCusker reported the same effect for D-A pairs using $[Ru(dmb)_2(mcb)]^+$ and $[Ru(btfmb)_2(mcb)]^+$.[16]

The average lifetime for each D-A pair, along with the driving forces for electron transfer are shown in Table 5.4. Because of the spectral shift observed for the steady-state emission data (Figure 5.13), E_0 were calculated by fitting the spectra obtained in the presence of the quenchers instead of using the data for unquenched Ru^{F}mcb.

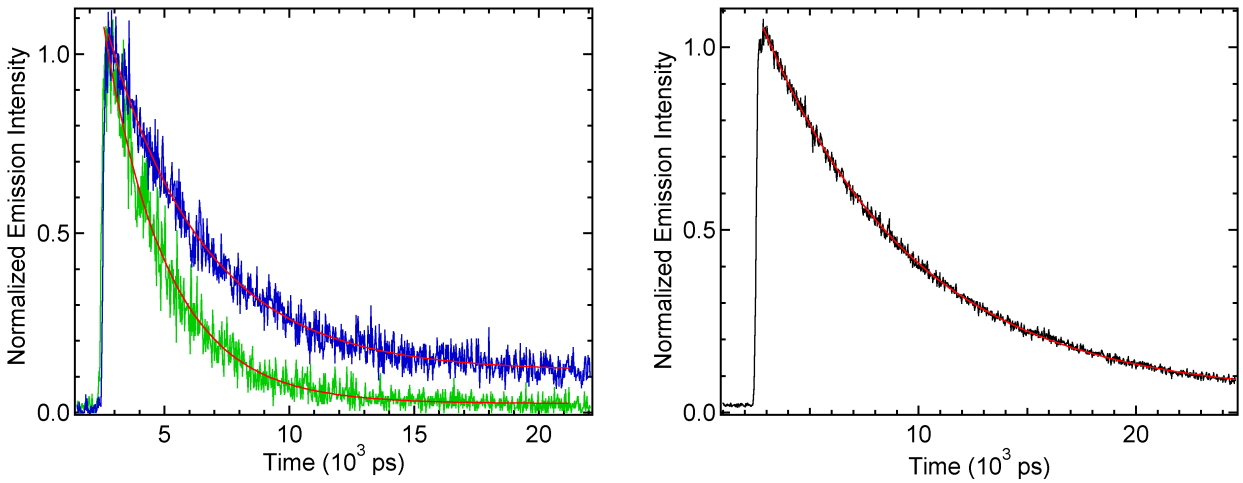


Figure 5.17. Time-resolved emission traces for Ru^Fmcb in the presence of the different acceptors. Left: $(Tp)_2Fe_2O(O_2CCHCl_2)_2$ (blue), $(Tp)_2Fe_2O(O_2CCF_3)_2$ (green). Right: $[(Tp)_2Fe_2(OH)(O_2CCH_3)_2](OTf)$. The red lines are fits to a monoexponential decay.

Table 5.4. Driving forces for electron transfer for the D-A pairs using Ru^Fmcb as the donor. The D-A distances were determined using geometry optimizations for the assemblies. See text for details.

bridges (acceptor)	ΔG_0^{ET} (eV)	τ (ns)	through-bond D-A distance (Å)
OH/O_2CCH_3	0.40	7.0 ± 0.1	11.10
O/O_2CHCl_2	0.19	3.8 ± 0.2	11.09
O/O_2CCF_3	0.00	2.4 ± 0.1	11.09

The trend observed for the bimolecular studies is reverted here: the hydroxo-bridged acceptor is the slowest quencher when the unimolecular processes are considered (cfr. Figure 5.8 and Figure 5.14). Despite electron transfer being endothermic for these systems (with the possible exception of the $(Tp)_2Fe_2O(O_2CCF_3)_2$), the lifetimes of the assemblies track the ΔG_0^{ET} values. This inversion in the reactivity trends between the bimolecular quenching to the intramolecular one suggests that different mechanisms are operational for either kind of process.

5.3.5. Quenching Mechanisms: Bimolecular vs Intramolecular

As was mentioned before, identifying and quantifying each contribution to the quenching processes in these systems is not an easy task. However, based on the available information, some conclusions can be drawn. Let us turn our attention to the bimolecular processes taking place in both the Rumcb-based and Ru^{F}mcb-based D-A pairs. Each of the traces from Figure 5.14 can be fitted to a monoexponential decay, yielding the lifetimes compiled in Table 5.5; the lifetime in the presence of the oxo-bridged acceptor is 98% of the unquenched lifetime, whereas in the presence of the hydroxo-bridged core, it decreases to 83%. Using the k_q values for RumcbEt (Table 5.3), the expected lifetimes for the same concentrations of quenchers can be calculated (values shown in Table 5.5). In this case, the values are 83% (oxo-bridged acceptor) and 50% (hydroxo-bridged) of the unquenched lifetime. Taking into account that electron transfer is favorable for both D-A pairs featuring RumcbEt, but not for those with Ru^{F}mcbEt (Table 5.2), it seems clear that electron transfer is the main bimolecular quenching mechanism in these systems. The spectral overlap between the absorption of the oxo-bridged acceptor and the emission of either donor (Figure 5.18) is almost identical for RumcbEt and Ru^{F}mcbEt, which means that FRET cannot be invoked to account for differences in the extent of the quenching. DET may play a role, although we do not expect it to be the dominant pathway for bimolecular systems, due to its steep distance dependence (see Chapter 2).

Table 5.5. Measured lifetimes for Ru^{F}mcbEt with and without quenchers, and calculated lifetimes for RumcbEt in the presence of quenchers. See text for details.

	unquenched	with 0.24 mM {Fe_2O}	with 0.21 mM {Fe_2OH}
RumcbEt	1230 ns	1020 ns	610 ns
Ru^{F}mcbEt	890 ns	870 ns	740 ns

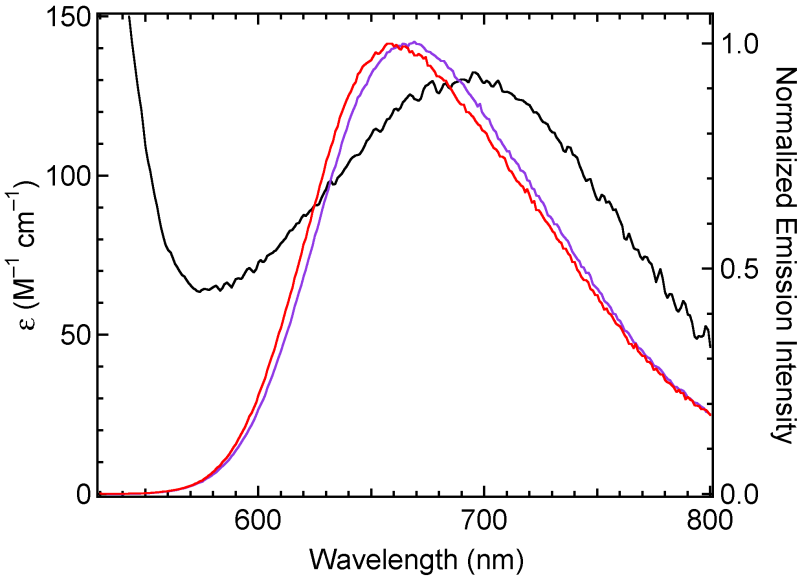


Figure 5.18. Overlay of the steady-state emission spectra of RumcbEt (purple trace) and Ru^{F}mcbEt (red trace) and the electronic absorption spectrum of $(Tp)_2Fe_2O(O_2CCHCl_2)_2$ (black trace).

Additionally, TA spectroscopy was used to determine whether electron transfer takes place in these systems. As was discussed in Chapter 2, it is possible to distinguish between electron and energy transfer using this technique; the most relevant data are presented in Figure 5.19. For both Ru(II) donors, in the presence of the hydroxo-bridged quencher, there is a bleach centered around 450 nm that persists for several microseconds (this is not observed when probing at other wavelengths, see Figure 5.42, appendix). These data are indicative of oxidative quenching taking place in these samples. In other

words, electron transfer occurs between RumcbEt and $[(Tp)_2Fe_2(OH)(O_2CCH_3)_2](OTf)$, which is expected because ΔG_0^{ET} is negative for this D-A pair. Despite an unfavorable ΔG_0^{ET} value (0.44 eV), electron transfer between Ru^FmcbEt and $[(Tp)_2Fe_2(OH)(O_2CCH_3)_2](OTf)$ is also observed. The most plausible explanation for this process involves excited spin states of the hydroxo-bridged acceptor and is discussed in section 5.3.6.

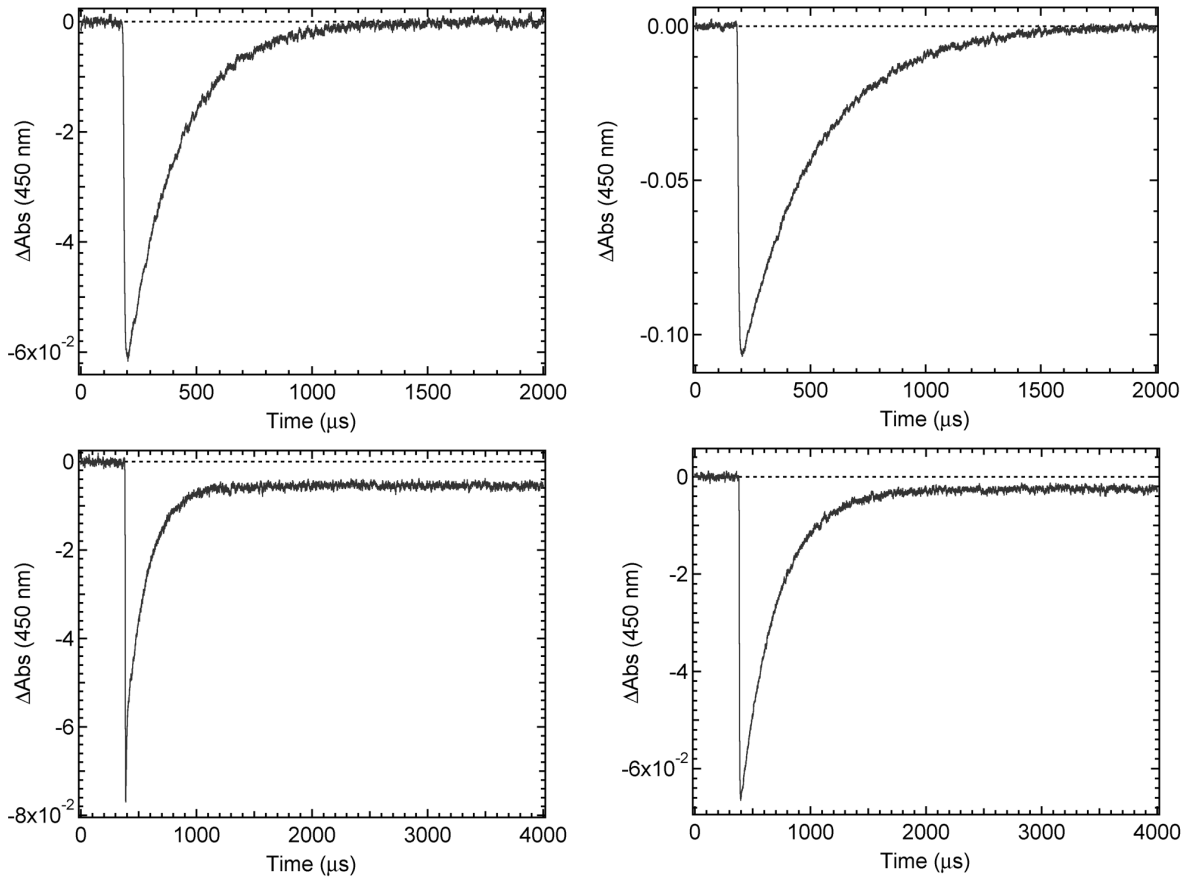


Figure 5.19. Transient absorption data (λ_{pump}: 475 nm, λ_{probe}: 450 nm). Top left: RumcbEt. Bottom left: RumcbEt + $[(Tp)_2Fe_2(OH)(O_2CCH_3)_2](OTf)$. Top right: Ru^FmcbEt. Bottom right: Ru^FmcbEt + $[(Tp)_2Fe_2(OH)(O_2CCH_3)_2](OTf)$.

We will now focus on the intramolecular D-A systems with Ru^Fmcb. As stated before, ΔG_0^{ET} is positive for all of these assemblies, which suggests that electron transfer

is unfavorable. We must bear in mind, however, that another important variable in the Marcus equation[20–22] is H_{AB}, a measure of the electronic communication between the donor and the acceptor. For bimolecular systems, this parameter is ill-defined, because the D-A distance and their relative orientations can vary. In contrast, for an intramolecular system, the electronic coupling between donor and acceptor is expected to be much stronger (both due to a shortened distance and the covalent linkage). To determine the value of H_{AB} in the systems discussed in this chapter, computational methods will be necessary.[23]

Regarding energy transfer, FRET is favorable for both oxo-bridged acceptors (see Figure 5.20), and its contributions to the quenching in either case are comparable; the contribution of FRET in the case of the hydroxo-bridge quencher should be negligible. On the other hand, DET is a viable pathway for all three acceptors.

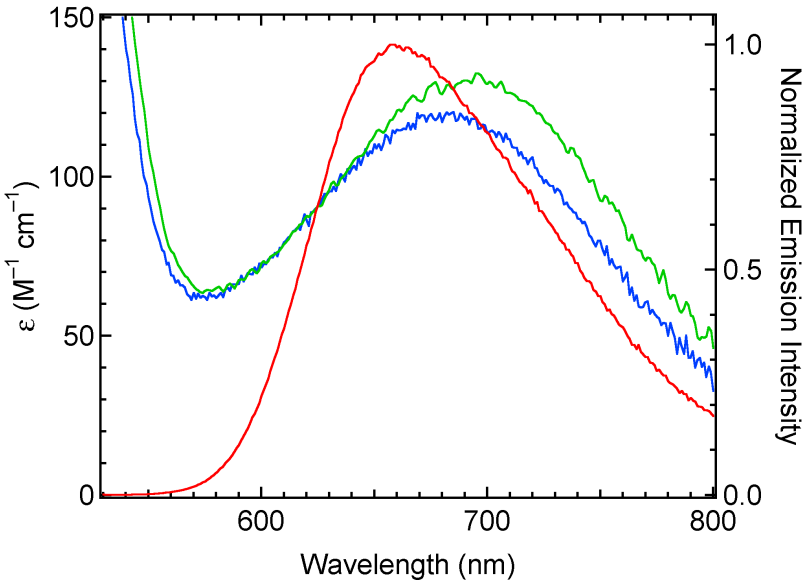


Figure 5.20. Overlay of the steady-state emission spectrum of Ru^{F}mcbEt (red trace) and the electronic absorption spectra of $(Tp)_2Fe_2O(O_2CCF_3)_2$ (blue trace) and $(Tp)_2Fe_2O(O_2CCHCl_2)_2$ (green trace). All spectra were collected in acetonitrile.

Figure 5.21 shows simulated plots of the rate of energy transfer, k_{ET}, as a function of the D-A distance for these systems. For FRET, k_r of the donor was taken to be 3.3 x10^4 s^{-1}, as reported by Soler and McCusker,[16] and R_0 was approximated as 30 Å (see Chapter 3). For DET, r_c was taken to be 5 Å, β was 0.5 $Å^{-1}$, and A = 10^{13} s^{-1}.[6,24] While the plots presented here are only an approximation (as the values of r_c, β and A must be determined experimentally,[24] and R_0 depends on the spectral overlap integral, so it is different for each D-A pair), it is worth noting that around 11 Å DET is dominant (although it cannot be seen in the plot, k_{FRET} ~10^{10} s^{-1} at this distance). We cannot completely dismiss other contributions (FRET and/or electron transfer), but it seems that DET is the major quenching pathway in the D-A assemblies. Any contributions from FRET will only affect the assemblies containing an oxo-bridged acceptor, which agrees with their lifetimes being shorter.

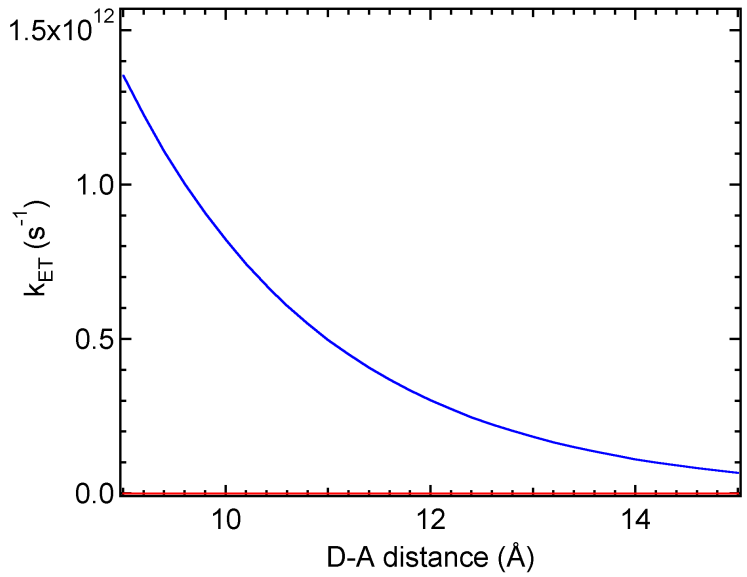


Figure 5.21. Simulated plot of k_{ET} vs. the D-A distance for the Ru^Fmcb systems. Dexter transfer is shown in blue, and Förster in red.

In summary, there is strong evidence that electron transfer is the main quenching mechanism for bimolecular systems, whereas Dexter energy transfer seems to be the dominant pathway for the intramolecular systems. Femtosecond transient absorption studies on the D-A assemblies using Rumcb will allow us to understand how important electron transfer is at very short distances. As mentioned before, these experiments are underway.

5.3.6. Spin Conservation and Quenching Pathways

Based on the discussion above, it is not surprising that $(Tp)_2Fe_2O(O_2CCF_3)_2$ is the most efficient quencher within the Ru^Fmcb-based D-A assemblies, followed by $(Tp)_2Fe_2O(O_2CCHCl_2)_2$ and finally $[(Tp)_2Fe_2(OH)(O_2CCH_3)_2](OTf)$. What is harder to explain is why the hydroxo-bridged dimer is the fastest quencher when bimolecular reactions are considered.[2] While more data are necessary to obtain a more complete picture, it seems clear that different quenching mechanisms are operative (or at least dominant) in either case. We can now take into account the spin states of the systems of interest, for electron transfer as well as energy transfer. These processes are shown in equations 5.1 and 5.2, respectively.

$$[RuL_3]^{2+*} + (Fe^{III}Fe^{III}) \xrightarrow{e-transfer} [RuL_3]^{3+} + (Fe^{II}Fe^{III}) \qquad \textbf{(5.1)}$$

$$[RuL_3]^{2+*} + (Fe^{III}Fe^{III}) \xrightarrow{E\ transfer} [RuL_3]^{2+} + (Fe^{III}Fe^{III})^{*} \qquad \textbf{(5.2)}$$

Regarding spin conservation, our analysis will follow Guo et al.:[25] we will consider the spin states available to each of the reactants for (5.1) and (5.2), as well as for the products, and then identify the pathways that conserve the total spin of the system (see

Chapter 1). Irrespective of the reaction considered, the spin of the reactants is the same in both cases: ^{3}MLCT state of the Ru(II) donor, and the spin states from S_T = 0 to S_T = 5 for the diiron acceptor. In the case of electron transfer (eq 5.1), the products will be Ru(III) (which is a low-spin d^5 compound, and as such its ground state is a doublet, S = ½) and a mixed-valent $Fe^{II}Fe^{III}$ core. Based on other reported compounds, it is reasonable to expect this mixed-valent dimer to be antiferromagnetically coupled:[26,27] the corresponding spin ladder is shown on the left side of Figure 5.22. If energy transfer takes place, the products will be a ground-state Ru(II) compound (a singlet, S = 0) and an excited diferric core, where one of the Fe(III) centers will be in a ligand-field excited state, most likely a quartet (S = $^3/_2$).[28,29] Assuming that this dimer is also antiferromagnetically coupled, its spin ladder will be as shown in the right side of Figure 5.22.

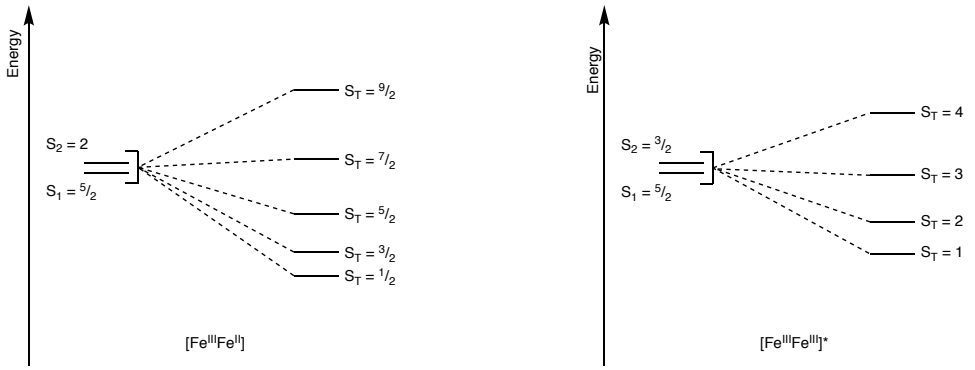


Figure 5.22. Left: Spin ladder for a mixed-valence iron dimer. Right: Spin ladder for an excited diferric core.

For an electron transfer such as shown in (5.1), there will be a set of S_T values for the reactants, depending on the spin state of the acceptor. All the possible combinations are shown on the left side of Table 5.6. The total spin of the products will depend on the spin state of the reduced acceptor ($Fe^{II}Fe^{III}$ in eq 5.1); those values are shown on the right side of the table. For any of the oxo-bridged acceptors, only the first two spin states (S_A =

0, 1) are populated at room temperature:[2,30] therefore, the only spin-allowed pathways involve S_{A-} = ½ and $^3/_2$. In the hydroxo-bridged acceptors, on the other hand, all the spin states are thermally accessible at room temperature,[2,17] which opens up more spin-allowed reaction channels. This analysis is consistent with the hydroxo-brigded dimers being more efficient quenchers, and agrees with what was postulated by Bominaar et al.[31] Using these arguments, we can account for electron transfer taking place between Ru^FmcbEt and $[(Tp)_2Fe_2(OH)(O_2CCH_3)_2](OTf)$, despite the positive value of ΔG_0^{ET} for this D-A pair.

Admittedly, more information is necessary at this point; using computational methods to study the electron exchange in the mixed-valence dimer[29,31–33] would help us quantify the energetics of each of the spin-allowed electron transfer pathways, which would in turn give us a more complete picture of the reaction channels available for these systems.

Table 5.6. All possible values of S_T for the reactants and products of eq 5.1 (electron transfer).

S_{D*}	S_A	S_T^R
1	0	1
	1	0, 1, 2
	2	1, 2, 3
	3	2, 3, 4
	4	3, 4, 5
	5	4, 5, 6

S_{D^+}	S_{A^-}	S_T^P
½	$\frac{1}{2}$	0, 1
	$\frac{3}{2}$	1, 2
	$\frac{5}{2}$	2, 3
	$\frac{7}{2}$	3, 4
	$\frac{9}{2}$	4, 5

Finally, let us consider the case of energy transfer (eq 5.2). With the spin ladder shown in Figure 5.22, the total spin values obtained are presented in Table 5.7. While there are fewer pathways overall, both the oxo- and hydroxo-bridged acceptors can access spin-allowed reaction channels. Just as before, it is not possible to assess the energetics of each of these, which prevents us from drawing firmer conclusions. In principle, the hydroxo-bridged cores seem to have more thermally accessible reaction pathways, which should make them more efficient quenchers than their oxo-bridged counterparts. However, this is not the case: the analysis described here seems to be flawed, most likely due to one or more of the many assumptions involved. It is necessary to gather more information about the electronic structure of these systems before a more in-depth evaluation can be made. It is unlikely that we will be able to experimentally study the spin coupling in either $Fe^{II}Fe^{III}$ or $[Fe^{III}Fe^{III}]^*$, so we will have to heavily rely on computational methods towards this end.

Table 5.7. All possible values of S_T for the reactants and products of eq 5.2 (energy transfer).

S_{D*}	S_A	S_T^R
1	0	1
	1	0, 1, 2
	2	1, 2, 3
	3	2, 3, 4
	4	3, 4, 5
	5	4, 5, 6

S_D	S_{A^*}	S_T^P
0	1	1
	2	2
	3	3
	4	4

5.4. Concluding Remarks

The D-A pairs investigated in this chapter wave shown more complex reactivity patterns than originally expected. The bimolecular processes followed what was previously observed for this kind of compounds,[2] but the photophysics of the D-A assemblies presented opposite trends. Based on the results discussed here, it may be necessary to gradually vary the distance between the donor and the acceptor to assess which quenching mechanism dominates as the D-A distance changes. Ideally, we would like to have three systems with the same donor and acceptor: a bimolecular one (which is the easiest to synthesize), and then two D-A assemblies, one where electron transfer is the main quenching route, and one where energy transfer prevails. Preparing such systems will require careful design and will be a challenge on its own. Work towards such D-A assemblies is in progress and it is discussed in the next chapter.

Initially, we suspected that the reason why the hydroxo-bridged acceptors are more efficient quenchers in these D-A systems was related to the spin states that are populated at a given temperature for these diferric cores. Our preliminary analysis of spin conservation on bimolecular electron transfer in these D-A pairs suggests that this is indeed the case. For Ru^Fmcb and $[(Tp)_2Fe_2(OH)(O_2CCH_3)_2](OTf)$, electron transfer is observed in the TA data even though ΔG_0^{ET} is positive. In contrast, $(Tp)_2Fe_2O(O_2CCHCl_2)_2$ does not quench the emission of Ru^Fmcb. The most reasonable explanation for these observations involves excited spin states taking part in the electron transfer, as was proposed by Bominaar and co-workers.[31] For a quantitative analysis of these results more work is necessary, which will likely involve high-level computational methods to study

Heisenberg spin exchange in the iron dimers that result from electron transfer between the Ru(II) donors and the diiron(III) acceptors.

We expect that ultrafast transient absorption experiments will help us identify the mechanism of intramolecular quenching at play in the D-A assemblies discussed in this chapter. Knowing what processes are taking place in the bimolecular and intramolecular systems will allow us to better understand the reactivity trends observed in either case.

APPENDIX

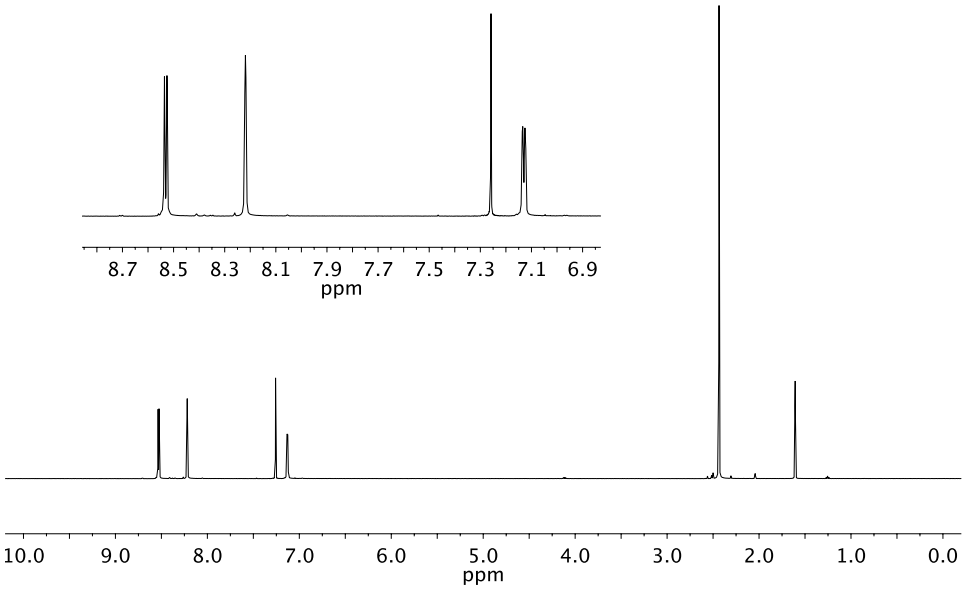


Figure 5.23. ^{1}H NMR of 4,4'-dimethyl-2,2'-bipyridine in $CDCl_3$.

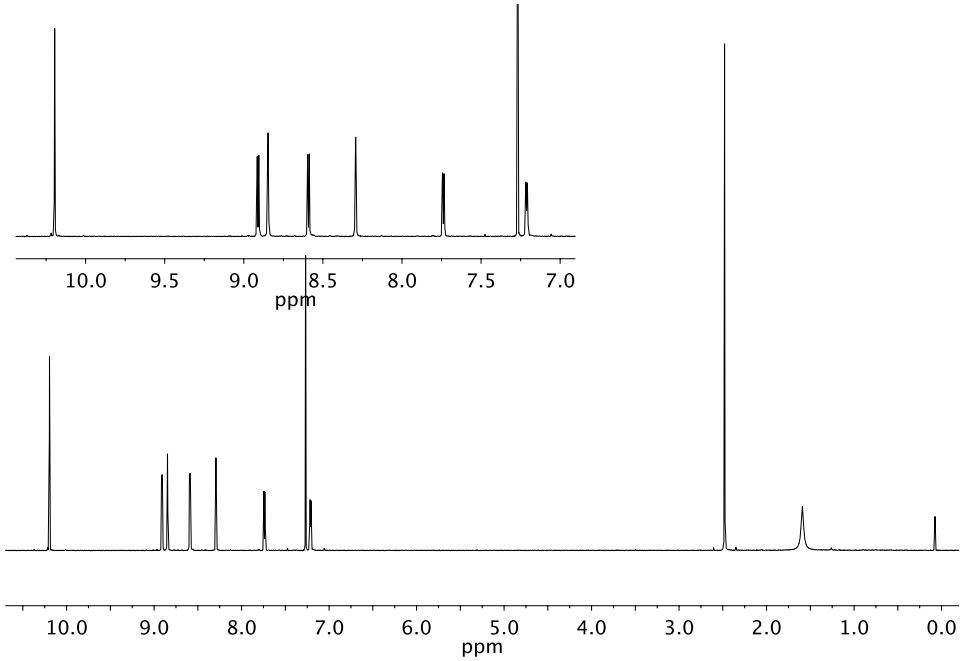


Figure 5.24. ^{1}H NMR of 4'-methyl-2,2'-bipyridine-4-carboxaldehyde in $CDCl_3$.

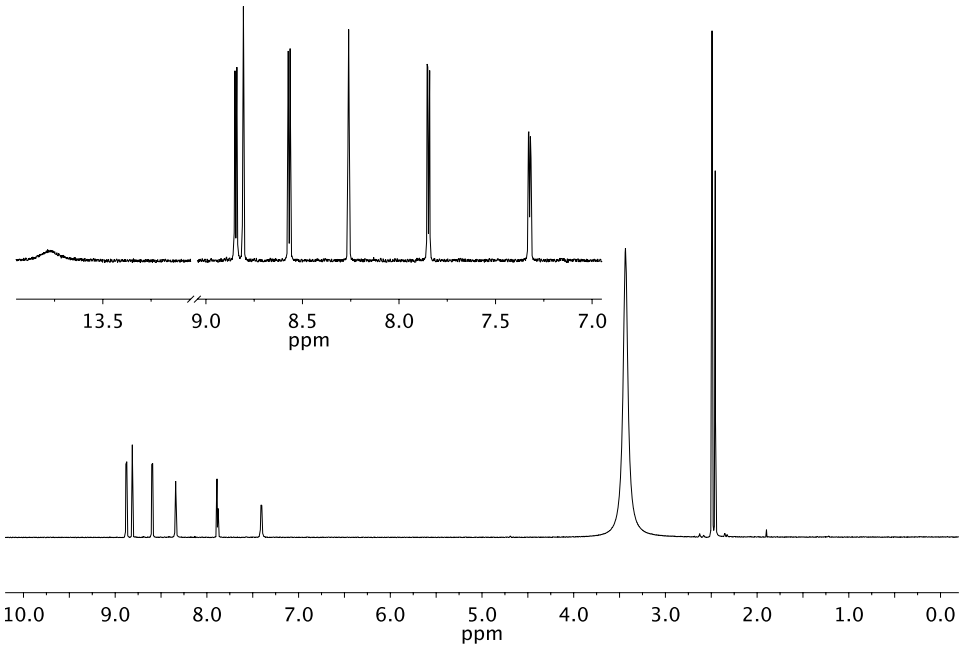


Figure 5.25. ^{1}H NMR of 4'-methyl-2,2'-bipyridine-4-carboxylic acid in DMSO-d_6.

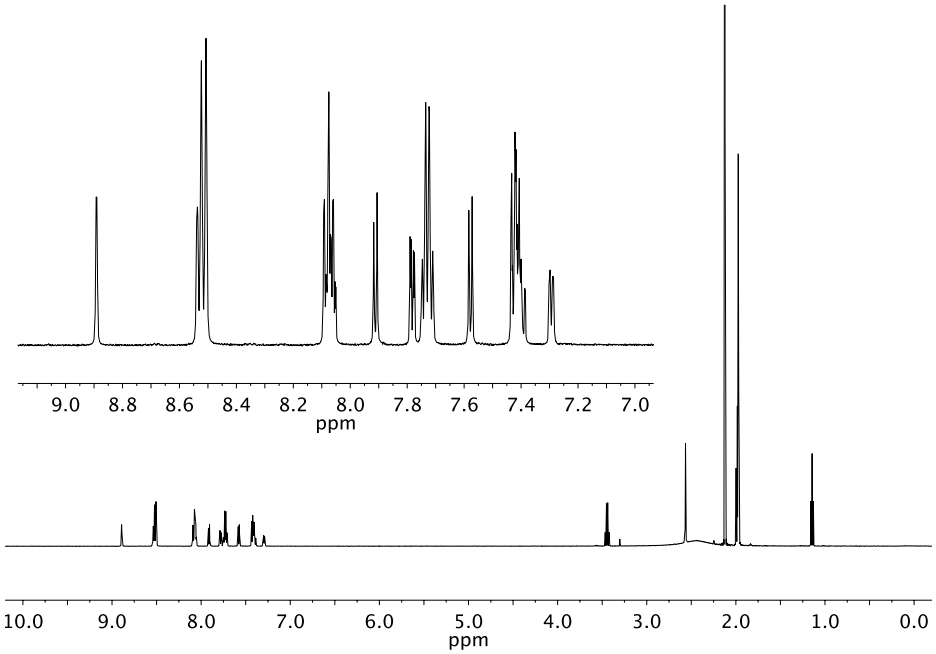


Figure 5.26. ^{1}H NMR of Rumcb in CD_3CN.

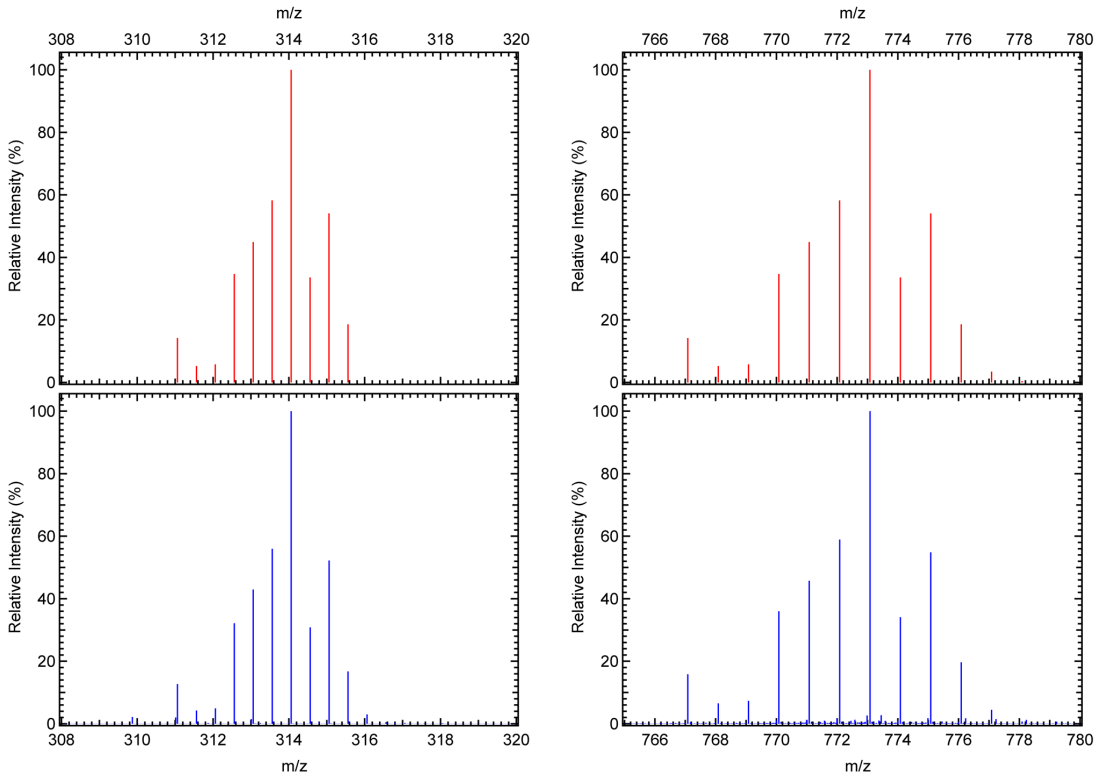


Figure 5.27. ESI-MS of Rumcb. Top left: predicted isotope pattern for $[M–2PF_6]^{2+}$ ($C_{32}H_{26}N_6O_2Ru$). Top right: predicted isotope pattern for $[M–PF_6]^{+}$ ($C_{32}H_{26}N_6O_2RuPF_6$).Bottom: experimental results.

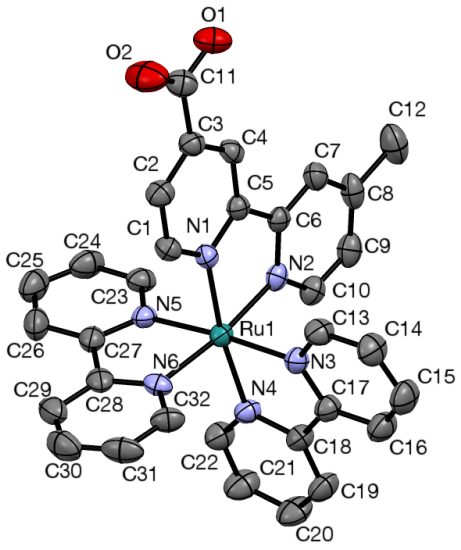


Figure 5.28. ORTEP drawing of $[Ru(bpy)_2(mcb)]^{2+}$ obtained from single-crystal X-ray structure determination, showing all atomic labels. Atoms are represented as 50% probability thermal ellipsoids. Hydrogen atoms and anions are omitted for clarity.

Table 5.8. Bond lengths for the X-ray structure of Rumcb.

Atoms	Length/Å	Atoms	Length/Å	Atoms	Length/Å
Ru1 N1	2.041(3)	C2 C3	1.383(6)	C25 C26	1.371(8)
Ru1 N2	2.056(4)	C3 C4	1.388(6)	C26 C27	1.379(7)
Ru1 N3	2.061(3)	C3 C11	1.497(6)	C27 C28	1.482(7)
Ru1 N4	2.057(3)	C4 C5	1.374(6)	C28 C29	1.380(7)
Ru1 N5	2.056(3)	C5 C6	1.472(6)	C29 C30	1.373(8)
Ru1 N6	2.061(4)	C6 C7	1.378(6)	C30 C31	1.371(8)
O1 C11	1.303(6)	C7 C8	1.395(7)	C31 C32	1.365(7)
O2 C11	1.207(6)	C8 C9	1.387(7)	P1 F1	1.589(4)
N1 C1	1.354(5)	C8 C12	1.520(7)	P1 F2	1.587(3)
N1 C5	1.361(5)	C9 C10	1.361(6)	P1 F3	1.593(4)
N2 C6	1.359(5)	C13 C14	1.371(7)	P1 F4	1.595(3)
N2 C10	1.350(6)	C14 C15	1.381(7)	P1 F5	1.585(3)
N3 C13	1.346(5)	C15 C16	1.375(7)	P1 F6	1.593(3)
N3 C17	1.360(6)	C16 C17	1.387(6)	P2 F7	1.535(5)
N4 C18	1.367(6)	C17 C18	1.459(6)	P2 F8	1.580(4)
N4 C22	1.345(5)	C18 C19	1.374(6)	P2 F9	1.555(5)
N5 C23	1.348(6)	C19 C20	1.377(7)	P2 F10	1.563(4)
N5 C27	1.357(6)	C20 C21	1.368(7)	P2 F11	1.549(5)
N6 C28	1.364(6)	C21 C22	1.364(7)	P2 F12	1.571(5)
N6 C32	1.346(6)	C23 C24	1.380(7)	N1S C2S	1.143(11)
C1 C2	1.377(6)	C24 C25	1.374(8)	C1S C2S	1.366(12)

Table 5.9. Bond angles for the X-ray crystal structure of Rumcb.

Atoms	Angle/º	Atoms	Angle/º	Atoms	Angle/º
N1 Ru1 N2	78.87(13)	C5 C4 C3	119.9(4)	N6 C28 C29	121.7(5)
N1 Ru1 N3	96.11(14)	N1 C5 C4	121.7(4)	C29 C28 C27	123.5(4)
N1 Ru1 N4	172.61(14)	N1 C5 C6	114.9(4)	C30 C29 C28	119.6(5)
N1 Ru1 N5	87.36(13)	C4 C5 C6	123.5(4)	C31 C30 C29	118.7(5)
N1 Ru1 N6	95.65(14)	N2 C6 C5	114.2(4)	C32 C31 C30	119.8(5)
N2 Ru1 N3	86.91(13)	N2 C6 C7	121.8(4)	N6 C32 C31	122.9(5)
N2 Ru1 N4	95.48(14)	C7 C6 C5	123.9(4)	F1 P1 F3	179.5(2)
N2 Ru1 N5	96.43(14)	C6 C7 C8	120.6(4)	F1 P1 F4	90.7(2)
N2 Ru1 N6	172.81(14)	C7 C8 C12	120.7(5)	F1 P1 F6	89.6(2)

Table 5.9 (cont'd)

Atoms	Angle/°	Atoms	Angle/°	Atoms	Angle/°
N3 Ru1 N6	98.39(15)	C9 C8 C7	116.8(4)	F2 P1 F1	90.0(2)
N4 Ru1 N3	78.70(13)	C9 C8 C12	122.5(5)	F2 P1 F3	89.5(2)
N4 Ru1 N6	90.35(14)	C10 C9 C8	120.0(5)	F2 P1 F4	179.1(2)
N5 Ru1 N3	175.60(14)	N2 C10 C9	123.8(4)	F2 P1 F6	89.91(18)
N5 Ru1 N4	98.08(13)	O1 C11 C3	113.2(4)	F3 P1 F4	89.7(2)
N5 Ru1 N6	78.54(15)	O2 C11 O1	124.8(5)	F5 P1 F1	90.06(19)
C1 N1 Ru1	125.7(3)	O2 C11 C3	122.0(5)	F5 P1 F2	89.69(18)
C1 N1 C5	118.3(4)	N3 C13 C14	122.5(4)	F5 P1 F3	90.2(2)
C5 N1 Ru1	116.0(3)	C13 C14 C15	119.2(5)	F5 P1 F4	90.70(18)
C6 N2 Ru1	116.0(3)	C16 C15 C14	119.1(5)	F5 P1 F6	179.4(2)
C10 N2 Ru1	127.1(3)	C15 C16 C17	119.6(5)	F6 P1 F3	90.2(2)
C10 N2 C6	116.9(4)	N3 C17 C16	121.2(4)	F6 P1 F4	89.70(19)
C13 N3 Ru1	126.1(3)	N3 C17 C18	115.4(4)	F7 P2 F8	89.9(3)
C13 N3 C17	118.5(4)	C16 C17 C18	123.4(4)	F7 P2 F9	175.5(4)
C17 N3 Ru1	115.3(3)	N4 C18 C17	114.5(4)	F7 P2 F10	88.9(3)
C18 N4 Ru1	115.7(3)	N4 C18 C19	120.7(4)	F7 P2 F11	93.4(4)
C22 N4 Ru1	126.4(3)	C19 C18 C17	124.8(4)	F7 P2 F12	92.0(4)
C22 N4 C18	117.8(4)	C18 C19 C20	120.4(5)	F9 P2 F8	86.9(3)
C23 N5 Ru1	125.5(3)	C21 C20 C19	118.4(5)	F9 P2 F10	94.3(3)
C23 N5 C27	117.7(4)	C22 C21 C20	119.6(5)	F9 P2 F12	85.0(3)
C27 N5 Ru1	116.6(3)	N4 C22 C21	122.9(5)	F10 P2 F8	178.8(3)
C28 N6 Ru1	115.8(3)	N5 C23 C24	122.6(5)	F10 P2 F12	88.3(3)
C32 N6 Ru1	126.9(3)	C25 C24 C23	118.9(5)	F11 P2 F8	89.3(3)
C32 N6 C28	117.3(4)	C26 C25 C24	119.4(5)	F11 P2 F9	89.7(3)
N1 C1 C2	122.1(4)	C25 C26 C27	119.4(5)	F11 P2 F10	90.5(3)
C1 C2 C3	119.7(4)	N5 C27 C26	122.0(5)	F11 P2 F12	174.4(4)
C2 C3 C4	118.3(4)	N5 C27 C28	114.0(4)	F12 P2 F8	92.0(3)
C2 C3 C11	119.9(4)	C26 C27 C28	124.1(5)	N1S C2S C1S	178.6(10)
C4 C3 C11	121.7(4)	N6 C28 C27	114.7(4)		

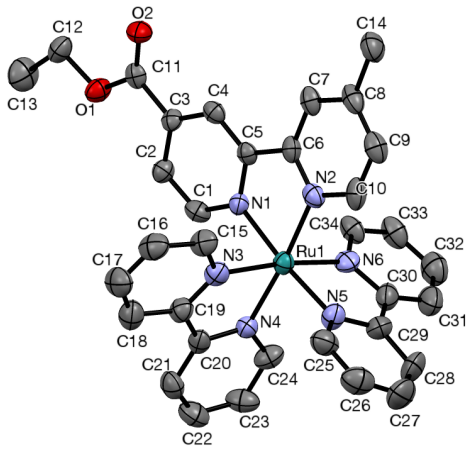


Figure 5.29. ORTEP drawing of $[Ru(bpy)_2(mcbEt)]^{2+}$ obtained from single-crystal X-ray structure determination, showing all atomic labels. Atoms are represented as 50% probability thermal ellipsoids. Hydrogen atoms and anions are omitted for clarity.

Table 5.10. Bond lengths for the X-ray crystal structure of RumcbEt.

Atoms	Length/Å	Atoms	Length/Å	Atoms	Length/Å
Ru1 N1	2.047(7)	C3 C4	1.388(13)	C29 C30	1.438(16)
Ru1 N2	2.062(8)	C3 C11	1.477(12)	C30 C31	1.371(16)
Ru1 N3	2.080(9)	C4 C5	1.371(14)	C31 C32	1.363(18)
Ru1 N4	2.066(8)	C5 C6	1.432(13)	C32 C33	1.389(16)
Ru1 N5	2.047(7)	C6 C7	1.391(14)	C33 C34	1.370(16)
Ru1 N6	2.036(9)	C7 C8	1.382(15)	P2 F7	1.572(8)
O1 C11	1.327(11)	C8 C9	1.402(16)	P2 F8	1.590(8)
O1 C12	1.452(12)	C8 C14	1.520(16)	P2 F9	1.601(8)
O2 C11	1.207(10)	C9 C10	1.366(16)	P2 F10	1.571(8)
N1 C1	1.361(12)	C12 C13	1.510(16)	P2 F11	1.596(7)
N1 C5	1.380(12)	C15 C16	1.397(17)	P2 F12	1.606(7)
N2 C6	1.338(13)	C16 C17	1.338(17)	P1 F1	1.571(9)
N2 C10	1.368(13)	C17 C18	1.395(17)	P1 F2	1.558(11)
N3 C15	1.353(13)	C18 C19	1.394(16)	P1 F3	1.541(9)
N3 C19	1.356(15)	C19 C20	1.436(16)	P1 F4	1.544(10)
N4 C20	1.357(12)	C20 C21	1.395(15)	P1 F5	1.580(10)
N4 C24	1.366(12)	C21 C22	1.351(16)	P1 F6	1.538(12)
N5 C25	1.349(15)	C22 C23	1.362(17)	O1S C2S	1.43(2)
N5 C29	1.371(15)	C23 C24	1.374(16)	O1S C3S	1.442(19)

Table 5.10 (cont'd)

Atoms	Length/Å	Atoms	Length/Å	Atoms	Length/Å
N6 C30	1.371(13)	C25 C26	1.366(16)	C1S C2S	1.42(2)
N6 C34	1.345(14)	C26 C27	1.34(2)	C3S C4S	1.54(2)
C1 C2	1.385(13)	C27 C28	1.38(2)	N1S C6S	1.101(19)
C2 C3	1.395(12)	C28 C29	1.394(17)	C5S C6S	1.46(2)

Table 5.11. Bond angles for the X-ray crystal structure of RumcbEt.

Atoms	Angle/º	Atoms	Angle/º	Atoms	Angle/º
N1 Ru1 N2	77.4(3)	N1 C5 C6	113.8(9)	C32 C31 C30	119.6(12)
N1 Ru1 N3	83.4(4)	C4 C5 N1	121.0(9)	C31 C32 C33	120.5(12)
N1 Ru1 N4	98.3(3)	C4 C5 C6	125.3(9)	C34 C33 C32	117.4(12)
N2 Ru1 N3	99.1(3)	N2 C6 C5	115.5(9)	N6 C34 C33	123.2(12)
N2 Ru1 N4	174.9(3)	N2 C6 C7	122.3(9)	F7 P2 F8	88.0(5)
N4 Ru1 N3	77.5(3)	C7 C6 C5	122.3(10)	F7 P2 F9	176.3(6)
N5 Ru1 N1	174.6(4)	C8 C7 C6	120.1(11)	F7 P2 F11	89.7(4)
N5 Ru1 N2	97.4(4)	C7 C8 C9	117.6(10)	F7 P2 F12	92.6(4)
N5 Ru1 N3	99.1(4)	C7 C8 C14	121.7(11)	F8 P2 F9	88.4(5)
N5 Ru1 N4	87.0(3)	C9 C8 C14	120.7(10)	F8 P2 F11	88.9(4)
N6 Ru1 N1	99.6(4)	C10 C9 C8	119.5(10)	F8 P2 F12	88.8(4)
N6 Ru1 N2	87.9(3)	C9 C10 N2	122.9(11)	F9 P2 F12	88.1(4)
N6 Ru1 N3	172.9(4)	O1 C11 C3	112.2(8)	F10 P2 F7	92.9(6)
N6 Ru1 N4	95.6(3)	O2 C11 O1	123.9(9)	F10 P2 F8	178.4(5)
N6 Ru1 N5	78.4(4)	O2 C11 C3	123.9(8)	F10 P2 F9	90.7(6)
C11 O1 C12	116.1(7)	O1 C12 C13	106.3(9)	F10 P2 F11	89.8(5)
C1 N1 Ru1	125.6(7)	N3 C15 C16	121.0(11)	F10 P2 F12	92.5(5)
C1 N1 C5	117.7(7)	C17 C16 C15	119.5(11)	F11 P2 F9	89.4(4)
C5 N1 Ru1	116.2(6)	C16 C17 C18	120.7(12)	F11 P2 F12	176.7(5)
C6 N2 Ru1	116.6(7)	C19 C18 C17	118.4(12)	F1 P1 F5	84.9(6)
C6 N2 C10	117.6(9)	N3 C19 C18	120.9(11)	F2 P1 F1	88.9(6)
C10 N2 Ru1	125.7(8)	N3 C19 C20	115.1(10)	F2 P1 F5	85.2(7)
C15 N3 Ru1	124.5(8)	C18 C19 C20	124.0(12)	F3 P1 F1	176.6(7)
C15 N3 C19	119.5(10)	N4 C20 C19	115.3(10)	F3 P1 F2	89.5(6)
C19 N3 Ru1	115.3(7)	N4 C20 C21	119.9(10)	F3 P1 F4	90.1(6)
C20 N4 Ru1	116.0(7)	C21 C20 C19	124.8(10)	F3 P1 F5	92.0(8)

Table 5.11 (cont'd)

Atoms	Angle/°	Atoms	Angle/°	Atoms	Angle/°
C20 N4 C24	119.6(10)	C22 C21 C20	120.4(11)	F4 P1 F1	91.2(6)
C24 N4 Ru1	124.3(7)	C21 C22 C23	119.2(12)	F4 P1 F2	175.2(8)
C25 N5 Ru1	126.6(9)	C22 C23 C24	120.8(12)	F4 P1 F5	90.1(7)
C25 N5 C29	117.7(9)	N4 C24 C23	120.0(12)	F6 P1 F1	92.0(8)
C29 N5 Ru1	115.7(8)	N5 C25 C26	124.0(13)	F6 P1 F2	93.0(9)
C30 N6 Ru1	116.3(7)	C27 C26 C25	118.5(13)	F6 P1 F3	91.1(8)
C34 N6 Ru1	125.4(8)	C26 C27 C28	120.0(11)	F6 P1 F4	91.8(9)
C34 N6 C30	118.3(10)	C27 C28 C29	120.0(13)	F6 P1 F5	176.4(8)
N1 C1 C2	123.0(9)	N5 C29 C28	119.6(12)	C2S O1S C3S	111.3(14)
C1 C2 C3	118.8(9)	N5 C29 C30	114.9(10)	C1S C2S O1S	111.5(18)
C2 C3 C11	121.2(9)	C28 C29 C30	125.5(12)	O1S C3S C4S	106.2(14)
C4 C3 C2	118.1(8)	N6 C30 C29	114.4(10)	N1S C6S C5S	177.0(19)
C4 C3 C11	120.6(8)	N6 C30 C31	120.9(12)		
C5 C4 C3	121.3(9)	C31 C30 C29	124.6(11)		

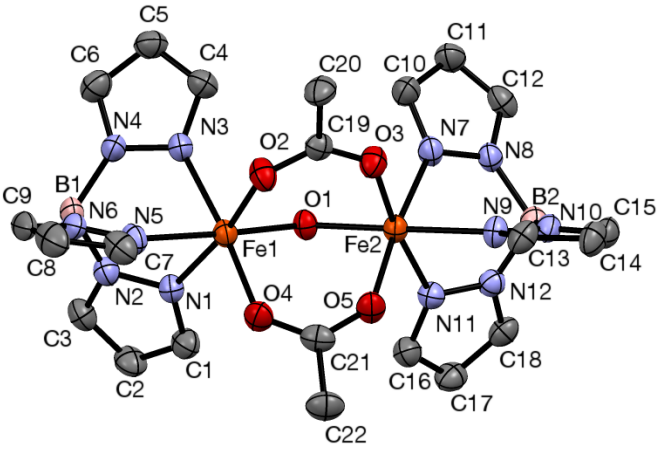


Figure 5.30. ORTEP drawing of $[Tp_2Fe_2(OH)(O_2CCH_3)_2]^+$ obtained from single-crystal X-ray structure determination, showing the atom labels. Atoms are represented as 50% probability thermal ellipsoids. Hydrogen atoms and anions are omitted for clarity.

Table 5.12. Bond lengths for the X-ray crystal structure of $[(Tp)_2Fe_2(OH)(O_2CCH_3)_2](OTf)$.

Atoms	Length/Å	Atoms	Length/Å	Atoms	Length/Å
Fe1 O1	1.930(4)	N4 C6	1.342(7)	C7 C8	1.380(9)
Fe1 O2	2.011(4)	N4 B1	1.541(8)	C8 C9	1.364(10)
Fe1 O4	1.993(4)	N5 N6	1.368(7)	C10 C11	1.396(8)
Fe1 N1	2.093(4)	N5 C7	1.333(8)	C11 C12	1.362(9)
Fe1 N3	2.110(5)	N6 C9	1.360(7)	C13 C14	1.394(8)
Fe1 N5	2.133(4)	N6 B1	1.525(9)	C14 C15	1.350(9)
Fe2 O1	1.942(4)	N7 N8	1.357(6)	C16 C17	1.381(8)
Fe2 O3	2.016(4)	N7 C10	1.330(7)	C17 C18	1.374(8)
Fe2 O5	2.000(4)	N8 C12	1.334(7)	C19 C20	1.495(7)
Fe2 N7	2.097(4)	N8 B2	1.545(7)	C21 C22	1.499(8)
Fe2 N9	2.112(4)	N9 N10	1.372(6)	S1 O6	1.385(8)
Fe2 N11	2.109(5)	N9 C13	1.324(7)	S1 O7	1.394(6)
O2 C19	1.260(6)	N10 C15	1.338(7)	S1 O8	1.382(7)
O3 C19	1.246(7)	N10 B2	1.556(8)	S1 C23	1.764(9)
O4 C21	1.268(7)	N11 N12	1.370(6)	F1 C23	1.331(8)
O5 C21	1.254(7)	N11 C16	1.320(7)	F2 C23	1.356(11)
N1 N2	1.366(6)	N12 C18	1.335(7)	F3 C23	1.264(10)
N1 C1	1.341(7)	N12 B2	1.537(7)	O9 C24	1.208(8)
N2 C3	1.333(7)	C1 C2	1.380(8)	C24 C25	1.451(10)
N2 B1	1.540(9)	C2 C3	1.362(9)	C24 C26	1.514(11)
N3 N4	1.375(6)	C4 C5	1.383(8)		
N3 C4	1.344(7)	C5 C6	1.365(9)		

Table 5.13. Bond angles for the X-ray crystal structure of $[(Tp)_2Fe_2(OH)(O_2CCH_3)_2](OTf)$.

Atoms	Angle/º	Atoms	Angle/º	Atoms	Angle/º
O1 Fe1 O2	92.67(16)	C3 N2 N1	109.1(5)	C9 C8 C7	105.5(6)
O1 Fe1 O4	93.10(16)	C3 N2 B1	130.6(5)	N6 C9 C8	108.6(5)
O1 Fe1 N1	94.85(17)	N4 N3 Fe1	120.2(3)	N7 C10 C11	110.5(5)
O1 Fe1 N3	92.63(17)	C4 N3 Fe1	132.8(4)	C12 C11 C10	104.4(5)
O1 Fe1 N5	176.74(18)	C4 N3 N4	106.8(4)	N8 C12 C11	109.2(5)
O2 Fe1 N1	171.13(17)	N3 N4 B1	119.3(4)	N9 C13 C14	110.0(5)

Table 5.13 (cont'd)

Atoms	Angle/°	Atoms	Angle/°	Atoms	Angle/°
O2 Fe1 N3	88.98(18)	C6 N4 N3	108.5(4)	C15 C14 C13	105.8(5)
O2 Fe1 N5	88.02(17)	C6 N4 B1	131.8(5)	N10 C15 C14	108.4(5)
O4 Fe1 O2	91.34(17)	N6 N5 Fe1	119.7(4)	N11 C16 C17	110.5(5)
O4 Fe1 N1	92.93(17)	C7 N5 Fe1	133.3(4)	C18 C17 C16	105.1(5)
O4 Fe1 N3	174.23(17)	C7 N5 N6	106.8(5)	N12 C18 C17	108.6(5)
O4 Fe1 N5	90.06(17)	N5 N6 B1	119.8(5)	O2 C19 C20	117.5(5)
N1 Fe1 N3	85.99(17)	C9 N6 N5	108.5(5)	O3 C19 O2	125.1(5)
N1 Fe1 N5	84.21(18)	C9 N6 B1	131.6(5)	O3 C19 C20	117.5(5)
N3 Fe1 N5	84.19(18)	N8 N7 Fe2	120.6(3)	O4 C21 C22	118.0(5)
O1 Fe2 O3	92.91(16)	C10 N7 Fe2	133.2(4)	O5 C21 O4	124.6(5)
O1 Fe2 O5	91.57(16)	C10 N7 N8	106.2(4)	O5 C21 C22	117.4(6)
O1 Fe2 N7	92.69(16)	N7 N8 B2	119.5(4)	N2 B1 N4	108.2(5)
O1 Fe2 N9	177.16(18)	C12 N8 N7	109.7(5)	N6 B1 N2	109.1(5)
O1 Fe2 N11	93.59(17)	C12 N8 B2	130.7(5)	N6 B1 N4	106.7(5)
O3 Fe2 N7	91.28(18)	N10 N9 Fe2	119.7(3)	N8 B2 N10	108.3(5)
O3 Fe2 N9	88.86(16)	C13 N9 Fe2	134.2(4)	N12 B2 N8	108.6(4)
O3 Fe2 N11	173.09(16)	C13 N9 N10	106.0(4)	N12 B2 N10	107.1(4)
O5 Fe2 O3	92.47(17)	N9 N10 B2	119.3(4)	O6 S1 O7	124.2(6)
O5 Fe2 N7	174.17(17)	C15 N10 N9	109.7(5)	O6 S1 C23	105.2(4)
O5 Fe2 N9	90.57(17)	C15 N10 B2	131.0(5)	O7 S1 C23	102.7(4)
O5 Fe2 N11	89.71(17)	N12 N11 Fe2	119.9(3)	O8 S1 O6	109.8(8)
N7 Fe2 N9	85.04(17)	C16 N11 Fe2	133.3(4)	O8 S1 O7	109.7(5)
N7 Fe2 N11	86.06(18)	C16 N11 N12	106.8(4)	O8 S1 C23	102.8(7)
N11 Fe2 N9	84.56(17)	N11 N12 B2	119.6(4)	F1 C23 S1	114.1(6)
Fe1 O1 Fe2	122.6(2)	C18 N12 N11	109.0(4)	F1 C23 F2	101.4(7)
C19 O2 Fe1	135.4(4)	C18 N12 B2	131.4(5)	F2 C23 S1	110.4(6)
C19 O3 Fe2	132.1(4)	N1 C1 C2	110.2(5)	F3 C23 S1	114.2(7)
C21 O4 Fe1	131.9(4)	C3 C2 C1	105.1(5)	F3 C23 F1	107.3(8)
C21 O5 Fe2	136.5(4)	N2 C3 C2	109.4(5)	F3 C23 F2	108.5(9)
N2 N1 Fe1	120.2(3)	N3 C4 C5	109.7(5)	O9 C24 C25	123.0(7)
C1 N1 Fe1	133.6(4)	C6 C5 C4	105.6(5)	O9 C24 C26	118.1(7)
C1 N1 N2	106.2(4)	N4 C6 C5	109.4(5)	C25 C24 C26	118.9(7)
N1 N2 B1	120.1(4)	N5 C7 C8	110.5(6)		

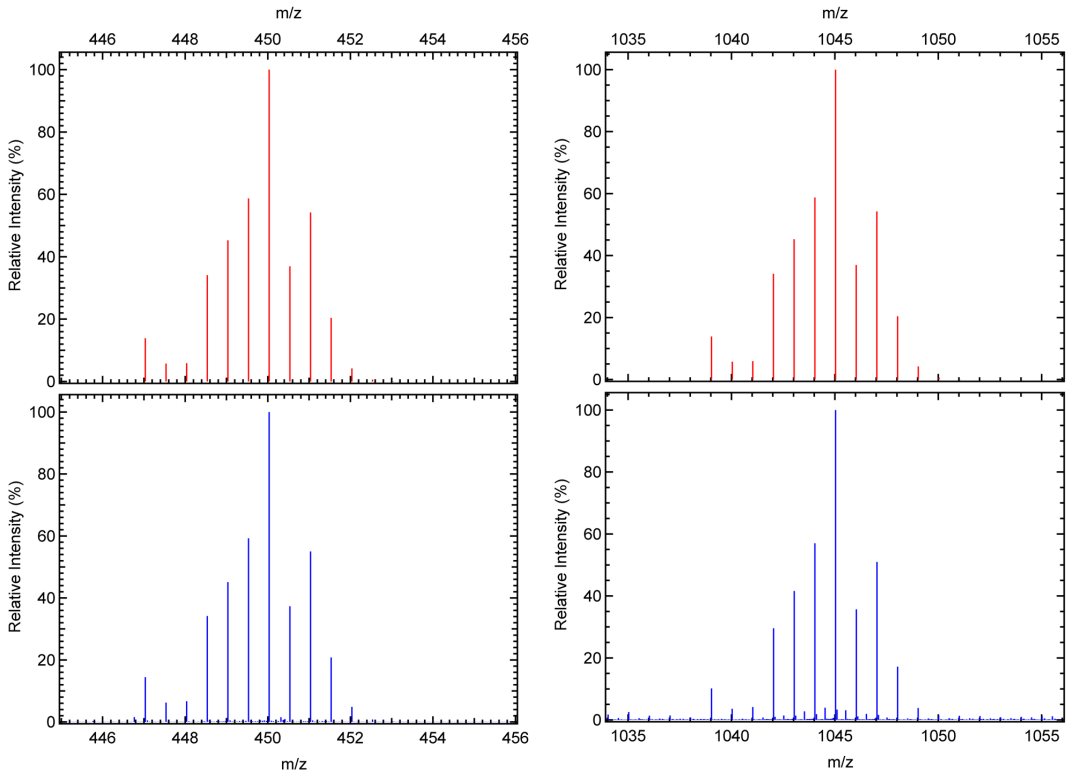


Figure 5.31. ESI-MS of Ru^{F}mcb. Top left: predicted isotope pattern for $[M–2PF_6]^{2+}$ ($C_{36}H_{22}N_6O_2F_{12}Ru$). Top right: predicted isotope pattern for $[M–PF_6]^{+}$ ($C_{36}H_{22}N_6O_2F_{12}RuPF_6$).Bottom: experimental results.

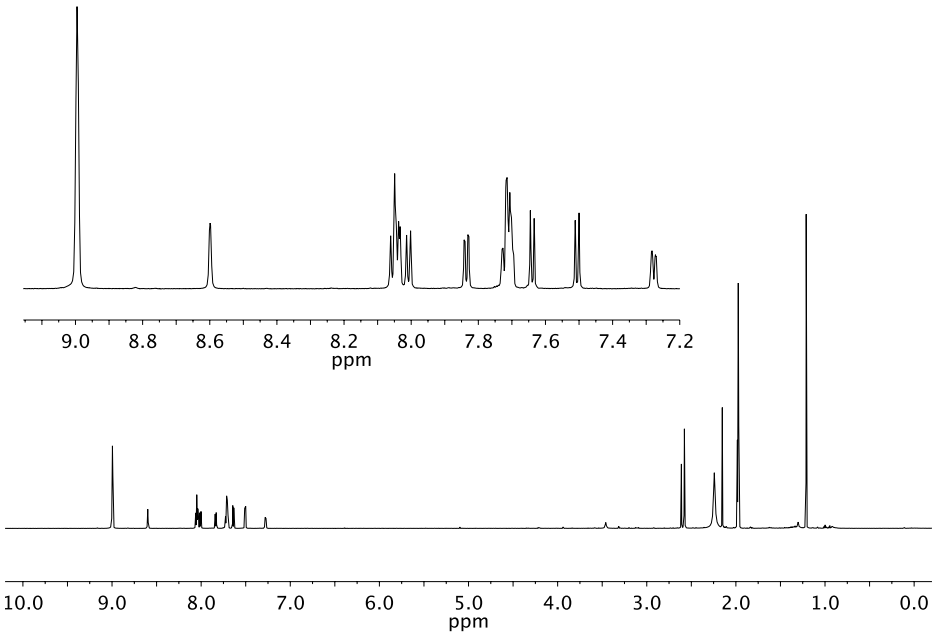


Figure 5.32. ^{1}H NMR of Ru^{F}mcb in CD_3CN.

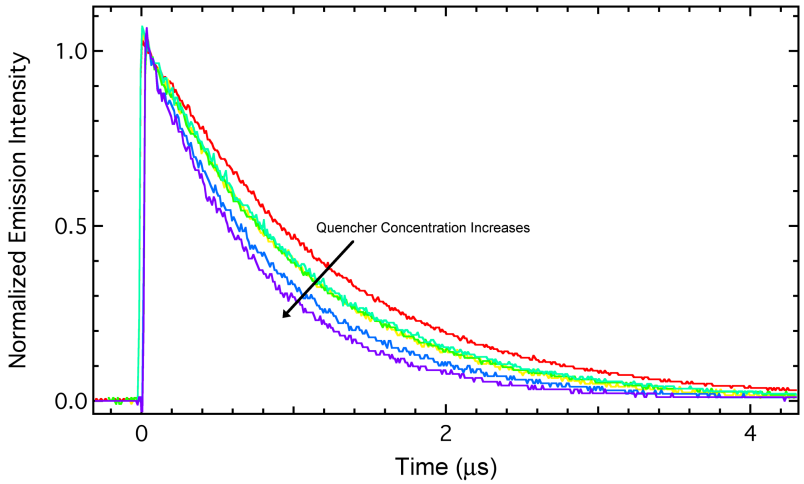


Figure 5.33. Time-resolved emission traces for Rumcb in the presence of varying concentrations of $(Tp)_2Fe_2O(O_2CCHCl_2)_2$.

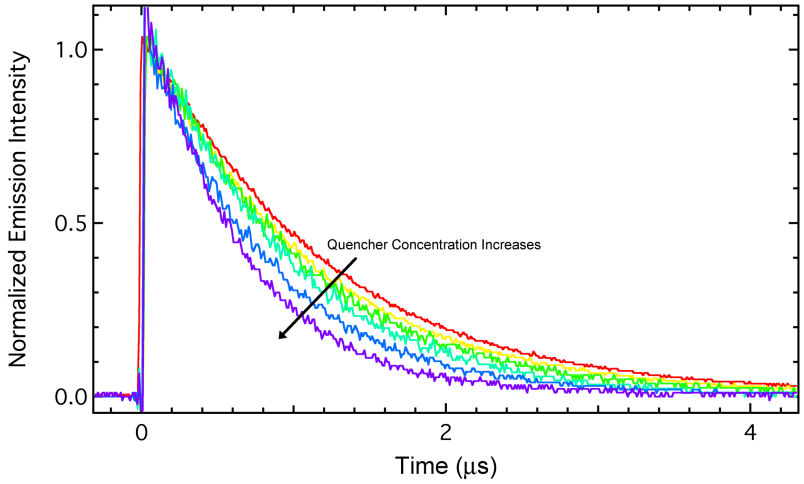


Figure 5.34. Time-resolved emission traces for Rumcb in the presence of varying concentrations of $[(Tp)_2Fe_2(OH)(O_2CCH_2Cl)_2](ClO_4)$.

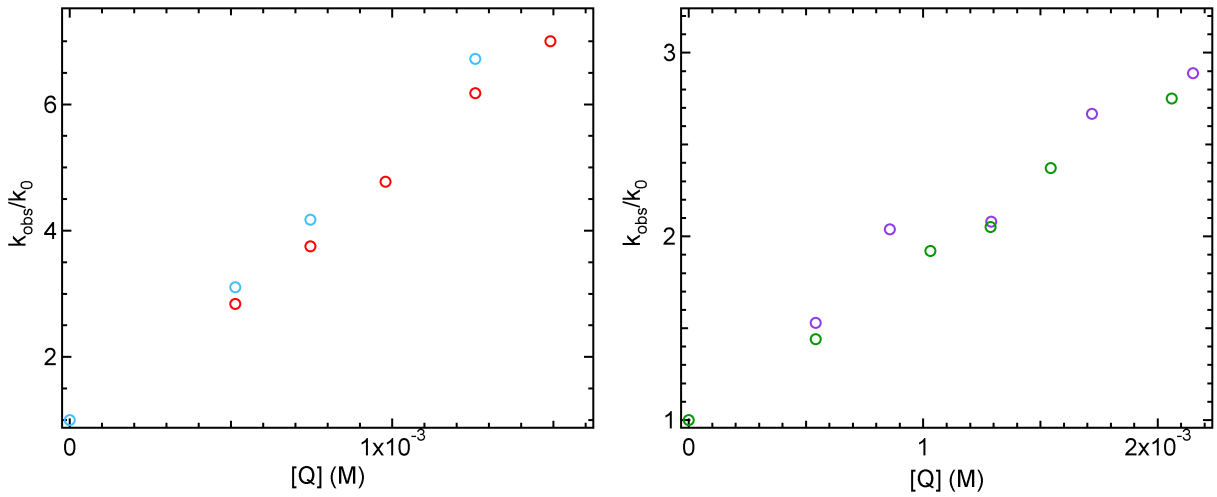


Figure 5.35. Left: Stern-Volmer plots for $[(Tp)_2Fe_2(OH)(O_2CCH_2Cl)_2](ClO_4)$/Rumcb (red), $[(Tp)_2Fe_2(OH)(O_2CCH_2Cl)_2](ClO_4)$/RumcbEt (blue). Right: Stern-Volmer plots for $(Tp)_2Fe_2O(O_2CCHCl_2)_2$/Rumcb (purple) and $(Tp)_2Fe_2O(O_2CCHCl_2)_2$/RumcbEt (green).

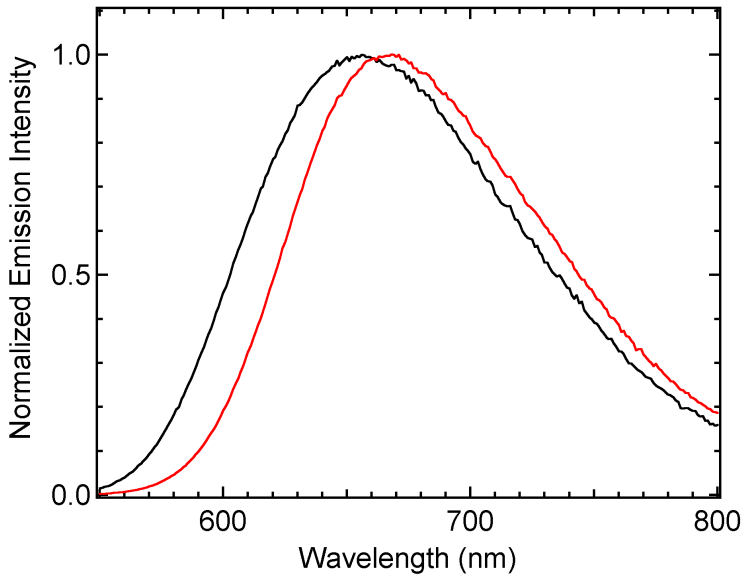


Figure 5.36. Steady-state emission spectra for Rumcb (black trace) and RumcbEt (red trace) in deoxygenated acetonitrile solution at room temperature.

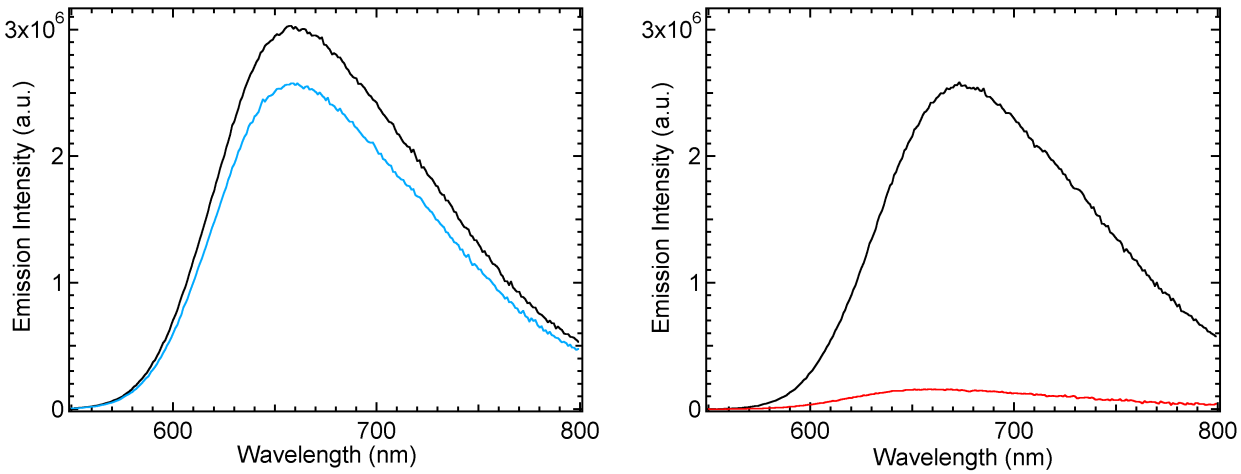


Figure 5.37. Left: Steady-state emission spectrum of Ru^{F}mcbEt alone (black trace) and in the presence of $[(Tp)_2Fe_2(OH)(O_2CCH_3)_2](OTf)$ (blue trace). Right: Ru^{F}mcb without quencher (black trace) and combined with $[(Tp)_2Fe_2(OH)(O_2CCH_3)_2](OTf)$ (red trace). The concentration of the quencher is the same in both cases.

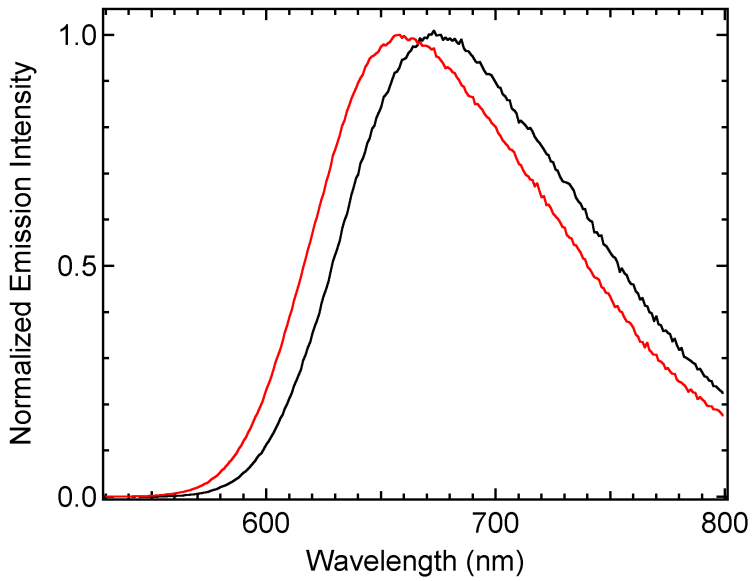


Figure 5.38. Steady-state emission spectra for Ru^{F}mcb (black trace) and Ru^{F}mcbEt (red trace) in deoxygenated acetonitrile solution at room temperature.

Table 5.14. Electrochemical and photophysical data for the Ru(II) donors used in this chapter.

	$E(Ru^{III/II})$ (V)	E_0 (eV)	τ (ns)
Rumcb	0.91	2.13	1050
RumcbEt	N/A	1.89	1230
Ru^{F}mcb	1.21	1.86	610
Ru^{F}mcbEt	1.14	1.91	890

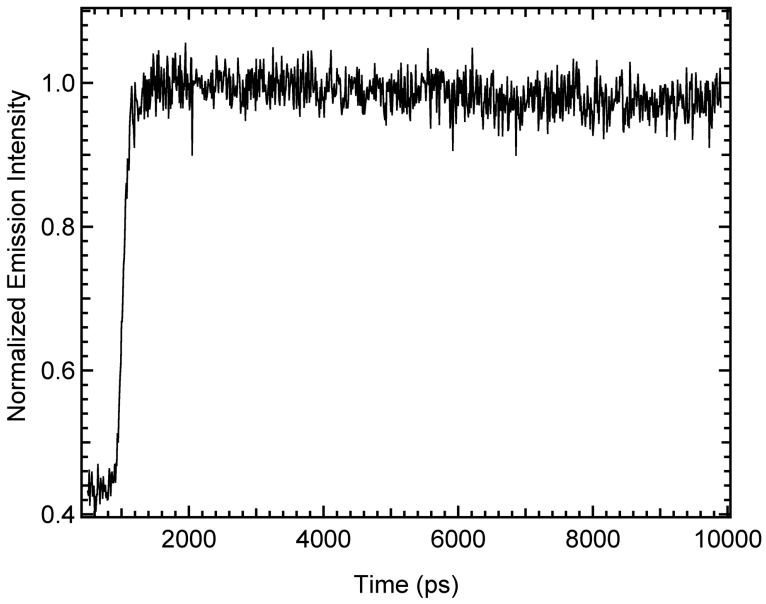


Figure 5.39. Time-resolved emission trace for Ru^{F}mcb in the absence of a quencher, showing no short-lived processes in the timescale relevant to the D-A assemblies**.**

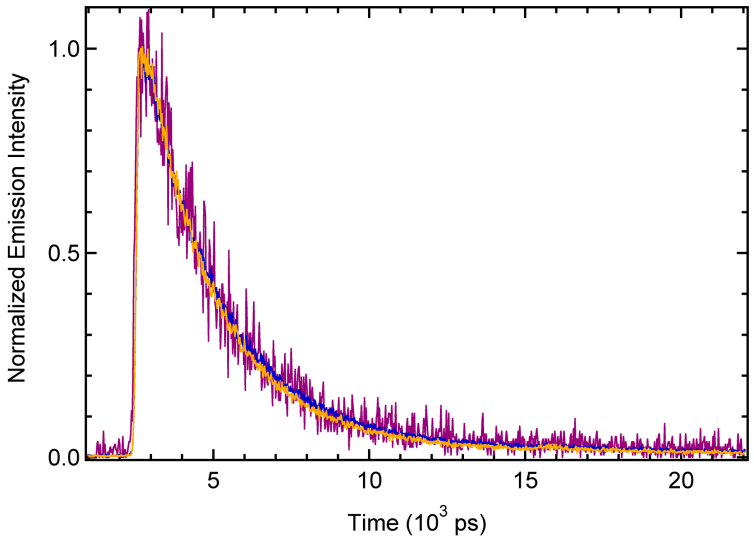


Figure 5.40. Time-resolved emission traces for Ru^{F}mcb in the presence of $(Tp)_2Fe_2O(O_2CCF_3)_2$ 0.16 mM (orange trace), 0.18 mM (purple trace) and 0.20 mM (blue trace).

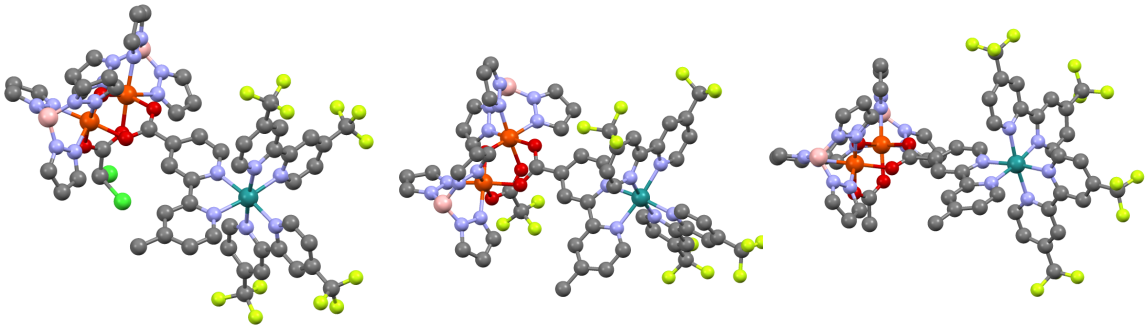


Figure 5.41. Ball-and-stick renderings of the Ru^{F}mcb-containing D-A assemblies, as obtained from geometry optimizations. From left to right: $(Tp)_2Fe_2O(O_2CCHCl_2)_2$, $(Tp)_2Fe_2O(O_2CCF_3)_2$ and $[(Tp)_2Fe_2(OH)(O_2CCH_3)_2]^+$.

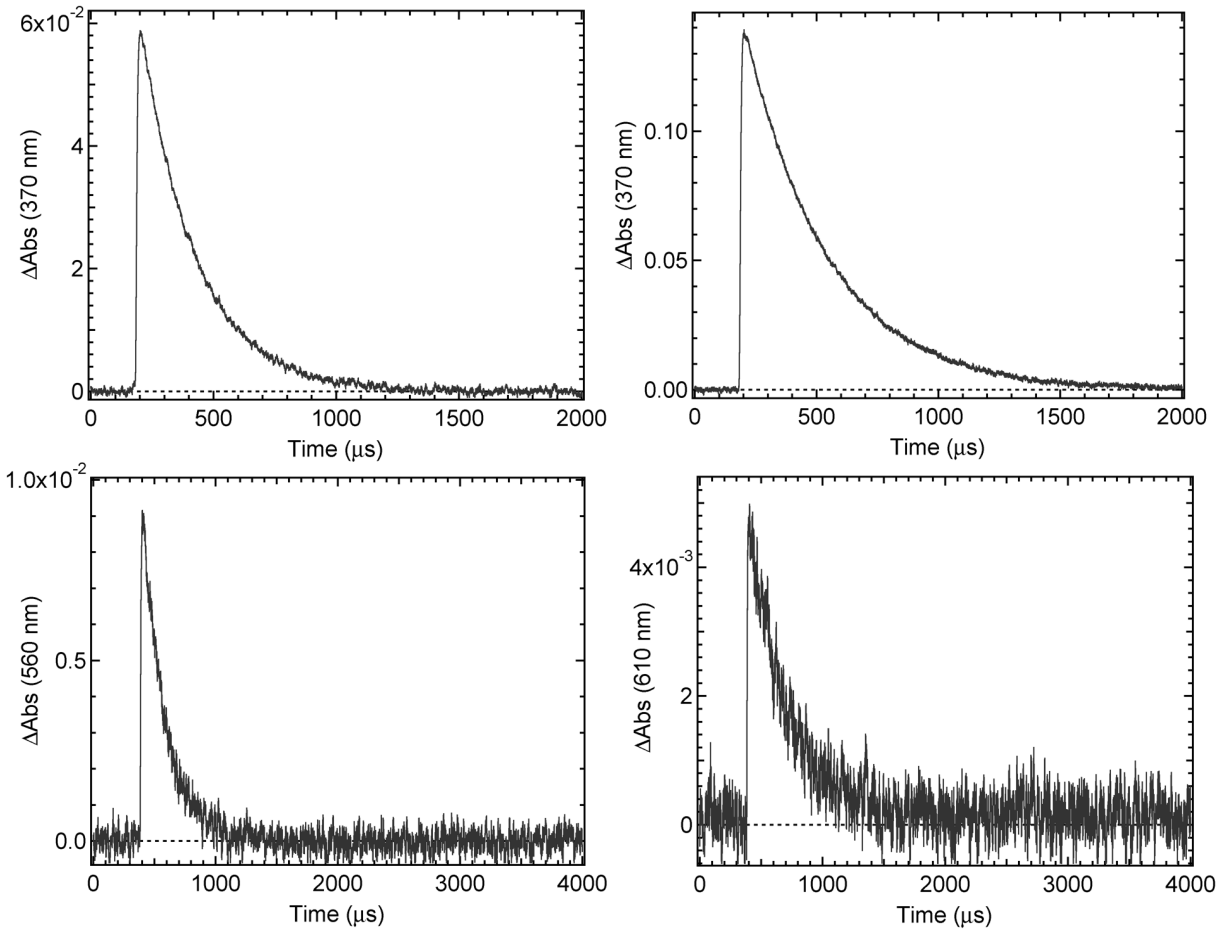


Figure 5.42. Transient absorption data (λ_{pump}: 475 nm). Top left: RumcbEt (λ_{probe}: 370 nm). Bottom left: RumcbEt + $[(Tp)_2Fe_2(OH)(O_2CCH_3)_2](OTf)$ (λ_{probe}: 560 nm). Top right: Ru^{F}mcbEt (λ_{probe}: 370 nm). Bottom right: Ru^{F}mcbEt + $[(Tp)_2Fe_2(OH)(O_2CCH_3)_2](OTf)$ (λ_{probe}: 610 nm).

REFERENCES

REFERENCES

(1) Doyle, A. C. *The Adventures of Sherlock Holmes*; 1892.

(2) Weldon, B. T.; Wheeler, D. E.; Kirby, J. P.; McCusker, J. K. *Inorg. Chem.* **2001**, *40*, 6802–6812.

(3) Sprintschnik, G.; Sprintschnik, H. W.; Kirsch, P. P.; Whitten, D. G. *J. Am. Chem. Soc.* **1977**, *99*, 4947–4954.

(4) Peek, B. M.; Ross, G. T.; Edwards, S. W.; Meyer, G. J.; Meyer, T. J.; Erickson, B. W. *Int. J. Pept. Protein Res.* **1991**, *38*, 114–123.

(5) Aldridge, W. S.; Hornstein, B. J.; Serron, S.; Dattelbaum, D. M.; Schoonover, J. R.; Meyer, T. J. *J. Org. Chem.* **2006**, *71*, 5186–5190.

(6) Lakowicz, J. R. *Principles of Fluorescence Spectroscopy*, 3rd ed.; Springer US: Boston, 2006.

(7) Damrauer, N. H.; Boussie, T. R.; Devenney, M.; McCusker, J. K. *J. Am. Chem. Soc.* **1997**, *119*, 8253–8268.

(8) Picraux, L. B.; Smeigh, A. L.; Guo, D.; McCusker, J. K. *Inorg. Chem.* **2005**, *44*, 7846–7859.

(9) Pillman, H. A.; Blanchard, G. J. *J. Phys. Chem. B* **2010**, *114*, 3840–3846.

(10) Richardson, D. E.; Taube, H. *Inorg. Chem.* **1981**, *20*, 1278–1285.

(11) Frisch, M. J.; Trucks, G. W.; Schlegel, H. B.; Scuseria, G. E.; Robb, M. A.; Cheeseman, J. R.; Montgomery, Jr., J. A.; Vreven, T.; Kudin, K. N.; Burant, J. C.; Millam, J. M.; Iyengar, S. S.; Tomasi, J.; Barone, V.; Mennucci, B.; Cossi, M.; Scalmani, G.; Rega, N.; Petersson, G. A.; Nakatsuji, H.; Hada, M.; Ehara, M.; Toyota, K.; Fukuda, R.; Hasegawa, J.; Ishida, M.; Nakajima, T.; Honda, Y.; Kitao, O.; Nakai, H.; Klene, M.; Li, X.; Knox, J. E.; Hratchian, H. P.; Cross, J. B.; Bakken, V.; Adamo, C.; Jaramillo, J.; Gomperts, R.; Stratmann, R. E.; Yazyev, O.; Austin, A. J.; Cammi, R.; Pomelli, C.; Ochterski, J. W.; Ayala, P. Y.; Morokuma, K.; Voth, G. A.; Salvador, P.; Dannenberg, J. J.; Zakrzewski, V. G.; Dapprich, S.; Daniels, A. D.; Strain, M. C.; Farkas, O.; Malick, D. K.; Rabuck, A. D.; Raghavachari, K.; Foresman, J. B.; Ortiz, J. V.; Cui, Q.; Baboul, A. G.; Clifford, S.; Cioslowski, J.; Stefanov, B. B.; Liu, G.; Liashenko, A.; Piskorz, P.; Komaromi, I.; Martin, R. L.; Fox, D. J.; Keith, T.; Al-Laham, M. A.; Peng, C. Y.; Nanayakkara, A.; Challacombe, M.; Gill, P. M. W.; Johnson, B.; Chen, W.; Wong, M. W.; Gonzalez, C.; Pople, J. A.

Gaussian 03, Revision D.01. Gaussian, Inc., Wallingford CT, 2004.

(12) Monat, J. E.; Rodriguez, J. H.; McCusker, J. K. *J. Phys. Chem. A* **2002**, *106*, 7399–7406.

(13) Bock, C. R.; Connor, J. A.; Gutierrez, A. R.; Meyer, T. J.; Whitten, D. G.; Sullivan, B. P.; Nagle, J. K. *J. Am. Chem. Soc.* **1979**, *101*, 4815–4824.

(14) Clark, C. D.; Hoffman, M. Z. *Coord. Chem. Rev.* **1997**, *159*, 359–373.

(15) Nickita, N.; Belousoff, M. J.; Bhatt, A. I.; Bond, A. M.; Deacon, G. B.; Gasser, G.; Spiccia, L. *Inorg. Chem.* **2007**, *46*, 8638–8651.

(16) Soler, M.; McCusker, J. K. *J. Am. Chem. Soc.* **2008**, *130*, 4708–4724.

(17) Armstrong, W. H.; Lippard, S. J. *J. Am. Chem. Soc.* **1984**, *106*, 4632–4633.

(18) Armarego, W. L. F.; Chai, C. L. L. *Purification of Organic Chemicals*, 6th ed.; Elsevier, 2009.

(19) Crosby, G. A.; Demas, J. N. *J. Phys. Chem.* **1971**, *75*, 991–1024.

(20) Marcus, R. A.; Sutin, N. *Biochim. Biophys. Acta - Rev. Bioenerg.* **1985**, *811*, 265–322.

(21) Marcus, R. A. *Angew. Chem. Int. Ed.* **1993**, *32*, 1111–1121.

(22) Barbara, P. F.; Meyer, T. J.; Ratner, M. A. *J. Phys. Chem.* **1996**, *100*, 13148–13168.

(23) Wu, Q.; Van Voorhis, T. *J. Chem. Phys.* **2006**, *125*, 164105-1-164105–164109.

(24) Barigelletti, F.; Flamigni, L. *Chem. Soc. Rev.* **2000**, *29*, 1–12.

(25) Guo, D.; Knight, T. E.; McCusker, J. K. *Science* **2011**, *334*, 1684–1687.

(26) Kurtz, D. M. *Chem. Rev.* **1990**, *90*, 585–606.

(27) Borovik, A. S.; Papaefthymiou, V.; Taylor, L. F.; Anderson, O. P.; Que, L. *J. Am. Chem. Soc.* **1989**, *111*, 6183–6195.

(28) Drago, R. S. *Physical Methods for Chemists*; Saunders College Pub.: Philadelphia, 1992.

(29) Kouzelos, J. A. The Effect of Electronic Spin on the Reactivity of Spin-Coupled Transition Metal Complexes, Michigan State University, 2015.

(30) Armstrong, W. H.; Spool, A.; Papaefthymiou, G. C.; Frankel, R. B.; Lippard, S. J. *J. Am. Chem. Soc.* **1984**, *106*, 3653–3667.

(31) Bominaar, E. L.; Achim, C.; Borshch, S. A.; Girerd, J.-J.; Münck, E. *Inorg. Chem.* **1997**, *36*, 3689–3701.

(32) Bominaar, E. L.; Achim, C.; Borshch, S. A. *J. Chem. Phys.* **1999**, *110*, 11411–11422.

(33) Rodriguez, J. H.; McCusker, J. K. *J. Chem. Phys.* **2002**, *116*, 6253–6270.

Chapter 6. Progress Towards the Synthesis of an Intramolecular Assembly Using a Scorpionate Bifunctional Ligand

"I had managed to become quite good at rearranging what I liked to think of as the building blocks of the universe." -Flavia de Luce[1]

6.1. Introduction

As was discussed in Chapter 1, the need to study electron and energy transfer as intramolecular processes arose from the diffusion-limited kinetics encountered when using bimolecular D-A systems.[2] All the efforts towards this goal described thus far made use of the carboxylate bridges to append the Ru(II) donor to the diiron(III) core.[3,4] An alternative design makes use of the capping ligand (a trispyrazolyl borate) as the bridge between donor and acceptor. The main advantage of this approach is that it frees up the carboxylate groups, so that they can be used to alter the redox potentials of the diferric core.[2] On the other hand, this design is synthetically challenging, as will be described in this chapter.

Considering the donor and acceptor moieties of interest, it is clear that the bridging ligand must have both a bipyridine and a trispyrazolyl borate unit; it is also desirable for this ligand to have enough electronic communication between both parts of the molecule, and not be too sterically encumbered. Instead of directly attaching one of the pyridine rings to the boron atom of Tp, a phenyl linker may be used. If the linker is directly attached to the bipyridine, it keeps the conjugation; at the same time, the ring can rotate around the single bonds to the groups it is bridging, and it functions as a spacer, reducing

the steric constraints of the system. Alternatively, an alkyne bridge may be included between the phenyl ring and the bipyridine. Such ligands are shown in Figure 6.1.

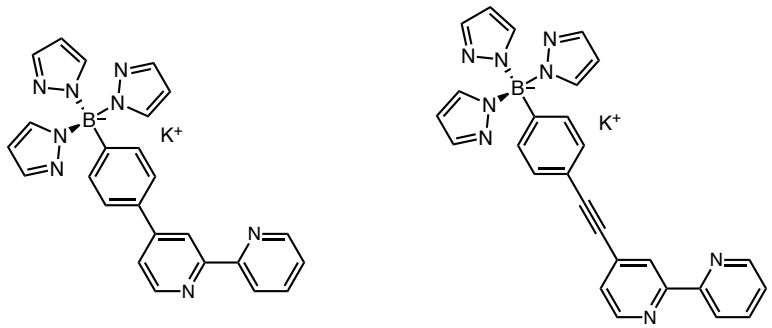


Figure 6.1. Possible bifunctional ligand designs incorporating a trispyrazolyl borate unit and a 2,2'-bipyridine. Their syntheses are discussed in this chapter.

Previous work in our group[5] used a Stille coupling[6] between 4-(trimethylstannyl)-2,2′-bipyridine and potassium trispyrazolyl-(4-bromobenzyl) borate to synthesize the "*ext*-Tp" ligand on the left side of Figure 6.1. This synthetic route is displayed in Figure 6.2: unfortunately, 4-(4-bromophenyl)-2,2′-bipyridine was the only obtained product, instead of the intended one.

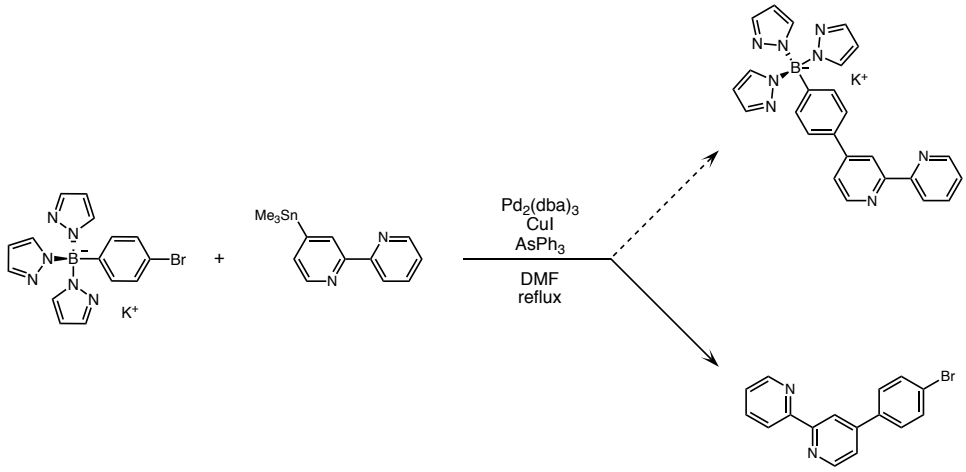


Figure 6.2. Previously attempted route to make *ext*-Tp via a Stille coupling.[5]

In this chapter, alternative routes to prepare such *ext*-Tp ligand are described. Additionally, the ligand on the right side of Figure 6.1 was pursued, in hopes that these molecules would be amenable to a Sonogashira coupling.[6] Indeed, work by Reger and co-workers[7] has shown that $[Fe(Tp')_2]^+$ with modified scorpionate ligands may be further modified using couplings of this kind. Unfortunately, this route has not yielded satisfactory results, and this second design was abandoned. Work towards the original *ext*-Tp is still ongoing.

6.2. Experimental Section

General. All chemicals and solvents were obtained from Fisher Scientific or Sigma-Aldrich and used without purification unless otherwise stated. $RuCl_3 \cdot xH_2O$ and yttrium (III) hexafluoroacetylacetonate were purchased from Strem Chemicals and stored in a desiccator, silica gel from SiliCycle, and Sephadex LH-20 from GE Life Sciences. Diisoproplyamine (DIPA), triethylamine (TEA) and piperidine were distilled from NaOH/activated carbon, and freeze-pump-thaw degassed prior to use. Copper(I) iodide was recrystallized[8] and stored in the glovebox. Molecular sieves (4 Å) were stored in the oven and activated prior to use.

3-(4-Bromo-phenyl)-1-pyridin-2-yl-propenone,[9] $[Ru(bpy)_2(ebpy)](PF_6)_2$[10] and 2,2'-bipyridine-4-boronic acid[11] were prepared following previously reported procedures. The synthesis of $Ru(bpy)_2Cl_2$ was described in Chapter 3.

^1H NMR spectra were collected on Agilent DDR2 500 MHz NMR spectrometers equipped with 7600AS 96-sample autosamplers. Mass spectra were obtained at the

Michigan State University Mass Spectrometry and Metabolomics Core. Elemental analyses were obtained through the analytical facilities at Michigan State University. Solvent included in calculated elemental analysis percentages was included to give the best fit based on solvents identified by NMR[12] or XRD.

6.2.1. Syntheses

2,2'-bipyridine-N-oxide (bpy-N-oxide).[13] 2,2'-bipyridine (10.1 g, 65 mmol) was dissolved in 50 mL of trifluoroacetic acid. Then, 11 mL of 30% H_2O_2 were added and the solution was stirred for 2 h at room temperature. After this time, the reaction mixture was cooled down using an ice bath and it was brought to pH 10 with 5 M NaOH. The product was extracted into chloroform (4 × 60 mL), the organic layers were dried with $MgSO_4$ and then the solvent was evaporated under reduced pressure to yield a colorless oil that crystallized upon standing. Yield: 10.8 g (97%). ^{1}H NMR ($CDCl_3$, 500 MHz) δ (ppm): 8.86 (d, *J* = 8.1 Hz, 1H), 8.69 (ddd, *J* = 4.8, 1.9, 0.9 Hz, 1H), 8.28 (dt, *J* = 6.5, 0.6 Hz, 1H), 8.14 (dd, *J* = 8.0, 2.1 Hz, 1H), 7.80 (td, *J* = 7.8, 1.8 Hz, 1H), 7.32 (m, 2H), 7.24 (td, *J* = 7.0, 2.3 Hz, 1H).

4-nitro-2,2'-bipyridine-N-oxide (bpy-NO_2).[5,10] bpy-N-oxide (8.35g, 48 mmol) was dissolved in concentrated H_2SO_4 (48 mL) while keeping the solution at 0 °C. To this, a mixture of HNO_3 (83 mL) and H_2SO_4 (40 mL) was added dropwise, still at 0 °C. The reaction mixture was heated to 95 °C for 5 h, after which it was allowed to cool down, poured over 500 g of ice and brought to pH 10 with 5 M NaOH. At this point, the product precipitated as a yellow solid, which was collected by vacuum filtration and washed with

large amounts of water. Yield: 5.16 g (49%). ^{1}H NMR ($CDCl_3$, 500 MHz) δ (ppm): 9.18 (d, *J* = 3.3 Hz, 1H), 8.90 (dt, *J* = 8.1, 1.1 Hz, 1H), 8.80 (ddd, *J* = 4.8, 1.8, 1.0 Hz, 1H), 8.37 (d, *J* = 8.2 Hz, 1H), 8.07 (dd, *J* = 7.2, 3.3 Hz, 1H), 7.89 (td, *J* = 7.8, 1.8 Hz, 1H), 7.44 (ddd, *J* = 7.6, 4.7, 1.1 Hz, 1H).

4-bromo-2,2'-bipyridine-N-oxide (Br-bpy-NO).[5,10] Over an ice bath, bpy-NO_2 (4.52 g, 20 mmol) was combined with glacial acetic acid (105 mL); acetyl bromide (60 mL) was then added. The mixture was refluxed under nitrogen for 4 h, after which it was poured over ice and brought to pH 10 with 5 M NaOH. The product was extracted into $CHCl_3$; the resulting orange solution was dried with $MgSO_4$ and the solvent was evaporated under reduced pressure. The product was used without further purification; some 4-bromo-2,2'-bipyridine was obtained as a side product. Yield: 4.63 g (88% if pure). ^{1}H NMR ($CDCl_3$, 500 MHz) δ (ppm): 8.94 (d, *J* = 8.1 Hz, 1H), 8.73 (d, *J* = 4.8 Hz, 1H), 8.39 (d, *J* = 3.0 Hz, 1H), 8.15 (d, *J* = 7.0 Hz, 1H), 7.84 (td, *J* = 7.8, 1.8 Hz, 1H), 7.38 (m, 2H).

4-bromo-2,2'-bipyridine.[5,10] Br-bpy-NO (3.47 g, 14 mmol) was suspended in 90 mL of dry acetonitrile and PBr_3 (8 mL) was added. The mixture was heated to reflux for 15 h under nitrogen. Then it was allowed to cool down, poured over ice and brought to pH 11 with NaOH. The product was extracted into $CHCl_3$, the organic layers were dried with $MgSO_4$ and the solvent was evaporated to yield a tan solid. The product was further purified using a basic alumina plug, eluting with CH_2Cl_2 and finally obtained as a white solid. Yield: 3.06 g (95%). ^{1}H NMR ($CDCl_3$, 500 MHz) δ (ppm): 8.67 (ddd, *J* = 4.8, 1.8, 1.0 Hz, 1H), 8.62 (dd, *J* = 1.9, 0.6 Hz, 1H), 8.47 (dd, *J* = 5.3, 0.7 Hz, 1H), 8.38 (dt, *J* = 8.0, 1.0 Hz,

1H), 7.81 (td, *J* = 7.5, 1.8 Hz, 1H), 7.46 (dd, *J* = 5.2, 1.9 Hz, 1H), 7.32 (ddd, *J* = 7.5, 4.8, 1.2 Hz, 1H).

4-((trimethylsilyl)ethynyl)-2,2'-bipyridine (TMS-ebpy).[14] Under a nitrogen atmosphere, Br-bpy (0.20 g, 0.85 mmol) was dissolved in 20 mL of THF. To this solution, trimethylsilylacetylene (0.25 mL, 1.73 mmol), $Pd(PPh_3)_4$ (6 mol%) and diisopropylamine (8 mL) were added. The mixture was refluxed overnight, over which time it turned orange-brown. The solvent was evaporated under reduced pressure, and the residue was loaded on a silica gel column and eluted with CH_2Cl_2/MeOH 99:1 to afford the product as a colorless oil. Alternatively, a basic alumina column eluting with hexanes/EtOAc 4:1 was also a viable purification method. Yield: 0.18 g (81%). ^{1}H NMR ($CDCl_3$, 500 MHz) δ (ppm): 8.68 (ddd, *J* = 4.8, 1.8, 0.9 Hz, 1H), 8.62 (dd, *J* = 5.0, 0.9 Hz, 1H), 8.47 (dd, *J* = 1.6, 0.9 Hz, 1H), 8.39 (dt, *J* = 8.0, 1.0 Hz, 1H), 7.80 (ddd, *J* = 8.0, 7.5, 1.8 Hz, 1H), 7.32 (dd, *J* = 5.0, 1.5 Hz, 1H), 7.30 (ddd, *J* = 7.5, 4.8, 1.2 Hz, 1H), 0.28 (s, 9H).

4-ethynyl-2,2'-bipyridine (ebpy).[14] TMS-ebpy (all that was obtained from 0.24 g (1.0 mmol) on the previous step) was dissolved in 10 mL of THF and 10 mL of MeOH, and KF (0.07 g, 1.2 mmol) was added. The solution was stirred overnight at room temperature, and then the solvent was removed under reduced pressure. The resulting solid was dissolved using CH_2Cl_2 and water, and extracted into CH_2Cl_2. The combined organic layers were dried with $MgSO_4$ and rotovapped to dryness to give the product as a white solid. Yield: 0.16 g (88% over two steps). ^{1}H NMR ($CDCl_3$, 500 MHz) δ (ppm): 8.69 (ddd, *J* = 4.8, 1.8, 0.9 Hz, 1H), 8.65 (dd, *J* = 5.0, 0.9 Hz, 1H), 8.50 (dd, *J* = 1.4, 0.9 Hz, 1H), 8.39 (dt,

J = 7.9, 1.0 Hz, 1H), 7.82 (ddd, *J* = 7.9, 7.5, 1.8 Hz, 1H), 7.36 (dd, *J* = 4.9, 1.6 Hz, 1H), 7.32 (ddd, *J* = 7.5, 4.8, 1.2 Hz, 1H), 3.30 (s, 1H).

4-iodo-trimethyl benzene (I-Ph-TMS).[15] Under a nitrogen atmosphere, p-diiodobenzene (3.11 g, 9.4 mmol) was dissolved in diethyl ether (20 mL), and cooled down to –78°C using a dry ice/acetone bath. Using an addition funnel, 1.6 M nBuLi (5.9 mL, 9.4 mmol) was added dropwise; after the addition, the reaction was stirred at –78°C for 2h. TMS-Cl (1.9 mL, 15.0 mmol) was added with a syringe, and the reaction was allowed to stir under nitrogen and reach room temperature overnight. To quench the reaction, H_2O (18 mL) was added, leading to the formation of two separate layers (the organic layer was yellow). The product was extracted into Et_2O, and the combined organic layers were dried over $MgSO_4$ and the solvent was removed under reduced pressure, yielding a dark red oil. The product was purified with a silica gel plug, eluting with hexanes; after removing the solvent, a colorless oil was obtained, which was the product contaminated with the starting material (δ: 7.53 ppm in $CDCl_3$) and $(TMS)_2C_6H_4$ (δ: 7.42 ppm in $CDCl_3$). After leaving this oil in the fridge overnight, a colorless solid crashed out, which was a ~1:1 mixture of product and starting material. The remaining oil, which still contained ~3% of the starting material and $(TMS)_2C_6H_4$, was freeze-pump-thaw degassed and stored in the glove box. Yield: 1.76 g (67% if pure). ^{1}H NMR ($CDCl_3$, 500 MHz) δ (ppm): 7.74 (d, *J* = 8.2 Hz, 2H), 7.29 (d, *J* = 8.2 Hz, 2H), 0.30 (s, 9H).

(4-iodophenyl)dibromoborane (I-Ph-BBr_2).[15] Under a nitrogen atmosphere, a Schlenk tube was charged with I-Ph-TMS (all the product that was obtained starting with 5.07 g of p-diiodobenzene, <15.4 mmol), BBr_3 (5 mL, 52.7 mmol) and a stir bar. The reaction was

heated to 60°C overnight, during which time the solution darkened. The excess BBr_3 and any side products were removed *via* vacuum distillation, leaving an off-white/light pink solid residue in the round-bottom flask. This solid was pumped back into the glove box to use without further purification. ^{1}H NMR ($CDCl_3$, 500 MHz) δ (ppm): 7.89 (d, *J* = 8.3 Hz, 2H), 7.86 (d, *J* = 8.3 Hz, 2H).

Potassium (4-iodophenyl)tris(1-pyrazolyl)borate (I-Ph-TpK).[15,16] In a nitrogen-filled glove box, I-Ph-BBr_2 (all the solid obtained in the previous step, <15.4 mmol) was dissolved in 10 mL of toluene. In a separate flask, pyrazole (3.14 g, 46.1 mmol) and triethylamine (4.3 mL, 30.8 mmol) were dissolved in 50 mL of toluene. To this solution, the I-Ph-BBr_2 solution was added dropwise, while stirring. A white precipitate formed almost immediately, but the reaction was stirred overnight at room temperature. The white solid was filtered off, and to the resulting yellowish filtrate KOEt (1.57 g, 18.7 mmol) was added. The mixture was stirred overnight at room temperature; after this time, it was taken out of the glove box and a white solid was collected by vacuum filtration. ^{1}H NMR of this solid showed it to contain both the product and unreacted pyrazole. The solid was triturated with hexanes until all the pyrazole had been removed. Yield: 1.66 g (24% over three steps). ^{1}H NMR (CD_3OD, 500 MHz) δ (ppm): 7.55 (dd, *J* = 1.6, 0.5 Hz, 3H), 7.29 (d, *J* = 8.2 Hz, 2H), 7.49 (d, *J* = 8.3 Hz, 2H), 7.11 (dd, *J* = 2.2, 0.5 Hz, 3H), 7.09 (d, *J* = 8.2 Hz, 2H), 6.15 (dd, *J* = 1.7, 2.2 Hz, 3H). HRMS (ESI-TOF) m/z: $[M-K]^-$ Calcd for $C_{15}H_{13}N_6BI$ 415.0342; Found 415.0380.

Potassium (4-([2,2'-bipyridin]-4-ylethynyl)phenyl)tris(1-pyrazolyl)borate (ebpy-TpK).[7] Under a nitrogen atmosphere, ebpy (82 mg, 0.46 mmol), I-Ph-TpK (0.25 g, 0.55

mmol), $Pd(PPh_3)_2Cl_2$ (33 mg, 0.047 mmol), CuI (43 mg, 0.23 mmol) and triethylamine (10 mL) were dissolved in 40 mL THF. The mixture was refluxed under nitrogen until no ebpy was seen on TLC (basic alumina, hexanes/EtOAc 4:1), about 36 h. The reaction mixture was allowed to cool down and was filtered through a celite pad to remove a black/purple solid, which was rinsed with MeOH several times. The brown filtrate was evaporated to dryness under reduced pressure, and the resulting brown solid was used without further purification. No yield was calculated. HRMS (ESI-TOF) m/z: $[M-K]^-$ Calcd for $C_{27}H_{20}N_8B$ 467.1909; Found 467.1907.

Bis(2,2′-bipyridine) ((4-([2,2'-bipyridin]-4-ylethynyl)phenyl)tris(1-pyrazolyl)borate) ruthenium(II) hexafluorophosphate, $[Ru(bpy)_2(ebpy\text{-}Tp)](PF_6)$. Inside a nitrogen-filled glovebox, $Ru(bpy)_2Cl_2$ (0.21 g, 0.43 mmol) and $AgNO_3$ (0.16 g, 0.95 mmol) were dissolved in 70 mL of MeOH; the flask was covered with aluminum foil and the reaction was stirred at room temperature for 4 h. After this time, the mixture was filtered through a celite pad to remove AgCl (this step was also performed in the dark). To the filtrate was added the solid from the synthesis of ebpy-TpK dissolved in a small amount of MeOH. The solution was refluxed overnight under nitrogen, and the solvent was removed under reduced pressure; the resulting solid was purified using a neutral alumina column, eluting with MeCN until the first orange band exited the column, then switching to MeCN/KNO_3 (saturated aqueous solution) 5:1. The ^1H NMR of the column fractions was inconclusive, but the product was detected in several of them using mass spectroscopy. HRMS (ESI-TOF) m/z: $[M–PF_6]^+$ Calcd. For $C_{47}H_{36}N_{12}BRu$ 881.2341; Found 881.2336.

Attempted synthesis of [Ru(bpy)$_2$(ebpy-Tp)](PF$_6$). In a nitrogen-filled glove box, [Ru(bpy)$_2$(ebpy)](PF$_6$)$_2$ (79 mg, 0.09 mmol) was dissolved in 8 mL of THF and 1 mL of MeCN. To this solution, I-Ph-TpK (63 mg, 0.14 mmol), Pd(PPh$_3$)$_2$Cl$_2$ (8 mg, 0.01 mmol), CuI (14 mg, 0.07 mmol) and piperidine (2 mL) were added. The mixture was refluxed under nitrogen for 24 h, after which time the solvent was removed under reduced pressure. The solid was loaded onto a neutral alumina column, eluting with MeCN, followed by 10:1 MeCN/KNO$_3$ (aq, sat) and 5:1 MeCN/KNO$_3$ (aq, sat). The fractions were analyzed by ESI-MS, but the intended product was not observed.

Attempted synthesis of [Ru(bpy)$_2$(ebpy-Tp)](PF$_6$).[17] Under a nitrogen atmosphere, [Ru(bpy)$_2$(ebpy)](PF$_6$)$_2$ (60 mg, 0.07 mmol) was dissolved in 1.7 mL of DMF, and combined with I-Ph-TpK (45 mg, 0.1 mmol), Pd(PPh$_3$)$_4$ (4 mg, 5 mol%), CuI (4 mg, 30 mol%), and 0.35 mL of diisopropylamine. The resulting solution was stirred under nitrogen at room temperature for 48 h. The solvent was evaporated and the solid was loaded onto a neutral alumina column, eluting with MeCN, followed by 10:1 MeCN/KNO$_3$ (aq, sat) and 5:1 MeCN/KNO$_3$ (aq, sat). The fractions were analyzed by ESI-MS.

2-[4-(4-bromophenyl)-2-ethoxy-3,4-dihydro-2*H*-pyran-6-yl]pyridine (7). This compound was prepared as described by Cordaro et al.,[18] but the purification procedure was modified: 3-(4-Bromo-phenyl)-1-pyridin-2-yl-propenone (3.25 g, 11.3 mmol) was dissolved in THF (55 mL) and added to a flame-dried round-bottom flask containing approximately 3 g of 4 Å freshly activated molecular sieves. Ethyl vinyl ether (11.2 mL, 0.12 mol) and yttrium (III) hexafluoroacetylacetonate (0.45 g, 0.60 mmol) were added and

the reaction mixture was stirred at room temperature under nitrogen until no more starting material was seen on TLC (silica gel, eluting with CH_2Cl_2), about 20 h. The mixture (initially yellow) turned purple over time; it was filtered through a celite pad, which was rinsed with Et_2O. Rotary evaporation of the solvent yielded a dark blue/purple oil that was loaded onto a silica column and eluted with hexanes/EtOAc 7:3. The product was obtained as a colorless oil that turned yellow upon standing. Yield: 3.98 g (98%). ^{1}H NMR ($CDCl_3$, 500 MHz) δ (ppm): 8.51 (ddd, *J* = 4.8, 1.7, 0.9 Hz, 1H), 7.70 (td, *J* = 7.7, 1.6 Hz, 1H), 7.65 (dt, *J* = 7.9, 1.0 Hz, 1H), 7.40 (d, *J* = 8.4 Hz, 2H), 7.19 (ddd, *J* = 7.3, 4.8, 1.1 Hz, 1H), 7.17 (d, *J* = 8.4 Hz, 2H), 6.17 (dd, *J* = 2.9, 1.1 Hz, 1H), 5.26 (dd, *J* = 8.3, 2.0 Hz, 1H), 4.10 (dq, *J* = 9.4, 7.1 Hz, 1H), 3.76 (ddd, *J* = 9.8, 6.9, 2.9 Hz, 1H), 3.70 (dq, *J* = 9.4, 7.1 Hz, 1H), 2.31 (dddd, *J* = 13.3, 6.9, 1.9, 1.3 Hz, 1H), 1.93 (ddd, *J* = 13.3, 9.9, 8.4 Hz, 1H), 1.25 (t, *J* = 7.1 Hz, 1H).

4-(4-bromophenyl)-2,2'-bipyridine (bpy-Ph-Br). This compound was prepared as described by Cordaro et al.,[18] but the isolation and purification steps were modified: **(7)** (1.46 g, 4.06 mmol) and $H_2NOH{\cdot}HCl$ (5.20 g, 75 mmol) were dissolved in 40 mL of MeCN. The solution was refluxed for 6 h, and then it was evaporated at reduced pressure. To the resulting solid, 50 mL of CH_2Cl_2 and 50 mL of a saturated NaCl/NaOH aqueous solution were added; the mixture was stirred until all the solid dissolved. The product was extracted into CH_2Cl_2 until the organic layer tested negative with Fe(II), and the combined organic layers were dried with Na_2SO_4 and evaporated to dryness to give a beige solid. That solid was purified using a basic alumina column, eluting with CH_2Cl_2, and then recrystallized from hot MeOH. Yield: 0.45 g (35%). ^{1}H NMR ($CDCl_3$, 500 MHz)

δ (ppm): 8.74 (dd, *J* = 5.1, 0.7 Hz, 1H), 8.72 (ddd, *J* = 4.8, 1.6, 0.8 Hz, 1H), 8.65 (dd, *J* = 1.9, 0.8 Hz, 1H), 8.46 (dt, *J* = 7.9, 1.0 Hz, 1H), 7.85 (ddd, *J* = 7.9, 7.5, 1.8 Hz, 1H), 7.64 (s, 4H), 7.51 (dd, *J* = 5.1, 1.9 Hz, 1H), 7.35 (ddd, *J* = 7.5, 4.8, 1.2 Hz, 1H). HRMS (ESI-TOF): m/z: $[M+H]^+$ Calcd. for $C_{16}H_{12}N_2Br$ 311.0184; Found 311.0186.

Bis(2,2'-bipyridine) mono(4-(4-bromophenyl)-2,2'-bipyridine)ruthenium(II) hexafluorophosphate, $[Ru(bpy)_2(bpy\text{-}Ph\text{-}Br)](PF_6)_2$. In a nitrogen-filled glovebox, $Ru(bpy)_2Cl_2$ (97 mg, 0.20 mmol) and AgOTf (0.11 g, 0.43 mmol) were dissolved in 18 mL of MeOH and stirred in the dark, at room temperature for 4 h. The dark red mixture was then filtered through a celite pad into a flask containing bpy-Ph-Br (75 mg, 0.24 mmol) dissolved in 2 mL of CH_2Cl_2. The resulting solution was refluxed under nitrogen overnight, during which time it turned red-orange; it was allowed to cool down and then it was filtered through a celite pad, which was rinsed with MeOH. The solvent was removed under reduced pressure and the residue was taken up in a minimum amount of water. Upon addition of KPF_6 (saturated aqueous solution), an orange solid was obtained. The solid was collected by vacuum filtration and washed with water and Et_2O. X-ray quality crystals were obtained by layering an aqueous solution of KPF_6 over a solution of the compound in CH_2Cl_2 and toluene. Yield: 0.11 g (52%). ^1H NMR (CD_3CN, 500 MHz) δ (ppm): 8.74 (dd, *J* = 2.0, 0.4 Hz, 1H), 8.69 (ddd, *J* = 8.3, 0.8, 0.4 Hz, 1H), 8.54 (m, 4H), 8.09 (m, 5H), 7.80 (m, 10H; this is the superposition of 3 signals) 7.64 (dd, *J* = 6.0, 2.0 Hz, 1H) 7.44 (m, 5H). HRMS (ESI-TOF): m/z: $[M–2PF_6]^{2+}$ Calcd. for $C_{36}H_{27}N_6BrRu$ 363.0262; Found 363.0280, $[M–PF_6]^+$ Calcd. for $C_{36}H_{27}N_6BrRuPF_6$ 871.0165; Found 871.0126.

4-(4-(trimethylsilyl)phenyl)-2,2'-bipyridine (bpy-Ph-TMS).[19] Under a nitrogen atmosphere, Br-Ph-bpy (0.15 g, 0.48 mmol) and TMS-Cl (0.5 mL, 3.94 mmol) were dissolved in 5 mL of THF. The solution was cooled down to –78°C (dry ice/acetone bath) and 1.6 M nBuLi (0.5 mL, 0.8 mmol) was added dropwise, while stirring. The reaction mixture turned dark red and was stirred for 35 minutes, after which time the cold bath was removed, and 2 mL of H_2O were added. Two layers formed, both of them yellow. The product was extracted into Et_2O until the organic layer tested negative with Fe(II). The ether extracts were combined, dried with $MgSO_4$ and evaporated to give an orange-brown oil. The product was purified with a neutral alumina column, eluting with hexanes/EtOAc 4:1. A colorless oil was obtained. Yield: 35 mg (24%). ^{1}H NMR ($CDCl_3$, 500 MHz) δ (ppm): 8.74 (dd, *J* = 5.1, 0.6 Hz, 1H), 8.72 (ddd, *J* = 4.8, 1.7, 0.9 Hz, 1H), 8.69 (dd, *J* = 1.2 Hz, 1H), 8.46 (d, *J* = 7.8 Hz, 1H), 7.85 (td, *J* = 7.6, 1.8 Hz, 1H), 7.77 (d, *J* = 8.1 Hz, 2H), 7.67 (d, *J* = 8.1 Hz, 2H), 7.56 (dd, *J* = 5.1, 1.8 Hz, 1H), 7.35 (ddd, *J* = 7.4, 4.8, 0.9 Hz, 1H). HRMS (ESI-TOF): m/z: $[M+H]^+$ Calcd. for $C_{19}H_{21}N_2Si$ 305.1474; Found 305.1485.

Bis(2,2'-bipyridine) mono(4-(4-(trimethylsilyl)phenyl)-2,2'-bipyridine) ruthenium(II) hexafluorophosphate, $[Ru(bpy)_2(bpy\text{-}Ph\text{-}TMS)](PF_6)_2$. In a nitrogen-filled glove box, $Ru(bpy)_2Cl_2$ (73 mg, 0.15 mmol) and AgOTf (82 mg, 0.32 mmol) were dissolved in MeOH (15 mL) and stirred in the dark, at room temperature, for 4 h. The mixture was filtered through a celite pad, and cannula transferred into a round-bottom flask containing bpy-Ph-TMS (50 mg, 0.16 mmol). The reaction was refluxed under nitrogen, in the dark, overnight. After allowing it to cool down, it was filtered thorugh a celite pad and evaporated to dryness. The residue was loaded onto a neutral alumina column using

MeCN as the eluent, and the main orange band was collected. The solvent was removed, the residue was redissolved in a minimum amount of H_2O/MeCN, and KPF_6 (aqueous saturated solution) was added, causing the product to precipitate. Crystals suitable for X-ray diffraction were obtained by layering an aqueous saturated solution of KPF_6 over a solution of the compound in dichloromethane/toluene. Yield: 63 mg (42%). ^{1}H NMR (CD_3CN, 500 MHz) δ (ppm): 8.77 (d, *J* = 1.8 Hz, 1H), 8.70 (d, *J* = 8.0 Hz, 1H), 8.54 (m, 4H), 8.10 (m, 5H), 7.87 (d, *J* = 8.2 Hz, 2H), 7.78 (m, 8H), 7.68 (dd, *J* = 6.0, 2.0 Hz, 1H), 7.44 (m, 5H), 0.34 (s, 9H). HRMS (ESI-TOF): m/z $[M–2PF_6]^{2+}$ Calcd. for $C_{39}H_{36}N_6RuSi$ 359.0912; Found 359.0918, $[M–PF_6]^+$ Calcd. for $C_{39}H_{36}N_6RuSiPF_6$ 863.1466; Found 863.1475.

Test reaction: synthesis of sodium phenyltris(1-pyrazolyl)borate.[20] Under a nitrogen atmosphere, phenylboronic acid (0.13 g, 1.03 mmol), pyrazole (0.33 g, 4.91 mmol) and NaH (40 mg, 1.67 mmol) were combined in a Schlenk tube, which was sealed and heated to 150°C for 24 h. The residue was analyzed by mass spectrometry. HRMS (ESI-TOF): m/z $[M–Na]^-$ Calcd. for $C_{15}H_{14}N_6B$ 289.1376; Found 289.1399; $[2M+Na]^-$ Calcd. for $C_{30}H_{28}N_{12}B_2Na$ 601.2654; Found 601.2682.

Test reaction: synthesis of sodium 4-[tris(1-pyrazolyl)borate]-2,2'-bipyridine.[20] Under a nitrogen atmosphere, $bpyB(OH)_2$ (0.20 g, 0.98 mmol), pyrazole (0.33 g, 4.80 mmol) and NaH (41 mg, 1.71 mmol) were combined in a Schlenk tube, which was sealed and heated to 120 °C for 24 h. After allowing it to cool down, the resulting solid was analyzed by mass spectrometry. HRMS (ESI-TOF): m/z $[M–Na]^-$ Calcd. for $C_{19}H_{16}N_8B$ 367.1595; Found 367.1608.

6.3. Results and Discussion

As has been previously discussed in this dissertation, the key component in the quest for a D-A intramolecular assembly is a bifunctional ligand that incorporates coordination sites compatible with both the acceptor and donor units. In the preceding chapters, these ligands have been 2,2'-bipyridines with a carboxylate group, which have been relatively straightforward to prepare. These modified bypiridines have achieved different degrees of success, but the main drawback of this approach is that using the carboxylate bridges in this way limits our ability to vary the redox potential of the diferric core.[2] In this chapter, a different way to attach the donor and the acceptor is explored, using an modified scorpionate ligand,[21,22] as shown in Figure 6.1. The desired ligand has three components: a tris(1-pyrazolyl)borate to cap the diferric core, a 2,2'-bipyridine to bind to the Ru(II) donor, and a phenyl linker to connect the two. In addition, to increase the electronic coupling, it is desirable to have the phenyl linker bound to the 4-position of one of the pyridine rings.[23,24] As long as those conditions are met, the final design of the target ligand might be tweaked as necessary (mostly for ease of synthesis).

6.3.1 Attempts Employing a Sonogashira Coupling

In the past, attempts to prepare *ext*-Tp using a Stille coupling were unsuccessful;[5] a Suzuki coupling, which uses conditions similar to the Stille route,[6] did not appear to be a viable option. However, Reger et al.[7] have reported the synthesis of compounds of the form $[Fe(Tp')_2]^+$ where the scorpionate ligand was further modified using a Sonogashira coupling. An example of these reactions is shown in Figure 6.3; the authors were not able

to achieve complete conversion of the starting material, finding evidence of products where one or both of the iodobenzene groups had reacted. This was not seen as an obstacle, because in our case, only one alkyne group was necessary. Additionally, there being evidence of these reactions working was encouraging enough to attempt this route on our system.

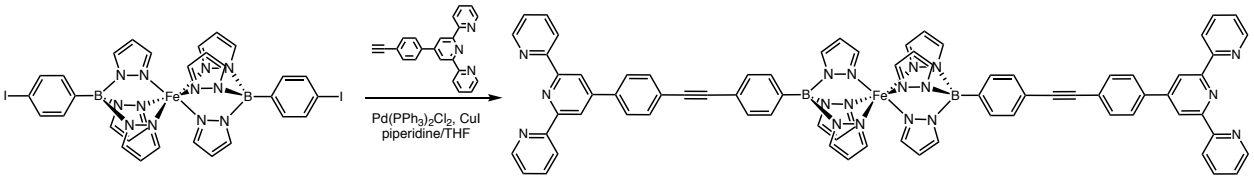


Figure 6.3. Use of a Sonogashira coupling to modify scorpionate ligands post-coordination. Adapted from Ref. 7.

Initial efforts were focused on coupling I-Ph-TpK and ebpy; both compounds had been previously reported,[5,14,15] and their syntheses presented no particular difficulty. It is worth mentioning that I-Ph-BBr_2 can be purified by sublimation,[25] which removes most side products that the vacuum distillation leaves behind. However, I-Ph-BBr_2 is fairly air and water sensitive, so it must be handled under an inert atmosphere at all times, which made the sublimation step burdensome to say the least. Additionally, despite extreme care being taken to prevent this, bromine-containing byproducts made it past the liquid nitrogen trap in the Schlenk line and contaminated the vacuum pump oil. It was thus decided that the benefits of the extra purification step did not compensate for the necessary efforts, since the end product (I-Ph-TpK) could be obtained pure regardless of the purity of the starting material.

The next reaction, the Sonogashira coupling, worked moderately well, as the ebpy-Tp ligand was observed on ESI-MS. There were instances where both starting materials

were recovered along with the product; unfortunately, the solubilities of these three compounds were very similar, and no recrystallization or column conditions were found to isolate the product. Interestingly, even after refluxing for 36-48 hours, I-Ph-TpK was intact; while this was obviously disappointing because the reaction had not worked as expected, it was encouraging to see that this molecule could withstand the reaction conditions, unlike what had happened with the Stille coupling attempts.

Seeing that the desired product was obtained, but there were many challenges regarding its isolation, a less elegant solution was attempted: the coupling reaction was carried out using ebpy as the limiting reagent until it was no longer seen on TLC, and, after minimal workup, the crude product was reacted with $[Ru(bpy)_2(MeOH)_2]^{2+}$ in the same fashion as described in Chapter 3. If the only bipyridine moiety present in the mixture was part of ebpy-Tp, then its coordination was expected to be favored over other species. Additionally, it was assumed that separating I-Ph-TpK and the Ru(II) product would be straightforward, in part due to their opposite charges. However, when the solid obtained in this last reaction was analyzed using TLC, more than one orange spot was observed, suggesting that many Ru(II)-containing products had formed. Column chromatography on neutral alumina led to several orange fractions, which when analyzed using ESI-MS revealed several peaks with the isotope pattern characteristic of Ru(II) polypyridyls. None of those peaks matched $[Ru(bpy)_2(ebpy)]^{2+}$ or $[Ru(bpy)_3]^{2+}$, or other reasonable side products. The desired product was observed on ESI-MS, but multiple attempts to isolate it using column chromatography (with silica gel, neutral alumina, or reversed-phase silica gel) or recrystallization techniques were unsuccessful.

It should be noted that the intensity of the $[M–PF_6]^+$ peak on ESI-MS for the product was much lower than that for many of the other Ru(II)-containing peaks detected. While the intensity of a peak does not necessarily reflect its concentration (other factors, like the ionization efficiency of the compounds or matrix-induced ion suppression, also play a role),[26] for a sample containing two or more closely related compounds one may use the intensity of a signal as an indicator of relative abundance in the mixture.[27,28] With that, it seems that $[Ru(bpy)_2(ebpy\text{-}Tp)]^+$ was only formed in very small quantities in this reaction.

Another factor to consider is the ability of polypyrazolylborates to coordinate to ruthenium.[21] As was mentioned above, the synthetic route employing $[Ru(bpy)_2(MeOH)_2]^{2+}$ was expected to favor the coordination of the bipyridine moiety in ebpy-Tp over the Tp unit; this was mostly due to the latter being tridentate and there only being two coordination positions easily accessible in the bis-solvento species. Nevertheless, several products containing Ru(II) seemed to have formed, suggesting that the formation of Tp-Ru complexes should not be underestimated.

These results indicated that both ebpy-Tp and $[Ru(bpy)_2(ebpy\text{-}Tp)]^+$ can be made, but the attempted routes were neither clean nor high-yielding. A new strategy was then pursued, the coupling of $[Ru(bpy)_2(ebpy)]^{2+}$ and I-Ph-TpK. In this way, there would be no species competing to coordinate to the metal center. A handful of Sonogashira couplings on Ru(II) polypyridyl compounds have been reported;[17,29,30] this, combined with Reger's work[7] and the previously described results was encouraging enough to explore this avenue. The main drawback of this approach is that these reactions must be

performed in a smaller scale, due to the cost of making ruthenium compounds. As a consequence, most of the reactions were carried out using 100 μmol or less of the starting material, which in many cases made any isolation attempts very cumbersome. The first route explored was analogous to Reger's method;[7] $[Ru(bpy)_2(ebpy)](PF_6)_2$ is not completely soluble in THF, so MeCN was added to improve solubility. The additional solvent was not expected to interfere with the reaction, because the Sonogashira coupling is compatible with a wide variety of solvents, including water.[31,32] With this procedure, some red-orange fractions were obtained from a neutral alumina column, which was taken as a good sign. Unfortunately, despite observing many peaks with a Ru(II)-polypyridyl isotope pattern in ESI-MS, none of them were easily identifiable. Moreover, the starting material was not recovered.

A second route was attempted, based on what Fraysse et al. have reported.[17] The main differences with the previous method are the palladium catalyst used ($Pd(PPh_3)_4$ instead of $Pd(PPh_3)_2Cl_2$), and the solvent (DMF instead of THF). The amines used also differ, with the first method using piperidine (pK_a = 11.22) and the second, diisopropylamine (pK_a = 11.05)[33] however, this was not expected to have a large impact because the latter is used in the synthesis of ebpy with good results. The use of DMF as the solvent seemed to be an advantage, given the aforementioned limited solubility of $[Ru(bpy)_2(ebpy)](PF_6)_2$ in THF. The ESI-MS analysis of column fractions for this reaction showed a very small peak for the intended product in the main fraction, and another peak consistent with $[M–(pz^-)]^{2+}$ in many of the fractions. A large number of other Ru(II) polypyridyl peaks were observed; no starting material was recovered. Several ways to

crystallize the product were attempted, but only oils were obtained. Similarly to what happened when synthesizing ebpy-Tp and coordinating it to Ru(II), the target compound was obtained in very low yield, and the reaction was not clean. While this is still a potential avenue, other options were explored, in hopes of finding a more suitable synthetic route.

6.3.2 Building a Scorpionate Ligand from a Bipyridine

At this point, considering that Pd-catalyzed couplings had not worked, it seemed clear that a whole new approach was necessary to make *ext*-Tp. The synthesis of X-Ph-TpK (with X being Br or I) is outlined in Figure 6.4: the plan was to have a 2,2'-bipyridine instead of the second halogen atom and build the trispyrazolylborate portion of *ext*-Tp off of the phenyl ring. The first obstacle here was the possibility of a reaction between BBr_3 and the nitrogen rings on bipyridine, examples of which have been reported.[34] To circumvent this, Br-Ph-bpy would be coordinated to Ru(II) before proceeding.

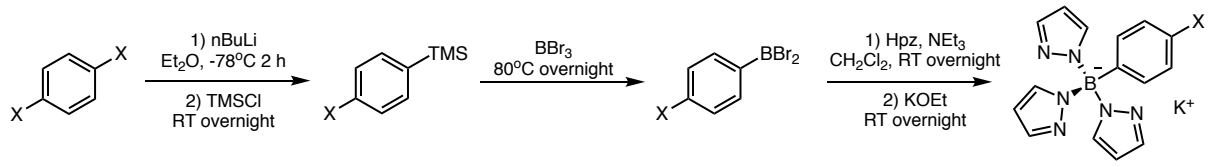


Figure 6.4. Synthetic route to prepare X-Ph-TpK.

The first step, then, was to prepare Br-Ph-bpy. Following previously published methods,[9,18] this ligand was obtained in good yield from cheap commercially available starting materials (2-acetylpyridine and 4-bromobenzaldehyde) in three steps. Coodinating bpy-Ph-Br to Ru(II) to make $[Ru(bpy)_2(bpy\text{-}Ph\text{-}Br)](PF_6)_2$ presented no

difficulty (the ORTEP drawing of its crystal structure is shown in Figure 6.5). Sadly, several attempts to make $[Ru(bpy)_2(bpy\text{-}Ph\text{-}TMS)]^{2+}$ by adapting the reaction shown on the first step of Figure 6.4 were usuccessful; in many cases, the starting material was recovered. While this was not the expected result, it is important to notice that $[Ru(bpy)_2(bpy\text{-}Ph\text{-}Br)]^{2+}$ was not affected by nBuLi: this opens the door to synthetically modifying the ligands post-coordination for other Ru(II) polypyridyl compounds.

It was unclear why the synthesis of $[Ru(bpy)_2(bpy\text{-}Ph\text{-}TMS)]^{2+}$ had not worked: the reason could be related to having bpy-Ph-Br coordinated to Ru(II), or it could be directly related to the reactivity the ligand itself. To figure this out, the synthesis of uncoordinated bpy-Ph-TMS was then attempted. Just as before, the first attempt used the same procedure to make I-Ph-TMS; the product was detected using ESI-MS, but the yield was too low to be calculated. No starting material was recovered, which suggested that the reaction of bpy-Ph-Br with nBuLi was taking place, but the second step was not working as expected.

A solution to this problem was suggested by the work of Li et al.;[19] they focused on an alternative method to prepare some pyridylboronic acids from the corresponding bromides. Their technique, which they dubbed "in situ quench", consists in not letting the aryl bromide react only with nBuLi, because the resulting lithiated species is too unstable and will undergo undesired side reactions. This method has been satisfactorily employed to prepare 2,2′-bipyridine-4-boronic acid,[11] and appeared to be a plausible route, albeit counter-intuitive. To adapt this method to the synthesis of bpy-Ph-TMS, bpy-Ph-Br and TMSCl were combined and brought to –78°C before nBuLi was added. The

reaction time was much shorter than what was previously attempted (35 min vs. overnight) as well. With this approach, clean bpy-Ph-TMS was obtained in 24% yield, and the reaction was reproducible. This result suggests that, indeed, the lithiated Ph-bpy is quite unstable, which could explain why previous attempts had failed.

The synthesis of $[Ru(bpy)_2(bpy\text{-}Ph\text{-}TMS)](PF_6)_2$ was then successfully pursued, utilizing the same strategies outlined in Chapter 3 for the preparation of heteroleptic Ru(II) polypyridyls. The product was obtained in 42% yield; this could be improved on, but this reaction has not yet been optimized. A drawing of $[Ru(bpy)_2(bpy\text{-}Ph\text{-}TMS)]^{2+}$ is shown in Figure 6.5, and the corresponding crystallographic data are compiled in Table 6.1. There are two formula units, one molecule of toluene and one of CH_2Cl_2 per unit cell, which is reflected in the empirical formula. The Flack parameter is used to determine the chirality of the crystal: a value of 0.5 indicates that the crystal consists of a racemic mixture of the two enantiomers, as is the case for this compound.

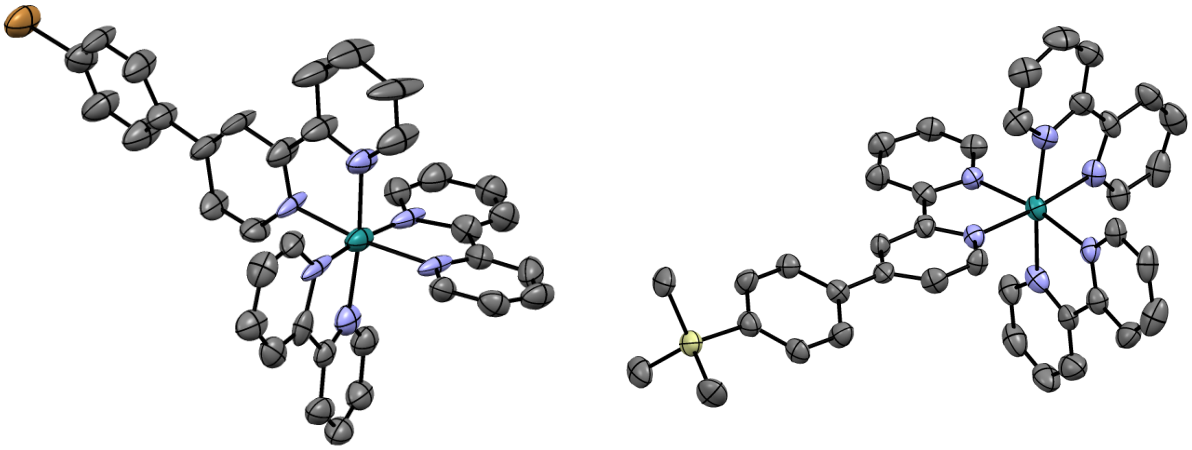


Figure 6.5. ORTEP drawing of $[Ru(bpy)_2(bpy\text{-}Ph\text{-}Br)]^{2+}$ (left) and $[Ru(bpy)_2(bpy\text{-}Ph\text{-}TMS)]^{2+}$ (right) obtained from single-crystal X-ray structure determinations. Atoms are represented as 50% probability thermal ellipsoids. Hydrogen atoms and anions are omitted for clarity. The complete lists of bond lengths and angles are compiled in the appendix to this chapter.

Table 6.1. Crystallographic data for $[Ru(bpy)_2(bpy\text{-}Ph\text{-}TMS)](PF_6)_2$ and $[Ru(bpy)_2(bpy\text{-}Ph\text{-}Br)](PF_6)_2$.

	$[Ru(bpy)_2(bpy\text{-}Ph\text{-}Br](PF_6)_2$	**$[Ru(bpy)_2(bpy\text{-}Ph\text{-}TMS](PF_6)_2$**
empirical formula	$C_{36}H_{27}BrF_{12}N_6P_2Ru$	$C_{43}H_{41}ClF_{12}N_6P_2RuSi$
formula weight	1014.55	1096.37
temperature (K)	173(2)	173(2)
crystal color, habit	red, chunks	red, needles
crystal system	monoclinic	monoclinic
space group	*C2/c*	*Cc*
Flack Parameter	N/A	0.49(4)
cell dimensions:		
a (Å)	22.934(6)	29.403(2)
b (Å)	30.166(11)	11.7770(10)
c (Å)	15.973(4)	27.761(2)
Volume (Å^3)	9043(5)	9119.2(13)
Z	8	8
D_{calc} (g cm^{-3})	1.490	1.597
goodness of fit (F^2)	0.951	0.932
R_1 (I >2(I))	0.0941	0.0596

The next step in the synthesis is the reaction of $[Ru(bpy)_2(bpy\text{-}Ph\text{-}TMS)]^{2+}$ with BBr_3 and then pyrazole to obtain $[Ru(bpy)_2(bpy\text{-}Ph\text{-}Tp)]^+$. Work on these steps is underway. This route has showed more promise than the one with an alkyne linker, but there are still some challenges to overcome. In the first place, it would be desirable to improve the yield on the synthesis of bpy-Ph-TMS. One possibility would be to adapt the route described by Cordaro et al.,[18] starting with 4-(trimethylsilyl)benzaldehyde instead.

6.3.3 Use of Boronic Acids to Prepare Scorpionates

Another route that has been investigated uses boronic acids to make trispyrazolyl borates. Desrochers et al.[20] reported the synthesis of sodium phenyltris(1-pyrazolyl)borate from phenylboronic acid, pyrazole and sodium hydride in a microwave reactor. A sealed Schlenk tube was tested as a replacement for the microwave reactor; the

reaction time was increased to make up for the different conditions.[36] The product was easily detected using ESI-MS, meaning that the reaction did work despite not using a microwave reactor (although the yield in our case was likely lower). Encouraged by this result, the next concern was whether having a bipyridine in this reaction would present a problem (the main issue being the possibility of forming thermodynamically favorable B-N bonds).[34,37] To test this compatibility, a new reaction was performed, using 2,2'-bipyridine-4-boronic acid instead of phenylboronic acid. Under the same conditions as before, the desired product was observed by ESI-MS. No attempt to isolate this compound has been made, but it should be possible to triturate the solid with hexanes to remove the excess of pyrazole.

These results suggest that the reaction of (4-([2,2'-bipyridin]-4-yl)phenyl)boronic acid with pyrazole and sodium hydride should allow us to obtain *ext*-Tp. This boronic acid has been prepared before, albeit in low yield (20%).[38] Based on the above discussion, the "in situ quench" method[19] appears to be a reasonable alternative to attempt to prepare this compound. Efforts along these lines are currently underway.

It is worth pointing out that in this route, the possibility of *ext*-Tp coordinating to Ru(II) via the pyrazolylborate moiety cannot be overlooked. While it is still expected that the coordination *via* the bipyridine side will be favored, the formation of side products may still pose a major challenge. On the other hand, if it were possible to prepare and isolate *ext*-Tp prior to its reaction with Ru(II), even if byproducts are obtained, the odds of purifying the desired compound seem to improve. Let us not forget that in the case of

the alkyne-bridged ebpy-Tp, neither its synthesis nor the coordination step were clean reactions, which only made matters worse.

Another possibility for this route would be to prepare $[Ru(bpy)_2(bpy\text{-}Ph\text{-}B(OH)_2)](PF_6)_2$ and then react that with pyrazole and NaH; this approach should prevent the coordination of Ru to anything other than the bipyridines. A valid concern, in this case, would be the stability of Ru(II) polypyridyl compounds in a microwave reactor. The feasibility of preparing Ru(II) compounds using microwave techniques has been documented extensively;[39–42] not only homoleptic compounds may be obtained with these routes, reactions of $Ru(bpy)_2Cl_2$ with another bipyridine to give heteroleptic compounds have been reported with high yield as well. This indicates that, while changes to the coordination sphere may take place, under the proper conditions it should be possible to carry out reactions on the bipyridine backbone without affecting other parts of the molecule.

6.4. Concluding Remarks

This chapter described the different routes explored in the pursuit of a bifunctional scorpionate ligand that incorporates a bipyridine unit. Although the target has not been obtained yet, significant progress has been made towards this goal. Of all the routes presented here, the ones involving the modification of bpy-Ph-Br are the most promising ones.

The synthetic routes outlined here are not without obstacles; for the synthesis of the ligand, the main problem is the possibility of side reactions involving the boron

precursors, especially between BBr_3 and bipyridine. Coordination to Ru(II) in the early stages of synthesis should prevent this, but this might limit the scale of these reactions and affect the reactivity of the relevant species. Other prospects use boronic acids or Grignard reagents; however, it may be that preparing the bifunctional ligand prior to coordination to Ru(II) will lead to more side products due to the coordination of the Tp group instead of the bpy. Alternatively, using these routes to build the scorpionate starting from a {Ru(bpy-Ph-X)} fragment might resolve these issues, but yield other side products. While many synthetic routes for scorpionate ligands are available in the literature, there is little precedent for these in the context of Ru(II) polypyridyls. In the end, the only way to select the best strategy for the compounds of interest will be based on trial and error. Luckily, there is enough flexibility in the design of the bifunctional ligand that the choice of a synthetic route may be guided by practicality, and small adjustments to the structure of the ligand may be made to simplify its synthesis.

The development of this chemistry will be key to the progress of this project; hopefully, the experimental results and proposed synthetic routes presented here will simplify the next steps

APPENDIX

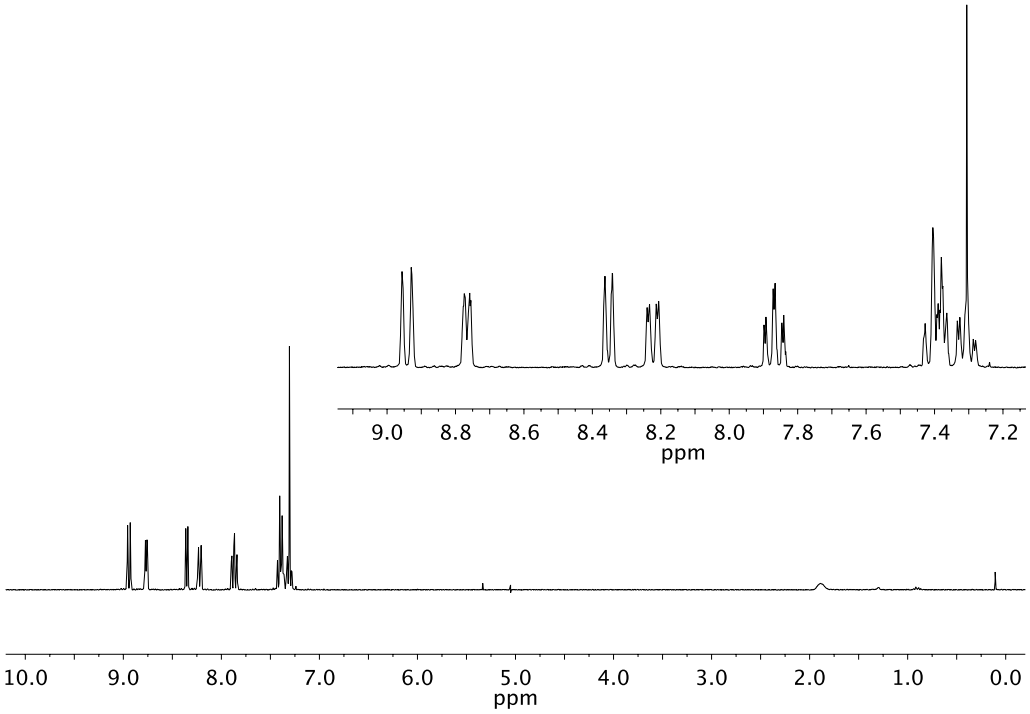


Figure 6.6. ^{1}H NMR of 2,2'-bipyridine-N-oxide in $CDCl_3$.

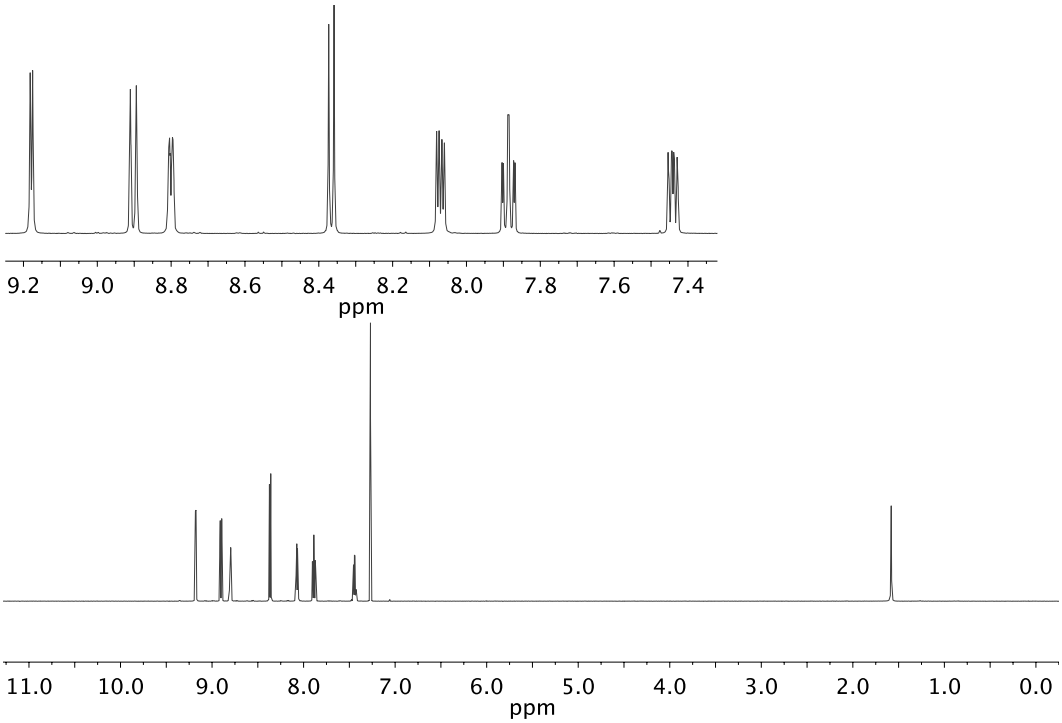


Figure 6.7. ^{1}H NMR of 4-nitro-2,2'-bipyridine-N-oxide in $CDCl_3$.

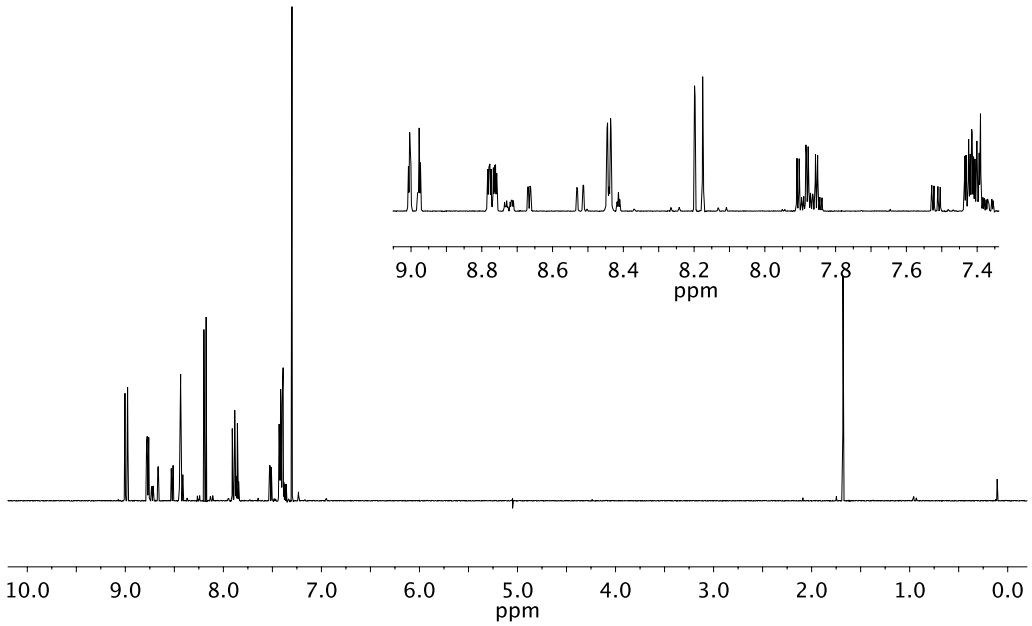


Figure 6.8. ^{1}H NMR of 4-bromo-2,2'-bipyridine-N-oxide in $CDCl_3$. The small peaks correspond to 4-bromo-2,2'-bipyridine, which is obtained as a side product.

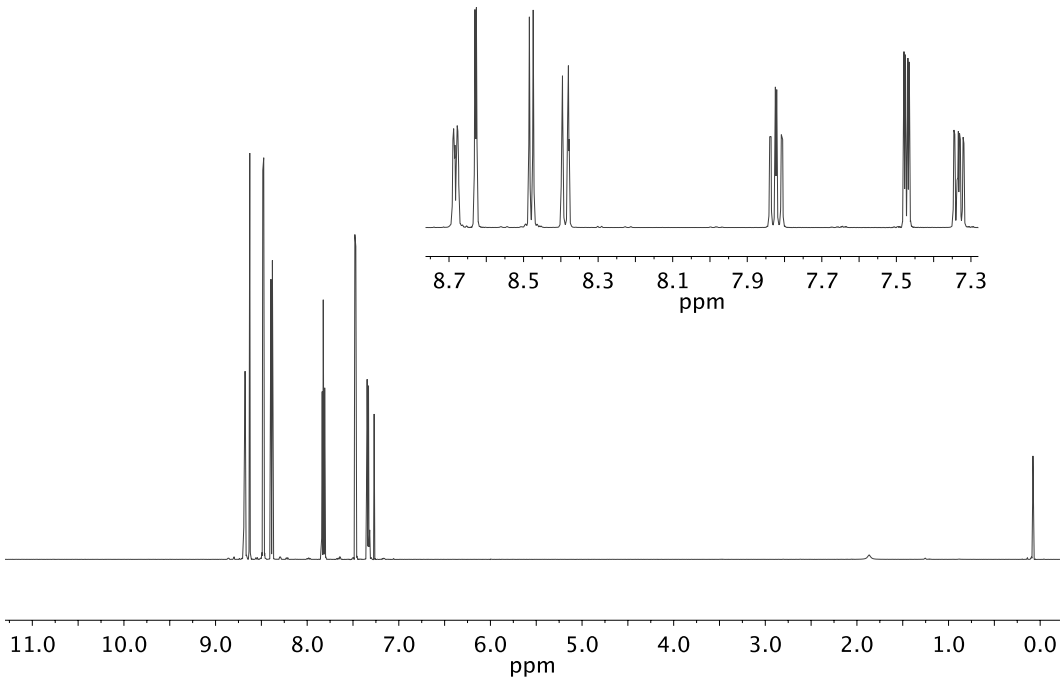


Figure 6.9. ^{1}H NMR of 4-bromo-2,2'-bipyridine in $CDCl_3$.

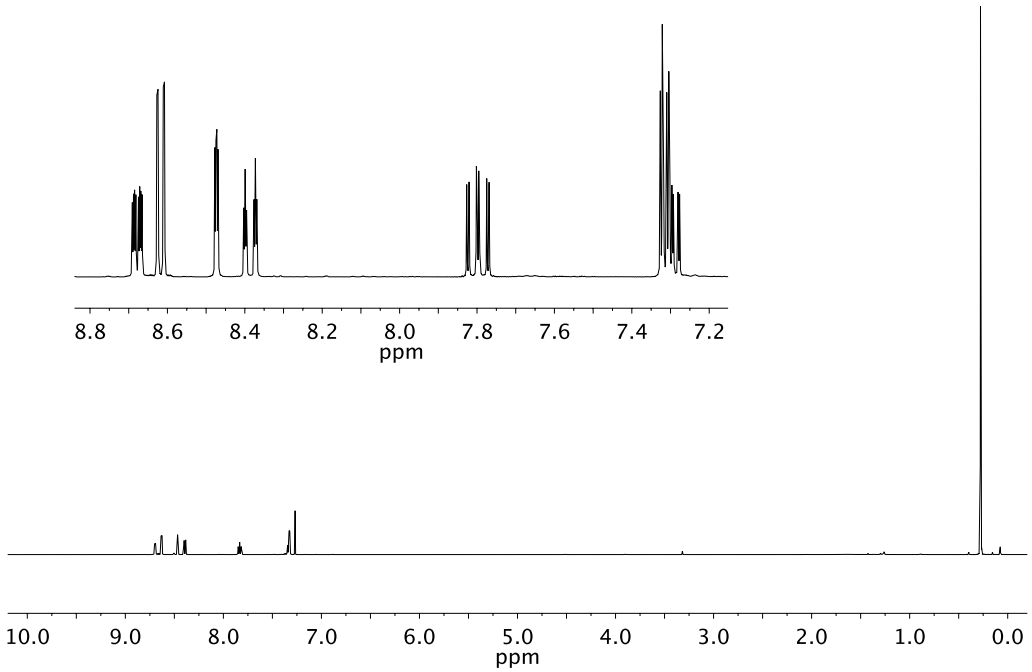


Figure 6.10. ^{1}H NMR of 4-((trimethylsilyl)ethynyl)-2,2'-bipyridine in $CDCl_3$.

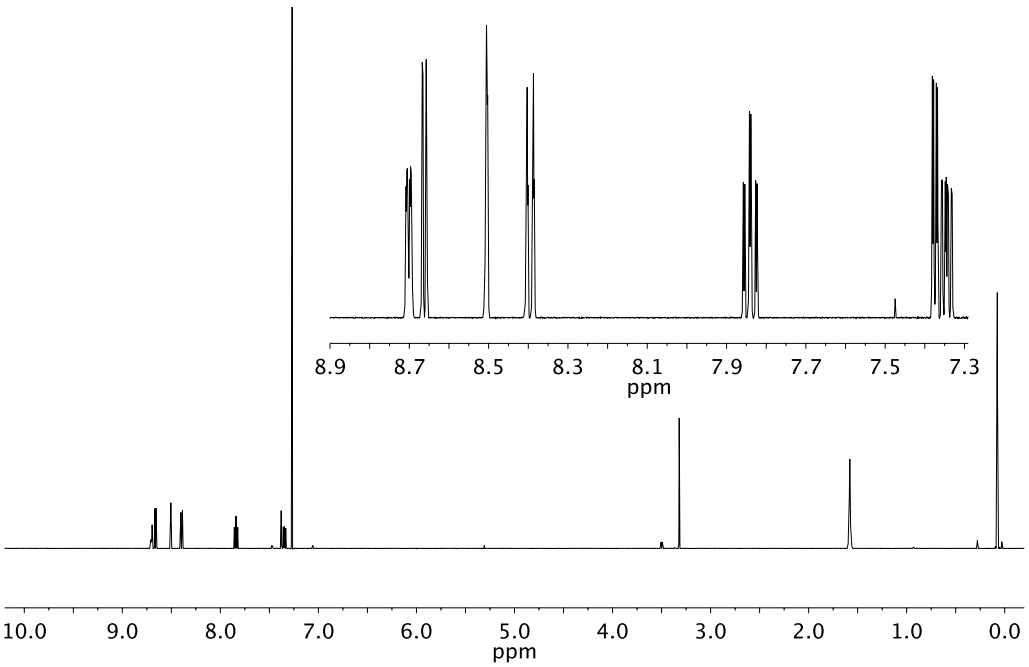


Figure 6.11. ^{1}H NMR of 4-ethynyl-2,2'-bipyridine in $CDCl_3$.

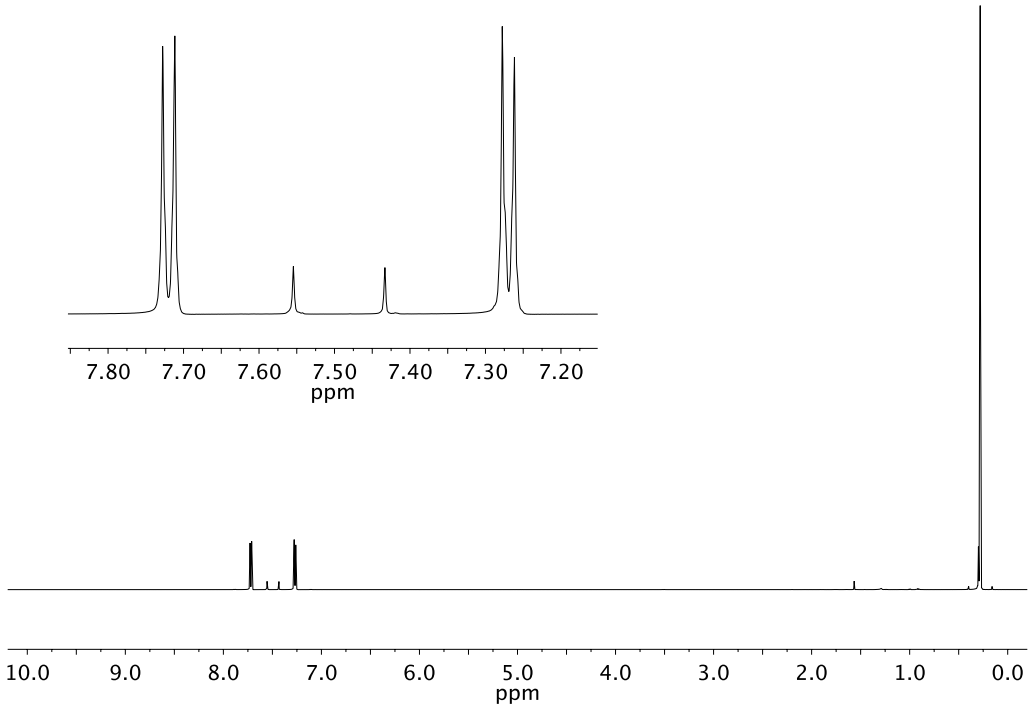


Figure 6.12. ^{1}H NMR of p-(trimethylsilyl)iodobenzene in $CDCl_3$. The small peaks at 7.42 ppm and 7.53 ppm correspond to p-diiodobenzene and p-bis(trimethylsilyl)benzene, respectively.

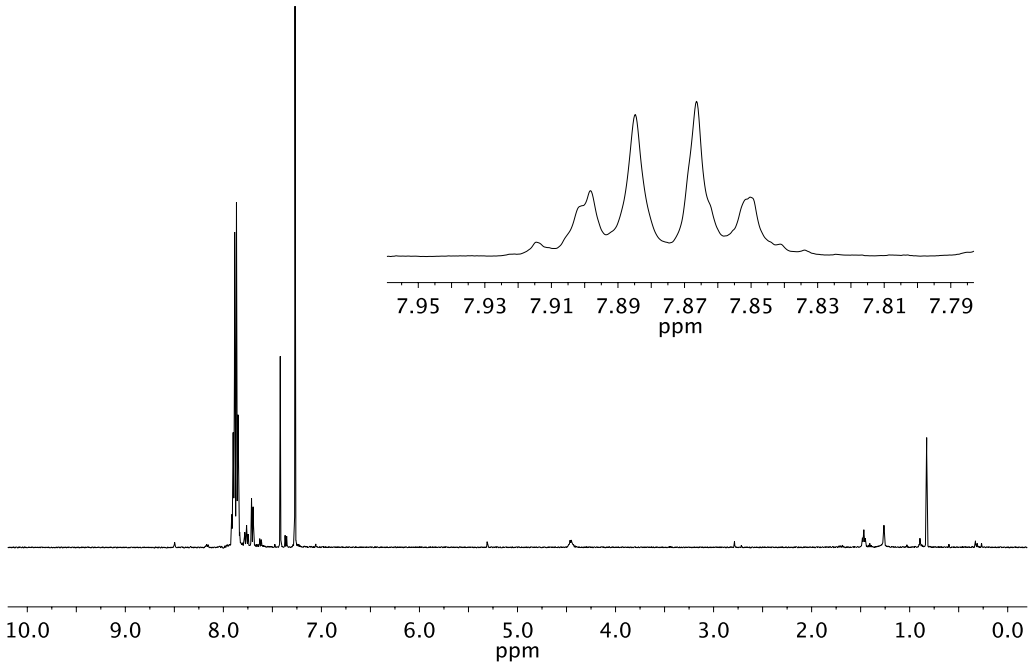


Figure 6.13. ^{1}H NMR of (4-iodophenyl)dibromoborane in $CDCl_3$.

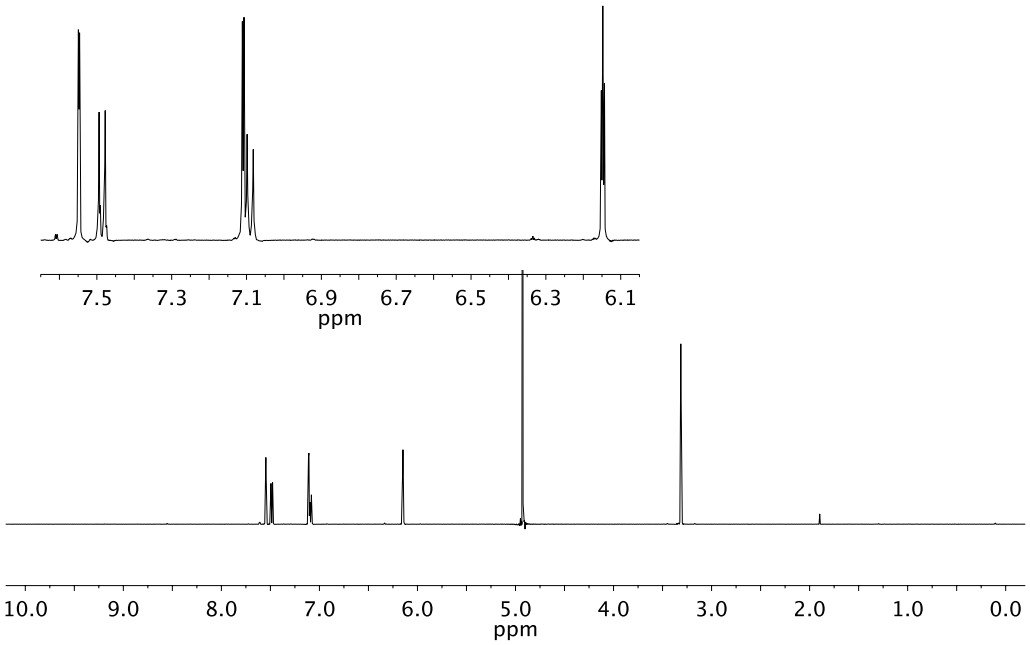


Figure 6.14. ^{1}H NMR of potassium (4-iodophenyl)tris(1-pyrazolyl)borate in CD_3OD.

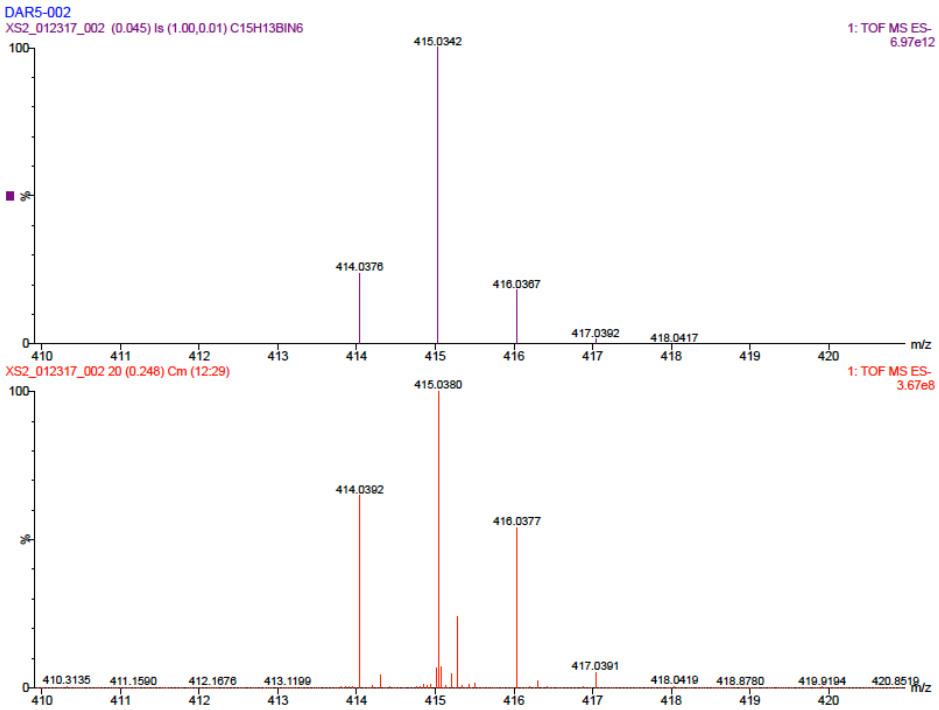


Figure 6.15. HRMS (ESI-TOF) of (4-iodophenyl)tris(1-pyrazolyl)borate. Top: predicted pattern for $[M–K]^-$ ($C_{15}H_{13}N_6BI$). Bottom: experimental result.

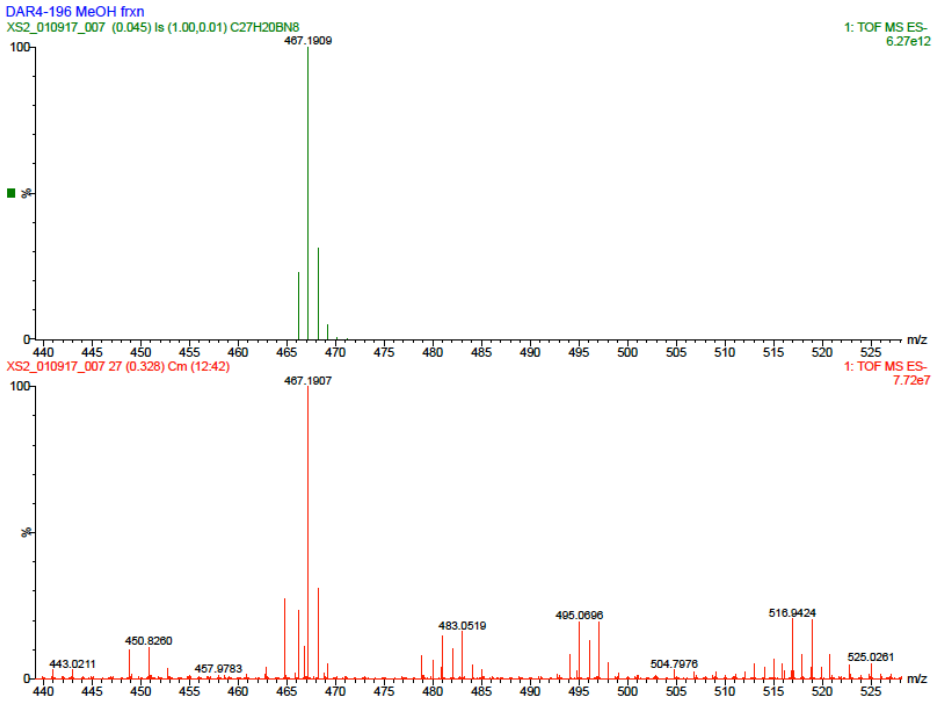


Figure 6.16. HRMS (ESI-TOF) of potassium (4-([2,2'-bipyridin]-4-ylethynyl)phenyl)tris(1-pyrazolyl)borate. Top: predicted isotope pattern for $[M–K]^-$ ($C_{27}H_{20}N_8B$). Bottom: experimental result.

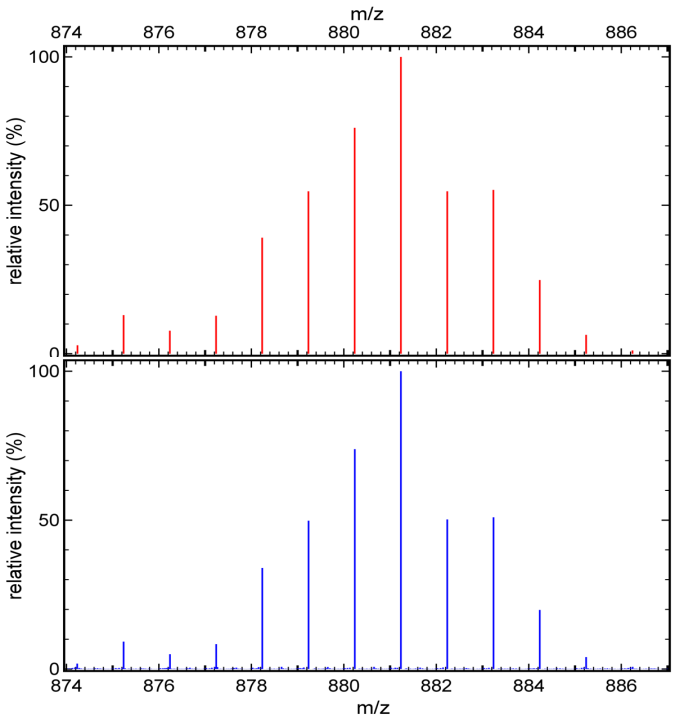


Figure 6.17. ESI-MS of $[Ru(bpy)_2(ebpy\text{-}Tp)](PF_6)$. Top: predicted isotope pattern for $[M–PF_6]^+$ ($C_{47}H_{36}N_{12}BRu$). Bottom: experimental result.

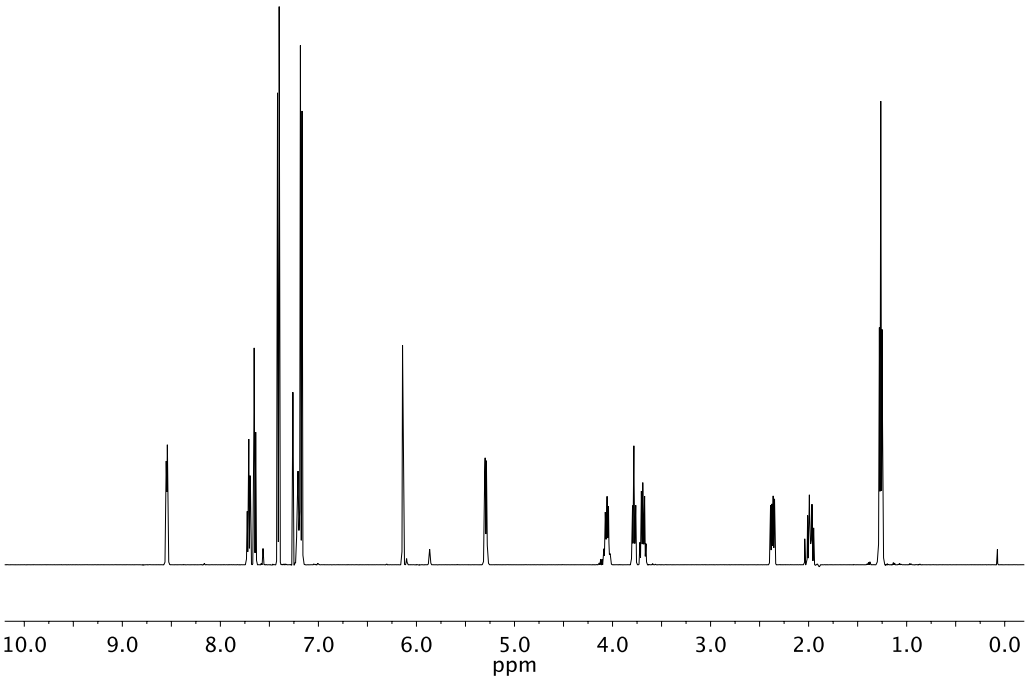


Figure 6.18. ^{1}H NMR of 2-[4-(4-bromophenyl)-2-ethoxy-3,4-dihydro-2H-pyran-6-yl]pyridine in $CDCl_3$.

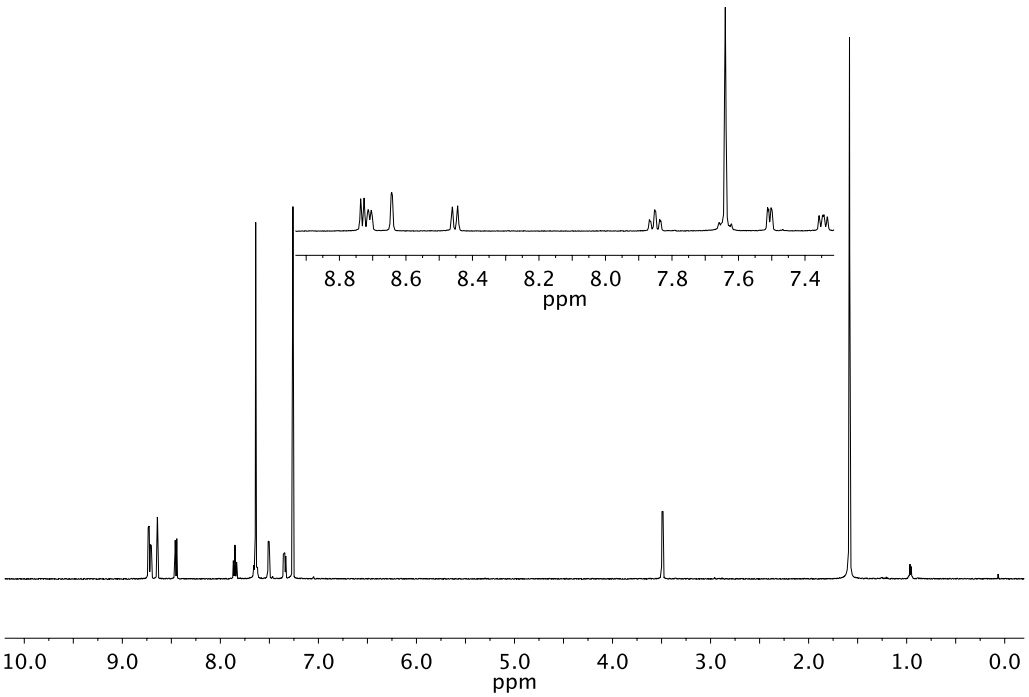


Figure 6.19. ^{1}H NMR of 4-(4-bromophenyl)-2,2'-bipyridine in $CDCl_3$. The peaks at 3.5 ppm (d, J = 5.2 Hz, 3H) and 0.9 ppm (q, J = 5.2 Hz, 1H) correspond to MeOH, used to recrystallize the compound.

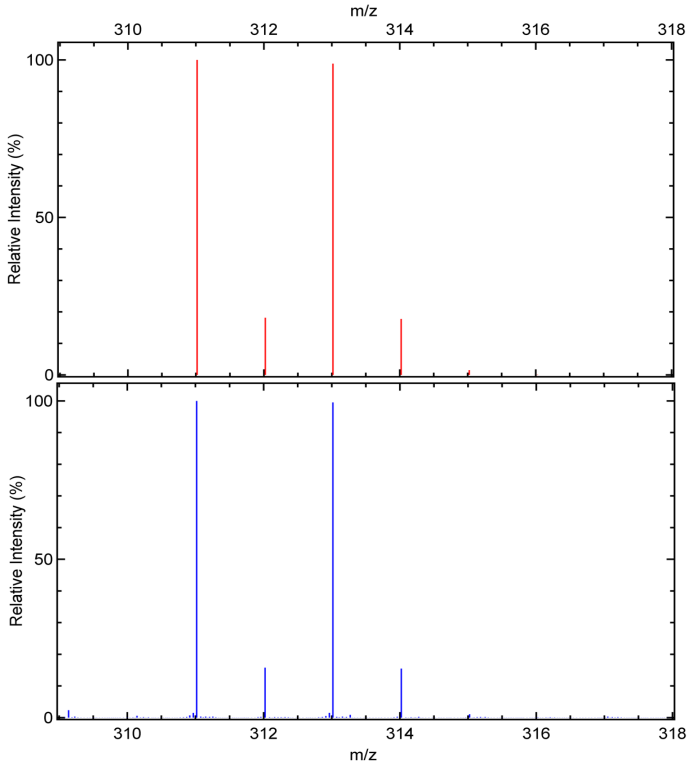


Figure 6.20. ESI-MS of 4-(4-bromophenyl)-2,2'-bipyridine. Top: predicted isotope pattern for $[M+H]^+$ ($C_{16}H_{12}N_2Br$). Bottom: experimental result.

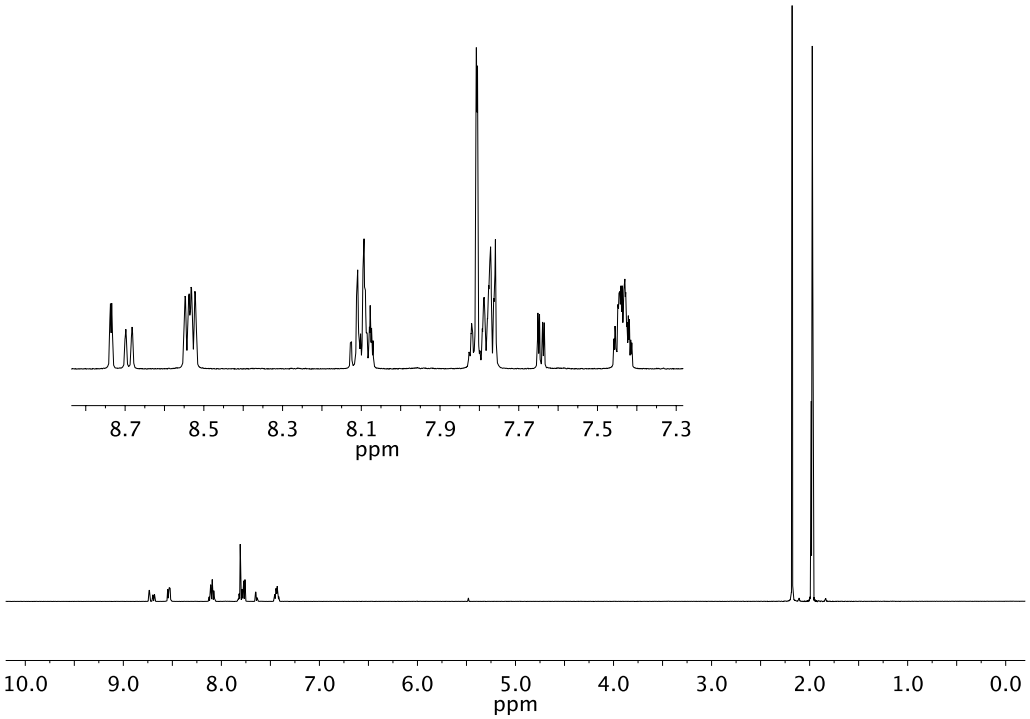


Figure 6.21. ^1H NMR of $[Ru(bpy)_2(bpy\text{-}Ph\text{-}Br)](PF_6)_2$ in CD_3CN.

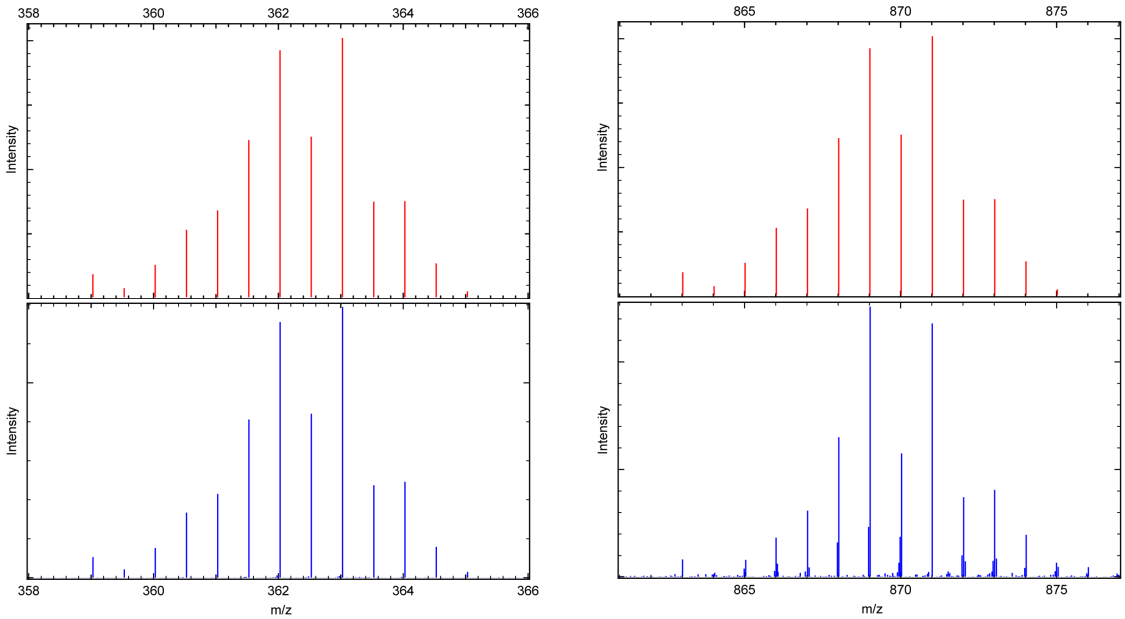


Figure 6.22. ESI-MS of $[Ru(bpy)_2(bpy\text{-}Ph\text{-}Br)](PF_6)_2$. Top left: predicted isotope pattern for $[M–2PF_6]^{2+}$ ($C_{36}H_{27}N_6BrRu$). Bottom left: experimental result. Top right: predicted isotope pattern for $[M–PF_6]^{+}$ ($C_{36}H_{27}N_6BrRuPF_6$). Bottom right: experimental result.

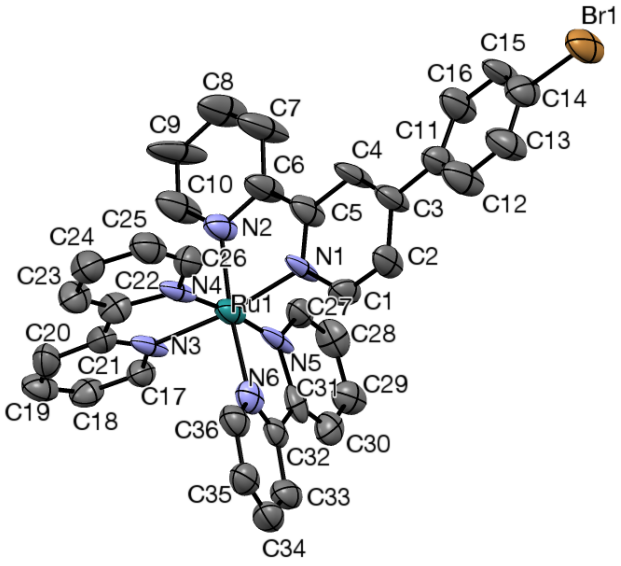


Figure 6.23. ORTEP drawing of $[Ru(bpy)_2(bpy\text{-}Ph\text{-}Br)]^{2+}$ showing the labelling system. Atoms are represented as 50% probability thermal ellipsoids. Anions and solvent molecules omitted.

Table 6.2. Bond lengths for the X-ray structure of $[Ru(bpy)_2(bpy\text{-}Ph\text{-}Br)](PF_6)_2$.

Atoms	Length/Å	Atoms	Length/Å	Atoms	Length/Å
Ru1 N1	2.028(6)	C5 C6	1.472(12)	C31 C32	1.486(12)
Ru1 N2	2.036(7)	C6 C7	1.424(13)	C32 C33	1.422(12)
Ru N3	2.081(7)	C7 C8	1.360(14)	C33 C34	1.359(14)
Ru1 N4	1.903(10)	C8 C9	1.410(15)	C34 C35	1.348(13)
Ru1 N5	1.872(10)	C9 C10	1.334(14)	C35 C36	1.353(13)
Ru1 N6	2.066(8)	C11 C12	1.386(13)	P1 F1	1.570(10)
Br1 C14	1.928(10)	C11 C16	1.411(13)	P1 F2	1.585(8)
N1 C1	1.386(10)	C12 C13	1.377(13)	P1 F3	1.560(8)
N1 C5	1.305(11)	C13 C14	1.351(14)	P1 F4	1.561(8)
N2 C6	1.352(11)	C14 C15	1.304(14)	P1 F5	1.591(7)
N2 C10	1.324(11)	C15 C16	1.365(13)	P1 F6	1.572(8)
N3 C17	1.332(12)	C17 C18	1.365(12)	P2 F7	1.595(11)
N3 C21	1.359(12)	C18 C19	1.342(14)	P2 F8	1.549(8)
N4 C22	1.440(12)	C19 C20	1.380(14)	P2 F8[1]	1.549(8)
N4 C26	1.402(13)	C20 C21	1.368(13)	P2 F9	1.592(11)
N5 C27	1.437(12)	C21 C22	1.478(13)	P2 F10	1.587(7)
N5 C31	1.486(12)	C22 C23	1.293(13)	P2 F10[1]	1.587(7)
N6 C32	1.327(11)	C23 C24	1.379(14)	P3 F11[2]	1.471(9)
N6 C36	1.327(12)	C24 C25	1.416(14)	P3 F11	1.471(9)
C1 C2	1.311(12)	C25 C26	1.400(15)	P3 F12[2]	1.555(7)
C2 C3	1.430(12)	C27 C28	1.358(13)	P3 F12	1.555(7)
C3 C4	1.352(12)	C28 C29	1.369(14)	P3 F13	1.605(14)
C3 C11	1.487(12)	C29 C30	1.361(13)	P3 F14	1.558(15)
C4 C5	1.406(11)	C30 C31	1.339(13)	F13 F11[2]	1.67(2)

[1]2-x, +y, 3/2-z; [2]1-x, +y, 3/2-z

Table 6.3. Bond angles for the X-ray structure of $[Ru(bpy)_2(bpy\text{-}Ph\text{-}Br)](PF_6)_2$.

Atoms	Angle/º	Atoms	Angle/º	Atoms	Angle/º
N1 Ru1 N2	78.3(3)	C7 C6 C5	124.4(9)	F1 P1 F5	90.2(5)
N1 Ru1 N3	171.5(4)	C8 C7 C6	120.9(10)	F2 P1 F5	90.5(4)
N1 Ru1 N6	98.5(3)	C7 C8 C9	115.5(11)	F3 P1 F1	178.9(6)
N2 Ru1 N3	96.8(3)	C10 C9 C8	119.6(10)	F3 P1 F2	91.3(5)
N2 Ru1 N6	173.3(4)	N2 C10 C9	126.4(10)	F3 P1 F4	89.1(5)
N4 Ru1 N1	94.5(3)	C12 C11 C3	120.6(9)	F3 P1 F5	89.6(4)
N4 Ru1 N2	90.2(3)	C12 C11 C16	117.1(9)	F3 P1 F6	90.6(5)
N4 Ru1 N3	78.5(4)	C16 C11 C3	122.2(9)	F4 P1 F1	91.9(6)
N4 Ru1 N6	96.0(3)	C13 C12 C11	120.5(10)	F4 P1 F2	178.9(5)

Table 6.3 (cont'd)

Atoms	Angle/°	Atoms	Angle/°	Atoms	Angle/°
N5 Ru1 N1	91.4(3)	C14 C13 C12	119.3(10)	F4 P1 F5	90.6(4)
N5 Ru1 N2	94.6(3)	C13 C14 Br1	116.9(8)	F4 P1 F6	90.4(5)
N5 Ru1 N3	95.9(3)	C15 C14 Br1	120.7(8)	F6 P1 F1	89.5(5)
N5 Ru1 N4	173.1(3)	C15 C14 C13	122.2(10)	F6 P1 F2	88.5(5)
N5 Ru1 N6	79.5(3)	C14 C15 C16	121.0(10)	F6 P1 F5	178.9(5)
N6 Ru1 N3	87.1(3)	C15 C16 C11	119.8(10)	F8 P2 F7	89.7(3)
C1 N1 Ru1	126.7(6)	N3 C17 C18	123.2(10)	F8[1] P2 F7	89.7(3)
C5 N1 Ru1	117.7(5)	C19 C18 C17	117.4(10)	F8[1] P2 F8	179.4(5)
C5 N1 C1	115.5(7)	C18 C19 C20	121.1(10)	F8[1] P2 F9	90.3(3)
C6 N2 Ru1	115.0(5)	C21 C20 C19	119.5(11)	F8 P2 F9	90.3(3)
C10 N2 Ru1	128.9(7)	N3 C21 C20	119.3(10)	F8 P2 F10[1]	91.1(4)
C10 N2 C6	116.0(8)	N3 C21 C22	115.4(9)	F8 P2 F10	88.9(4)
C17 N3 Ru1	125.2(8)	C20 C21 C22	125.3(10)	F8[1] P2 F10	91.1(4)
C17 N3 C21	119.4(8)	N4 C22 C21	108.6(9)	F8[1] P2 F10[1]	88.9(4)
C21 N3 Ru1	115.4(7)	C23 C22 N4	128.0(9)	F9 P2 F7	180.0
C22 N4 Ru1	122.2(6)	C23 C22 C21	123.3(9)	F9 P2 F10[1]	92.7(4)
C26 N4 Ru1	131.0(7)	C22 C23 C24	122.6(10)	F9 P2 F10	92.7(4)
C26 N4 C22	106.8(9)	C23 C24 C25	116.7(11)	F10 P2 F7	87.3(4)
C27 N5 Ru1	133.9(6)	C26 C25 C24	116.6(11)	F10[1] P2 F7	87.3(4)
C27 N5 C31	104.6(9)	C25 C26 N4	129.2(10)	F10 P2 F10[1]	174.6(8)
C31 N5 Ru1	121.5(6)	C28 C27 N5	129.2(9)	F11 P3 F11[2]	94.8(14)
C32 N6 Ru1	114.6(6)	C27 C28 C29	121.1(10)	F11 P3 F12	90.9(5)
C36 N6 Ru1	126.5(8)	C30 C29 C28	115.2(11)	F11[2] P3 F12	89.5(5)
C36 N6 C32	118.6(9)	C31 C30 C29	124.1(10)	F11[2] P3 F12[2]	90.9(5)
C2 C1 N1	124.9(8)	N5 C31 C32	106.1(9)	F11 P3 F12[2]	89.5(5)
C1 C2 C3	119.2(8)	C30 C31 N5	125.8(9)	F11 P3 F13	160.0(11)
C2 C3 C11	121.5(8)	C30 C31 C32	127.9(10)	F11[2] P3 F13	65.5(8)
C4 C3 C2	116.6(8)	N6 C32 C31	117.4(9)	F12[2] P3 F12	179.4(5)
C4 C3 C11	121.8(8)	N6 C32 C33	120.2(9)	F12[2] P3 F13	87.9(7)
C3 C4 C5	119.9(8)	C33 C32 C31	122.3(10)	F12 P3 F13	91.8(7)
N1 C5 C4	123.5(8)	C34 C33 C32	118.9(11)	F14 P3 F11	154.8(9)
N1 C5 C6	113.6(8)	C35 C34 C33	119.2(10)	F14 P3 F11[2]	110.4(8)
C4 C5 C6	122.6(8)	C34 C35 C36	119.5(11)	F14 P3 F12[2]	90.0(7)
N2 C6 C5	114.6(8)	N6 C36 C35	123.4(11)	F14 P3 F12	89.4(7)
N2 C6 C7	120.7(8)	F1 P1 F2	87.7(5)	P3 F13 F11[2]	53.4(6)

[1]2-x, +y, 3/2-z; [2]1-x, +y, 3/2-z

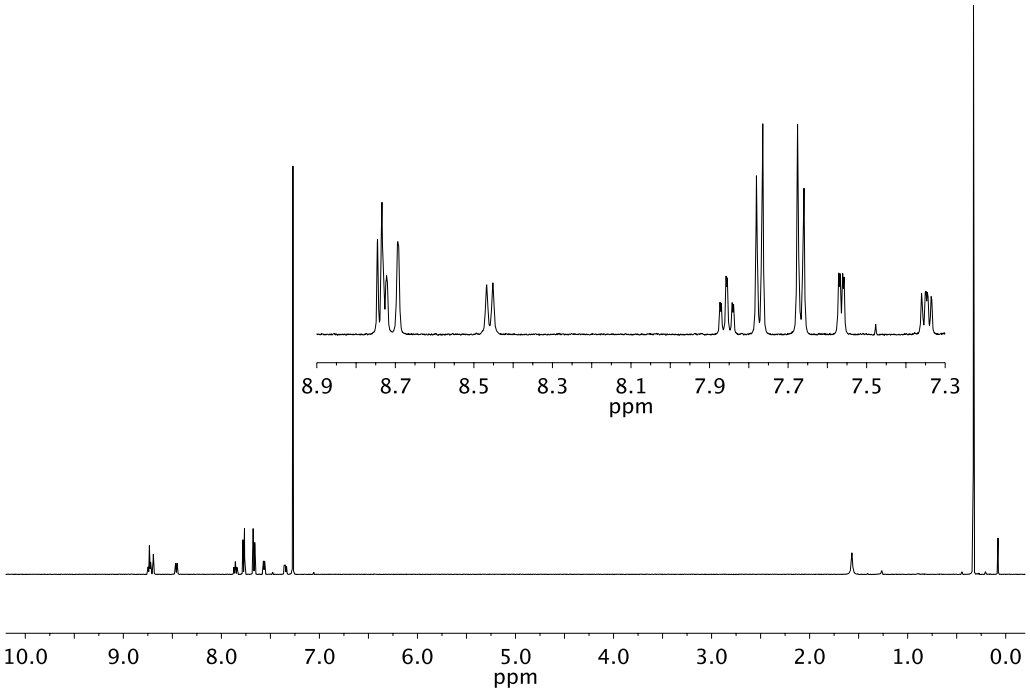


Figure 6.24. ^{1}H NMR of 4-(4-(trimethylsilyl)phenyl)-2,2'-bipyridine in $CDCl_3$.

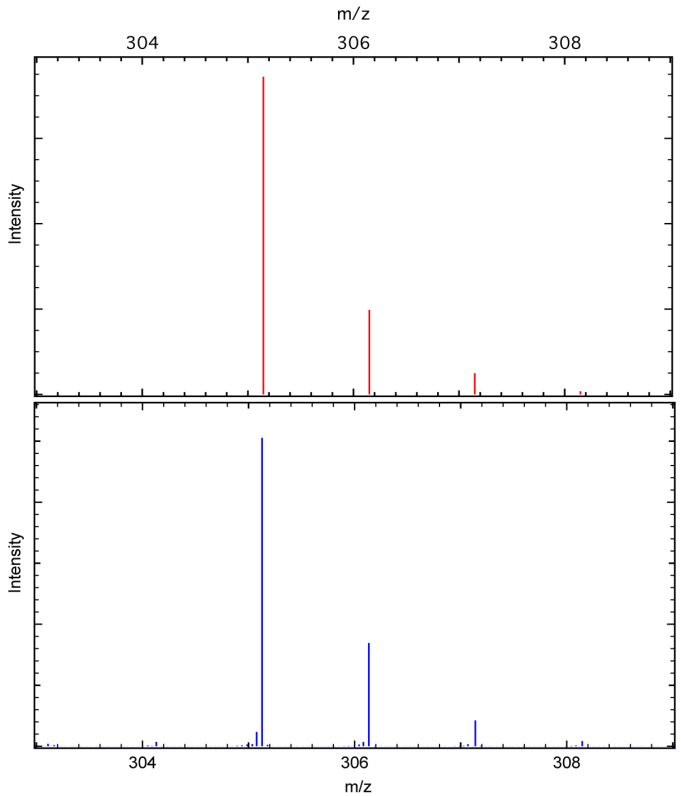


Figure 6.25. ESI-MS of 4-(4-(trimethylsilyl)phenyl)-2,2'-bipyridine. Top: predicted isotope pattern for $[M+H]^+$ ($C_{19}H_{21}N_2Si$). Bottom: experimental result.

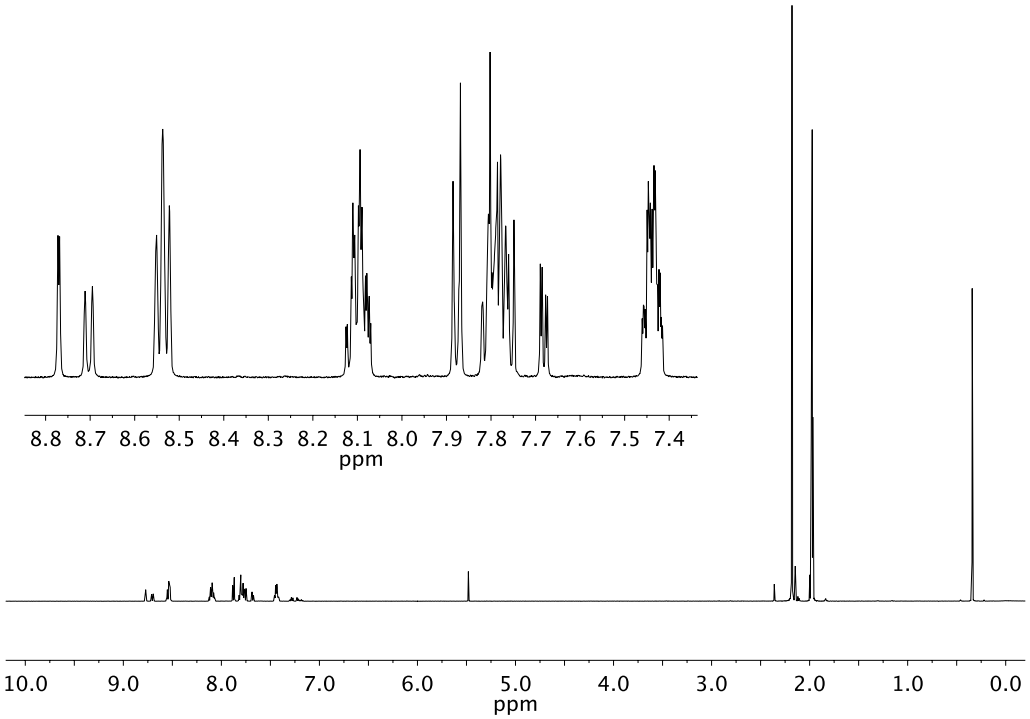


Figure 6.26. ^{1}H NMR of $[Ru(bpy)_2(bpy\text{-}Ph\text{-}TMS)](PF_6)_2$ in CD_3CN.

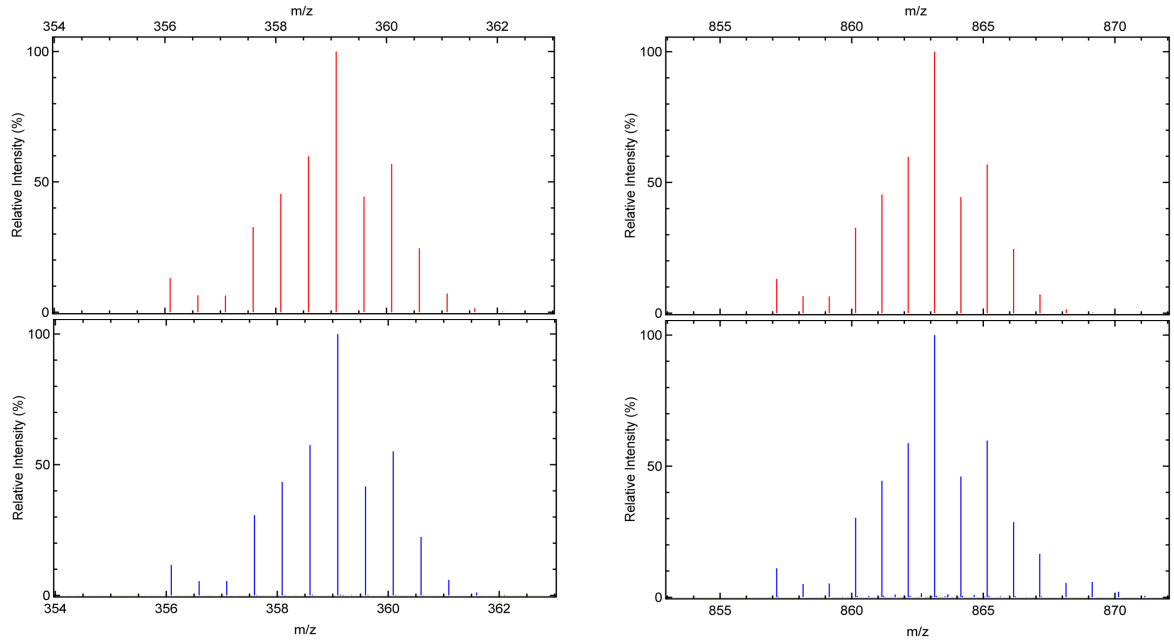


Figure 6.27. ESI-MS of $[Ru(bpy)_2(bpy\text{-}Ph\text{-}TMS)](PF_6)_2$. Top left: predicted isotope pattern for $[M–2PF_6]^{2+}$ ($C_{39}H_{36}N_6RuSi$). Bottom left: experimental result. Top right: predicted isotope pattern for $[M–PF_6]^{+}$ ($C_{39}H_{36}N_6RuSiPF_6$). Bottom right: experimental result.

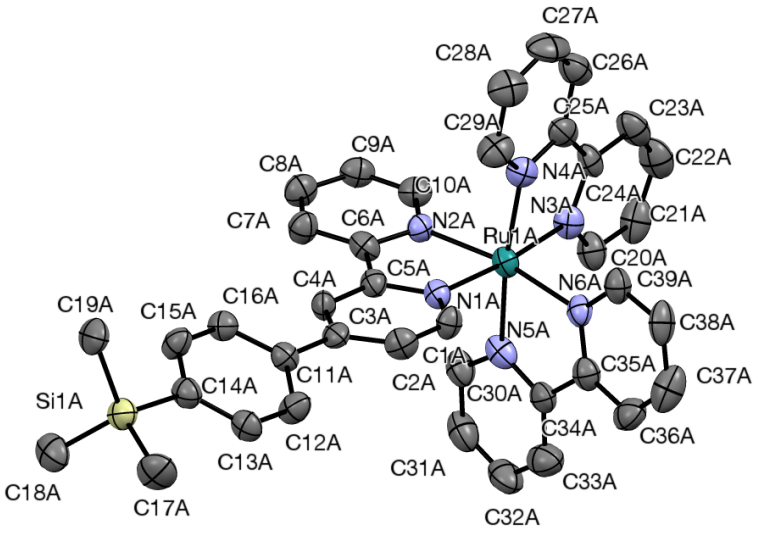


Figure 6.28. ORTEP drawing of $[Ru(bpy)_2(bpy\text{-}Ph\text{-}TMS)]^{2+}$ showing the labelling system. Atoms are represented as 50% probability thermal ellipsoids. Anions and solvent molecules omitted.

Table 6.4. Bond lengths for the X-ray structure of $[Ru(bpy)_2(bpy\text{-}Ph\text{-}TMS)](PF_6)_2$.

Atoms	Length/Å	Atoms	Length/Å	Atoms	Length/Å
Ru1A N1A	2.050(8)	C5A C6A	1.451(15)	C37A C38A	1.392(19)
Ru1A N2A	2.061(8)	C6A C7A	1.408(15)	C38A C39A	1.373(16)
Ru1A N3A	2.048(8)	C7A C8A	1.357(16)	P2 F7	1.567(12)
Ru1A N4A	2.050(9)	C8A C9A	1.379(16)	P2 F8	1.574(9)
Ru1A N5A	2.044(9)	C9A C10A	1.356(16)	P2 F9	1.550(11)
Ru1A N6A	2.058(9)	C11A C12A	1.394(14)	P2 F10	1.582(9)
Si1A C14A	1.872(11)	C11A C16A	1.421(14)	P2 F11	1.600(8)
Si1A C17A	1.874(13)	C12A C13A	1.384(14)	P2 F12	1.578(8)
Si1A C18A	1.878(13)	C13A C14A	1.397(15)	P1 F1	1.608(8)
Si1A C19A	1.865(12)	C14A C15A	1.389(15)	P1 F2	1.575(8)
N1A C1A	1.353(13)	C15A C16A	1.363(14)	P1 F3	1.561(10)
N1A C5A	1.366(13)	C20A C21A	1.379(16)	P1 F4	1.589(8)
N2A C6A	1.359(13)	C21A C22A	1.375(19)	P1 F5	1.602(10)
N2A C10A	1.342(13)	C22A C23A	1.351(19)	P1 F6	1.559(9)
N3A C20A	1.353(14)	C23A C24A	1.368(16)	Cl1S C8S	1.77(2)
N3A C24A	1.359(14)	C24A C25A	1.462(16)	Cl1S C9S	1.76(2)
N4A C25A	1.371(14)	C25A C26A	1.385(16)	Cl2S C9S	1.77(2)
N4A C29A	1.350(14)	C26A C27A	1.380(19)	Cl3S C8S	1.79(2)
N5A C30A	1.379(15)	C27A C28A	1.363(19)	C1S C2S	1.45(3)

Table 6.4 (cont'd)

Atoms	Length/Å	Atoms	Length/Å	Atoms	Length/Å
N5A C34A	1.358(14)	C28A C29A	1.369(16)	C1S C6S	1.37(3)
N6A C35A	1.334(14)	C30A C31A	1.400(17)	C1S C7S	1.58(3)
N6A C39A	1.363(14)	C31A C32A	1.358(19)	C2S C3S	1.49(3)
C1A C2A	1.352(14)	C32A C33A	1.363(19)	C3S C4S	1.33(3)
C2A C3A	1.395(15)	C33A C34A	1.391(16)	C4S C5S	1.38(4)
C3A C4A	1.377(15)	C34A C35A	1.478(15)	C5S C6S	1.40(3)
C3A C11A	1.456(13)	C35A C36A	1.382(16)	C5S C6S	1.40(3)
C4A C5A	1.392(14)	C36A C37A	1.389(18)		

Table 6.5. Bond angles for the X-ray structure of $[Ru(bpy)_2(bpy\text{-}Ph\text{-}TMS)](PF_6)_2$.

Atoms	Angle/°	Atoms	Angle/°	Atoms	Angle/°
N1A Ru1A N2A	78.8(3)	N1A C5A C4A	119.8(9)	C36A C37A C38A	117.8(11)
N1A Ru1A N6A	92.2(3)	N1A C5A C6A	114.9(9)	C39A C38A C37A	119.2(11)
N3A Ru1A N1A	174.4(4)	C4A C5A C6A	125.3(9)	N6A C39A C38A	122.7(11)
N3A Ru1A N2A	97.0(3)	N2A C6A C5A	115.4(9)	F7 P2 F8	93.3(8)
N3A Ru1A N4A	78.6(4)	N2A C6A C7A	120.7(10)	F7 P2 F10	88.1(8)
N3A Ru1A N6A	92.3(3)	C7A C6A C5A	123.9(10)	F7 P2 F11	86.9(6)
N4A Ru1A N1A	97.5(3)	C8A C7A C6A	118.6(11)	F7 P2 F12	91.8(6)
N4A Ru1A N2A	90.1(3)	C7A C8A C9A	120.9(11)	F8 P2 F10	178.5(8)
N4A Ru1A N6A	97.0(3)	C10A C9A C8A	117.7(11)	F8 P2 F11	89.1(5)
N5A Ru1A N1A	88.3(3)	N2A C10A C9A	124.0(11)	F8 P2 F12	90.0(5)
N5A Ru1A N2A	95.0(4)	C12A C11A C3A	122.1(9)	F9 P2 F7	176.1(8)
N5A Ru1A N3A	95.8(3)	C12A C11A C16A	117.4(9)	F9 P2 F8	90.0(7)
N5A Ru1A N4A	172.9(4)	C16A C11A C3A	120.5(9)	F9 P2 F10	88.6(7)
N5A Ru1A N6A	78.7(4)	C13A C12A C11A	121.1(10)	F9 P2 F11	91.0(7)
N6A Ru1A N2A	169.2(3)	C12A C13A C14A	121.6(10)	F9 P2 F12	90.3(7)
C14A Si1A C17A	109.6(6)	C13A C14A Si1A	122.2(8)	F10 P2 F11	90.7(5)
C14A Si1A C18A	107.5(5)	C15A C14A Si1A	121.2(8)	F12 P2 F10	90.2(6)
C17A Si1A C18A	111.2(6)	C15A C14A C13A	116.6(9)	F12 P2 F11	178.4(7)
C19A Si1A C14A	107.8(5)	C16A C15A C14A	123.2(10)	F2 P1 F1	89.1(5)
C19A Si1A C17A	111.3(7)	C15A C16A C11A	120.0(10)	F2 P1 F4	177.3(6)
C19A Si1A C18A	109.3(6)	N3A C20A C21A	122.4(12)	F2 P1 F5	88.7(5)
C1A N1A Ru1A	126.8(7)	C22A C21A C20A	119.1(12)	F3 P1 F1	176.5(6)
C1A N1A C5A	117.8(8)	C23A C22A C21A	119.3(12)	F3 P1 F2	90.4(5)
C5A N1A Ru1A	115.5(7)	C22A C23A C24A	119.9(12)	F3 P1 F4	91.3(5)
C6A N2A Ru1A	115.1(7)	N3A C24A C23A	122.6(11)	F3 P1 F5	90.2(7)

Table 6.5 (cont'd)

Atoms	Angle/°	Atoms	Angle/°	Atoms	Angle/°
C10A N2A Ru1A	126.9(7)	N3A C24A C25A	113.7(9)	F4 P1 F1	89.1(5)
C10A N2A C6A	118.0(9)	C23A C24A C25A	123.8(11)	F4 P1 F5	89.2(6)
C20A N3A Ru1A	126.3(8)	N4A C25A C24A	115.4(10)	F5 P1 F1	86.3(6)
C20A N3A C24A	116.8(9)	N4A C25A C26A	119.7(11)	F6 P1 F1	90.0(6)
C24A N3A Ru1A	116.9(7)	C26A C25A C24A	124.8(10)	F6 P1 F2	89.2(5)
C25A N4A Ru1A	115.4(7)	C27A C26A C25A	120.3(11)	F6 P1 F3	93.5(6)
C29A N4A Ru1A	125.4(8)	C28A C27A C26A	118.9(11)	F6 P1 F4	92.7(6)
C29A N4A C25A	119.3(10)	C27A C28A C29A	120.1(12)	F6 P1 F5	175.8(6)
C30A N5A Ru1A	125.2(8)	N4A C29A C28A	121.6(12)	Cl1S C8S Cl3S	111.7(18)
C34A N5A Ru1A	115.8(7)	N5A C30A C31A	119.5(12)	Cl1S C9S Cl2S	105.1(15)
C34A N5A C30A	119.0(10)	C32A C31A C30A	120.9(12)	C2S C1S C7S	117(2)
C35A N6A Ru1A	116.1(7)	C31A C32A C33A	119.2(13)	C6S C1S C2S	123(2)
C35A N6A C39A	117.9(9)	C32A C33A C34A	120.3(13)	C6S C1S C7S	119(2)
C39A N6A Ru1A	125.7(7)	N5A C34A C33A	120.9(11)	C1S C2S C3S	112(2)
C2A C1A N1A	123.6(9)	N5A C34A C35A	114.6(10)	C4S C3S C2S	126(3)
C1A C2A C3A	120.3(10)	C33A C34A C35A	124.4(11)	C3S C4S C5S	114(3)
C2A C3A C11A	119.8(10)	N6A C35A C34A	114.6(10)	C4S C5S C6S	127(3)
C4A C3A C2A	116.4(9)	N6A C35A C36A	122.4(11)	C1S C6S C5S	116(3)
C4A C3A C11A	123.7(9)	C36A C35A C34A	123.0(11)		
C3A C4A C5A	122.1(9)	C35A C36A C37A	120.0(12)		

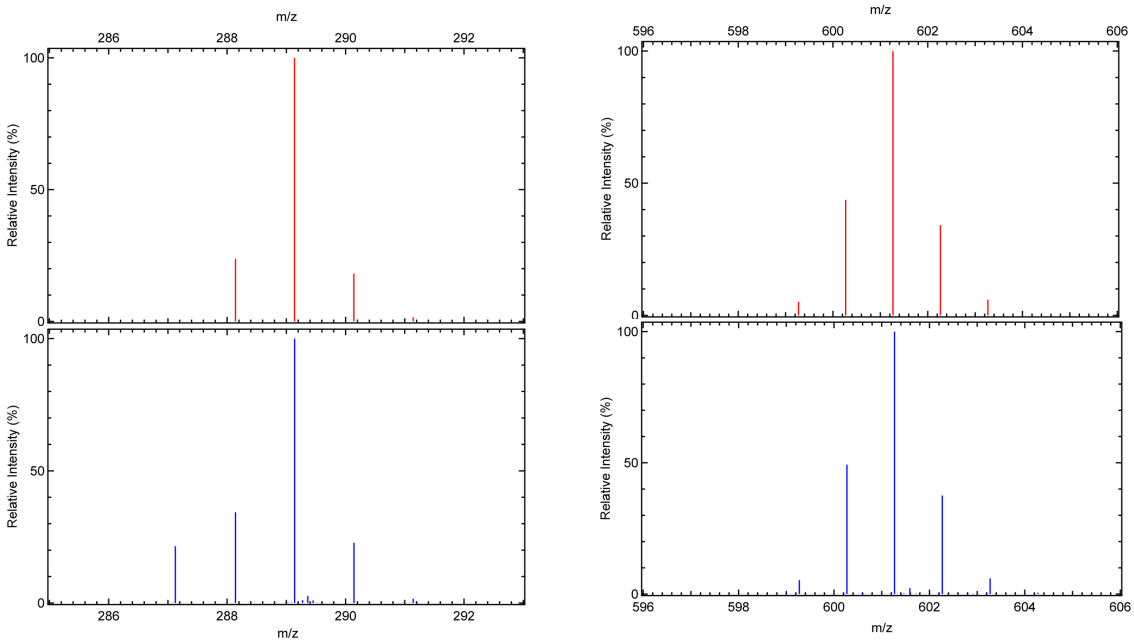


Figure 6.29. ESI-MS of sodium phenyltris(1-pyrazolyl)borate. Top left: predicted isotope pattern for $[M–Na]^-$ ($C_{15}H_{14}N_6B$). Bottom left: experimental result. Top right: predicted isotope pattern for $[2M+Na]^-$ ($C_{30}H_{28}N_{12}B_2Na$). Bottom right: experimental result.

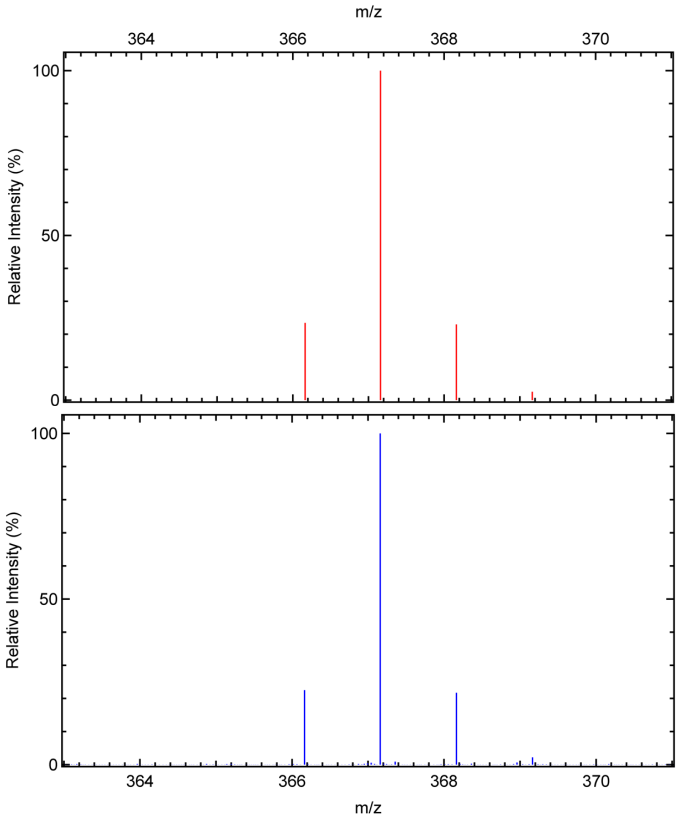


Figure 6.30. ESI-MS of sodium 4-[tris(1-pyrazolyl)borate]-2,2'-bipyridine. Top: predicted isotope pattern for $[M–Na]^+$ ($C_{19}H_{16}N_8B$). Bottom: experimental result.

REFERENCES

REFERENCES

(1) Bradley, A. *A Red Herring Without Mustard (Flavia de Luce #3)*; Bantam Books, 2011.

(2) Weldon, B. T.; Wheeler, D. E.; Kirby, J. P.; McCusker, J. K. *Inorg. Chem.* **2001**, *40*, 6802–6812.

(3) Picraux, L. B.; Weldon, B. T.; McCusker, J. K. *Inorg. Chem.* **2002**, *42*, 273–282.

(4) Picraux, L. B.; Smeigh, A. L.; Guo, D.; McCusker, J. K. *Inorg. Chem.* **2005**, *44*, 7846–7859.

(5) Picraux, L. B. Studies of Intramolecular Electron and Energy Transfer in Donor-Acceptor Assemblies Incorporating a Heisenberg Spin Coupled Metal Center, University of California, Berkeley, 2003.

(6) Johansson Seechurn, C. C. C.; Kitching, M. O.; Colacot, T. J.; Snieckus, V. *Angew. Chem. Int. Ed.* **2012**, *51*, 5062–5085.

(7) Reger, D. L.; Gardinier, J. R.; Bakbak, S.; Semeniuc, R. F.; Bunz, U. H. F.; Smith, M. D. *New J. Chem.* **2005**, *29*, 1035–1043.

(8) Armarego, W. L. F.; Chai, C. L. L. *Purification of Organic Chemicals*, 6th ed.; Elsevier, 2009.

(9) Korall, P.; Borje, A.; Norrby, P.-O.; Akermark, B. *Acta Chem. Scand.* **1997**, *51*, 760–766.

(10) Baron, A.; Herrero, C.; Quaranta, A.; Charlot, M.-F.; Leibl, W.; Vauzeilles, B.; Aukauloo, A. *Inorg. Chem.* **2012**, *51*, 5985–5987.

(11) Hirahara, M.; Masaoka, S.; Sakai, K. *Dalton Trans.* **2011**, *40*, 3967–3978.

(12) Fulmer, G. R.; Miller, A. J. M.; Sherden, N. H.; Gottlieb, H. E.; Nudelman, A.; Stoltz, B. M.; Bercaw, J. E.; Goldberg, K. I. *Organometallics* **2010**, *29*, 2176–2179.

(13) Joachim Demnitz, F. W.; D'Heni, M. B. *Org. Prep. Proced. Int.* **1998**, *30*, 467–469.

(14) Grosshenny, V.; Romero, F. M.; Ziessel, R. *J. Org. Chem.* **1997**, *62*, 1491–1500.

(15) Reger, D. L.; Gardinier, J. R.; Smith, M. D.; Shahin, A. M.; Long, G. J.; Rebbouh, L.; Grandjean, F. *Inorg. Chem.* **2005**, *44*, 1852–1866.

(16) Zagermann, J.; Kuchta, M. C.; Merz, K.; Metzler-Nolte, N. *Eur. J. Inorg. Chem.* **2009**, 5407–5412.

(17) Fraysse, S.; Coudret, C.; Launay, J.-P. *Eur. J. Inorg. Chem.* **2000**, 1581–1590.

(18) Cordaro, J. G.; McCusker, J. K.; Bergman, R. G. *Chem Commun.* **2002**, 1496–1497.

(19) Li, W.; Nelson, D. P.; Jensen, M. S.; Hoerrner, R. S.; Cai, D.; Larsen, R. D.; Reider, P. J. *J. Org. Chem.* **2002**, *67*, 5394–5397.

(20) Desrochers, P. J.; Pearce, A. J.; Rogers, T. R.; Rodman, J. S. *Eur. J. Inorg. Chem.* **2016**, 2465–2473.

(21) Trofimenko, S. *Chem. Rev.* **1993**, *93*, 943–980.

(22) Trofimenko, S. *Polyhedron* **2004**, *23*, 197–203.

(23) Damrauer, N. H.; Boussie, T. R.; Devenney, M.; McCusker, J. K. *J. Am. Chem. Soc.* **1997**, *119*, 8253–8268.

(24) McCusker, C. E.; McCusker, J. K. *Inorg. Chem.* **2011**, *50*, 1656–1669.

(25) Kuchta, M. C.; Gemel, C.; Metzler-Nolte, N. *J. Organomet. Chem.* **2007**, *692*, 1310–1314.

(26) Urban, P. L. *Philos. Trans. A. Math. Phys. Eng. Sci.* **2016**, *374*, 20150382.

(27) Bruins, A. P. *J. Chromatogr. A* **1998**, *794*, 345–357.

(28) Hoffmann, E. De; Stroobant, V. *Mass Spectrometry - Priniples and Applications*, 3rd ed.; John Wiley & Sons, Ltd., 2007; Vol. 29.

(29) Benniston, A. C.; Harriman, A.; Li, P.; Patel, P. V.; Rostron, J. P.; Sams, C. A. *J. Phys. Chem. A* **2006**, *110*, 9880–9886.

(30) Iranmanesh, H.; Arachchige, K. S. A.; Bhadbhade, M.; Donald, W. A.; Liew, J. Y.; Liu, K. T.-C.; Luis, E. T.; Moore, E. G.; Price, J. R.; Yan, H.; Yang, J.; Beves, J. E. *Inorg. Chem.* **2016**, *55*, 12737–12751.

(31) Negishi, E.; Anastasia, L. *Chem. Rev.* **2003**, *103*, 1979–2018.

(32) Kurti, L.; Czako, B. *Strategic Applications of Named Reactions in Organic Synthesis*; Elsevier: Amsterdam, 2005.

(33) Hall, H. K. *J. Am. Chem. Soc.* **1957**, *79*, 5441–5444.

(34) Ishida, N.; Moriya, T.; Goya, T.; Murakami, M. *J. Org. Chem.* **2010**, *75*, 8709–8712.

(35) Ye, B. H.; Naruta, Y. *Tetrahedron* **2003**, *59*, 3593–3601.

(36) *Microwaves in Organic Synthesis*, 3rd ed.; de la Hoz, A., Loupy, A., Eds.; John Wiley & Sons, Inc.: Weinheim, Germany, 2012.

(37) Turner, H. S.; Warne, R. J. *Adv. Chem.* **1964**, 290–300.

(38) Altobello, S.; Bignozzi, C. A.; Caramori, S.; Larramona, G.; Quici, S.; Marzanni, G.; Lakhmiri, R. *J. Photochem. Photobiol. A Chem.* **2004**, *166*, 91–98.

(39) Matsumura-Inoue, T.; Tanabe, M.; Minami, T.; Ohashi, T. *Chem. Lett.* **1994**, *12*, 2443–2446.

(40) Wu, F.; Riesgo, E.; Pavalova, A.; Kipp, R. A.; Schmehl, R. H.; Thummel, R. P. *Inorg. Chem.* **1999**, *38*, 5620–5628.

(41) Wu, F.; Thummel, R. P. *Inorg. Chim. Acta* **2002**, *327*, 26–30.

(42) Sun, Y.; Machala, M. L.; Castellano, F. N. *Inorg. Chim. Acta* **2010**, *363*, 283–287.

(43) Vitze, H.; Bolte, M.; Lerner, H.-W.; Wagner, M. *Eur. J. Inorg. Chem.* **2016**, 2443–2454.

(44) Miao, W.; Zhao, Y.; Ni, C.; Gao, B.; Zhang, W.; Hu, J. *J. Am. Chem. Soc.* **2018**, *140*, 880–883.

(45) van der Sluis, M.; Beverwijk, V.; Termaten, A.; Bickelhaupt, F.; Kooijman, H.; Spek, A. L. *Organometallics* **1999**, *18*, 1402–1407.

(46) *Handbook of Grignard Reagents*; Silverman, G. S., Rakita, P. E., Eds.; CRC Press, 1996.

(47) Pawar, G. M.; Sheridan, J. B.; Jäkle, F. *Eur. J. Inorg. Chem.* **2016**, 2227–2235.